Dark Matter Search
with CsI(Tℓ) Crystals

Hyun Su Lee

Under the supervision of
Professor Sun Kee Kim

A dissertation submitted to
the Graduate Faculty of Seoul National University
in partial fulfillment of the requirement
for the Degree of Doctor of Philosophy

School of Physics
The Graduate School of Natural Sciences
Seoul National University
Seoul, KOREA

February, 2007

Abstract

Existence of dark matter is strongly supported by astronomical observation and cosmological calculation. Observation of dark matter has been one of the most challenging research topics in physics. Weakly Interacting Massive Particle (WIMP) is one of the strongest candidate of dark matter which can explain most of astronomical observations and be supported by Super Symmetric (SUSY) model of particle physics. DAMA group claimed that they found WIMP using NaI(Tℓ) crystal detectors. However CDMS, EDEWEISS, and CRESST using low temperature detectors set limits which are incompatible with DAMA result. Still there are possible ways to explain both result without conflict because of differences in experimental techniques and target nuclei. Therefore another experiment compatible with DAMA is important.

The Korea Invisible Mass Search (KIMS) group has been carrying out WIMP search experiment with CsI(Tℓ) crystal detectors at the YangYang underground laboratory. A successful reduction of the internal background of the crystal was done and a good pulse shape discrimination was achieved. With four of full size ($8 \times 8 \times 30$ cm^3, 8.7 kg) crystals we have accumulated 3409 kg·days exposure to search WIMP. Using the result consistent with null observation of nuclear recoil events, we set the upper limits on the WIMP-nucleon cross sections at the 90 % confidence level. We also estimate sensitivity of our experiment with further reduction of backgrounds and successful growing of new crystals.

Keywords: Dark Matter, WIMP, CsI(Tℓ) Crystal, Scintillator, Pulse Shape

Discrimination, KIMS

Student Number: **2000-20453**

Contents

List of Figures

List of Tables

Chapter 1

Introduction

1.1 Dark Matter Problem

The question of what makes up the mass density of the universe is practically as old as extragalactic astronomy which began with the recognition that nebulae such as M31 in Andromeda are actually galaxies like our own. Some of them appear in gravitationally bound clusters. From the Doppler shifts of the spectral lines of the galaxies in the Coma cluster, Zwicky derived in 1933 their velocity dispersion and could thus estimate the cluster mass with the help of the virial theorem [1]. He concluded that the Coma cluster contained far more dark than luminous matter when he translated the luminosity of the galaxies into a corresponding mass. Since then evidence has mounted that on galactic scales and above the mass density associated with luminous matter (stars, hydrogen clouds, x-ray gas in clusters, etc.) cannot account for the observed dynamics on those scales. In the mid 1970s it had become clear that dark matter was an unavoidable reality and by the mid 1980s the view had become canonical that the universe is dominated by an unknown form of matter or by an unfamiliar class of dark astrophysical objects. Besides the origin of comic rays and γ-ray bursts the physical nature of dark matter is

1

no doubt the most stunning astrophysical mystery [2, 3, 4].

1.2 Standard Cosmology

Modern cosmology is rooted in the Friedmann solution of Einstein's field equations for an universe filled with an isotropic, homogeneous fluid of density ρ and pressure p.

$$\frac{\ddot{a}}{a} = -\frac{4\pi G}{3}(\rho + \frac{3p}{c^2}) + \frac{\Lambda}{3}, \qquad (1.1)$$

$$\frac{\dot{a}^2}{a} = \frac{8\pi G\rho}{3} + \frac{\Lambda}{3} - \frac{kc^2}{a^2}, \qquad (1.2)$$

where $a(t)$ is the fundamental distance scale parameter found in the metric $ds^2 = c^2 dt^2 - a^2(t)d\vec{x}^2$, Λ is the cosmological constant, and G is Newton's constant. The distance scale is related to Hubble's constant H_0 by the definition

$$H_0 \equiv (\dot{a}/a)_{t=t_0}, \qquad (1.3)$$

where t_0 is the present. The parameter k can be made equal to +1, 0 -1 by a rescaling of the metric coordinates which explain the types of universe by "closed" (k=+1), "flat" (k=0), or "open"(k=-1). The popular class of theories known as inflation include a mechanism to drive the universe into a state with k=0. If k=0 and $\Lambda = 0$ then Eq. 1.2 can be solved for the mass density in terms of the Hubble constant

$$\rho = \rho_c \equiv \frac{3H_0^2}{8\pi G}. \qquad (1.4)$$

Since we do not know Hubble's constant very well, it can be written in terms of Hubble's constant for critical density (ρ_c)

$$\rho_c = 1.1 \times 10^{11} h^2 \text{GeV/c}^2/\text{cm}^3.$$

Current estimated result for h from Cosmic Microwave Background (CMB) analysis [5] is $h = 0.72 \pm 0.05$.

Conventionally the mass density as fraction of the critical density, $\Omega_m = \rho_0/\rho_c$ is used in comology. To include the possibility of a non-zero cosmological constant, the total density can be written as $\Omega_{total} = \Omega_m + \Omega_\Lambda$, with $\Omega_\Lambda \equiv \Lambda/3H_0^2$. The value of Ω_Λ and Ω_m are well measured now [5] as follow:

$$\Omega_{total} = 1.02 \pm 0.02,$$

$$\Omega_m = 0.29 \pm 0.07,$$

which mean that $\Omega_\Lambda \sim 0.7$.

1.3 Dark matter and Dark energy

The expansion of the universe was discovered in 1929 by Hubble. The expansion slope, Hubble's constant, was measured with the Hubble Space Telescope. The value is to be

$$H_0 = 72 \pm 2 \pm 7 \text{ km/sec/Mpc}.$$

Type Ia supernovae, which treated as standard candles, suggest that the expansion of the universe is speeding up rather than slowing down [6]. This expansion has been attributed to a dark energy [7] component with negative pressure which can induce repulsive gravity and thus cause accelerated expansion.

It can be accounted from Einstein's theory. The cosmological constant (Λ), introduced from equation, has negative pressure and repulsive gravity. If dark energy is absent, a flat universe would decelerate by its own self-gravity, whereas dark energy allows for acceleration. The supernova measurements [6] show that the mass density of dark energy Ω_Λ is about 0.73.

The evidence for an accelerating universe from type Ia supernovae has now supported from an analysis of CMB fluctuations [5] which will be briefly discussed in Section 1.4.4. The result from CMB analysis has orthogonal degeneracy in parameter space $(\Omega_m, \Omega_\Lambda)$ with supernovae measurements. That
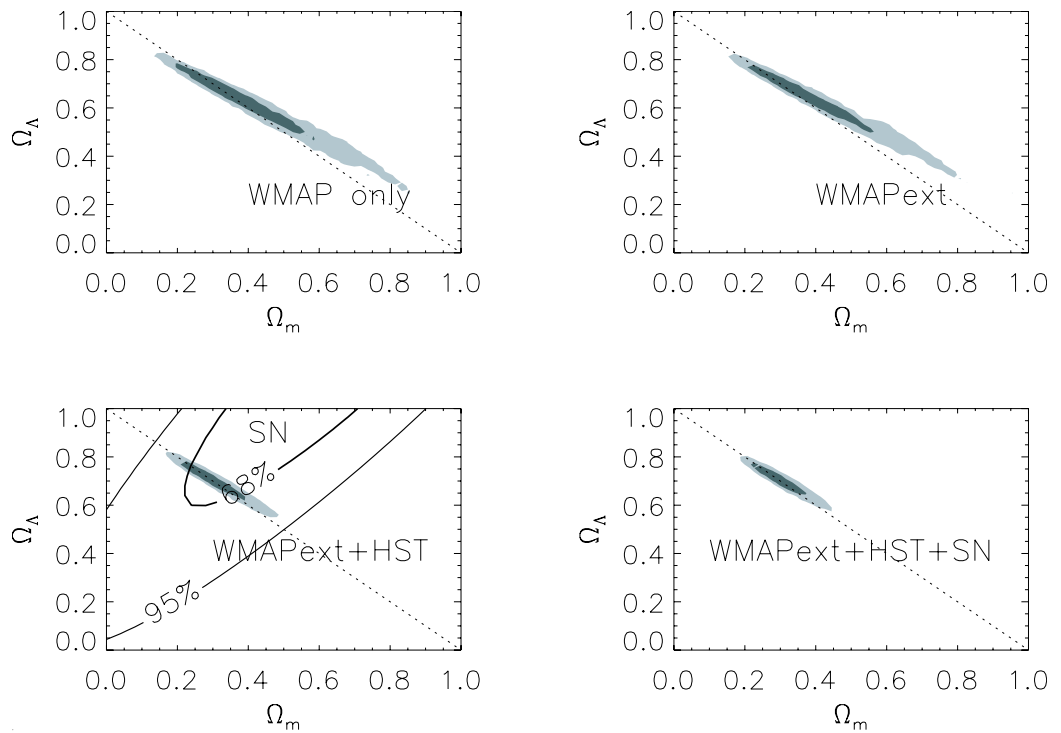
Figure 1.1: Constraints on the density of dark matter Ω_m and dark energy Ω_Λ, determined using WMAP (upper left), WMAP+other CMB experiments (WMAPext upper right), WMAPext+HST key project data (lower left) and WMAPext+HST+supernovae data (lower right) [5].

serves to significantly reduce the errors on Ω_m and Ω_Λ when the two sets of observations are combined, as shown in Fig. 1.1.

Finally we have results of $\Omega_{total} \sim 1$, $\Omega_m \sim 0.3$, and $\Omega_\Lambda \sim 0.7$.

1.4 Existence of dark matter and amounts

1.4.1 Rotation Curves of Spiral Galaxies

The most convincing and direct evidence for dark matter on galactic scales comes from the observations of the rotation curves of galaxies, namely the graph of rotational velocities of stars and gas as a function of their distance from the galactic center.

Spiral galaxies typically have neutral hydrogen in their disks which can be observed by its 21 cm line emission with optical surface photometry. Observed rotation curves usually exhibit a characteristic flat behavior at large distances as shown in Fig. 1.2. In Newtonian dynamics the circular velocity is given by

$$v(r) = \sqrt{\frac{GM(r)}{r}}, \tag{1.5}$$

where $M(r) \equiv 4\pi \int_0^r \rho(r')r'^2 dr'$, and $\rho(r)$ is the mass density profile, and should be falling $\propto 1/\sqrt{r}$ beyond the optical disc. The fact that $v(r)$ is approximately constant implies the existence of an halo with $M(r) \propto r$ and $\rho \propto 1/r^2$.

The difference from the rotation curve which is expected from the luminous material is ascribed to the gravitational effect of dark matter. A number of strong arguments suggest that this material cannot be part of the galactic disk itself. First, the distribution of stars vertically to the galactic disk in our galaxy together with their vertical velocity dispersion reveals that there cannot be any significant amount of dark matter confined to the disk.
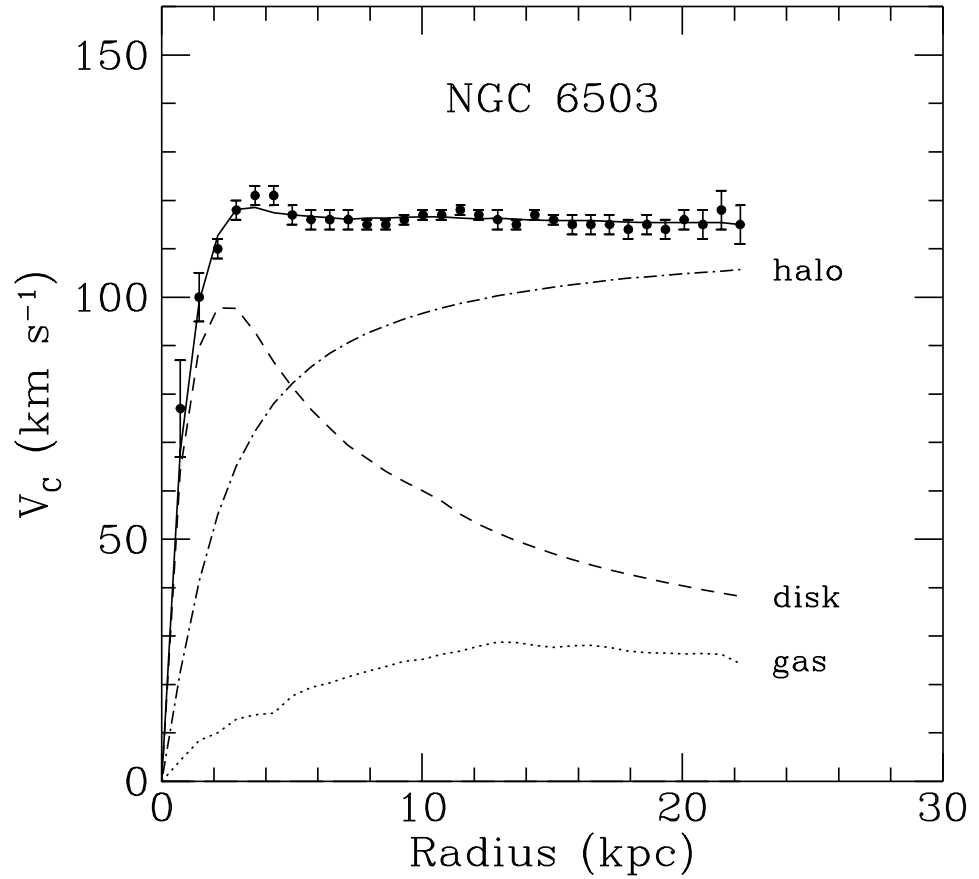
Figure 1.2: Rotation curve for the spiral galaxy NGC6503 as established from radio observations of hydrogen gas in the disk [9]. The points are the measured circular rotation velocities as a function of distance from the center of the galaxy. The dashed and dotted curves are the contribution to the rotational velocity due to the observed disk and gas, respectively, and the dot-dash curve is the contribution from the dark halo.
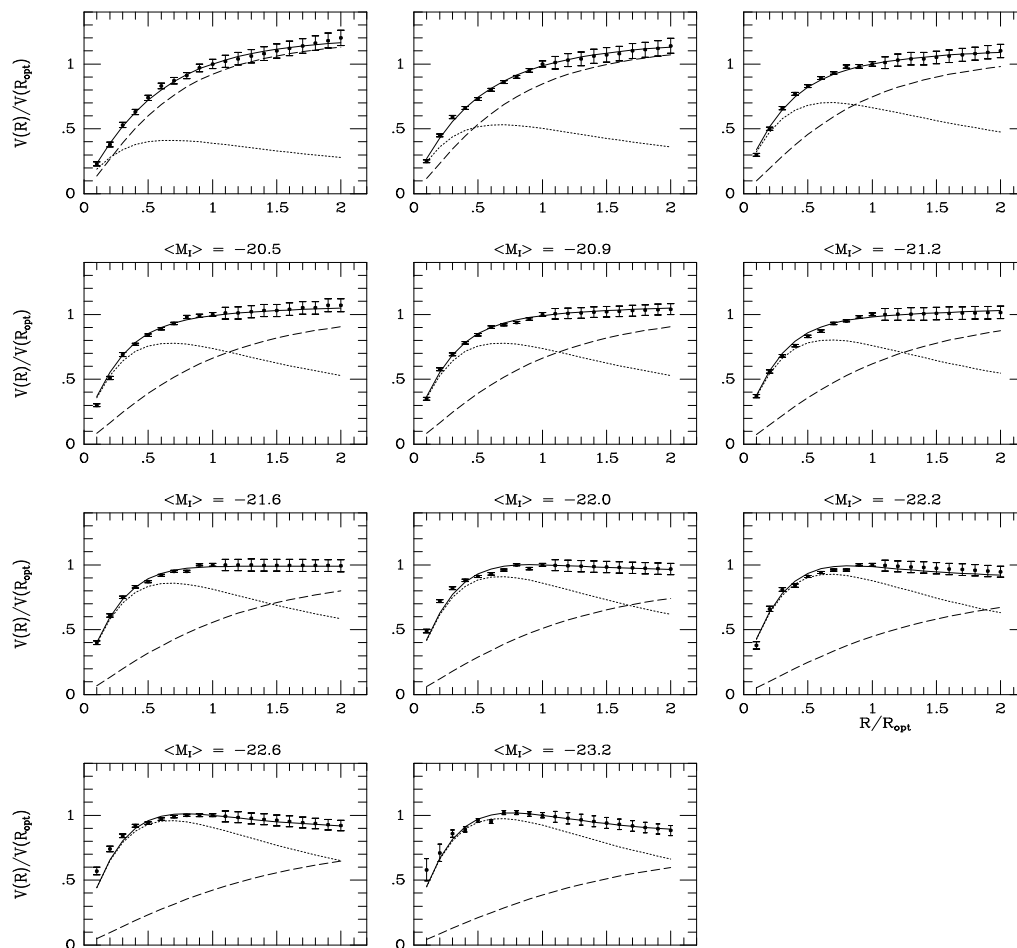
Figure 1.3: Rotation curve for 11 galaxies from Salucci and Persic, 1997 [10]. The velocity is normalized to the value at the optical radius R_{opt} , which is optical radius of galaxies that was defined as containing radius of 83% of the light, of is plotted as a function of r/R_{opt}. The points with error bar are the measured values. The contributions of the 2 components of the mass model are shown as a dashed line (dark halo), dotted line (disk), and solid line (sum).

Second, a thin self-gravitating disk is dynamically unstable. Third, the hydrogen of the disk tends to be vertically far more extended than would be expected if all of the gravitating matter were in the disk, especially at large galactocentric radii. Fourth, there exist "polar ring galaxies" with material orbiting perpendicular to the normal disk which appears to trace out a more or less spherical gravitational potential. An overall picture of spiral galaxies emerges where the bulge and disk are dynamically subdominant components immersed in a huge spherical "halo" or "corona" of dark matter [8].

For 1100 spiral galaxies, Persic and Salucci have analyzed and claim that they can all be described by a "universal rotation curve", which gives the shape of the velocity curve for any galaxy in terms of a single input parameter, the galaxy luminosity [10, 11] as shown in Fig. 1.3. The rotation curves of both low and high surface luminosity galaxies appear to suggest a universal density profile, which can be expressed as the sum of an exponential thin stellar disk, and a spherical dark matter halo.

1.4.2 Dark Matter in Our Galaxy

The knowledge of dark matter amount in the Solar system is important to the prospects for direct and indirect detection experiments. The local density of galaxy is determined by observing the rotation curve of the Milky way (see Fig. 1.4). But, our position in the Milky Way complicates the geometry that we study its structure and kinematics. It gives large error of estimation of dark matter amount in our galaxy. Furthermore we need the velocity distribution of dark matter in the vicinity of Solar system to calculate the local density of dark matter.

Different groups have come to somewhat different conclusions for the local density and velocity distribution of dark matter. For example, Bahcall *et al.*found a best-fit value of $\rho_D = 0.34$ GeV/cm^3 [12], Caldwell and Ostriker found $\rho_D = 0.23$ GeV/cm^3 [13], while Turner calculates $\rho_D = 0.3$ - 0.6 GeV/cm^3 [14].
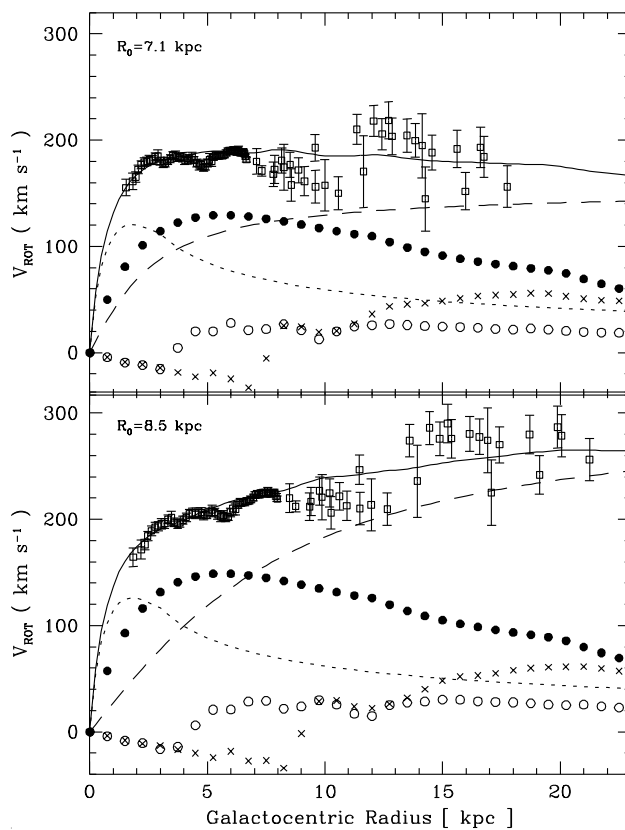
Figure 1.4: The rotation curve for the Milky Way [15] for values of $R_0 = 7.1$ kpc, $v_0 = 185$ km/s and $R_0 = 8.5$ kpc, $v_0 = 220$ km/s where R_0 is the distance from the center of the Milky Way to the solar system and v_0 is the linear velocity of solar system to galaxy center. The figure also shows one of the ways in which the rotation curve can be decomposed into the contributions from different mass components: the bulge (dotted line); the stellar disk (filled circles); the gas (crosses refer to cold hydrogen gas, where negative values mean that the force is directed outwards. Circles refer to giant molecule cloud); and the dark halo (dashed line). The best fit with those components is shown as a solid line.

1.4.3 Galaxy cluster

Galaxy clusters are groups of up to several thousand gravitationally bound galaxies. In 1933, Zwicky first noted, from measurements of the velocity dispersion of galaxies in the Coma cluster, these systems appear to contain large amounts of dark matter [1]. He used the virial theorem to obtain the masses of the cluster. The virial theorem tells us that an individual particle in a closed mechanical system will have time averaged potential (U) and kinetic energy (T) which are related

$$- < U > = 2 < T >$$

in equilibrium. Where kinetic energy can be written as $< T > = \frac{1}{2} m < v^2 >$ and potential energy can be written as $< U > = -m G_N < M/r >$. Therefore the mass of the system can be written as

$$M = \frac{2 < v^2 > < r >}{G_N}.$$

The velocity of objects are measured from the Doppler shifts of the spectral lines and the mean radii perpendicular to the line of sight. From that we can measure the total mass of these system. As Zwicky stressed, this "virial mass" of the clusters far exceeds their luminous matter content, typically leading to a mass-to-light ratio of around 300. An important example of the current observation is the work of Carlberg *et al.* [16]. They report a mean cluster mass-to-light ratio of 294 ± 50 and they obtained cosmic matter density,

$$\Omega_m = 0.24 \pm 0.05 \pm 0.09. \tag{1.6}$$

The galaxy clusters detection with X-ray telescopes from the mid 1960s said that galaxy clusters are the most powerful X-ray sources in the sky. If we assume the hydrostatic equilibrium for a system with spherical symmetry, we can get a mass fraction of X-ray for whole matter [17]. Allen *et al.* [18] calculated the X-ray mass fraction of a few galaxy clusters with Chandra telescope measurements. Also, the optically luminous baryonic mass in galaxies

is $0.19h^{0.5}$ times of the X-ray gas mass [19], Allen *et al.* [18] obtained the result $\Omega_m = 0.319 \pm 0.032$ with $h = 0.7$.

These conclusions can be checked against estimates from gravitational lensing data. The distortion of the images of background objects due to the galaxy cluster can be used to infer the shape of the gravitational potential well and thus the mass of the cluster by Eistein's theory of general relativity. D. Clowe *et al.* [20] found direct evidence for the existence of dark matter by using the interacting cluster 1E0657-558. With measured luminosity and reconstructed mass from weak lensing, they concluded that dark matter exists.

1.4.4 Cosmic Microwave Background (CMB)

Cosmic Microwave Background (CMB) was predicted by George Gamow and his collaborators in 1948 and discovered by Arno Penzias and Robert Wilson in 1965. Recently precision measurements on CMB have been made by COBE [21], BOOMERANG [22], and WMAP [23]. These measurements show that CMB is isotropic at the 10^{-5} level and with the spectrum of a black body corresponding to a temperature $T = 2.726K$.

Today, the measurements and analyses of CMB anisotropies enable accurate test of cosmological models and put stringent constraints on cosmological parameters. The observed temperature anisotropies in the sky are usually expanded as,

$$\frac{\delta T}{T}(\theta, \phi) = \sum_{l=2}^{+\infty} \sum_{m=-l}^{m=l} a_{lm} Y_{lm}(\theta, \phi), \qquad (1.7)$$

where $Y_{lm}(\theta, \phi)$ are spherical harmonics. The variance C_l of a_{lm} is given by

$$C_l \equiv\ <|a_{lm}|^2> \equiv \frac{1}{2l+1} \sum_{m=-l}^{l} |a_{lm}|^2. \qquad (1.8)$$

If the temperature fluctuations are assumed to be Gaussian, all the information contained in CMB maps can be compressed into the power spectrum,
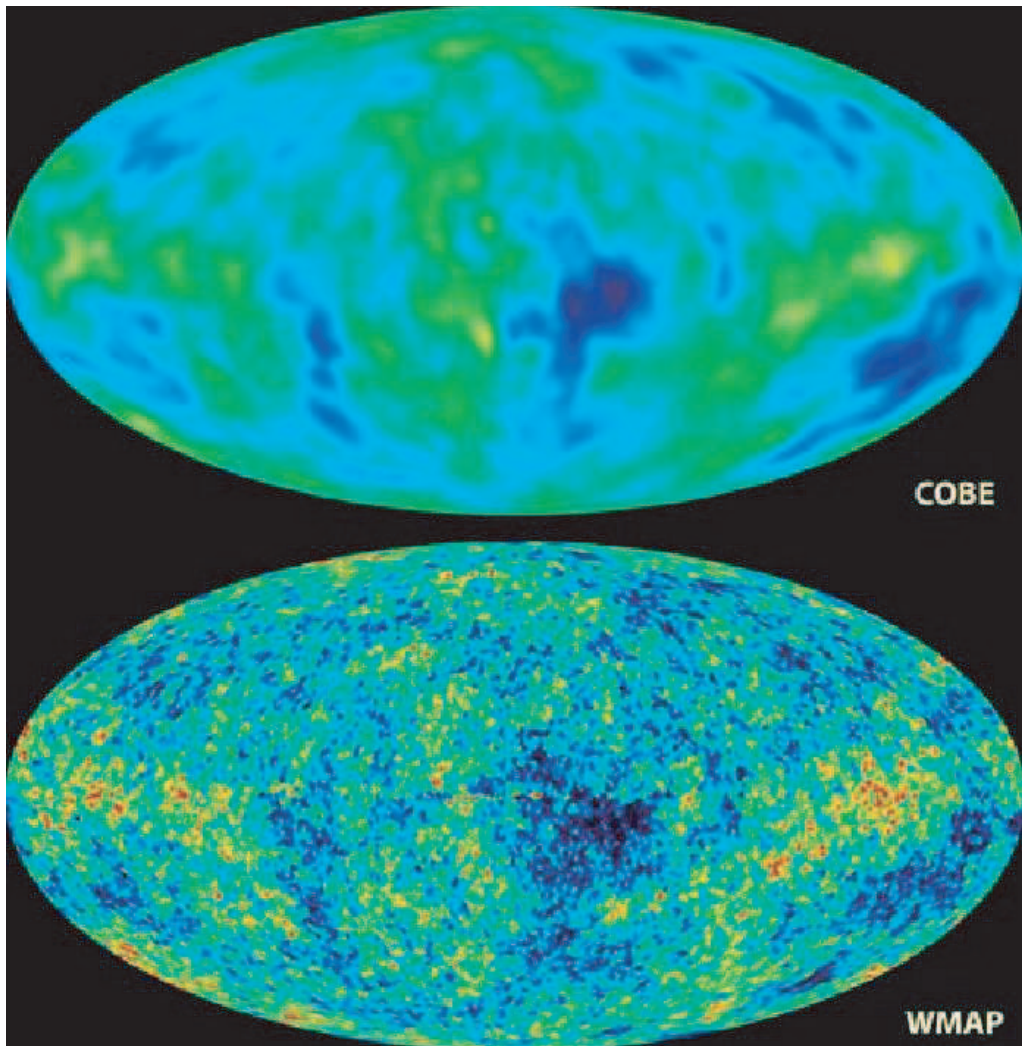
Figure 1.5: CMB temperature fluctuations: A comparison between COBE and WMAP Image from http://map.gsfc.nasa.gov
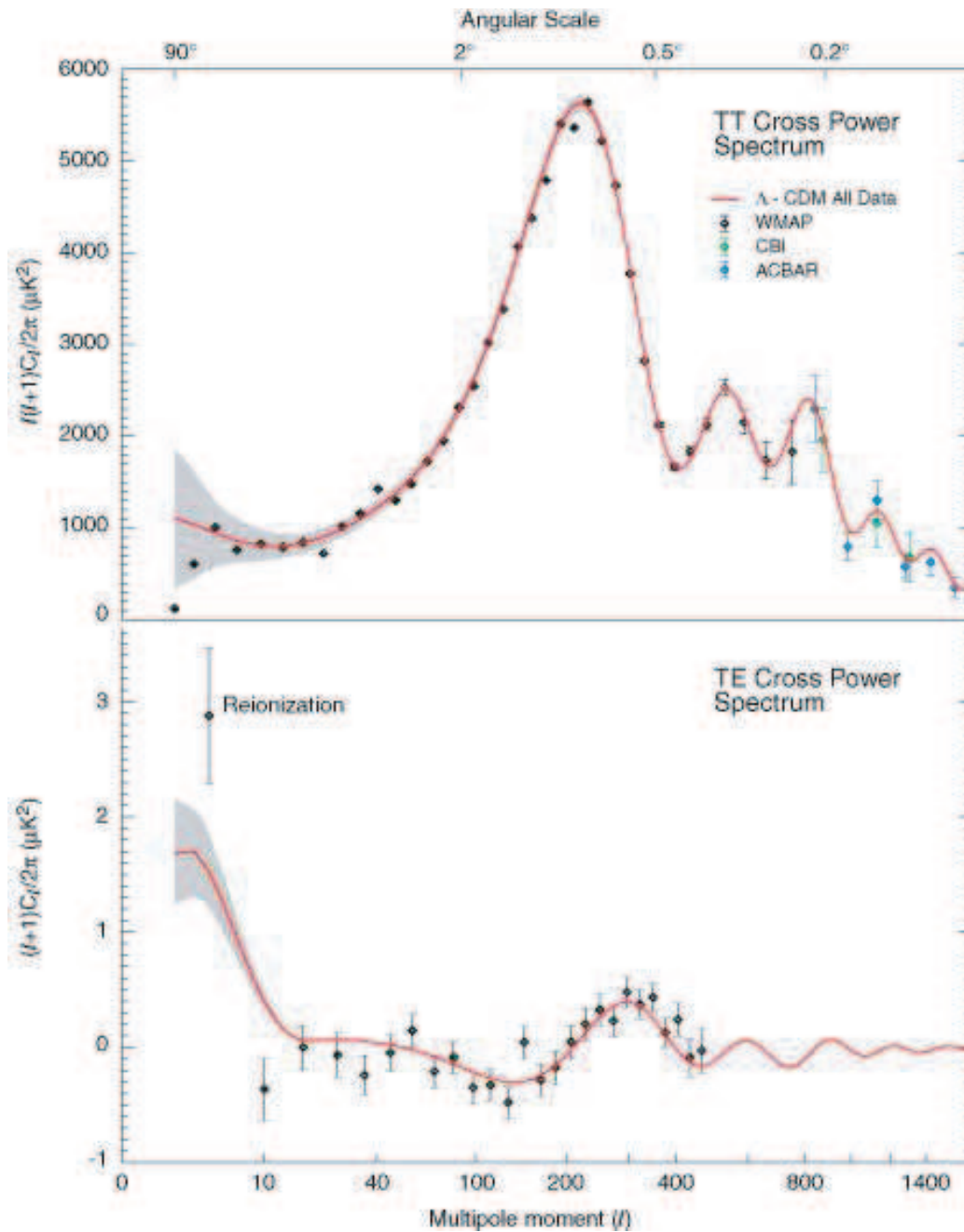
Figure 1.6: The WMAP angular power spectrum [23]

essentially giving the behavior of C_l as a function of l. Usually plotted power spectrum is $l(l+1)C_l/2\pi$ as shown in Fig. 1.6.

Starting from a cosmological model with a fixed number of parameters, the best-fit parameters are determined from the peak of the N-dimensional likelihood surface. From this analysis, one can extract cosmological information.

Taking into account data from CMB experiments, the following values are found for the abundance of baryons and matter in the Universe [5],

$$\Omega_b h^2 = 0.0224 \pm 0.0009, \qquad \Omega_m h^2 = 0.135^{+0.008}_{-0.009}, \tag{1.9}$$

which mean

$$\Omega_b = 0.047 \pm 0.006, \qquad \Omega_m = 0.29 \pm 0.07, \tag{1.10}$$

under $h = 0.72 \pm 0.05$.

1.4.5 Primordial Big Bang Nucleosynthesis

Big Bang Nucleosynthesis (BBN) is a generic scenario for explanation of abundances of light element using a hot Big Bang scenario [24, 25, 26]. In the very early universe the temperature was very high that all matter was fully ionized and nucleons were dissociated. Approximately 3 minutes after Big Bang, the universe had cooled down from 10^{32} to 10^9 K. At this state, light elements, for instance photons, protons, neutrons and electrons, could take place. In the short time from 3 minutes, universe had cooled to the point where deutrium can be formed. Deutrium formation is the first step in a whole sequence of nuclear reactions to make helium by two kinds reaction as follows:

$$d + d \rightarrow t + p,$$

$$t + d \rightarrow^4 He + p,$$

$$d + d \rightarrow^3 He + n,$$

$$^3He + d \rightarrow^4 He + p.$$
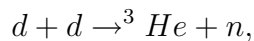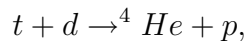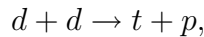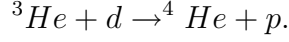
Further reactions can make Lithium.

$$^4He + t \rightarrow^7 Li + \gamma.$$
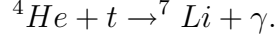
The yield of D, ^3He, ^4He, ^7Li elements depends on various physical parameters. Most importantly, they depend on the baryon density ρ_b. The increasing of baryon density make increasing of process of producing ^4He. By the measurement of light elements, we can give constraints of ρ_b. The measurements are summarized in Fig. 1.7 which shows the dependence of the abundances relative to hydrogen and the present constraints. The present allowed range given by HIRES [26] measurements is

$$0.018 < \Omega_b h^2 < 0.022$$

accounting for less than 15% of the matter density Ω_m. This result is comparable to the measured baryonic matter density from CMB. This result implies that the majority of dark matter is non-baryonic.

1.4.6   Structure formation and Cold Dark matter

The large scale structure of the universe in the present arises from the gravitational instability of small fluctuation of the early universe [4, 24, 25]. To understand of that, the large scale structure of universe was measured with 2dF galaxy redshift survey (2dFGRS) [27]. Fig. 1.8 shows a thin slice through the three-dimensional map of 213703 galaxies produced by the 2dFGRS.

The analysis with theoretical predictions from inflation and the cold dark matter model, they estimate the matter density as $\Omega_m \sim 0.3$ which is compatible with the other survey (SDSS [28]) result.

If most of the dark matter in the universe were hot dark matter, then we would expect the early structure of universe as to be a supercluster, and that galaxies would be relatively young. The observation of large scale structure implies that most of dark matter in the universe must be cold dark matter.
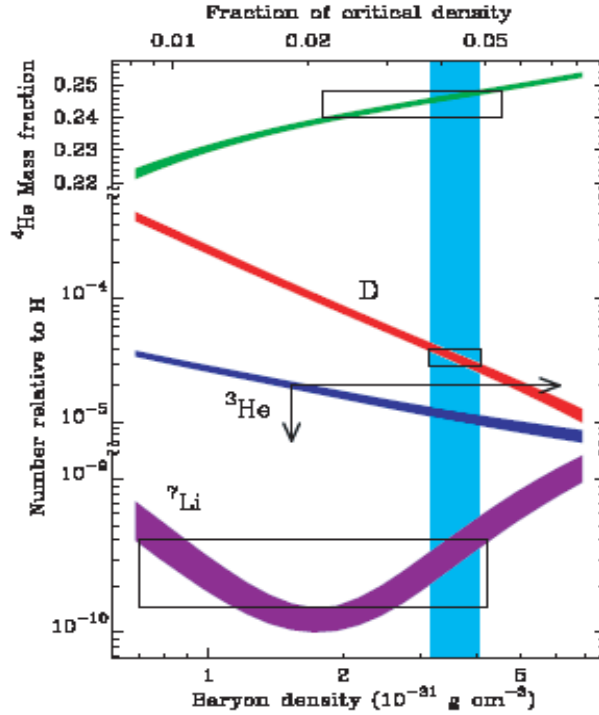
Figure 1.7: The predicted abundance of the light elements vs. baryon density. The vertical band indicates the narrow range of baryon densities consistent with the deuterium measurements; the boxes (the arrows for ^{3}He) indicate the range in baryon density (horizontal extent of box) that is consistent with the measured light-element abundance (vertical extent of box). The overlap of the boxes with the deuterium band indicates the general consistency of the observed abundances of the other light elements with their predicted abundances for this baryon density. Where $h^2 = 0.5$ is assumed. It was well explained in the Ref. [26].
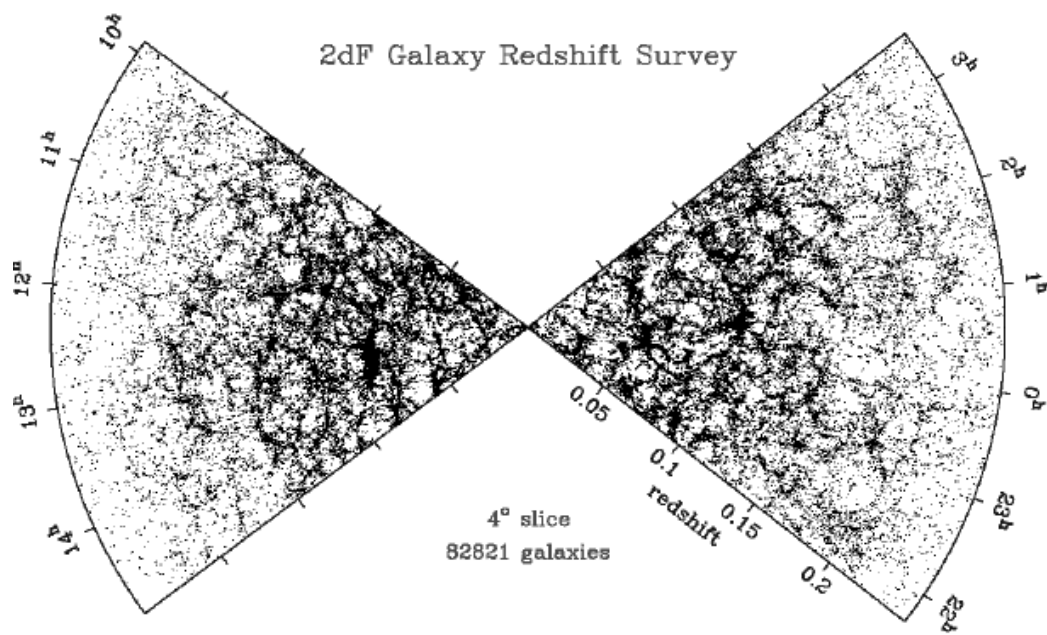
Figure 1.8: The large-scale structures in the galaxy distribution of 82821 galaxies. The figure was obtained from Ref [27].
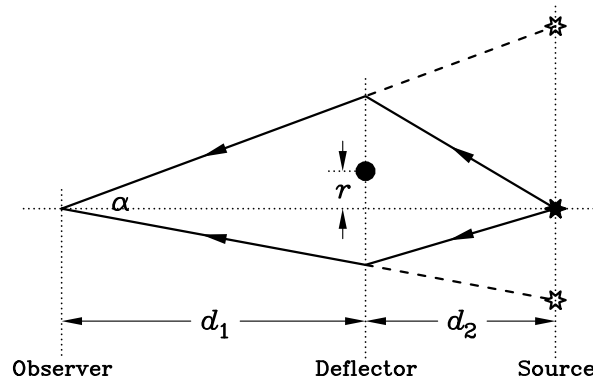
Figure 1.9: Geometry of light deflection by a point-like mass which yields two images of a source viewed by an observer.

1.5   Dark Matter Candidate

1.5.1   Baryonic dark matter

Since ordinary matter is baryonic, one may think that the galactic dark halo consist of purely baryonic material in some nonluminous form. The contribution from stars and gases is not enough to explain amounts of matter, so astrophysical bodies collectively known as MAssive Compact Halo Objects (MACHOs) are the main baryonic dark matter candidates [29]. These candidates include brown and white dwarfs, neutron stars, and stellar black hole remnants.

Since these objects are dark, one way to search for them is gravitational lensing. In particular, one can observe temporary brightening of a star due to a MACHO passing near the line-of-sight between the observer and the star as shown in Fig. 1.9. In usual case, d_1, distance between observer and deflector, is much larger than d_2, distance between deflector and source. In this case, the two image can not be separated. Therefore, the only effect will be an apparent brightening of the star as shown in Fig 1.10.

MACHO and EROS collaborations monitored large samples of stars in the Large and the Small Magellanic Clouds (LMC and SMC) long enough to identify the characteristic lightcurve shown in Fig 1.10. In Fig. 1.10, one can see the first three MACHO candidates reported by MACHO collaboration [30]. Over a 5.7-year period, MACHO observed 13-17 events (depending on the classification) toward the LMC of typical duration of about 100 days, and one towards the SMC (also observed by EROS [31]). This rate is larger than the expected background of 2-4 events due to known stellar populations, but not enough to account for a significant fraction of the halo. The result of EROS is consistent with MACHO. Therefore results from MACHO and EROS show that an all-MACHO halo is ruled out at 95% confidence for mass range of deflector between $10^{-4}M_{sun}$ and $0.03M_{sun}$. That means although the MACHOs have been shown to exist, they cannot account for all of dark matter. This give strong evidence that dark matter are mainly composed by non-baryonic material.

1.5.2 Neutrinos

Neutrinos have been considered excellent dark matter candidates because it is proved that neutrinos have small but non-zero masses by neutrino oscillation detection [32]. However, the measurements and calculations with understanding neutrinos show that the neutrinos can not be main components of dark matter.

A simple shows that, if we call m_i the mass of the ith neutrino, their total relic density is predicted to be [3]

$$\Omega_\nu h^2 = \sum_{i=1}^{3} \frac{m_i}{93\text{eV}}.$$ (1.11)

The upper limit of neutrino masses from tritium β-decay [33] is reported as

$$m_\nu < 2.05 \text{ eV (95\% CL)}.$$ (1.12)
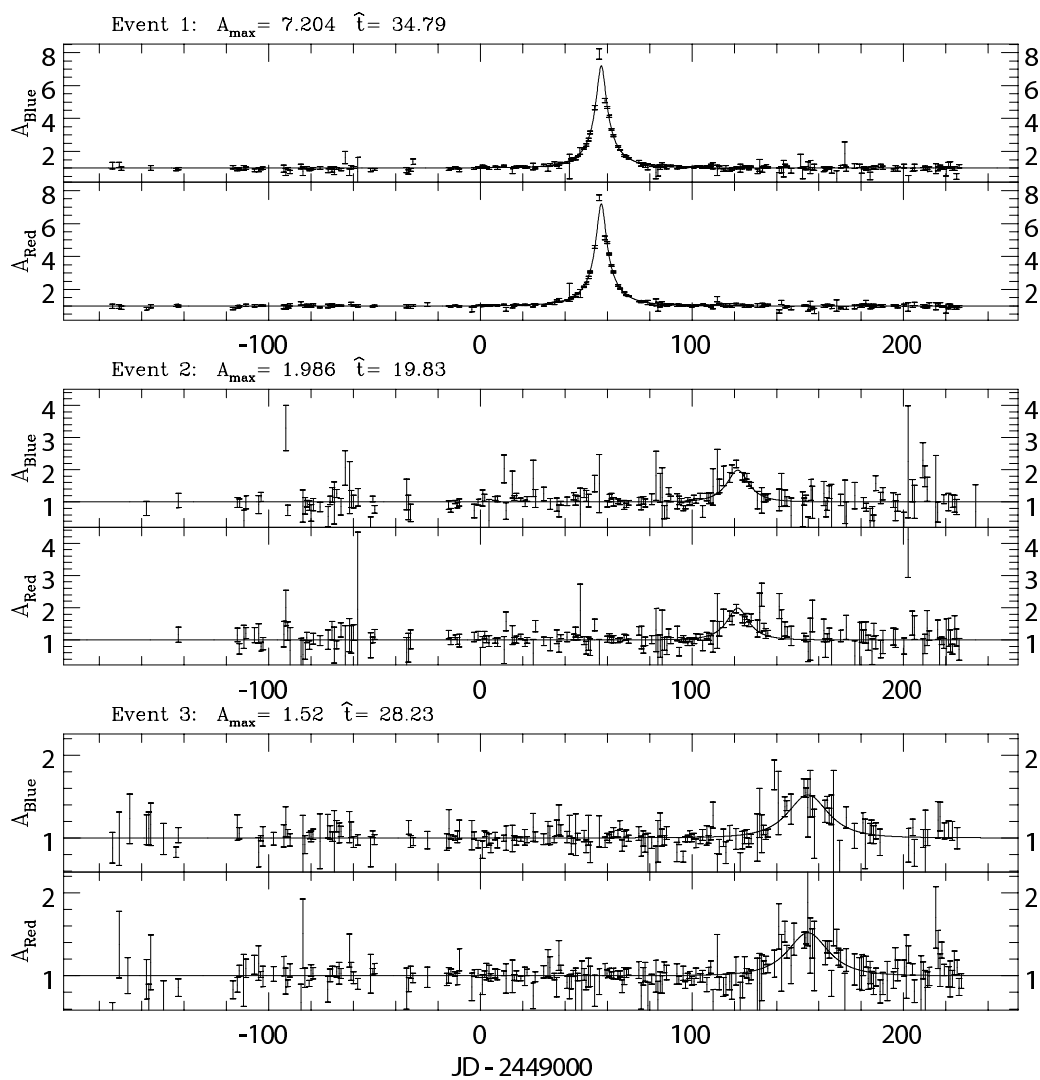
Figure 1.10: First three microlensing cadidates of the MACHO collaboration toward the LMC [30]. The horizontal axis is measured in days with the zero point at Julian Day , corresponding to January 12, 1993.

This implies an upper bound on the total neutrino relic density of

$$\Omega_\nu h^2 < 0.07, \tag{1.13}$$

which means that neutrino can not be dominant component of dark matter. A more stringent constraint on the neutrino relic density comes from the analysis of CMB anisotropies [5], combined with large-scale structure data [34], suggesting $\Omega_\nu h^2 < 0.0067$ (95% CL).

Furthermore, being light and relativistic at the time of galaxy formation, neutrino free streaming erases fluctuations below a scale of ∼40 Mpc, called the free streaming length [35]. If it is dominant dark matter in the universe, the structure of universe should be quite different from current observation.

1.5.3 Axion

Axions [36] were suggested to solve the so-called "strong CP problem". Out of the vacuum structure of Quantum Chromodynamics there are a large CP-violating phase. A possible solution to this problem is that the CP-violating phase is the vacuum expectation value of a new field, called the axion.

Laboratory searches, stellar cooling and the dynamics of supernova 1987A [37] constrain axions to be very light ($\lesssim 3 \cdot 10^{-3}$eV). Furthermore, they are expected to be extremely weakly interacting with ordinary particles, which implies that they were not in thermal equilibrium in the early universe.

The axion production are explained by two non-thermal mechanisms which are vacuum alignment and emission from cosmic strings. In the vacuum alignment mechanism, a potential is generated for the axion field by chiral symmetry breaking. The axion field starts moving toward the minimum of the potential, then oscillates around it. The field oscillations generate axion particles. In the other mechanism, the axions are emitted from wiggling or decay of cosmic strings. Assuming that the ratio of the axion number density to the entropy density is constant, the vacuum alignment

contribution to axion mass density as follow [38]:

$$\Omega_a \simeq \left(\frac{0.6 \cdot 10^{-5} \ eV}{m_a}\right)^{\frac{7}{6}} \left(\frac{200 \ MeV}{\Lambda_{QCD}}\right)^{\frac{3}{4}} h^{-2}. \qquad (1.14)$$

The requirement that axions do not overclose the universe implies the constraint $m_a \geq 6 \cdot 10^{-6}$ eV. The contribution from axion string decay is the same order of magnitude with that from vacuum realignment by carrying out the computer simulation [39].

The axions produced by these mechanisms are cold state because they are non-relativistic from the moment of their first appearance at 1 GeV temperature. Therefore, axion can be a good candidate of cold dark matter.

Searches for axions as galactic dark matter rely on the coupling of axions to two photons. An incoming galactic axion can become a photon in the magnetic field in a resonant cavity. The axion-photon interaction is written in the usual form,

$$\mathcal{L} = \frac{1}{4} g_{a\gamma} F_{\mu\nu} \tilde{F}^{\mu\nu} a = g_{a\gamma} \vec{E} \cdot \vec{B} a. \qquad (1.15)$$

So, searches for galactic axions use tunable cavities, and scan over the cavity frequency.

CAST [40] collaboration searched Solar axion with laboratory magnetic field. They report the limit with null signal that $g_{a\gamma} < 1.16 \times 10^{-10}$ GeV^{-1} at 95% CL for $m_a \leq 0.02$eV as one can see in Fig. 1.11. But still it is remained as a possible dark matter candidate [41].

1.5.4 WIMPs

If there are massive and weakly interacting particles, a generic Weakly Interacting Massive Particle (WIMP), it could be a good candidate of dark matter. Because it is massive, the velocity of WIMP is non-relativistic. Therefore the large scale structure is well explained by WIMPs. Also, WIMPs could have a relic abundance in the universe that matches the dark matter density. Fortunately, supersymmetric extension of the standard model naturally motivate the existence of the requisite particles in the form of neutralinos [42, 43, 44].
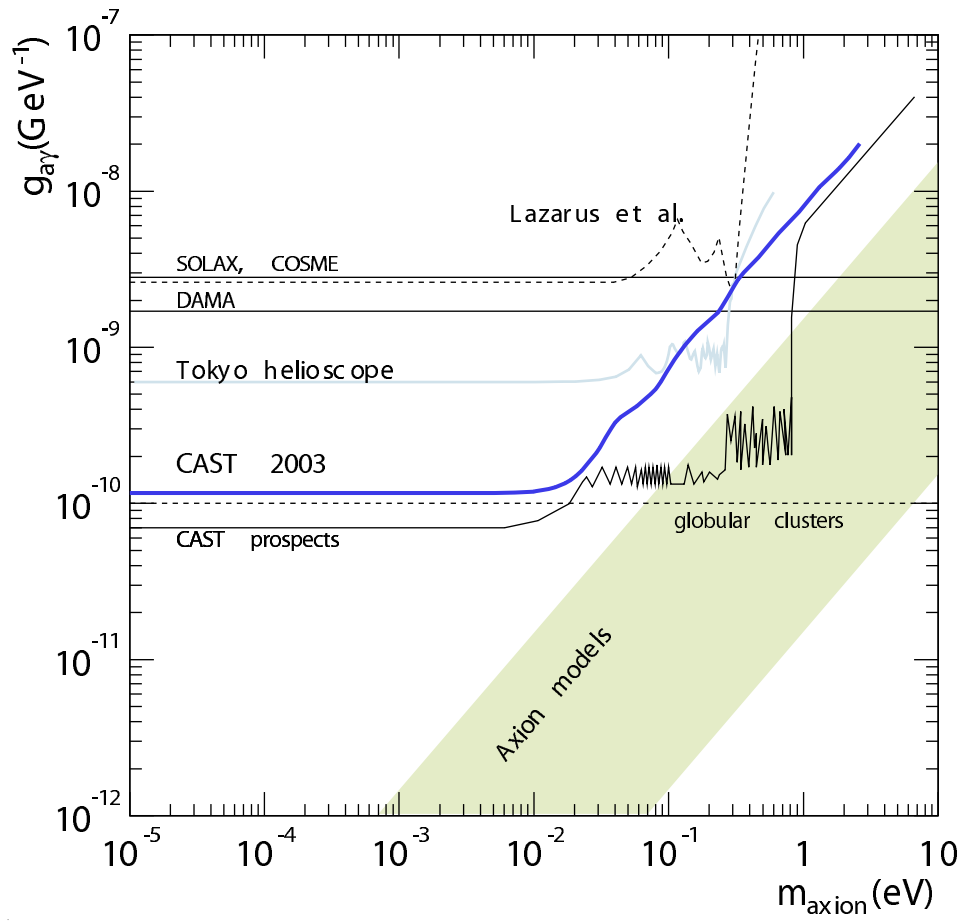
Figure 1.11: Experimental bound from various experiments, especially including CAST 2003 [40] data.

Supersymmetric extension of the standard model predict a doubling of the existing particles in that every bosonic degree of freedom is matched by a supersymmetric fermionic one and vice versa. Normal and supersymmetric particles differ by a quantum number called R-parity. If R-parity is conserved, the lightest supersymmetric particle (LSP) would have to be stable. If the LSP is the lightest "neutralino", i.e. the lightest mass eigenstate of a general superposition of the neutral spin-$\frac{1}{2}$ fermions, namely the photino (spin $\frac{1}{2}$ partner of the photon), Zino (spin $\frac{1}{2}$ partner of the Z^0 boson), and Higgsino (spin $\frac{1}{2}$ partner of the a neutral Higg boson), it can be a WIMP. We will have more discussion for neutralino and its detection in Chapter 2.

The Relic Density of neutralino

The relic density of neutralino is determined by the neutralino annihilation cross section and by the expansion rate of the Universe. In the early universe, the temperature was higher than the mass of WIMPs, therfore WIMPs could convert to standard model particles and also vice versa with Higgs or slepton exchange. Initially, two reactions were in equilibrium states. As the universe expanded, and the temperature became lower than the WIMP mass, the WIMPs diluted faster than the standard model particles. Therefore the rate for annihilation of WIMPs, $\Gamma =< \sigma_{ann} v >$, where $< \sigma_{ann} v >$ is the thermally averaged total cross section for annihilation of WIMPs into lighter particles, v is the relative velocity of the annihilating WIMPs, and n is the number density of WIMPs, drops below the expansion rate. The evolution of the number density of WIMPs is governed by the Boltzmman equation [44].

$$\frac{dn}{dt} = -3Hn - < \sigma_{ann} v > (n^2 - n_0^2), \qquad (1.16)$$

where H is the Hubble constant, n_0 is the equilibrium number density of WIMPs.As the universe cooled down further, WIMPs became so rare that the WIMP annihilation reactions could no longer occur, and from then on the number density of WIMPs decreased by expansion of universe. Using

Friedmann's equation, an order of magnitude of relic density of WIMPs can be calculated as [43]

$$\Omega h^2 \approx \frac{3 \times 10^{-27} \text{cm}^3/\text{s}}{< \sigma_{ann} v >}. \qquad (1.17)$$

An important property of this equation is that smaller annihilation cross sections correspond to large relic densities. This means that WIMPs with weaker interactions can be remained for a longer time.

1.5.5 Other dark matter candidates

In additional to neutralino there are other potential supersymmetry (SUSY) candidates for dark matter. One of it is the superpartner of the neutrino which is called as sneutrino. If their mass is in the range of 550 to 2300 GeV, sneutrinos will have a cosmologically interesting relic density [45]. However, the limit comes from direct dark matter detection experiments give information that sneutrino can not be dominant particle dark matter [45].

The gravitino, superpartner of the graviton, can be the lightest supersymmetric particle and be stable [46]. In the absence of inflation, the gravitino could give rise to the correct relic abundance if its mass is order of keV. However, the gravitinos would be undetectable because their interactions with ordinary matter are extremely weak [46].

Instead of using WIMPs with typical masses of order a hundred GeV, nonthermal WIMPs in the mass range 10^{12} to 10^{16} GeV are considered as dark matter candidate [47]. This is called as WIMPZILLA.

The axino (the superpartner of axion), LKP (the lightest Kaluza-Klein particle) and, other things from many theory and scenarios have been discussed [48]. Favorite region of well motivated particle dark matter was shown in Fig. 1.12.
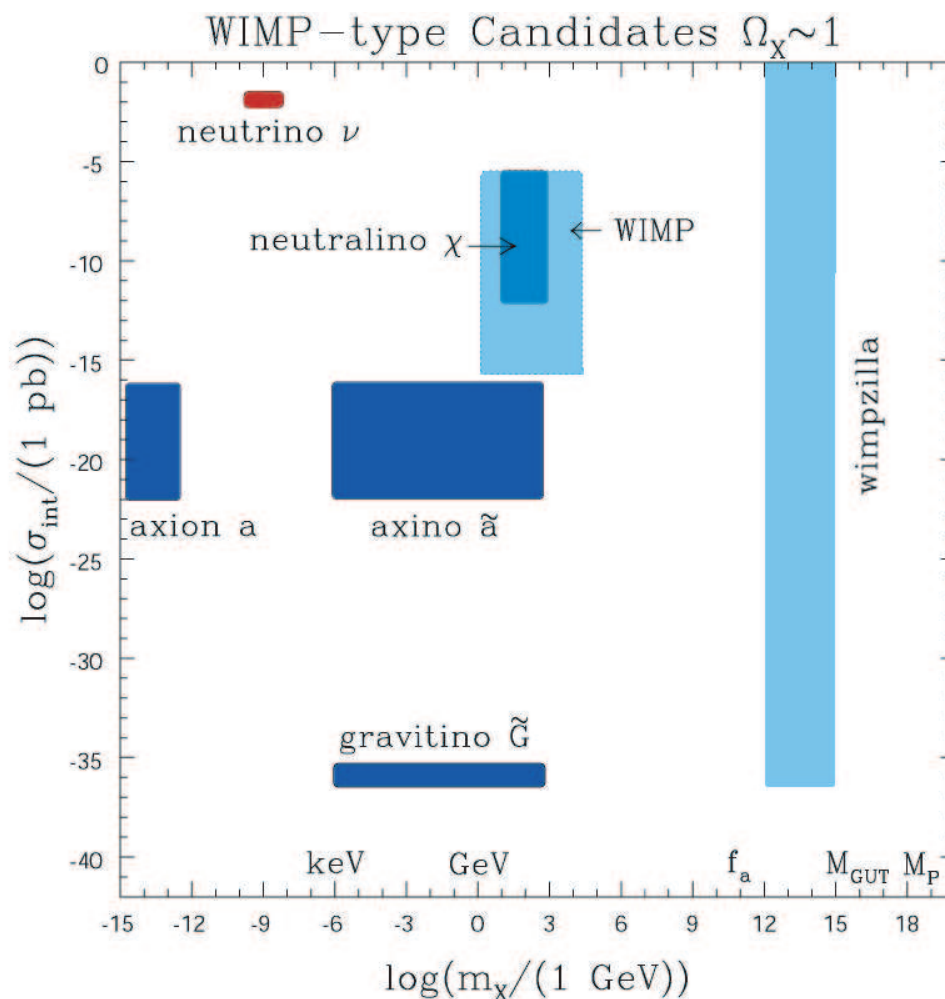
Figure 1.12: A schematic representations of some well-motivated particle dark matter. σ_{int} represents interaction strength with ordinary matter and m_χ is the mass of candidate [48]

Chapter 2

WIMP Detection

2.1 Supersymmetric Model

Supersymmetry (SUSY) starts from the question: what is the symmetry between boson, which is the mediators of interactions, and fermion, which is the constituents of matter? It may provide a sort of "unified" picture of matters and interactions. SUSY helps in stabilizing the masses of fundamental scalar particles in the Standard Model (SM) of particle physics, such as the Higgs boson. This is known as hierarchy problem, which helps to explain why gravity is so much weaker than the other forces. SUSY also helps to unify the fundamental forces of nature (electroweak, strong, and gravitation). With SUSY at the TeV scale, it was shown in Ref. [49], these forces naturally unify.

SUSY requires the existence of new particle for each particle in the SM because new generators introduced with SUSY change fermions into bosons and vise versa. The SUSY partners differ by half a unit of spin, and use the names sleptons (partner of leptons), squarks (partners of quarks), gauginos (partners of gauge bosons), and higgsinos (partners of Higgs bosons). Sleptons and squarks have spin 0, and gauginos and higgsinos have spin 1/2.

If SUSY was an explicit symmetry of nature, the superpartner would have the same mass as their corresponding SM particles. However, no such particles have been observed. It is therefore assumed that SUSY is broken like weak symmetry. Superpartners can be much heavier than their normal counterparts, which explains why they have not been detected so far. In terms of action of ordinary particle and superpartners on the components of the fields of the theory, a new discrete symmetry is defined by R parity.

$$R = (-1)^{3(B-L)+2S},$$

where B and L are baryon and lepton number operators, and S is the spin. This means that $R = 1$ for ordinary particles and $R = -1$ for their superpartners. If R-parity is conserved, the lightest SUSY particle can not decay and therefore stable.

In the minimal supersymmetric model (MSSM) the neutral gauginos and the neutral higgsinos can mix together [50]. This superposition is referred to as a neutralino, χ, and is the lightest supersymmetric particle (LSP). Therefore MSSM with R-parity conservation are attractive for the study of dark matter as it predicts the existence of a new stable particle which is the LSP.

The Weakly Interacting Massive Particle (WIMP) is most likely the electrically neutral lightest neutralino. It is the dark matter candidate that has been most widely investigated theoretically and experimentally. The direct and indirect dark matter search experiments are sensitive to this particle, or its annihilation products.

The density of WIMPs was also calculated in SUSY theory. Even the MSSM has 106 parameters beyond those in the standard model: 102 SUSY-breaking parameters, 1 complex SUSY parameter μ, and 1 complex electroweak symmetry-breaking parameter $\tan\beta$ [51]. Since it has little predictive power due to many input parameters, simplified scenarios with a reduced number of parameters are used in phenomenological studies. One of the most studied cases is the constraint MSSM (CMSSM), which reduces the number of parameters to five: three real mass parameters at the Grand Unification
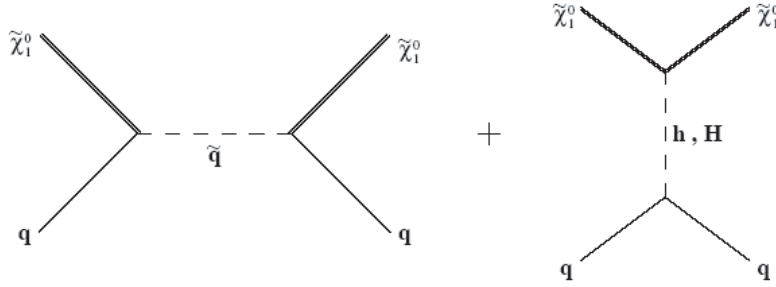
Figure 2.1: Feynman diagrams contributing to the neutralino-nucleon cross section through squark ($\tilde{s}$) exchange and CP-even light (h) and heavy (H) neutral Higgs exchange.

scale (the scalar mass m_0, the scalar trilinear coupling A_0, and the gaugino mass $m_{1/2}$) and two real parameters at the weak scale (the ratio of Higgs expectation values $\tan\beta$ and the sign of the μ parameters). Another scenario relevant to dark matter studies is a class of models with seven parameters specified at the weak scale [52].

2.2 WIMP-nucleon Scattering

The elastic scattering of a WIMP with a nucleus in a detector depends on the interactions of WIMP with quark and gluon. Fig. 2.1 shows Feynman diagrams contributing to the scalar elastic-scattering of a neutralino from quarks through the exchange of Higgs bosons or squarks.

WIMPs can be detected directly via the recoiling of a nucleus (A,Z) in the elastic scattering process,

$$\chi + (A, Z) \rightarrow \chi + (A, Z)^*.$$

The elastic scattering of a WIMP off a nuclei is commonly discussed in the context of two classes of couplings. First, scalar (spin-independent) scattering

result from the coherent part which is proportional to the number of nucleons in the nucleus. The lagrangian can be written as $L \sim (\chi\chi)(\bar{q}q)$, through a Higgs exchange or a squark exchange. The incoherent component of the WIMP-nucleus cross section results from an axial-current interaction of a WIMP with constituent quarks, given by $L \sim (\chi\gamma^\mu\gamma_5\chi)(\bar{q}\gamma_\mu\gamma_5 q)$, through a Z boson exchange or a squark exchange, and couples the spin of the WIMP with the total spin of the nucleus [52]. Therefore, the differential cross section for a WIMP scattering off a nucleus X_Z^A is given by

$$\frac{d\sigma}{d|\vec{q}|^2} = \frac{d\sigma^{scalar}}{d|\vec{q}|^2} + \frac{d\sigma^{axial}}{d|\vec{q}|^2}. \tag{2.1}$$

In the scalar part, contributions from individual nucleons in the nucleus add coherently and the finite size effects are accounted for by including the scalar nuclear form factor $F(q)$. In the low momentum-transfer limit, the differential cross section for the scalar part takes the form [52],

$$\frac{d\sigma^{scalar}}{d|\vec{q}|^2} = \frac{1}{\pi v^2} \left[Z f_p + (A - Z) f_n \right]^2 F^2(q), \tag{2.2}$$

where f_p and f_n are the effective WIMP coupling to protons and neutrons respectively. In most instances, $f_p \simeq f_n$.

Usually the Woods-Saxon form factor suggested by Engel [53] is adopted

$$F(Q) = \frac{3j_1(qR_1)}{qR_1} exp(-(qs)^2/2), \tag{2.3}$$

where $q = \sqrt{sm_N Q}$ is the momentum transferred, $R_1 = \sqrt{(R^2 - 5s^2)}$, $R \simeq 1.2 \times A^{1/3}$fm, j_1 is a spherical Bessel function and $s \simeq 1$fm. The $F(Q)$ is normalized to 1 at zero energy transfer, and that it is implicitly a function of $|\vec{q}|$. At the zero momentum transfer limit, Eq 2.2 can be written as

$$\sigma_0^{scalar} = \int_0^{4m_r^2 v^2} \frac{d\sigma^{scalar}(q=0)}{d|\vec{q}|^2} = \frac{4\mu_A^2}{\pi}[Z f_p + (A-Z)f_n]^2 \simeq \frac{4m_r^2}{\pi}A^2 f_p^2, \tag{2.4}$$

where v is the velocity of incident WIMP, and $\mu_A = \frac{m_A m_\chi}{m_A + m_\chi}$ is the reduced mass. This equation can be rewritten as a WIMP-proton cross section is

$\sigma_{\chi p}^{scalar}$ as follow:

$$\sigma_0 = \frac{\mu_A^2}{\mu_p^2}\frac{A^2}{p^2}\sigma_{\chi p}^{scalar}, \tag{2.5}$$

where μ_A and μ_p are reduced mass of WIMP nucleus and proton respectively. In most instances, the strength of WIMP scattering in the scalar interaction with zero momentum transfer is proportional to A^2. Furthermore, for heavy WIMPs, $m_\chi \gg m_N$, the reduced mass is $m_{R_A} \simeq m_N$, the strength of scalar elastic-scattering cross section as $\sigma_{0scalar} \propto m_N^4$.

Effective axial WIMP coupling to the nucleus depends on the spin contents of the nucleon and the overall expectation value of the nucleon group spin in the nucleus $< S_p >$ and $< S_n >$. For a nucleus with a total angular momentum J, the cross section can be written as follow [52, 54]:

$$\frac{d\sigma^{axial}}{d|\vec{q}|^2} = \frac{8}{\pi v^2}\Lambda^2 J(J+1)\frac{S(q)}{S(0)}, \tag{2.6}$$

where v is the velocity of the WIMP relative to the target,

$$S(q) = a_0^2 S_{00} + a_1^2 S_{11}(q) + a_0 a_1 S_{01}(q), \tag{2.7}$$

$$a_0 = a_p + a_n, \quad a_1 = a_p - a_n,$$

and the spin independent form factor $S_{ij}(q)$ are obtained from detailed nuclear calculations. The Λ is give by

$$\Lambda = \frac{1}{J}[a_p < S_p > + a_n < S_n >]. \tag{2.8}$$

The axial couplings

$$a_p = \frac{1}{\sqrt{2}}\sum_{u,d,s} d_q \triangle q^{(p)}, \quad a_n = \frac{1}{\sqrt{2}}\sum_{u,d,s} d_q \triangle q^{(n)} \tag{2.9}$$

are determined by the experimental values of the spin constants $\triangle u^{(p)} = \triangle d^{(n)} = 0.78$, $\triangle d^{(p)} = \triangle u^{(n)} = $ -0.5, and $\triangle s^{(p)} = \triangle s^{(n)} = $ -0.16. The effective couplings d_q depend on the WIMP properties.

At the zero momentum transfer limit of axial interaction, one finds

$$\sigma_0^{axial} \sim (32/\pi)G_F^2\mu_A^2\Lambda J(J+1), \tag{2.10}$$

where G_F is the Fermi constant.

Because axial vector coupling of WIMP-nucleus can be divide by two components, one for WIMP-proton and the other for WIMP-neutron which are different from axial vector coupling, we separately consider two kinds interaction. We use model independent technique in the WIMP-nucleus spin dependent interaction [55], Eq. 2.10 can be as follow:

$$\sigma^{axial} = (\sqrt{\sigma_A^p} + \sqrt{\sigma_A^n})^2, \qquad (2.11)$$

where σ_A^p and σ_A^n are proton and neutron contributions to the total cross section. We will first make an auxiliary assumption that $\sigma_0^{axial} \simeq \sigma_A^p$ for WIMP-proton cross section. In other words, we assume that the total WIMP-nucleus cross section is dominated by the proton contribution only. And then, WIMP-proton cross section σ_p corresponding to WIMP-target nucleus A cross section as

$$\sigma_p = \sigma_A \frac{\mu_p^2}{\mu_A^2} \frac{1}{C_A^p} C_p, \qquad (2.12)$$

where $C_A = (8/\pi)\mu_A^2 \Lambda J(J+1)$ which correspond to $C_A^p/C_p = 4/3 < S_p >^2 (J+1)/J$. The Eq. 2.10 can be rewrite as follow:

$$\sigma_0^{axial} = \sigma_p^{axial} \frac{\mu_A^2}{\mu_p^2} \frac{4}{3} < S_p >^2 (J+1)/J \qquad (2.13)$$

for WIMP proton interaction and,

$$\sigma_0^{axial} = \sigma_n^{axial} \frac{\mu_A^2}{\mu_n^2} \frac{4}{3} < S_n >^2 (J+1)/J \qquad (2.14)$$

for WIMP neutron interaction.

2.3 Direct Detection of WIMP

The WIMP can be looked for through direct observation of nuclear recoils in detectors directly. The response of WIMP in detector is well described in Ref. [56]. The formalism below follows by this Ref.

The event rate per unit mass on a target of atomic mass A with cross-section σ is given in Ref. [56] as

$$dR = \frac{N_0}{A}\sigma v dn, \tag{2.15}$$

where N_0 is the Avogadro number, n is the number density of incoming particles having speed v relative to the target. The total events rate can be obtained with integration over the WIMP velocity distribution.

The differential particle density is given by

$$dn = \frac{n_0}{k}f(\vec{v}, \vec{v_E})d^3v, \tag{2.16}$$

where k is the normalization constant such that

$$k = \int_0^{2\pi} d\phi \int_{-1}^{+1} d(cos\theta) \int_0^{v_{esc}} f(\vec{v}, \vec{v_E})v^2 dv \tag{2.17}$$

with

$$\int_0^{v_{esc}} dn = n_0, \tag{2.18}$$

where n_0 is the mean WIMP number density ($=\rho_\chi/M_\chi$, M_χ is WIMP mass and ρ_χ is WIMP density), $\vec{v}$ is Earth (target) velocity relative to the dark matter distribution, and v_{esc} is the local Galactic escape velocity.

With assumption of a Maxwellian velocity distribution of WIMP, $f(\vec{v}, \vec{v_E})$ is expressed as

$$f(\vec{v}, \vec{v_E}) = e^{-\frac{(\vec{v}+\vec{v_E})^2}{v_0^2}}, \tag{2.19}$$

where v_0 is characteristic of the WIMP kinetic energy and has value $v_0 \approxeq 230km/s$. For $v_{esc} = \infty$, Eq. 2.17 can be written as

$$k = k_0 = (\pi v_0^2)^{3/2}, \tag{2.20}$$

whereas the same distribution truncated at $|\vec{v} + \vec{v_E}| = v_{esc}$, we can write

$$k = k_1 = k_0\left[erf\left(\frac{v_{esc}}{v_0}\right) - \frac{2}{\pi^{1/2}}\frac{v_{esc}}{v_0}e^{-v_{esc}^2/v_0^2}\right], \tag{2.21}$$

where erf is the error function. In the zero-momentum transfer region, the cross-section is to be σ=constant=σ_0. From the integration of Eq. 2.15,

$$R = \frac{N_0}{A}\sigma_0 \sum v dn = \frac{N_0}{A}\sigma_0 n_0 <v>. \tag{2.22}$$

We define R_0 as the event rate per unit mass for $v_E = 0$ and $v_{esc} = \infty$.

$$R_0 = \frac{2}{\pi^{1/2}} \frac{N_0}{A} \frac{\rho_\chi}{M_\chi} \sigma_0 v_0, \tag{2.23}$$

so that

$$R = R_0 \frac{\pi^{1/2}}{2} \frac{<v>}{v_0} = R_0 \frac{k_0}{k} \frac{1}{2\pi v_0^4} \sum v f(\vec{v}, \vec{v_E}) d^3 v. \tag{2.24}$$

We shall use this as differential form

$$dR = R_0 \frac{k_0}{k} \frac{1}{2\pi v_0^4} v f(\vec{v}, \vec{v_E}) d^3 v. \tag{2.25}$$

Then,

$$\frac{R(v_E, v_{esc})}{R_0} = \frac{k_0}{k_1} \left[\frac{R(v_E, \infty)}{R_0} - \left(\frac{v_{esc}^2}{v_0^2} + \frac{v_E^2}{3v_0^2} + 1 \right) e^{-v_{esc}^2/v_0^2} \right]. \tag{2.26}$$

From Eq. 2.23, we can rewrite it as normalized contents to $\rho_\chi = 0.4 \, \text{GeV}/c^2/\text{cm}^3$ and $v_0 = 230$ km/s,

$$R_0 = \frac{540}{A M_\chi} \left(\frac{\sigma_0}{1 pb} \right) \left(\frac{\rho_\chi}{0.4 \, \text{GeV}/\text{c}^2/\text{cm}^3} \right) \left(\frac{v_0}{230 \, \text{km/s}} \right) \tag{2.27}$$

with M_χ in GeV/c^2.

The recoil energy of a nucleus scattering by a dark matter particle of $E = \frac{1}{2} M_\chi v^2$ and scattered at angle θ is

$$E_R = Er(1 - cos\theta)/2, \tag{2.28}$$

where E_R is recoil energy and $r = 4 M_\chi M_N/(M_\chi + M_T)^2$ with mass of target nucleus($M_T = 0.932 \, A \, \text{GeV}/c^2$). We assume the scattering is isotropic, which means uniform $cos\theta$, so that the recoils are distributed in E_R over the range $0 \leq E_R \leq Er$. Hence,

$$\frac{dR}{dE_R} = \int_{E_{min}}^{E_{max}} \frac{1}{Er} dR(E) = \frac{1}{E_0 r} \int_{v_{min}}^{v_{max}} \frac{v_0^2}{v^2} dR(v), \tag{2.29}$$

$$\frac{dR}{dE_R} = \frac{R_0}{E_0 r} \frac{k_0}{k} \frac{1}{2\pi v_0^2} \int_{v_{min}}^{v_{max}} \frac{1}{v} f(\vec{v}, \vec{v_E}) d^3 v, \tag{2.30}$$

where $E_{min} = E_R/r$, the smallest particle energy which can give a recoil energy of E_R, $E_0 = \frac{M_D v_0^2}{2}$, and v_{min} is the dark matter particle velocity corresponding to E_{min}. So, we can obtain

$$\frac{dR(0, \infty)}{dE_R} = \frac{R_0}{E_0 r} e^{-E_R/E_0 r}. \tag{2.31}$$

This is a good approximation with the velocity of WIMPs from 0 to v_{esc}, and $v_{esc} >> v_0$. If we consider the nuclear form factor $F(q^2)$, the expected WIMP nucleus recoil is

$$\frac{dR}{dE_R} = \frac{R_0}{E_0 r} e^{-E_R/E_0 r} F^2(q^2). \tag{2.32}$$

With non-zero v_E and finite v_{esc}, the Eq. 2.30 gives

$$\frac{dR(0, v_{esc})}{dE_R} = \frac{k_0}{k_1} \frac{R_0}{E_0 r} \left(e^{-E_R/E_0 r} - e^{-v_{min}^2/v_0^2} \right) = \frac{k_0}{k_1} \left[\frac{dR(0, \infty)}{dE_R} - \frac{R_0}{E_0 r} e^{-v_{esc}^2/v_0^2} \right], \tag{2.33}$$

$$\frac{dR(v_E, v_{esc})}{dE_R} = \frac{k_0}{k_1} \left[\frac{dR(v_E, \infty)}{dE_R} - \frac{R_0}{E_0 r} e^{-v_{esc}^2/v_0^2} \right]. \tag{2.34}$$

2.3.1 Direct detection experiments

Besides KIMS experiments, which will be described in detail later, there are more than 20 experiments to detect dark matter that are currently running or in preparation around the world [57]. There are two categories of detector types, one is typical detector which measures the ionization or scintillation signal [58] and the other is cryogenic detector which measures the ionization and phonon signal simultaneously [59]. The first decade from the mid 1980s to the mid 1990s was dominated by conventional high-purity Ge (and Si) ionization detectors [60, 61]. There are no discrimination of WIMP signal, this kind of detectors were limited by the absolute level of low energy background. In the mid 1990s, results from NaI scintillator detectors became competitive [62]. These detectors used pulse shape discrimination (PSD) to make statistical distinctions between electron recoil events and nuclear recoil events. Relatively poor discrimination power of NaI gives limited improvements. In the case of the DAMA experiment, the deployment of an
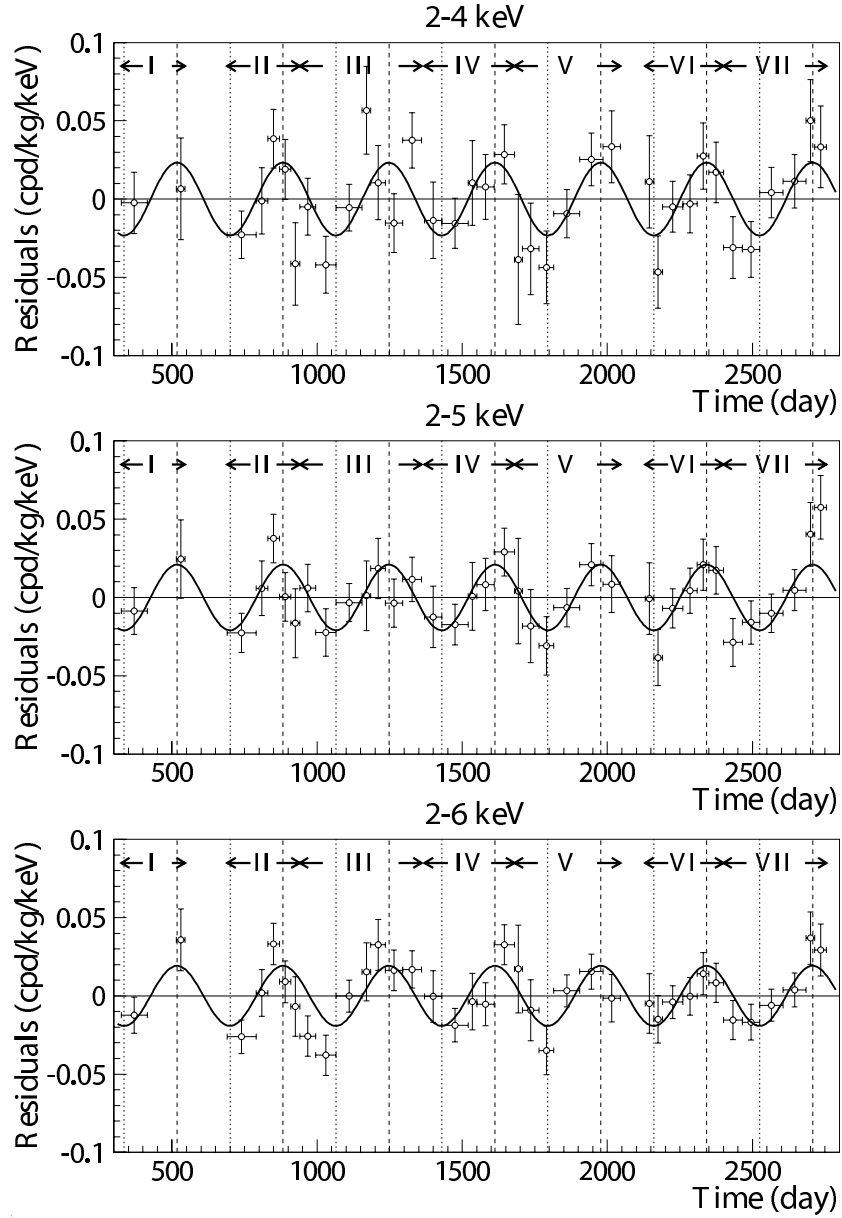
Figure 2.2: DAMA 7-year signature of annual modulation signal with 107731 kg·day exposure for 2-4, 2-5, and 2-6 keV energy bin. Figure is obtained from [64].
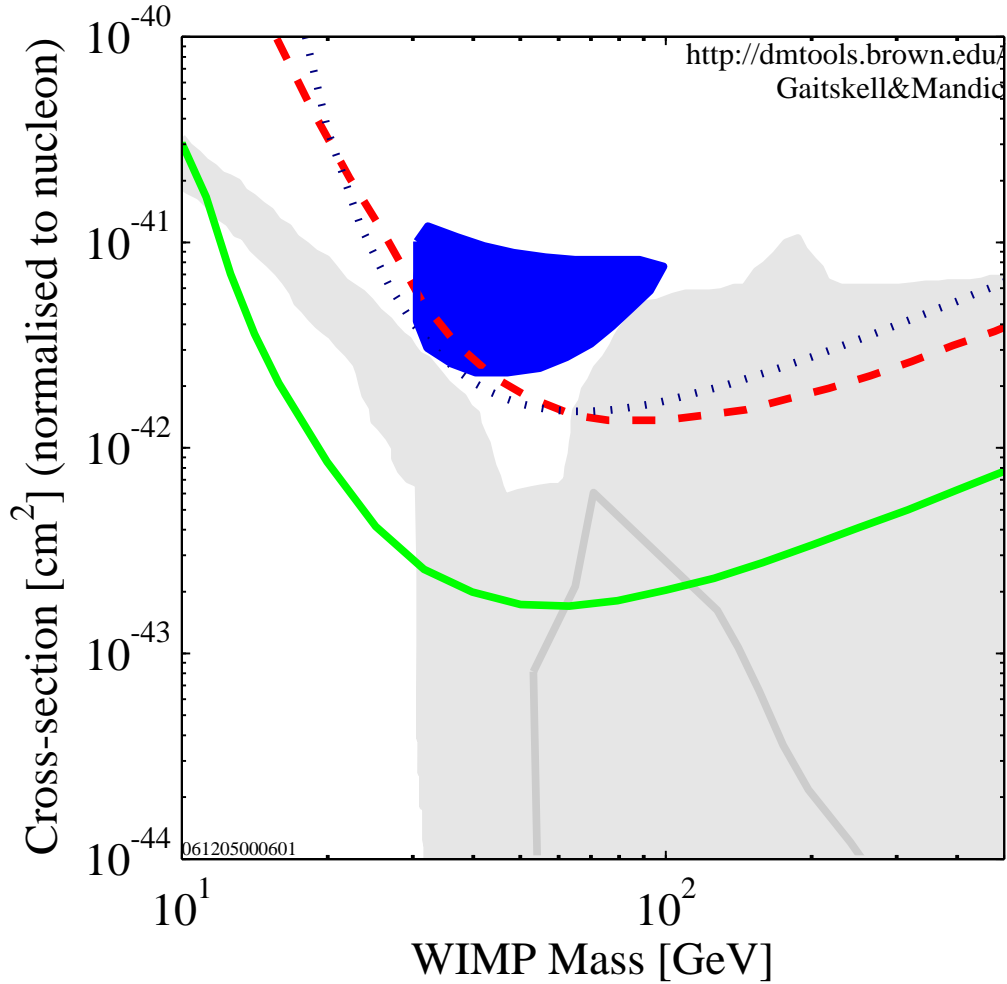
Figure 2.3:   WIMP-nucleon cross section upper limit (90 % confidence level) on spin independent interaction for CDMS (solid line) [65], EDEWEISS (dashed line) [66], and CRESST (dotted line) [67] with 3σ region of DAMA/NaI annual modulation signal [63]. Supersymmetric models allow the largest shaded region [68], and the smaller shaded region [69]. This plot generated by dmtool website [70]
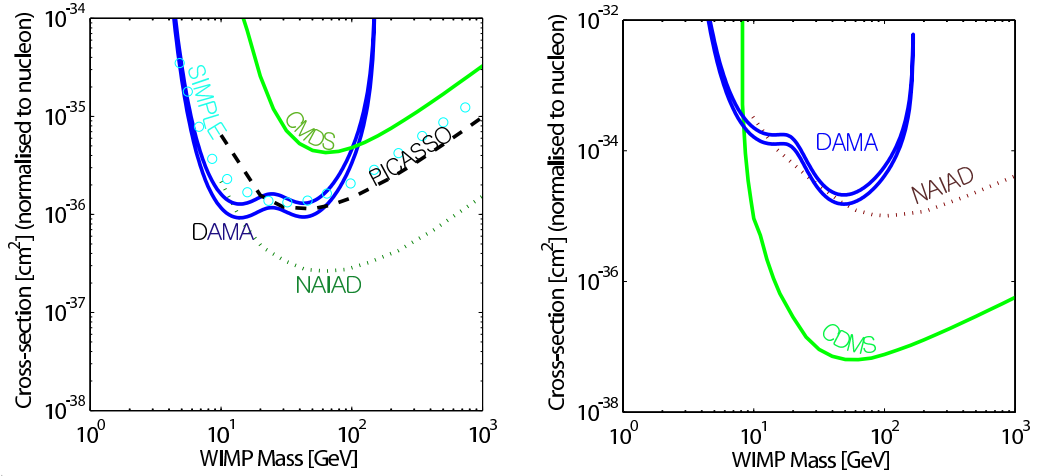
Figure 2.4: WIMP-nucleon cross section upper limit (90 % confidence level) on spin dependent interactions for pure proton interactions (left) and pure neutron interactions (right). We indicate DAMA modulation signal with Savage *et al.*estimation [71], CDMS [72], NAIAD [73], PICASSO [74], and SIMPLE [75] results. This plot generated by dmtool website [70]

~100 kg array of NaI also allowed the search for a WIMP annual modulation signal. They claimed positive signature of WIMP signal from annual modulation [63] as one can see in the Fig 2.2. At the end of the 1990s, new cryogenic detector technology came to operation after a long period of development. CDMS [65], EDELWEISS [66], and CRESST [67] group report more sensitive result than DAMA positive region with cryogenic detector in WIMP proton spin independent cross section as one can see in Fig. 2.3. The parameter space from minimal supersymmetric (MSSM) model [68] and constraint MSSM (CMSSM) model [69] is compared with experimental results.

For the pure spin dependent case, still there are region without any confliction between DAMA and other experiments [71, 76] for the low mass region as one can see in Fig. 2.4. Furthermore, for the pure spin independent case, there are possible ways to explain without any confliction in the low mass region [77]. They consider the conventional halo model and adding stream

of dark matter to the conventional halo. If there are large amount of dark matter stream, the remained region of DAMA signature is increased. Also, Foot [78] calculated allowed region from DAMA signature and CDMS null result using different dark matter type (especially mirror matter-type [79]). In the case of mixed interaction case, it is more complex. The DAMA collaboration claims that the region of signature is still alive [64, 80] because other experiments do not fully cover the all of interactions. Also there are significant uncertainty of calculation of form factor which is quite depending on the each isotope and halo model, they need another type experiments to understand the situation.

CsI(Tℓ) crystal has the same isotope (^{127}I) with DAMA (NaI(Tℓ)) and fully active for spin dependent and spin independent interaction. Furthermore we can explore annual modulation signal which is the same method with DAMA approach. The result from CsI(Tℓ) crystal help us understand the conflict between DAMA signature and other null signals.

2.3.2 Signature in CsI(Tℓ) crystal

As we discussed in Section 1.4.2, the local density of dark matter in the solar system has some uncertainty. But, most experimental group have assumption of ρ_χ =0.3 GeV/cm^3, $v_0 = 220$ km/s for comparison. If we consider central value of DAMA 3σ region [63], $M_\chi = 50$ GeV and $\sigma_{\chi p} = 7.2 \times 10^{-6}$ pb, R_0 from Eq. 2.23 with Eq. 2.5 to be 11.1/kg/day and 10.3/kg/day for Cs and I isotopes respectively. From Eq. 2.34 the recoil energy in Cs and I can be calculated as one can see in Fig. 2.5.

To know measured energy we must know quenching factor (this will be discussed in Section 3.4.3) of nuclear recoil. And also, we must consider energy resolution which smears the energy spectrum. As a result, we simulate WIMP signal spectrum in CsI(Tℓ) crystal with GEANT4 Monte Carlo (MC) simulation (see Appendix B). With central value of DAMA 3σ region we expected measured energy spectrum in CsI(Tℓ) crystal for WIMP signal is
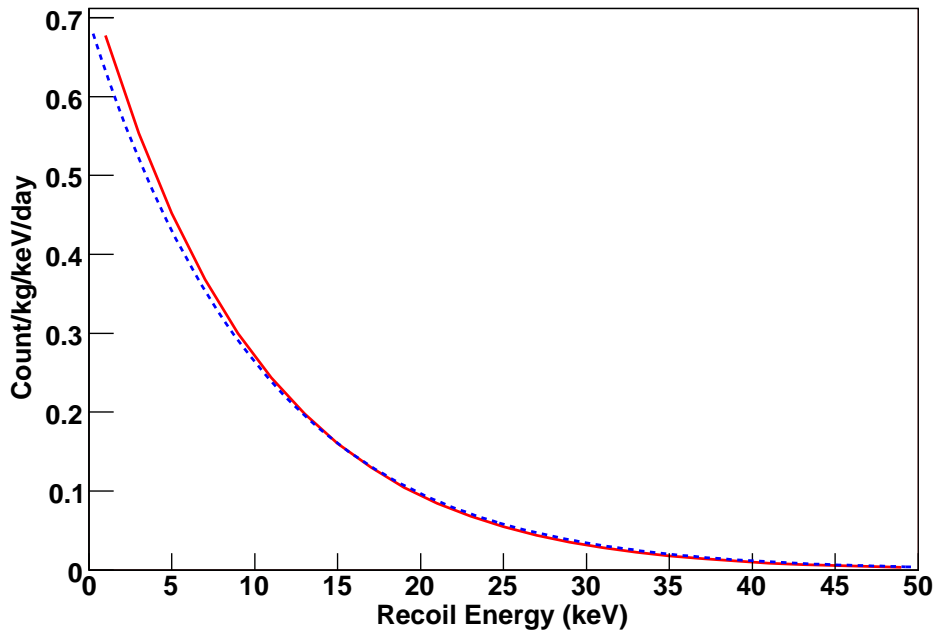
Figure 2.5: The differential event rate of Cs (solid line) and I (dashed line) for a WIMP-nucleon cross section $\sigma_{\chi p} = 7.2 \times 10^{-6}$ pb and a WIMP mass $M_\chi = 50$ GeV which is central value of DAMA 3σ region.
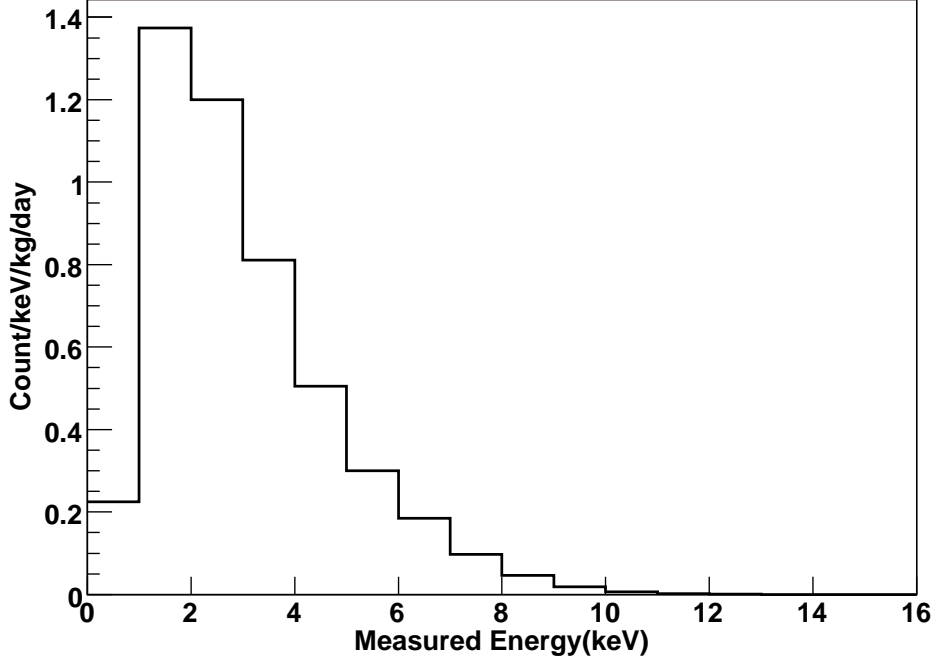
Figure 2.6:   Measured energy spectrum of WIMP signal in CsI(Tℓ) crystal for a WIMP-nucleon cross section of spin independent interaction with $\sigma_{\chi p} = 7.2 \times 10^{-6}$ pb and a WIMP mass $M_\chi = 50$ GeV which is central value of DAMA 3σ region using GEANT4 simulation.

given in Fig. 2.6.

2.4   Indirect Detection of WIMP

The neutralino can be found via the observation of annihilation products. The rate of such products is proportional to the annihilation rate, which in turn depends on the square of the dark matter density, $\Gamma_A \propto \rho_\chi^2$. Therefore the experiments searching for significant fluxes are focused to scan the region where large dark matter densities accumulate. Dense region such

as the galactic center is mainly focused region which generate gamma-rays, neutrinos, and other cosmic rays such as positrons and antiprotons. Other astrophysical objects, such as the Sun and the Earth, could be also interesting region which generates neutrinos.

2.4.1 High Energy Neutrinos

Neutralinos orbiting around the solar system can collide with nuclei in the Sun and the Earth. In these collisions, they may lose kinetic energy. If they lose enough energy to have a lower speed than the escape speed, they can be trapped by the gravitational force. After some time, the trapped neutralinos will sink to the core and will possibly reach to thermal equilibrium. In the center, the trapped neutrallinos could annihilate frequently. The annihilation rate depends on the relative strength of the annihilation and scattering cross sections, and ultimately on the parameters of the particle and halo models [52].

In the Earth and the Sun, only the neutrinos from annihilation products can reach to the surface. All the other products are absorbed or decayed. Direct production of a neutrino pair from neutralino is strongly suppressed in neutralino annihilation, due to the Majorana nature of the neutralino. The secondary neutrinos are produced in the decay chains of the primary particles which are heavy quarks, gauge bosons, tau leptons and Higgs bosons. As a result, the neutrino energy spectrum is continuum, and the typical energy of a neutrino from neutralino annihilation is about a tenth of the neutralino mass. Given the current constraints, this means a neutrino energy is in between a few GeVs and a few TeVs.

The neutrino from neutralino annihilation can be detected in the Cherenkov neutrino telescopes. Several experiments are potentially able to detect the high energy neutrinos from neutralino annihilations in the solar core. The AMANDA experiment [81] is currently the largest operating neutrino telescope. ANTARES [82], with a lower energy threshold (10 GeV) and Ice-

cube [83], with a much greater effective area, will each function as effective dark matter search experiment. The Super-Kamiokande detector [84] gave a result of WIMP exclusion limit and will continue to the search.

2.4.2 Gamma-rays and Cosmic Rays

Neutralino annihilations produce signals in the halo of our galaxy or in the halo of external galaxies. The annihilation products are divided by two categories. One is rare cosmic rays such as positrons, antiprotons, and antideuterons. The other is gamma-rays, whose spectrum are expected to contain a gamma-ray line at an energy corresponding to the neutralino mass. The gamma-ray line is produced directly by the primary neutralino annihilation into $\gamma\gamma$ or $Z\gamma$. Positrons, antiprotons, antideutrons, and the gamma continuums are generated in the particle cascades that follow the decay of the primary annihilation products. Therefore energy spectrum of them are broad within neutralino mass.

Recently there have been claims from both the CANGAROO [85] and HESS [86] experiments of detection of gamma rays from the Galactic Center, each with a very different energy spectrum. Horns [87] fit the CANGAROO data with a 2 TeV WIMP, and the HESS data with a 20 TeV WIMP. Also, there are report; an excess of WIMP mass below 100 GeV which is much compatible with SUSY model by ERGRET [88]. Until now, there are big uncertainty to understanding continuum gamma from galactic center. Therefore it is difficult to claim the observation of the WIMP signal. The GLAST project may help to understand this kind signal.

The HEAT balloon, using two entirely different instruments, found abnormal positron fluxes [89]. Baltz *et al.* shows that possible explanation is dark matter annihilation [90]. But, another possibility from not understanding cosmic ray propagation is still remained.

Chapter 3

Experiment

3.1 History of KIMS Experiment

Korea Invisible Mass Search (KIMS) collaboration started R&D for dark matter search with $CsI(T\ell)$ crystals in late 1997. The feasibility of $CsI(T\ell)$ crystal for WIMP search and pulse shape discrimination (PSD) were demonstrated [91]. Then, we started the measurement of intrinsic background of $CsI(T\ell)$ crystals with simple lead shielding at CheoungPyung Underground Laboratory (CPL) in 1999 summer. Because of intrinsic background from ^{137}Cs and ^{87}Rb , we had expensive work for reduction of intrinsic background [92, 93]. In the summer of 2001, we performed the neutron beam test of sample $CsI(T\ell)$ crystals ($3 \times 3 \times 3$ cm^3) for the study of nuclear recoil events in the CsI crystals with different doping type (Na, Tl) and dopant concentration [94]. We had moved to YangYang Underground Laboratory (Y2L) in the spring of 2003 because CPL had not enough space for full shielding and Y2L is twice deeper site. With successful reduction of intrinsic background of $CsI(T\ell)$ powder, we succeeded growth of crystals with background level of 6 counts/kg/keV/day (CPD) [95] at the less than 10 keV. From July to September 2004 we had taken first WIMP search data of 237 kg·days as

well as comparable amount of calibration data. The result was reported in the IDM 2004 conference [96] and published [97]. A brief history of KIMS experiments is summarized in Table 3.1.

Table 3.1: A history of KIMS Experiments

Date	Contents
1997	Starting of the R&D with CsI(Tℓ) for WIMP search
1998	Reporting of first result to the ICHEP98 conference
1999	Background measurements of CsI(Tℓ) crystals (lead 10cm)
2000	Installation of prototype shielding (10cm lead, 5cm Cu)
	Funded by Creative Research Initiatives program
2000∼	Reduction of intrinsic background of CsI(Tℓ) crystal
2001	Neutron beam test of CsI(Tℓ) crystals
2002	Starting the construction of new laboratory at Y2L
2003	Construction of Y2L and installation of the full shielding
	Move to Y2L
2004	Successful growing a 6 CPD level crystal (6.6kg)
	First physics run with one crystal
	Reporting the first result at IDM2004 conference
2005	Growing of two more full size (8.7 kg) crystals (6 CPD)
	Starting of mass production of 4 CPD background crystals
2006	Publication of first physics result to Physics Letter B

3.2   YangYang Underground Laboratory (Y2L)

As we discussed in Chapter 1 and Chapter 2, the main challenge for WIMP detection is to achieve low background rate in the low energy region that incorporates at least a few keV which corresponds to signal region of WIMPs. In this point of view, the ground or shallow sites are limited by high rate of muons and muon induced neutrons. Therefore, the deep underground sites are requested by WIMP search experiments.

Since a large amount of budget is needed to build a new underground laboratory, we took an approach to utilize an existing facility. KIMS began
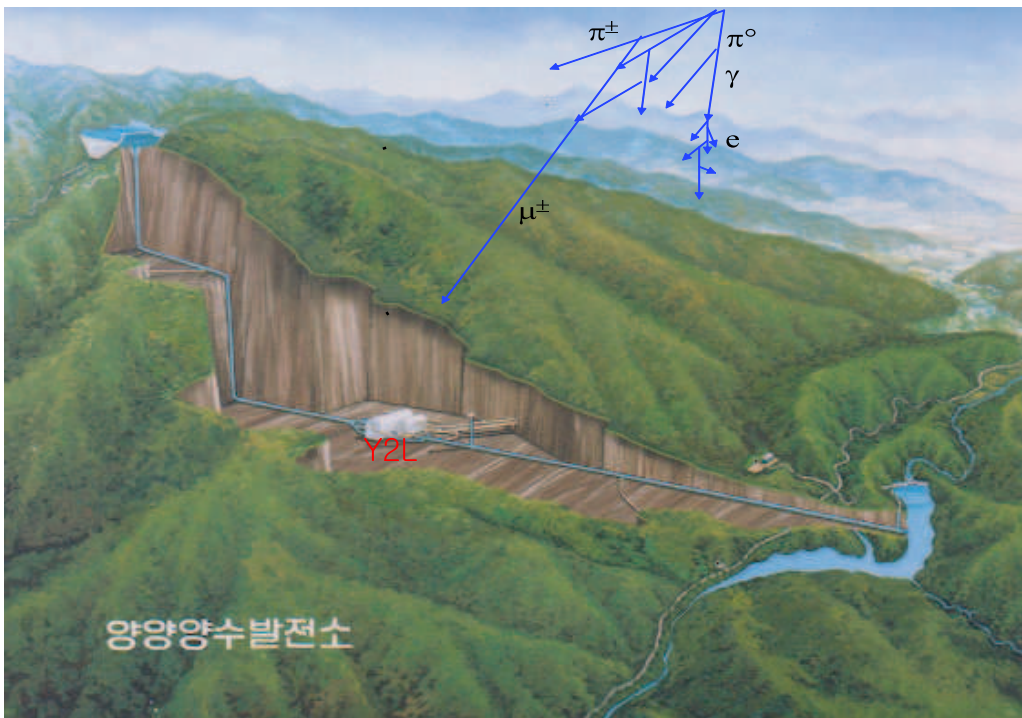
Figure 3.1: Picture of Y2L
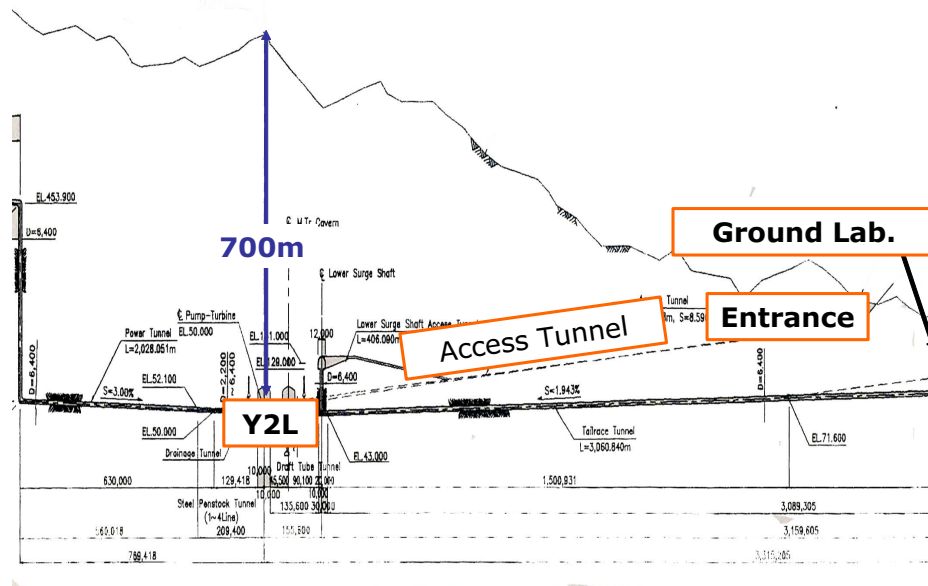
Figure 3.2: Vertical picture of Y2L

the experiment in the CPL which utilized the space provided by the Cheong-
Pyung Pumped Storage Power Plant. Because the vertical depth of the
underground laboratory was only 400 m and provided space by the company
was not enough to install our full shielding, we had moved the experimental
site to Y2L (see Fig. 3.1) in 2003. Y2L is utilizing space provided by the
YangYang Pumped Storage Power Plant of Korea Midland Power Co. The
underground laboratory is located in a tunnel where the vertical earth over-
burden is about 700 m (see Fig. 3.2). There is a 2 km long tunnel, which
is wide enough to use car, from the mountain's breast to the underground
laboratory. The ground laboratory was built near the entrance of the tunnel
for the working of data analysis and detector R&D. Table 3.2 shows under-
ground laboratories for rare event experiments in the world. Depth of Y2L
is compatible with Soudan mine (CDMS experiments).

Table 3.2: Underground Laboratories

Laboratory	Country	Depth(m)	Depth(mwe)	Type	Experiments
Gran Sasso	Italy	1400	3800	Tunnel	DAMA,CRESST
Soudan	USA	710	2200	Mine	CDMSII
Sudbury	Canada	2000	5400	Mine	SNO
Homstake	USA	2300	6700	Mine	Neutrino
Boulby	UK	1100	3000	Mine	UKDMC
Canfranc	Spain	900	2450	Tunnel	IGEX,ANAIS
Modane	France	1700	4800	Tunnel	EDELWISS
Kamioka	Japan	1000	2700	Mine	SK, KARMLAND
Oto	Japan	500	1500	Tunnel	ELEGANCE
Yangyang	Korea	700	2000	Tunnel	KIMS

3.2.1 Enviroment of Y2L

The muon flux measured with the muon detector is $2.7 \times 10^{-7}/\text{cm}^2/\text{s}$ [98], which is consistent with the water equivalent depth of 2000 m. The laboratory is equipped with a clean room with an air conditioning system for a constant temperature and humidity. Environment monitoring system is installed for the continuous monitoring of temperature and humidity. The temperature inside the CsI(Tℓ) detector volume is stable within $\pm 0.2^o$C. The rock composition was analyzed by ICP-MASS method and contamination of ^{238}U, ^{232}Th, and ^{40}K is reported to be at the level of < 0.5 ppm, 5.6 ± 2.6 ppm, and 270 ± 5 ppm respectively. The relatively low contamination of ^{238}U in the rocks of the tunnel results in the low level of Radon contamination in the air of the tunnel. A radon detector [99] is constructed to monitor the level of Radon in the experimental hall. The contamination level of ^{222}Rn in the air is measured to be 1-2 pCi/ℓ which is comparable to that at the ground level. Measurement of the neutron flux at the experimental hall is done with two of one liter liquid scintillators inside of shielding and outside of shielding. The estimated neutron flux at the experimental
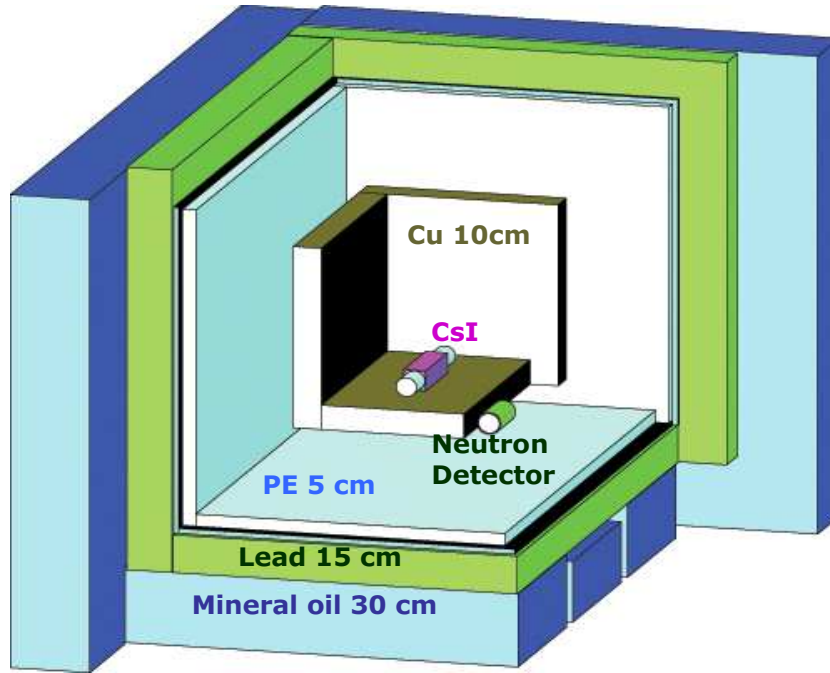
Figure 3.3: Scheme of our detector and shielding

hall is 8×10^{-7}/cm^2/s for 1.5 MeV$< E_{neutron} <$6.0 MeV which is much lower than 3×10^{-5}/cm^2/s of CPL [100]. We could only set the upper bound on neutron flux inside the CsI detector volume since all measured events were consistent with the internal background. Detailed system and measurement will be discuss in Section 3.5.2.

3.3 The Shielding Structure

We installed a shielding structure in the experimental hall to stop the external background from the external radioisotope sources. The shield consists of 10 cm thick Oxygen Free High Conductivity (OFHC) copper, 5 cm thick polyethylene (PE), 15 cm thick Boliden lead and 30 cm mineral oil (liquid parafin) from inside out. The mineral oil is mixed with 5% of pseudocumene based liquid scintillator and mounted with PMTs so that it can perform as
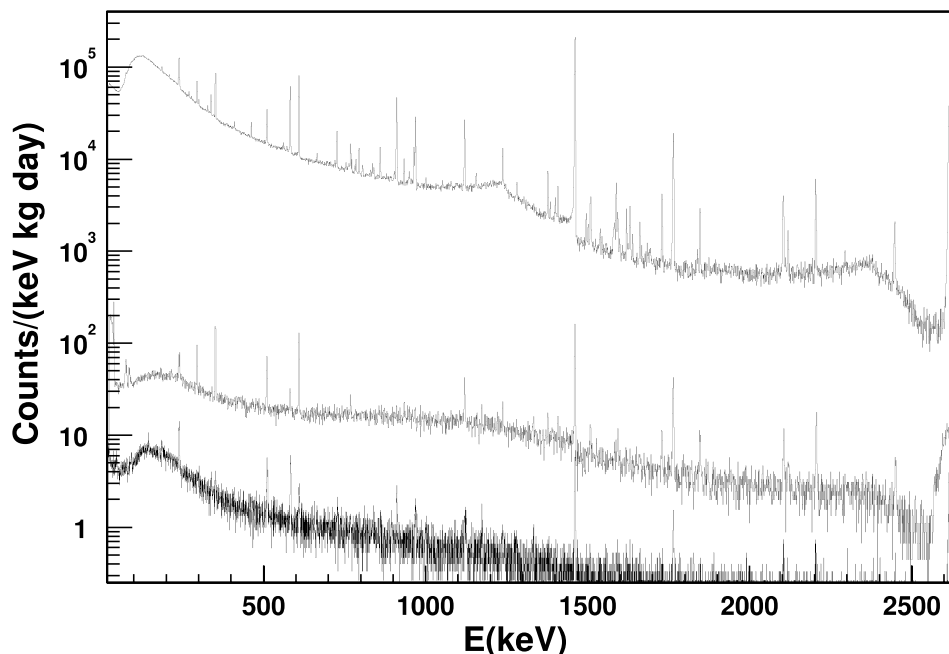
Figure 3.4: γ background spectrum at Y2L measured with a 100 % HPGe detector. Upper histogram is the measurement without shielding, middle one is with 10 cm Pb shielding and lower one is with full shielding and N_2 gas flowing

a muon detector [98]. Inside the copper chamber, N_2 gas evaporated from liquid N_2 is flown at 4 ℓ/min rate to reduce the Radon contamination as well as to keep the humidity low. The overall structure of the shield is shown in Fig. 3.3.

We measured the γ background with an ultra-low background 100% High Purity Ge (HPGe) detector to understand effect of shielding. As one can see in Fig. 3.4 the background level without shielding is about 10^5 counts/keV/kg/day at 200 keV, and with shielding and N_2 gas flowing it was reduced by a factor in excess of 10,000 (lower histogram). If we consider the internal background of HPGe detector, the external background level in the main shielding is much lower level than that of the histogram.

3.4   CsI(Tℓ) crystals

3.4.1   Characteristics of CsI(Tℓ) Crystal for WIMP search

Scintillation crystals are frequently used for WIMP search. NaI(Tℓ) crystals have been adopted by several experiments [63, 101]. Because of its high hygroscopicity, one needs to encapsulate the crystal and it can introduce unwanted surface background contamination. The CsI(Tℓ) crystal is a good candidate for WIMP search because its hygroscopicity is much lower than NaI(Tℓ) and its light yield is one of the highest. Also CsI(Tℓ) crystal has higher mass density than NaI(Tℓ) as shown in Table 3.3. Furthermore pulse shape discrimination (PSD) power is much better than NaI(Tℓ) [94, 101, 102].

But, the peak emission of CsI(Tℓ) crystal does not match with normal bi-alkali PMT which causes decreasing of effective photo-electron yield. In this reason we used RbCs photocathode PMT, which is extended to green region, for read-out. Also, internal background from radioisotopes of cesium (^{137}Cs , ^{134}Cs) and rubidium (^{87}Rb) can cause high background rate [93]. We did extensive work for the reduction of internal background [92, 93, 95].

Table 3.3: Comparison between CsI(Tℓ) and NaI(Tℓ) characteristics

Property	CsI(Tℓ)	naitl
Density(g/cm^3)	4.53	3.67
Decay constant(ns)	∼1000	∼250
Peak emission(nm)	550	415
Light yield($Photon/MeV$)	∼60000	∼40000
Hygroscopicity	Slight	Strong

3.4.2   Pulse Shape Discrimination of CsI(Tℓ) crystals

The expected event rate of the WIMP-nucleus interaction is less than 1 CPD. Such a low event rate requires an extremely low background rate. To reduce the background rate, the PSD between nuclear recoils and background γ's or electrons in several keV region can be utilized.

In many scintillating crystals, electrons and holes produced by ionization are captured to form certain meta-stable states and produce slow timing components. On the other hand, a large stopping power from the recoiling nucleus produces higher density of free electrons and holes which favor their recombination into loosely bound system and resulting in the fast timing components. By using this characteristic, we may be able to use PSD between nuclear recoils and γ backgrounds.

The PSD of CsI(Tℓ) crystals was studied with neutron beam test [94]. Fig. 3.5 shows the accumulated time spectrum of CsI(Tℓ) crystal for 4 keV $< E_{meas} < 10$ keV. The γ events were measured with Compton scattering electron from 661.6 keV γ of ^{137}Cs .

To quantify the separation capability for neutron-γ discrimination, a quality factor was introduced [103].

$$K \equiv \frac{\beta(1-\beta)}{(\alpha-\beta)^2},\tag{3.1}$$

where α is the fraction of signal events passed the event selection criteria and β is the fraction of background events which passed the same criteria. For an ideal detector, $\alpha = 1$ and $\beta = 0$. Therefore, a smaller quality factor means a better separation between signal and background events.

In the CsI(Tℓ) detector, we introduce a mean time parameter for separation as follow:

$$<t> = \frac{\sum A_i t_i}{\sum A_i} - t_0,\tag{3.2}$$

where A_i is the charge of the ith cluster, t_i is the time of the ith cluster, and t_0 is the time of the first cluster. Fig. 3.6 shows the mean time distribution of nuclear recoils and γ events for 4 keV $< E_{meas} < 6$ keV. By the fit we can
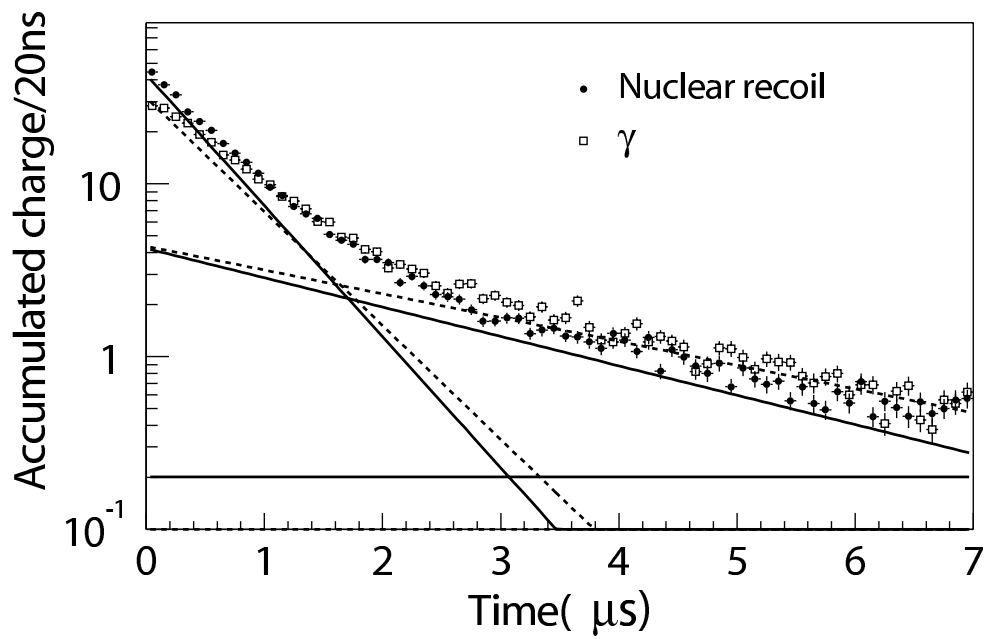
Figure 3.5: Time spectra from CsI(Tℓ) for nuclear recoil and γ events. The spectra are fitted with two components of exponential with constant backgrounds. The solid lines are for nuclear recoil data and the dashed lines are for γ data.
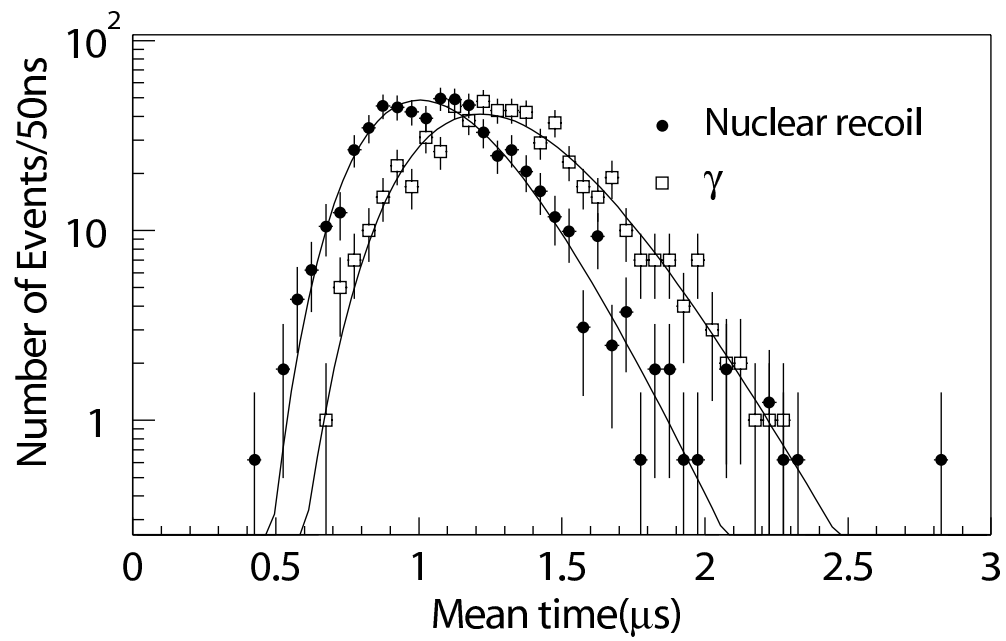
Figure 3.6: Mean-time distributions for CsI(Tℓ) from 4 keV to 6 keV nuclear recoils and γ events.
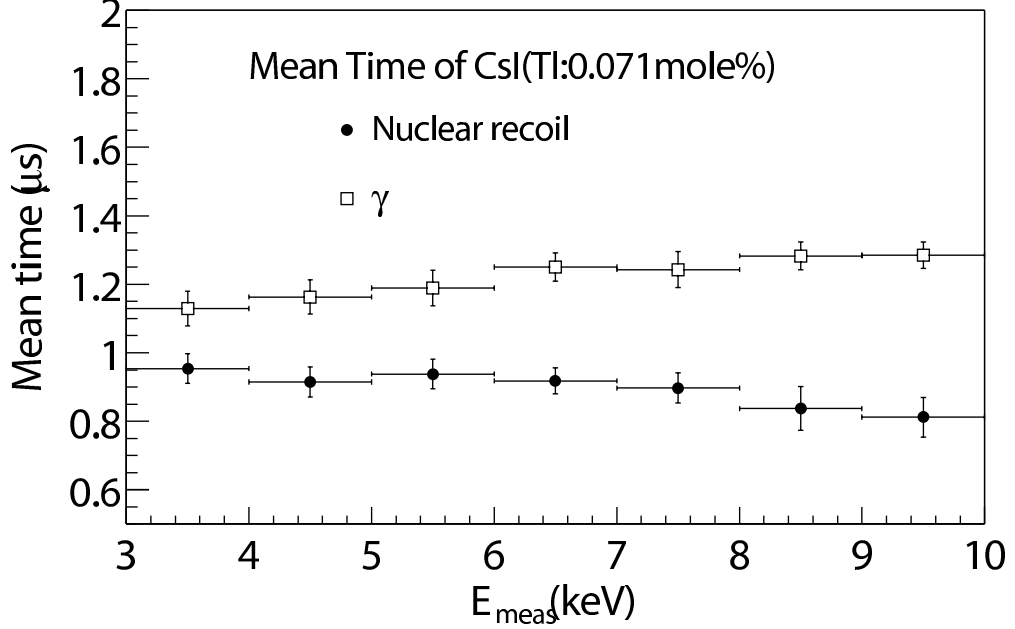
Figure 3.7: Mean time of CsI(Tℓ) for each energy bin.

calculate the mean time of nuclear recoil and γ for each energy bin as one can see in Fig. 3.7.

By selecting the proper signal window, we can choose the event sample which maximizes the signal-to-background ratio. In this window, we calculate the quality factor. Fig. 3.8 shows the quality factors for CsI(Tℓ) for various doping concentrations. The results from previous measurements for CsI(Tℓ) [101] and for NaI(Tℓ) [104] are overlaid. The most of CsI(Tℓ) measurements are comparable. CsI(Tℓ) shows, in comparison to NaI(Tℓ) , about a 10 times smaller quality factor.

3.4.3 Quenching factor

A small fraction of the kinetic energy lost by a charged particle in a scintillator is converted into fluorescent light [105]. The remainder is dissipated nonradiatively mainly in the form of lattice vibrations or heats. The fraction
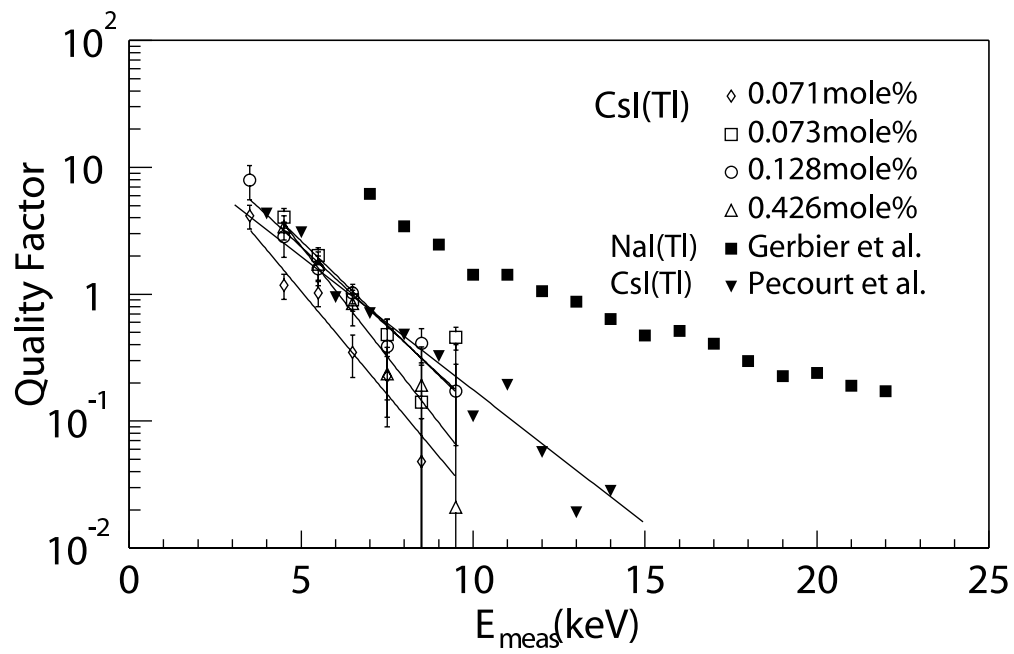
Figure 3.8: Quality factors for various CsI(Tℓ) crystals with NaI(Tℓ) crystal.

of the particle energy that is converted (the scintillation efficiency) depends on both the particle type and its energy.

It is well know that the light yield of neutron interaction is poorer than the light yield of gamma or beta interaction, i.e. the stopping of a fast electron produces more light than the stopping of a kicked-off nucleus [105, 106]. The effect is known for all scintillators and also for ionization detectors and is commonly called Quenching.

A widely accepted mechanism of quenching process first suggested by Birks [106] is based on the assumption that a high ionization density along the track of the particle leads to quenching from damaged molecules and a lowering of the scintillation efficiency. Because energy loss per unit length (dE/dx) of recoiled nucleus is much higher than that of electron recoil, quenching for nuclear recoil is occurred.

The measurements of quenching factor (QF) were performed for various materials [94, 101, 102, 104, 107]. The basic idea is measurement of light output with γ and neutron source. At first the detector response is obtained using calibrated γ-ray source. This yields the calibration of the signal amplitude in terms of an electron-equivalent energy, E_{ee}. In a second step, the detector is exposed to a source producing nuclear recoils with a known kinetic energy E_R. The separation of the nuclear recoil from the electronic recoil gives rise to the definition of the Quenching factor.

$$QF = \frac{E_{ee}}{E_R}.$$

The quenching factor measurements for CsI(Tℓ) crystals were performed by our neutron beam test [94] and other groups [101, 102]. The result of experiments is shown in Fig. 3.9. We use best fit curve as a quenching factor of CsI(Tℓ) crystal.

3.4.4 Internal Backgrounds of CsI(Tℓ) crystals

As we already reported [92, 93], ^{137}Cs , ^{134}Cs and ^{87}Rb is major internal background in CsI(Tℓ) crystals. ^{137}Cs $(t_{1/2} = 30.07$ y, Q=1175.6keV) is a beta-
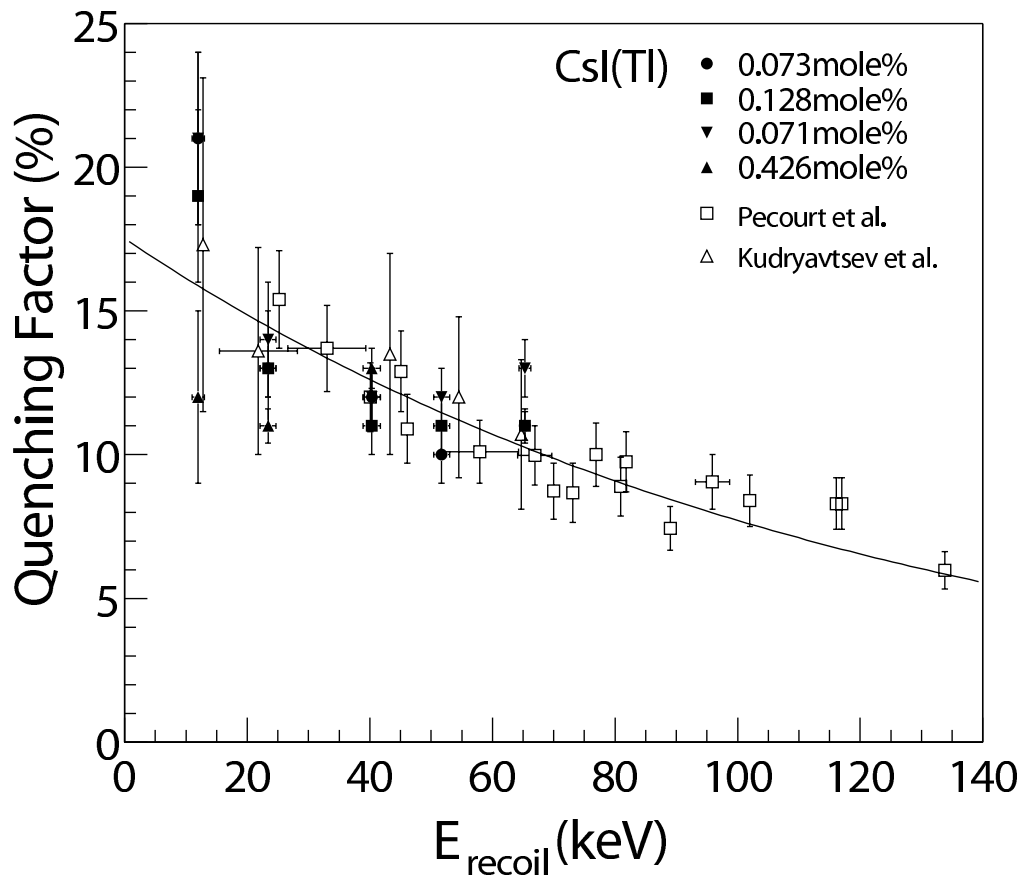
Figure 3.9: Quenching factors for various CsI(Tℓ) crystals from neutron beam test (closed markers) [94]. Different measurments [101, 102] (open markers) are compared. Solid line shows fit result of averaged value.

emitter decaying with a 95% branching ratio to the meta-stable state ($t_{1/2}$ = 2.55 minutes) of ^{137}Ba at 661.7 keV. The beta electron and the subsequent gamma ray are not correlated in time. Therefore, the low energy contribution from β electron and Compton scattering of γ ray cause high level of background in the WIMP signal region. ^{134}Cs ($t_{1/2}$ = 2.065 y, Q = 2058.7 keV) is also a beta-emitter decaying to ^{134}Ba, but the subsequent gamma ray is correlated with the beta electron. Therefore the background level from ^{134}Cs decays are not significant at low energies. ^{87}Rb ($t_{1/2}$ = 4.75 $\times 10^{10}$y, Q = 282 keV) is also beta-emitter decaying to the ground state of ^{87}Sr without gamma-ray emission. Since the Q value is small and it has very long half-life, the background level from ^{87}Rb decay is relatively high at low energies. Fig. 3.10 shows background spectrum of each radioisotope which is obtained by GEANT4 [108] simulation. This spectrum is well matched with previous CsI(Tℓ) crystal measurement [93]. As a result, we can quantify contribution of each isotope to the background level at 10 keV. 1 mBq/kg of ^{137}Cs and ^{134}Cs contribute 0.3 CPD and 0.07 CPD respectively and 1 ppb of ^{87}Rb does 1.07 CPD to the background rate. We measured contamination level of ^{137}Cs , ^{134}Cs , and ^{87}Rb in CsI(Tℓ) crystals commercially available from several companies [93]. Fig 3.11 shows the background spectrum of those crystals. The contaminations in CsI(Tℓ) crystal are 18 $\sim$ 210 mBq/kg for ^{137}Cs , 38 $\sim$ 586 mBq/kg for ^{134}Cs , and 3.2 $\sim$ 816 ppb for ^{87}Rb , respectively. Background level of commercially available crystals at 10 keV are higher than 65 CPD as one can see in Fig. 3.11. Also, we had grown a 20 CPD level crystal at 10 keV with careful powder selection, which contains 15.5 $\pm$ 2.6 mBq/kg of ^{137}Cs , 27.4 $\pm$ 4.6 mBq/kg of ^{134}Cs and 20 $\pm$ 1 ppb of ^{87}Rb [93].
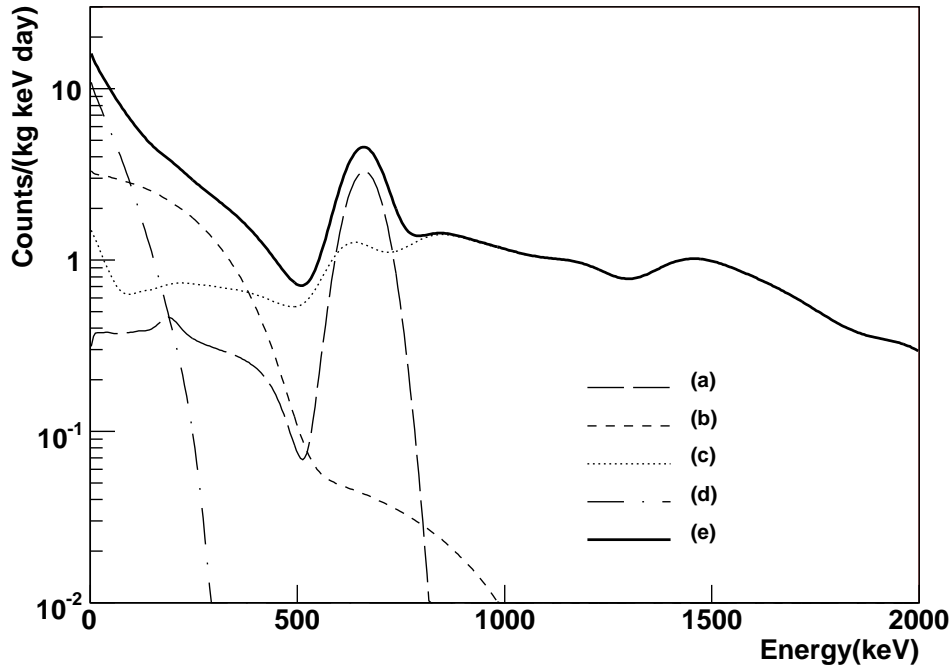
Figure 3.10: Background spectra obtained using GEANT4 [108] simulation for the $8 \times 8 \times 30$ cm^3 CsI(Tℓ) crystal with 10 mBq/kg ^{137}Cs contamination, 30 mBq/kg ^{134}Cs contamination, and 10 ppb ^{87}Rb contamination (a) spectrum of ^{137}Ba* (b) beta-ray spectrum of ^{137}Cs (c) ^{134}Cs spectrum (d) ^{87}Rb spectrum (e) total summed spectrum
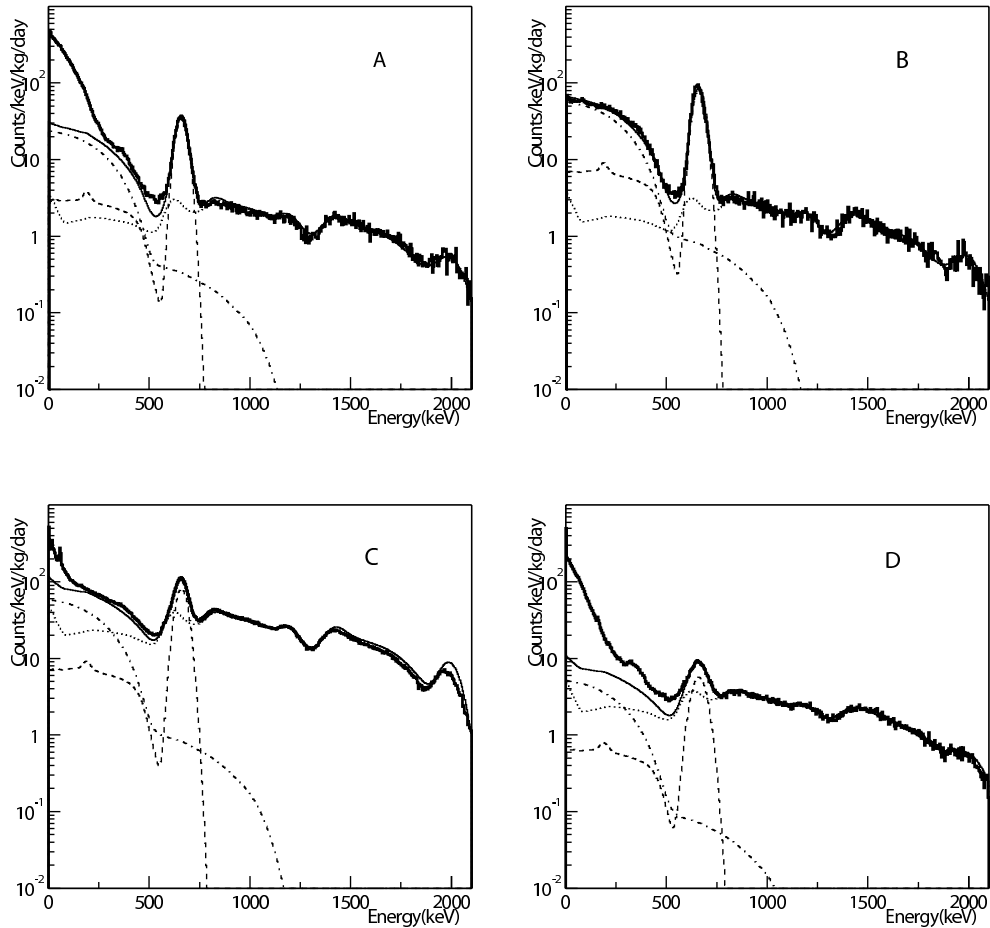
Figure 3.11: Background spectra and the best-fit curves with the GEANT4 simulation: thick solid line: measured spectrum; solid line: total spectrum of simulation; dashed-dotted line: beta-ray spectrum of ^{137}Cs ; dashed line: spectrum of ^{137}Ba*; dotted line: spectrum of ^{134}Cs .

3.4.5   Reduction of Internal Background

^{137}Cs

Radioactive sources are classified as primordial, cosmogenic, and man-made. Primordial radionuclides are left from the creation of the Earth. They typically have half-lives of hundreds of millions of years. As follow nucleosynthesis, all the heavy ($A >7$) radioactive nuclei occurs inside stars [109] and nuclei with long half life such as ^{238}U, ^{232}Th, and ^{40}K are the major sources of background radiation in the underground laboratory. There is also significant ^{222}Rn in the air. Cosmogenic radionuclides continuously produced by bombardment of stable nuclides by cosmic rays, primarily in the atmosphere. These cosmogenic radionuclides can have long half-lives, but the majority have shorter half-lives than the primordial radionuclides. Because of shorter half-lives, the cosmogenic radionuclides are not important background source in the underground experiment. But, the muon, secondary particle of cosmic ray contributes to significant background. Cosmic-ray muons interacting in the surrounding rock can generate both γ and neutron backgrounds. Man-made radionuclides are generated by nuclear bombs and nuclear reactors. Since ^{137}Cs is a man-made nuclide and is already known to exist in CsI(Tℓ) crystals, it is a major internal background sources.

Cesium is extracted from the pollucite ore which is in the form of

$$Cs_2Al_2Si_4O_{12}(H_2O).$$

Fig. 3.12 shows the extraction processes of the cesium from pollucite in one of major companies in cesium production, Chemetall GmbH, Special Metals Division in Germany [110]. One important thing to note with respect to ^{137}Cs contamination is that the whole processes needed about 70 ℓ of water to produce 1 kg of CsI powder.

We had measured the ^{137}Cs and ^{134}Cs contamination levels in various samples by directly measuring the 661.7 keV, 604.7 keV, and 795.8 keV γ rays with HPGe detector with 100% efficient, low-background co-axial detector.
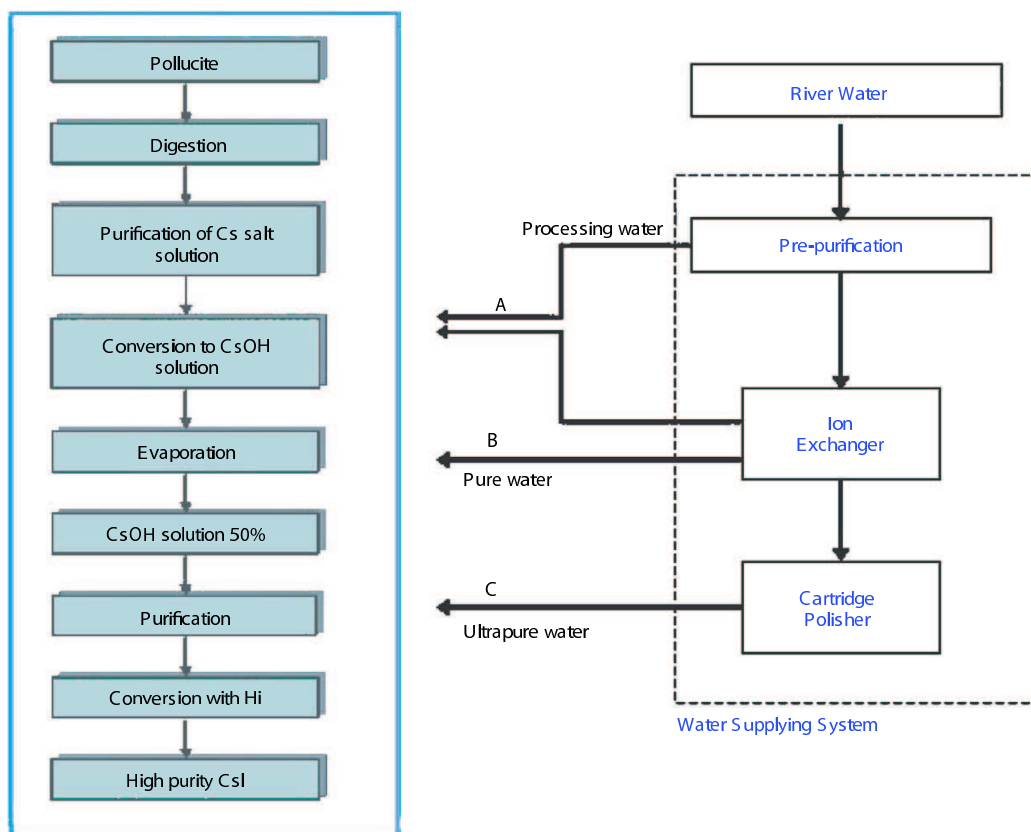
Figure 3.12:   The extraction processes and water supplying system at Chemetall GmbH in Germany.   For A, we used 50% of "processing" water and 50% of "pure" water, and used only "pure" water for B. For C, we used only "ultrapure" water

It is installed in Y2L. The shielding include 10 cm thick OFHC copper, and 15 cm thick lead of which the inner 10 cm is low-background Boliden lead. At present, there is a gap of about 10 cm between HPGe crystal and inner copper shielding to house a large volume of samples. The whole detection system including liquid nitrogen cryogenics bottle was encapsulated with a acryl box to inhibit the radon activities. Nitrogen gas from liquid nitrogen tank is flown continuously at the level of 1 ℓ/min. inside the acryl box.

To understand the contamination mechanism of ^{137}Cs and find out how to reduce the ^{137}Cs in CsI compound, we have asked Chemetall GmbH to produce CsI powder with different waters supplied as shown in Fig. 3.12. In normal production procedure, mixed water from "processing" and "pure" water were supplied with the ratio of 1:1 (A). CsI powder was produced with only "pure" water for the whole processes (B). 3rd, high quality ion exchangers(cartridge polisher) was installed after the usual ion exchanger, and only the "ultrapure" water from the cartridge polisher was supplied (C). The three kinds of water, "processing", "pure", and "ultrapure" waters were supplied from Chemetall to us in the amount of 20 ℓ each for analysis. We have measured the ^{137}Cs contamination of three different kinds of water samples.

Fig. 3.13 shows the energy spectra of each kinds water sample with HPGe detector. As one sees in this figure and Table 3.4, it is clear that the purification of water reduces ^{137}Cs amounts. It has been tried to produce CsI powder using only one kind of water in the powder company. We measured samples from the products and the results are shown in Fig. 3.14 and Table 3.4.

A crystal grown with CsI powder only using the 'Pure' water has 15.6 $\pm$ 0.17 CPD background in the energy range of 10-15 keV as shown in crystal (A) of Fig. 3.15. The ^{137}Cs amounts in this crystal is 7.5 $\pm$ 0.9 mBq/kg which can contribute 2.6 $\pm$ 0.3 CPD at 10 keV. The crystal production with powder produced by the 'Ultra pure' water was done and processed for fabrication. We can estimate background level of this crystal using the result of powder and crystal measurement with HPGe detector. As shown in Table 3.4, the ^{137}Cs amounts in the powder using the 'Ultra pure' water is
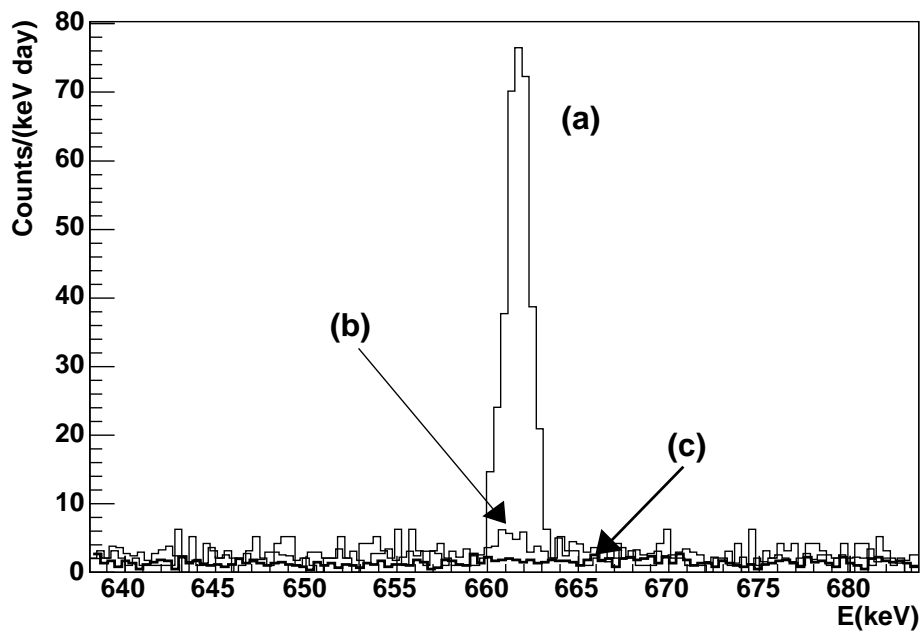
Figure 3.13: The measured spectra of water samples with HPGe detector for Cs-137. (a) "Processing" water, (b) "Pure" water, (c) "Ultra pure" water.
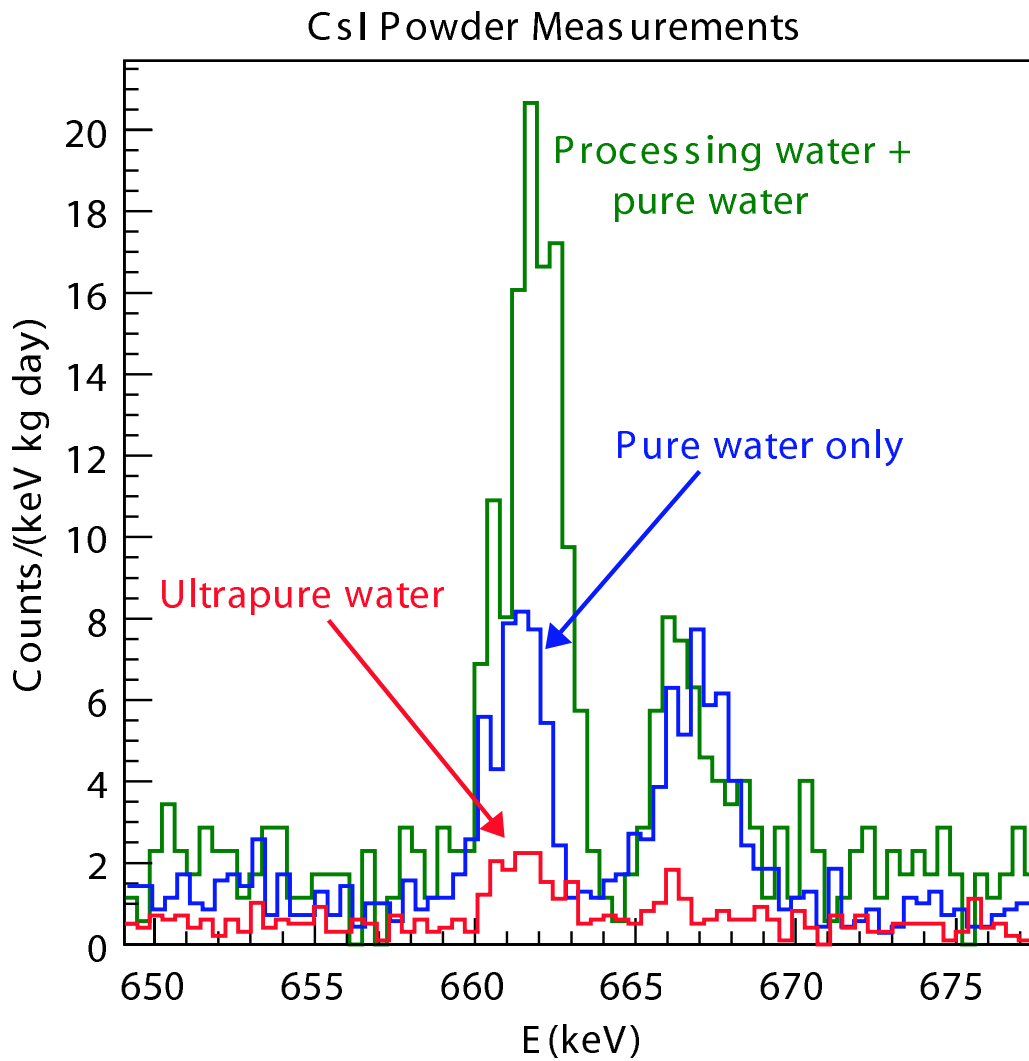
Figure 3.14:   The measured spectra of three CsI powder samples with HPGe detector

Table 3.4: Activity of ^{137}Cs isotopes (unit in mBq/kg)(error is statistical only). Measurement of water and CsI powder were done with HPGe detector. In the case of CsI(Tℓ) crystal using 'pure water' we used the spectrum from directly attached PMT.

	Water	CsI powder	CsI(Tℓ) Crystal
'Processing Water'	0.5∼1.66	20.5∼81.2	
'Pure' water	0.052±0.01	7.4±0.7	7.5±0.9
'Ultra pure' water	<0.01	1.9±0.5	1.7±0.3

1.9 ± 0.5 mBq/kg. The crystal measurement with HPGe detector shows consistent level, 1.7 ± 0.3 mBq/kg, with powder measurement. It will contribute about 0.7 CPD at 10 keV region.

^{87}Rb

Crystal (A) of Fig. 3.15 and Table 3.6 show that the Rb contamination of this crystal is 11.8 ±1.4 ppb, which can contribute 12.9 ± 1.5 CPD at 10 keV. This amount of Rb is consistent with ICP-Mass analysis result as one can see in Table 3.5. It is known that the Rb can be reduced by the recrystallization method.

The recyrstallization method [111] is well developed to purify the substances. The principle of recrystallization is that the amount of solute that can be dissolved by a solvent increases with temperature. The pure and impure materials can make compounds. Because two compounds have different solubility in the solvent (water for CsI), compounds which are less soluble will crystallize first by reducing temperature of solvent. As one can see in Fig. 3.16 , the CsI is less soluble than RbI. Therefore, CsI is crystallized first. Also, the crystallization process itself helps in the purification as the crystals form, they select the correct molecules which fit into the crystal lattice and ignore the wrong molecules. By one cycle of recrystallization in CsI crystal, about 25 % Rb can be reduced. The repeats of recrystallization make
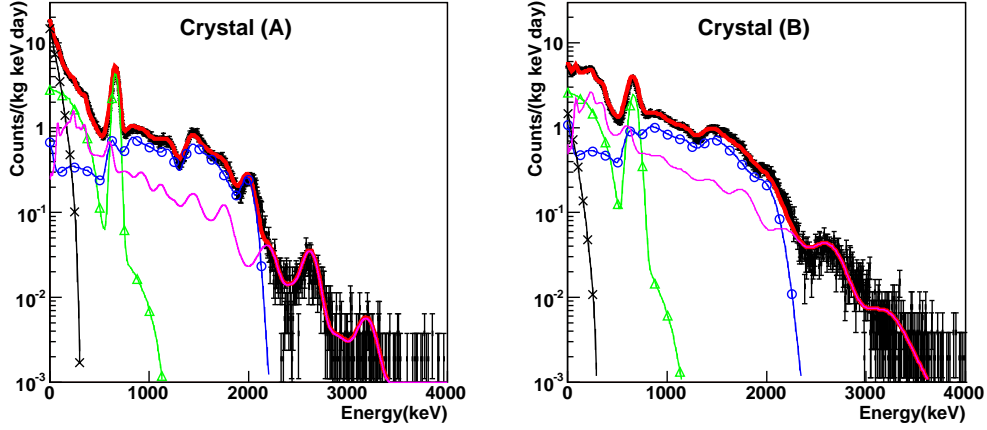
Figure 3.15: Background spectra (histogram with error bar) and the fit (thick solid line) to the spectra for the crystal (A) grown from ^{137}Cs reduced powder using the 'Pure' water and the crystal (B) grown from ^{137}Cs and ^{87}Rb reduced powder using the 'Pure' water and recrystallization method. The fit has been done from 20 keV to 3 MeV. Fit components are as follows: internal background of ^{87}Rb ("x"s), ^{137}Cs (triangles), and ^{134}Cs (circles) and external background (thin solid line) which will be discussed as followed section.

sufficiently low level of Rb amount in the CsI powder.

We have achieved less than 1 ppb contamination of the Rb in CsI powder using the method. Crystal (B) of Fig. 3.15 shows background spectrum of the crystal made of this powder. By using the 'Pure' water and the recrystallization method, we could obtain a background of 5.5 ± 0.1 CPD in the energy range of 10-15 keV. The Rb amounts in this crystal is 1.3 ± 0.4 ppb, which contributes 1.5 ± 0.5 CPD at 10 keV region. The ICP-Mass analysis of this crystal shows 2.8 ppb of Rb which is a little bit larger than the result obtained by the analysis energy spectrum of background in the crystal. We think this difference originated from the systematic error of ICP-Mass
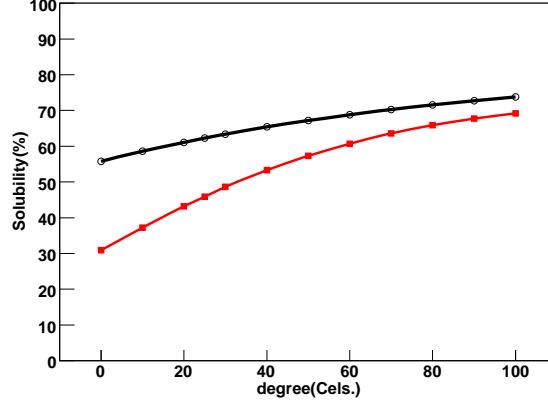
Figure 3.16: Solubility of CsI (filled square) and RbI (open circle) are shown. The values obtained from Ref. [112].

methods and may be due to the inhomogeneity of Rb in the crystal.

Table 3.5: ICP-Mass analysis of CsI(Tℓ) crystals (in ppb)

Element	**Rb**	**Th**	**U**	Tl	Li	Mg	Al	Fe	Ba
Crystal A	12.6	<0.02	0.038	255600	154	379	284	84	846
Crystal B	2.8	<0.02	0.08	176600	55	269	2898	234	949

[134]Cs

In the crystal (B) of Fig. 3.15, the [134]Cs contamination is 14.1 ± 1.14 mBq/kg, which contributes 1.00 ± 0.08 CPD at 10 keV. But suppression of [134]Cs contamination in CsI powder is very difficult because it was mainly made by neutron capture process of [133]Cs, which is the stable isotope. But γs from [134]Cs correlated with the beta electron, as described in Section 3.4.4, we can suppress low energy β with γ tagging with neighboring crystals. Fig. 3.17 shows the simulated background spectra from [134]Cs for the center crystal in 3×3 array of full size crystals with and without γ tagging by the surrounding crystals. We can reduce background from [134]Cs by about factor 20 if we
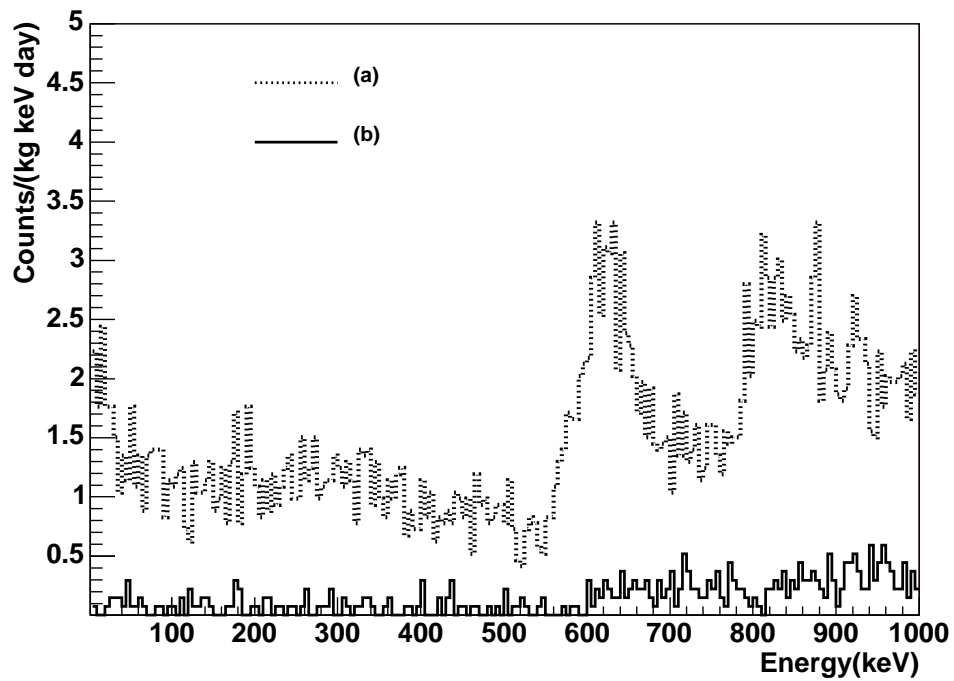
Figure 3.17: Background spectrum of ^{134}Cs obtained using Geant4 simulation at center of 3 × 3 array in the case of 30 mBq ^{134}Cs amounts and 8 × 8 × 30 cm^3 size (a) without Compton veto (b) with rejection of gamma tagged event in surrounding crystals

71

Table 3.6: Activity of Cs and Rb isotopes of various crystals in the step of background reduction(unit in mBq/kg)(error is statistical only); A: Crystal was made by ^{137}Cs reduced powder with 'Pure'water. B: Crystal was made by [87]Rb and ^{137}Cs reduced powder. C : Best crystal in the market [93]. D : Crystal was made by careful powder selection [93]. All of results were obtained from the binned χ^2 fit without Rb amount of crystal C and D which were obtained with ICP-Mass analysis.

radioisotope	A	B	C	D
[87]Rb (ppb)	11.8±1.4	1.32±0.43	3.2	10.4
[137]Cs (mBq/kg)	7.5±0.9	6.3±0.7	193.1±4.1	23.3±3.3
[134]Cs (mBq/kg)	8.95±1.11	14.1±1.14	38.0 ±3.2	34.4±2.6
total at 10-15 keV (CPD)	16	5.5	65	20

use surrounding crystals as veto detectors for gamma tagging.

U and Th

[238]U and [232]Th can remain naturally because of long half life. Many Daughter radioisotope from [238]U and [232]Th can make α, β and γ particles which contribute to low energy background. The mass concentration could be determined by α particle analysis [93, 113] as well as by ICP-Mass analysis [114]. Because it is difficult for ICP-Mass analysis to lower its sensitivity below the level of ppt, we tried to estimate the concentration with alpha particle analysis in the CsI(Tℓ) crystals.

Since the decay time of α is faster than that of γ, α can be well separated from γ as shown in Fig. 3.18 (a). The mean time in the figure is defined as

$$< t >= \frac{\sum h_i t_i}{\sum h_i},$$

where h_i is the pulse height in each time bin t_i. The measured energy spectrum of α is shown in Fig. 3.18 (b)
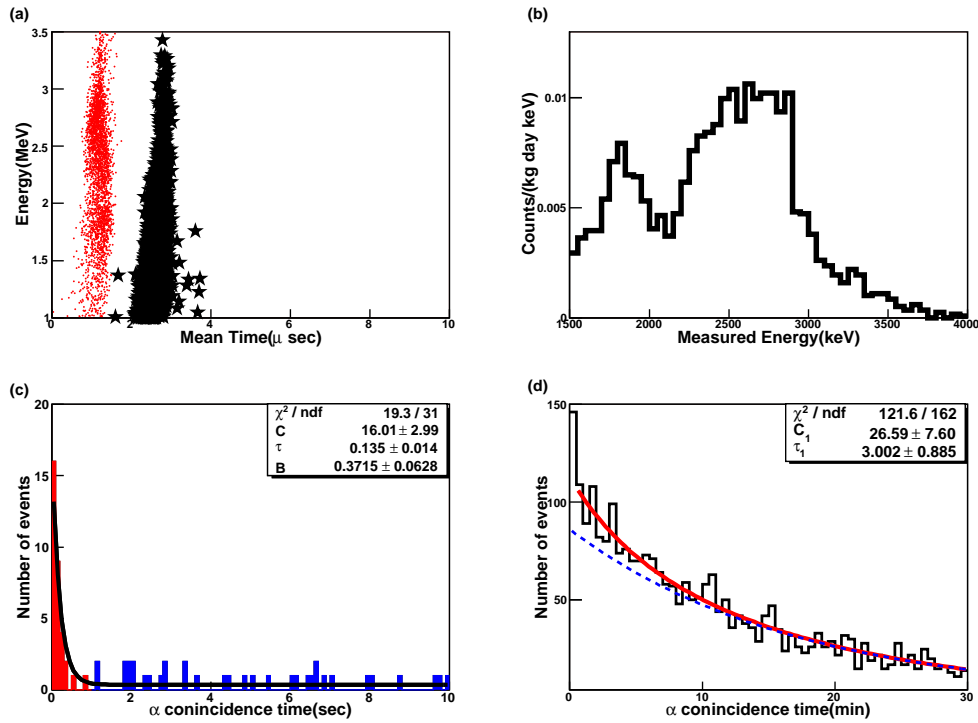
Figure 3.18: (a) Two-dimensional distribution of energy vs. mean time, (b) Measured energy spectrum of α particle, (c) α-α coincident spectrum for ^{216}Po to ^{212}Pb decay channel from ^{232}Th decay chain with overlaid best fit (solid line), and (d) ^{218}Po to ^{214}Pb decay channel from ^{238}U decay chain with overlaid best fit (solid line). Dashed line shows estimated background components from accidental β-α coincident event

Described in Ref. [113], ^{238}U and ^{232}Th amounts can be estimated by the α-α time coincident events study. In the ^{232}Th chain, ^{220}Rn $\to$ ^{216}Po $\to$ ^{212}Po channel have α-α coincident events with 0.145 sec half-life. Fig 3.18 (c) shows delay time distribution of crystal (B) for that channel. The background depend on the single α rates which are estimated as 0.00016/kg/sec or one event per 16.0 minutes for crystal (B). Because the single α rate is much longer than half-life of this channel, we can consider the background as constant in the fit. The fitting function is defined as

$$f(t) = Ce^{-ln(2)t/\tau} + B.$$

The fitted half-life of this channel is 0.135±0.014 sec which is consistent with the real value (0.145 sec). With an assumption of secular equilibrium, the mass concentration of ^{232}Th is estimated to be 0.38±0.07 ppt.

In the ^{238}U chain, ^{222}Rn $\to$ ^{218}Po $\to$ ^{214}Pb channel have α-α pairs with 3.10 minutes half-life. Because the delay time of this channel can be overlaid with accidental event from single α, we have estimated the accidental event from β-α coincidence. β-α coincident events having delay time higher than 1 minutes are fitted with one exponential components to avoid coincident events. In Fig. 3.18 (d), dashed line shows the estimated background components. The α-α delay time spectrum is fitted by fitting function

$$f(t) = C_1 e^{-ln(2)t/\tau_1} + C_2 e^{-ln(2)t/\tau_2},$$

where τ_2 is half-life obtained from the accidental β-α events and its fit. The obtained half-life of this channel is 3.00±0.89 minutes which is consistent with 3.10 min. We extract α-α pairs of this channel with subtraction of background from total histogram. In the process, we consider the fast α-α channel from ^{232}Th chain. Taking into account all the effects, we obtained 0.75 ± 0.23 ppt of ^{238}U mass concentration.

The contamination levels of ^{238}U and ^{232}Th are slightly lower than previous results of CsI(Tℓ) crystal [93, 113] and NaI(Tℓ) crystal [115]. The background spectrum originated from internal U/Th are estimated with GEANT4
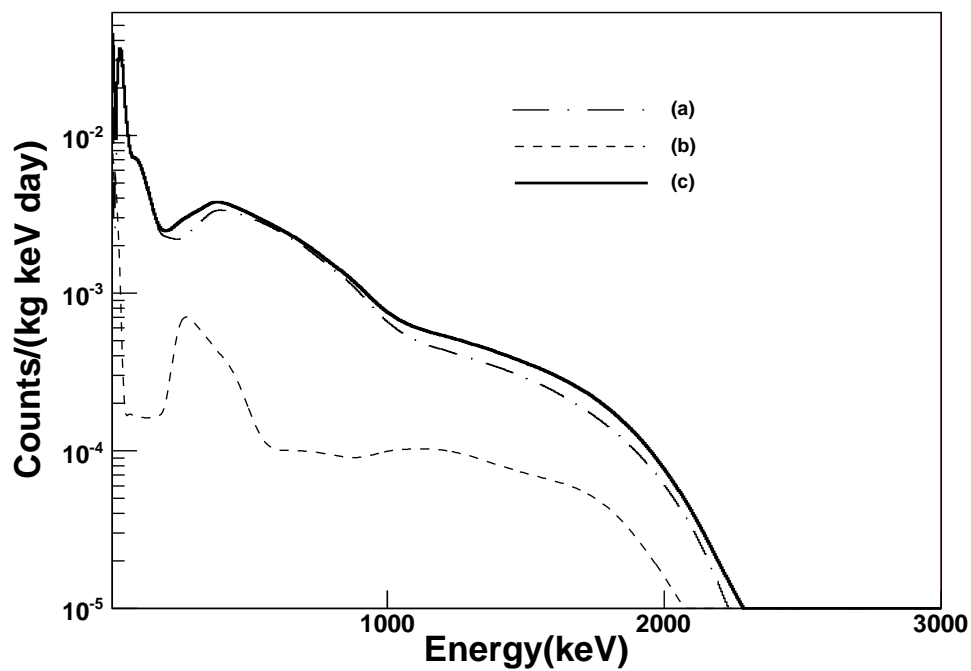
Figure 3.19: Estimated background spectrum from internal ^{238}U (a), ^{232}Th (b), and overall spectrum (c) using central value of results of α particle analysis which are 0.75 ± 0.23 ppt and 0.38 ± 0.07ppt for ^{238}U and ^{232}Th respectively.

simulation as one can see in Fig 3.19. The background level caused by internal U/Th concentration is much lower than the background from other sources.

3.4.6   External Background

Table 3.7: The ^{238}U, ^{232}Th, and ^{40}K contamination in the PMT measured with HPGe

Radioisotope	^{238}U	^{232}Th	^{40}K
Concentration (mBq/PMT)	78.2 ± 4.2	25.5 ± 4.4	504 ± 72

The reduction of ^{238}U, ^{232}Th, and ^{40}K amounts in PMT is important to develop the low-level crystal detectors [116]. We used the low background quartz window PMT and 5 cm long quartz light guide to reduce these background. The estimation of U/Th/K concentrations in the PMT are performed by the measurement of γ spectrum with HPGe detector. We identify the significant peak from those radioisotopes and calculate the activities with GEANT4 simulation. Table 3.7 shows the result of this measurement. We have included the measured PMT background as an external background to the spectrum fit (Fig. 3.20).

Because there is still an unexplained residual background component, we must consider the other sources. We have used the OHFC structure to assemble the PMT on crystal and black plastic sheet to shield light. We consider the U and Th contamination from the materials surrounding the crystal. We have also included the ^{222}Rn and ^{208}Tl backgrounds for the external background components. The ^{222}Rn in air is an important background source in the measurement. We have flown N^2 gas 4ℓ/minutes to the inner box of Cu shield. But, the air between Cu shield and lead shield has the same ^{222}Rn concentration in the detector room. The simulated ^{222}Rn decay from outside of Cu shield was included to fit as one component of the external background.
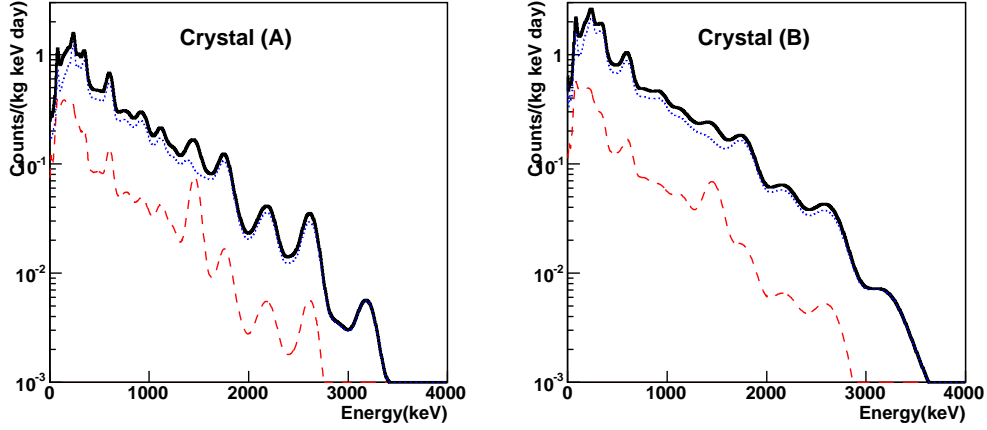
Figure 3.20: External background spectra (solid line) obtained by binned χ^2 fit from Fig. 3.15. The PMT background (dashed line) obtained from HPGe measurements and residual external background spectrum (dotted line) (see Fig. 3.21) were included.

The ^{208}Tl is also considered due to the enhancement of 2.614 MeV peak. The ^{208}Tl is beta-emitter decaying to ^{208}Pb, but the subsequent γ (2.614 MeV) have only 16.7 ps life time. Therefore, if ^{208}Tl was contaminated in the inside of crystal, the 2.614 MeV peak was disappeared. Especially we used stainless steel between lead shield and Cu shield for supporting the shield, we consider ^{208}Tl decay from the stainless steel. The estimated component of the external background from the best fit are shown in Fig. 3.21.

3.4.7   CsI(Tℓ) Crystal Detector

We have successfully reduced the internal background of CsI(Tℓ) crystal as one can see in Fig. 3.22. The crystal D of Fig. 3.22 is one of that crystal which is arrived in June of 2004. Size of it is $8 \times 8 \times 23$ cm^3. In January 2005 we got two more crystals which were same quality with the crystal (B) because we used same batch of CsI powder and grew crystals with same process in
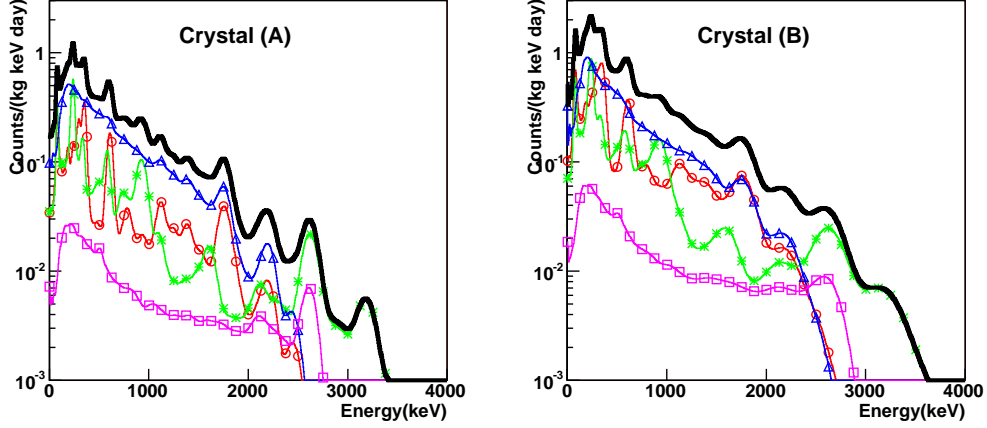
Figure 3.21: Residual external background spectra (solid line) with subtracting PMT background (Fig. 3.20). We considered the external ^{238}U (circles), ^{232}Th ("*"s). Furthermore, ^{222}Rn (triangles) in the air between Cu and lead shield and ^{208}Tl (squares) in the stainless steel were included.

the same company. But the size of two crystals were $8 \times 8 \times 30$ cm^3.

In the beginning of 2005 we successfully produced the powder in which ^{137}Cs is further reduced than previous one with 'ultra pure' water. And, we contacted another company (Beijing Hamamatsu Photon Techniques Inc. in China) for crystal growing because the light output of previous crystals were much lower than normal CsI(Tℓ) crystals. From the October of 2005, the company successfully had grown the full sized crystals ($8 \times 8 \times 30$ cm^3). The background spectrum was measured as one can see in Fig 3.22 E. Until now we have 13 of full sized crystals and continuous effort of adding more crystals up to 250 kg is in progress. The summary of provided crystals are shown in Table 3.8. As a matter of convenience we named the each crystal as S0406, S0501A, S0501B, B0510A, B0510B, B0511, B0512, B0601, B0605A, B0605B, B0606A, B0606B, B0607, B0609A, and B0609B which correspond to arrived date. The light output of beijing crystals is 20%~30% higher than that of shanghai crystals. This promise the better PSD power.
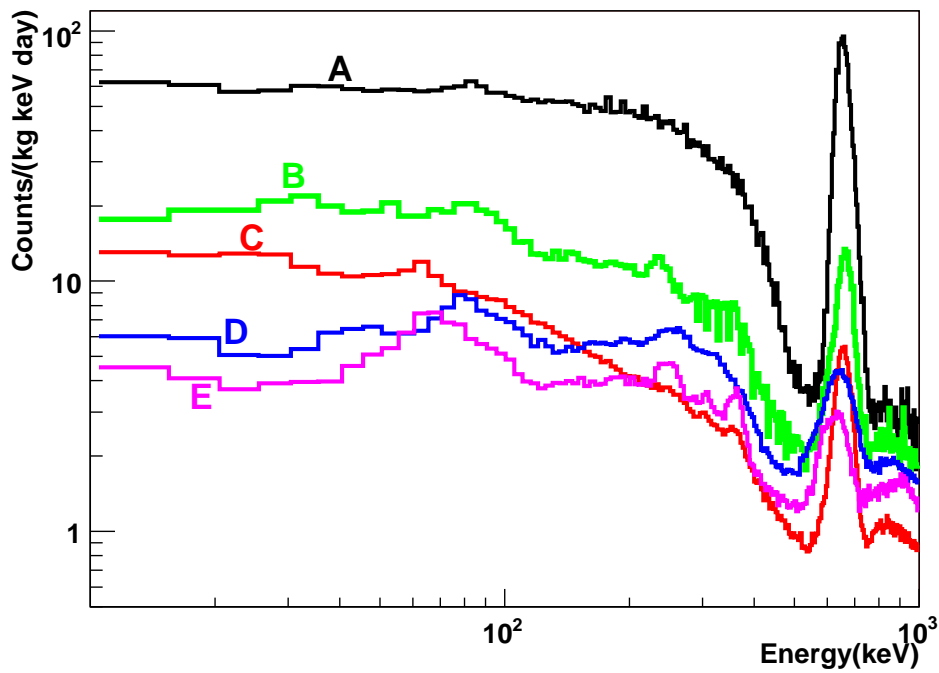
Figure 3.22: Background spectra of various crystals in the step of background reduction A : Best crystal in the market [93]. B : Crystal was made by careful powder selection [93]. C: Crystal was made by ^{137}Cs reduced powder with 'Pure'water. D: Crystal was made by ^{87}Rb and ^{137}Cs reduced powder with recrystallization and 'Pure' water. E: Crystal was made by ^{87}Rb and ^{137}Cs reduced powder with recrystallization and 'Ultra pure' water.

Table 3.8: Growing status of low background CsI(Tℓ) crystals

Label	Quality	Weight	light output	Company
S0406	6 CPD	6.7kg	5.5/keV	shanghai
S0501A	6 CPD	8.7kg	4.5/keV	shanghai
S0501B	6 CPD	8.7kg	4.2/keV	shanghai
B0510A	4 CPD	8.7kg	5.9/keV	beijing
B0510B	4 CPD	8.7kg	5.3/keV	beijing
B0511	4 CPD	8.7kg	4.9/keV	beijing
B0601	4 CPD	8.7kg	5.3/keV	beijing
B0605A	4 CPD	8.7kg		beijing
B0605B	4 CPD	8.7kg		beijing
B0606A	4 CPD	8.7kg		beijing
B0606B	4 CPD	8.7kg		beijing
B0607	4 CPD	8.7kg		beijing
B0609A	2 CPD	8.7kg		beijing
B0609B	2 CPD	8.7kg		beijing

To improve the light collection, CsI(Tℓ) crystals were wrapped with two layers of teflon (0.2 mm thick) sheet as a light reflector. Two 3-in. photomultiplier tubes (PMTs), 9269QA of Electron Tubes Ltd., were attached directly to both end faces of the crystal with optical grease as one can see in Fig. 3.23. The 9269QA has an RbCs photocathode with quartz window. The sensitivity of the RbCs photocathode is particularly enhanced in the green region which is better matched with scintillation from CsI(Tℓ) than the normal bialkali photocathode. The PMT signals are amplified 10 and 100 times with home-made fast amplifiers. The two signals of two amplification factors go to 500MHz digitizers which are home made VME modules. 500MHz FADC modules have a programmable trigger and a double buffering system to remove DAQ dead time. USB2 interface was used between the VME and the computer. The event trigger is generated by the requirement of 2 photoelectrons within 2 μs for each PMT. A DAQ system for the VME-USB2 interface with a Linux PC was developed using the ROOT package [117].

Figure 3.23: Sample of CsI detector

The digitizer sampled the signal at a rate of 500 MHz with an 8-bit pulse height value over 32 μs duration.

3.5 Neutron Monitoring

Because WIMP interacts with the target nuclei through a WIMP-nucleus elastic scattering, the neutron signals in the CsI(Tℓ) detectors are identical with WIMP signals. Therefore we need minimizing the neutron backgrounds as well as fully understand background sources through adequate shielding when using the pulse shape discrimination method for WIMP detection. To modulate neutrons, we have 30 cm mineral oil layer and 5 cm polyethylene (PE) layer. Using the GEANT4 simulation, we find that the neutron flux can be reduced sufficiently for dark matter search with these shielding. To understand remained background we installed neutron monitoring detectors outside of Cu box and inside of Pb shielding. Also, we installed neutron detectors outside of main shielding for neutron flux measurement of the underground laboratory.

3.5.1 Neutron Background

Neutrons at a deep underground site are produced from three major sources: comic-ray muon interactions, spontaneous fission of ^{238}U, and (α,n) reactions. Photonuclear interactions of muons generate neutrons by fragmenting the target nuclei. Neutrons can also be produced by muon capture, but the rate is much lower than that of photonuclear interactions at the depth of Y2L.

Fission of ^{238}U generates neutrons with an neutron energy spectrum similar to that of ^{252}Cf neutron source. Alpha particles from the decay of ^{238}U and ^{232}Th can generate neutrons through the (α,n) reaction. The energy and neutron flux of neutrons from this reaction depends on the cross-section of the (α,n) reaction. Thus the rock contents of ^{238}U and ^{232}Th play an important role in neutron production.

3.5.2   Neutron monitoring detector (NMD)

Among various organic scintillators used for the fast neutron spectroscopy and the time of flight measurement, the BC501A liquid scintillator has an additional advantage of an excellent pulse shape discrimination between neutrons and γs. We used the BC501A liquid scintillation counter for the measurement of the fast neutron flux at the underground laboratory and the monitoring of the fast neutron flux in the shield. We have constructed 0.5 ℓ [100] to 20 ℓ [118] neutron detectors with BC501A liquid scintillator with stainless-steel containers.

The 1 ℓ BC501A detectors used in the actual measurement are in cylindrical shape. The cylinder of 15 cm length and 5 cm inner diameter is made of 2 cm thick teplon. The end point of one side is composed with 1 cm quartz window to read light output. We mount 3-inch low background PMT for the signal readout. The picture of neutron detector is shown in Fig. 3.24.

The signal from PMT is amplified with preamplifier and transmitted to FADC through 20 m-long coaxial cable. The trigger is formed in the FPGA chip on the FADC board by the software set self-trigger system. Muon trigger time is also transmitted to the FADC for NMD signal of main shielding to get the information of muon induced neutron events.

The 662 keV γs from ^{137}Cs and the 1173 keV and 1332 keV γs from ^{60}Co are used to calibrate energy of neutron detectors. Because of low mass number (^{12}C and ^{1}H) of BC501A, it is difficult to see the full peak of ^{137}Cs and ^{60}Co. We use the Compton edge (478 keV and 1041 keV for ^{137}Cs and ^{60}Co

Figure 3.24: The teplon container for BC501A liquid scintillator

respectively) for the energy calibration using fit with a fitting function as follow:

$$f = \frac{p0}{e^{p1(x-p2)} + 1}.\tag{3.3}$$

In this equation, parameter p2 is the Compton edge. Fig. 3.25 shows the energy calibration for each source and the linear fitting of two calibrated point to extract calibration constant (ADC/keV).

As one can see in Fig. 3.26, the signal shape of γ is different from that of neutron. Therefore we can use the Digital Charge Comparison method (DCC) [119] is used to separate neutrons from γs. The DCC method uses the ratio between the total signal and the tail part of the signal. Fig. 3.27 shows an example of separation between γ and neutron with 0.5 ℓ BC501A liquid scintillator using DCC method. Also, the performance of 20 ℓ detector was well described in Ref. [118].

Although the DCC method was widely used in the BC501A liquid, we developed the weighted spectrum analysis to separate neutrons from γs. We made probability function of pulse shape for identified neutron and γ events as one can see in Fig. 3.28 using accumulation of pulse shape. The PSD
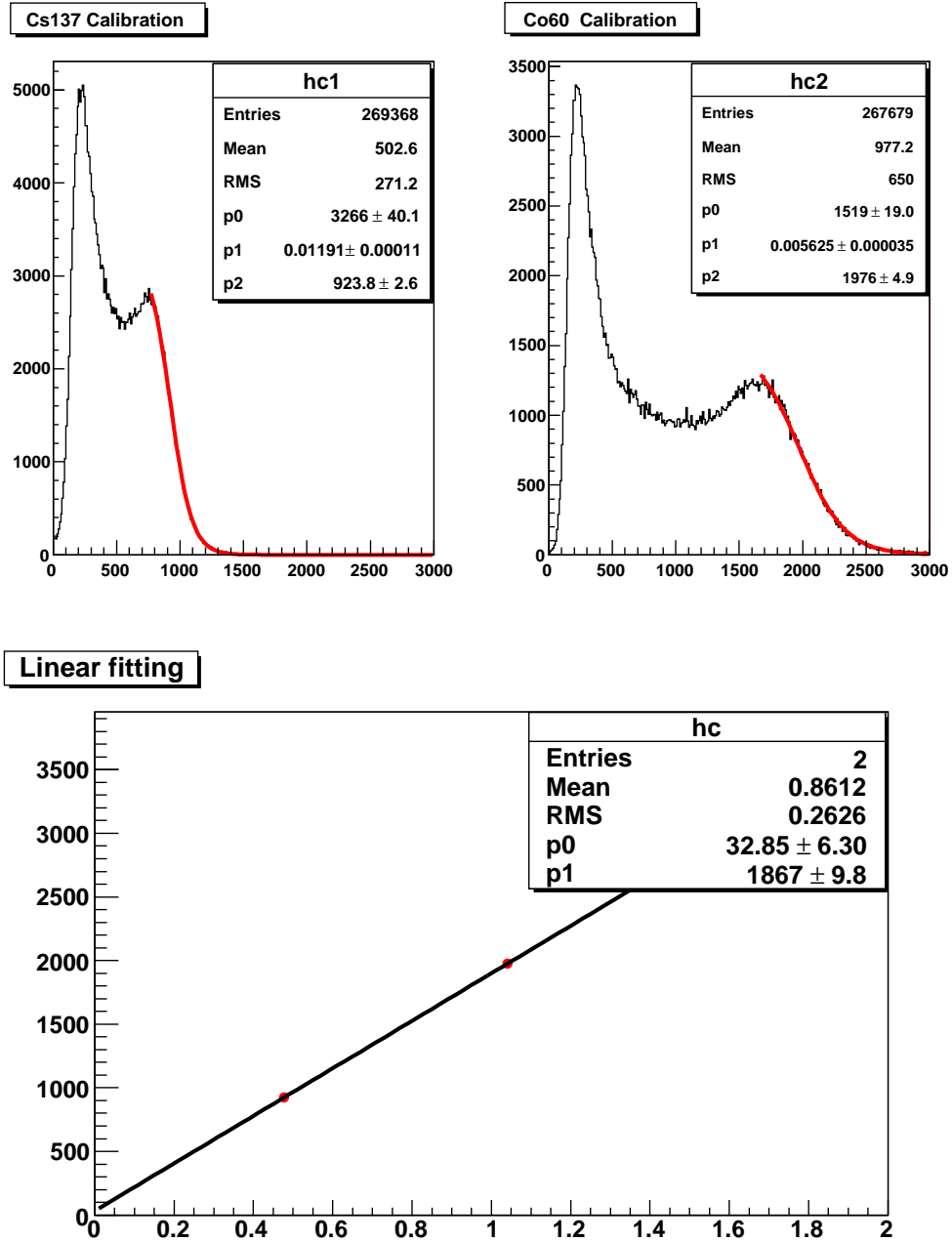
Figure 3.25: Energy calibration of neutron detector.
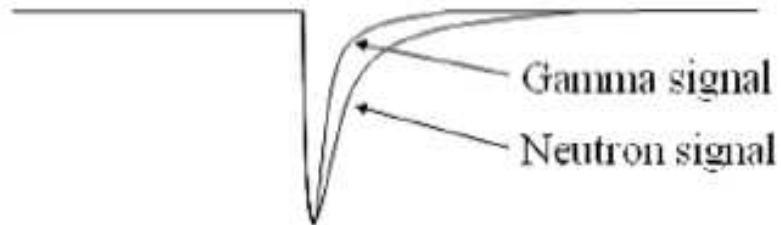
Figure 3.26: Shape of the γ and the neutron signals in BC501A.
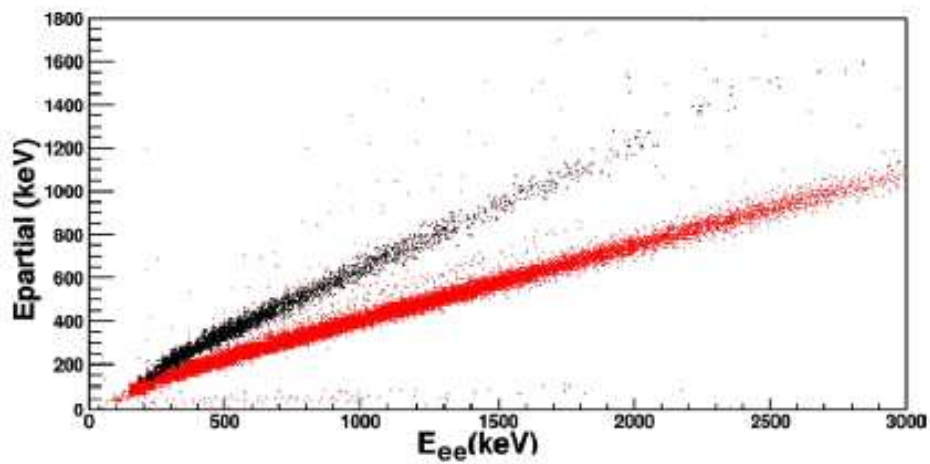
Figure 3.27: Neutron and γ seperation of 0.5 ℓ BC501A liquid scinitillaotr. The figure was obtained from Ref. [100].
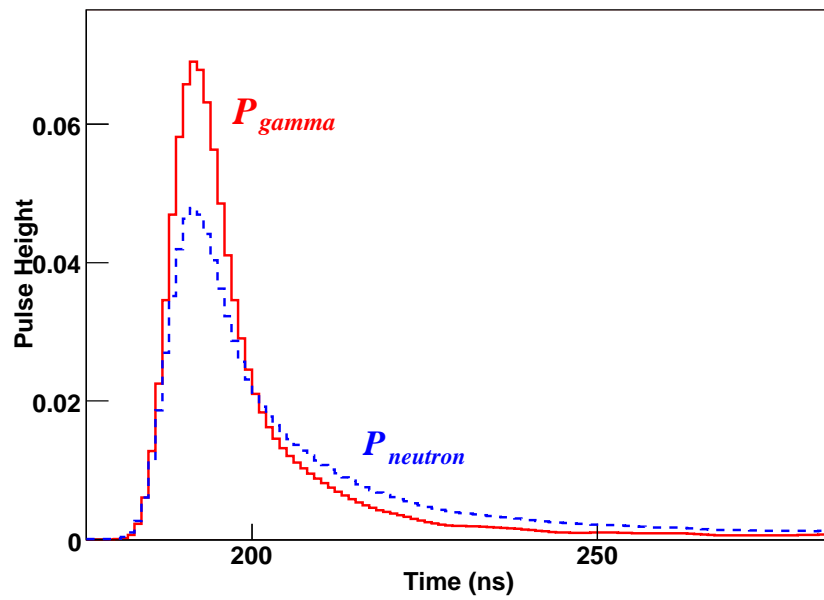
Figure 3.28: Normalized distribution of accumulated pulse shape. The neutron signals can be selected with DCC method for over than 300 keV events.

variable is defined by the ratio of weighted sum $A-$ and $A+$ defined by following formula:

$$If(P_{neutron_i} - P_{gamma_i} > 0)A- = \int (P_{neutron_i} - P_{gamma_i}) \times Pulse_i, \quad (3.4)$$

$$If(P_{neutron_i} - P_{gamma_i} < 0)A+ = \int (P_{gamma_i} - P_{neutron_i}) \times Pulse_i, \quad (3.5)$$

$$PSD = \frac{A-}{A+}, \quad (3.6)$$

where $P_{neutron_i}$ is the probability of neutron for i-th bin and P_{gamma_i} is the probability of γ. Fig. 3.29 (a) shows the separation between γs and neutrons from background data.

3.5.3 Underground Data

Neutron flux

In the main shielding, exactly saying between copper chamber and lead shielding which is also covered with 30 cm mineral oil and 5 cm PE of neutron modulators, we had been taking the neutron background with NMDs (neutron monitoring detectors). From July 2004 to October 2004, we used only one of NMD, which had 1.2 ℓ container, beside copper chamber. In October 2004, we installed one more detector, which had 1.0 ℓ container, to increase data amounts. At that time, the location of NMDs is moved to the top of the copper chamber because of the space problem.

In the outside of shielding, we made 5 cm lead shielding box to measure the neutron flux of experimental hall without any neutron modulator. Similar teplon containers with NMD of the main shield were used to construct detectors. Until October 2004, we used only one of detector, but we installed one more module at that time as we added one more detector inside of main shielding.

With data up to October 2004, we try to calculate the neutron flux for inside of main shielding and outside of shielding (5 cm lead shielding). Total
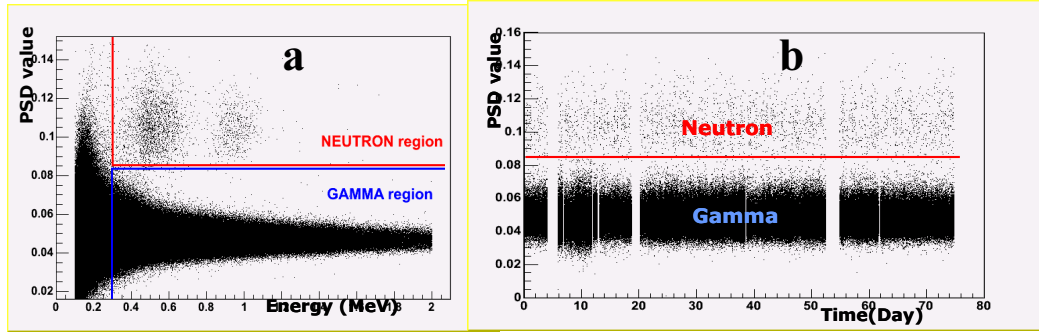
Figure 3.29:   The left shows the PSD value as a function of energy for 67.4 days background data from inside of main shielding. And the right shows the PSD value as a function of time for whole period.

effective data taking period is 67.4 days for inside. The outside is compatible with that of inside.

With weighted-DCC method, we can well separate the neutron signals from gammas as one can see in Fig. 3.29 (a) for background data from inside of main shielding. We apply the n/γ separation cut for energy range from 300 keV to 2 MeV. During whole period of data taking, the trigger rate and PSD distribution are very stable as one can see in Fig. 3.29 (b).

With good separation between neutron and γ we have the energy spectra of neutron and γ separately as one can see in Fig. 3.30. The events rate from 300 keV to 2 MeV was 33.65 counts/ℓ/day and 8611 counts/ℓ/day for neutron and gamma respectively. The total neutron events are 2722.

Before accounting the neutron band as neutron signals, we consider the α background contribution to the neutron band. Naturally, ^{238}U and ^{232}Th can be remained in the material because of long half life. The daughters of those can make a lot of γ, β, and α particles as one can see in Table 3.9 and Table 3.10. The signal from α is similar with nuclear recoil signal from neutrons in the NMDs. Therefore the α signals can contribute to the neutron band. The amounts of α particles from ^{238}U and ^{232}Th can be estimated by the α-α and α-β coincidence study [113].

88
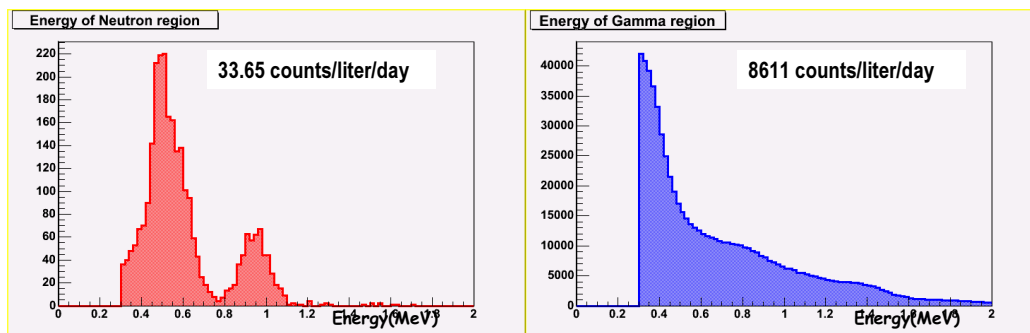
Figure 3.30: Energy spectrum of NMD in the inside of main shielding for neutron band and gamma band

From the ^{238}U chain, β-α coincidence between ^{214}Bi and ^{214}Po decay can easily identified due to the very fast life time of ^{214}Po (see Table 3.9 and Fig 3.31 (a)). The fitted life-time of ^{214}Po is obtained as 0.155 ± 0.008 ms which is consistent with the real value 0.164 ms. Estimated decay events with efficiency correction are 534 ± 25 events. Also, the α-α decay channel from ^{222}Rn and ^{218}Po can be identified as one can see in Fig. 3.31 (b). The fitted life-time of ^{218}Po is obtained as 3.42 ± 0.59 min which is consistent with the real value 3.10 min. Estimated decay events with efficiency correction are 553 ± 44 events which is compatible that of ^{214}Po decay. Fig. 3.31 (c), (d), and (e) show the measured energy spectrum of αs for ^{214}Po, ^{222}Rn, and ^{218}Po respectively. We can obtain quenching factors of αs as 12.0 %, 9.4 %, and 10.1 % for 7.83 MeV, 5.59 MeV, and 6.12 MeV respectively.

From the ^{232}Th chain, α-α coincidence between ^{220}Rn and ^{216}Po can be identified as one can see in Fig. 3.32. The fitted life-time of ^{216}Po is obtained as 0.114 ± 0.030 sec which is consistent with the real value 0.145 sec. Estimated decay events with efficiency correction are 26 ± 5 events. The quenching factors for 6.41 MeV and 6.91 MeV are obtained as 9.3 %.

To estimate the amounts of α, we need to know the equilibrium states of ^{238}U and ^{232}Th chain. As we describe above, events from ^{238}U decay are much larger than those from ^{232}Th. Therefore, we try to fit the neutron band spectrum with α spectrum from ^{238}U decay chain. To simulate α spectrum
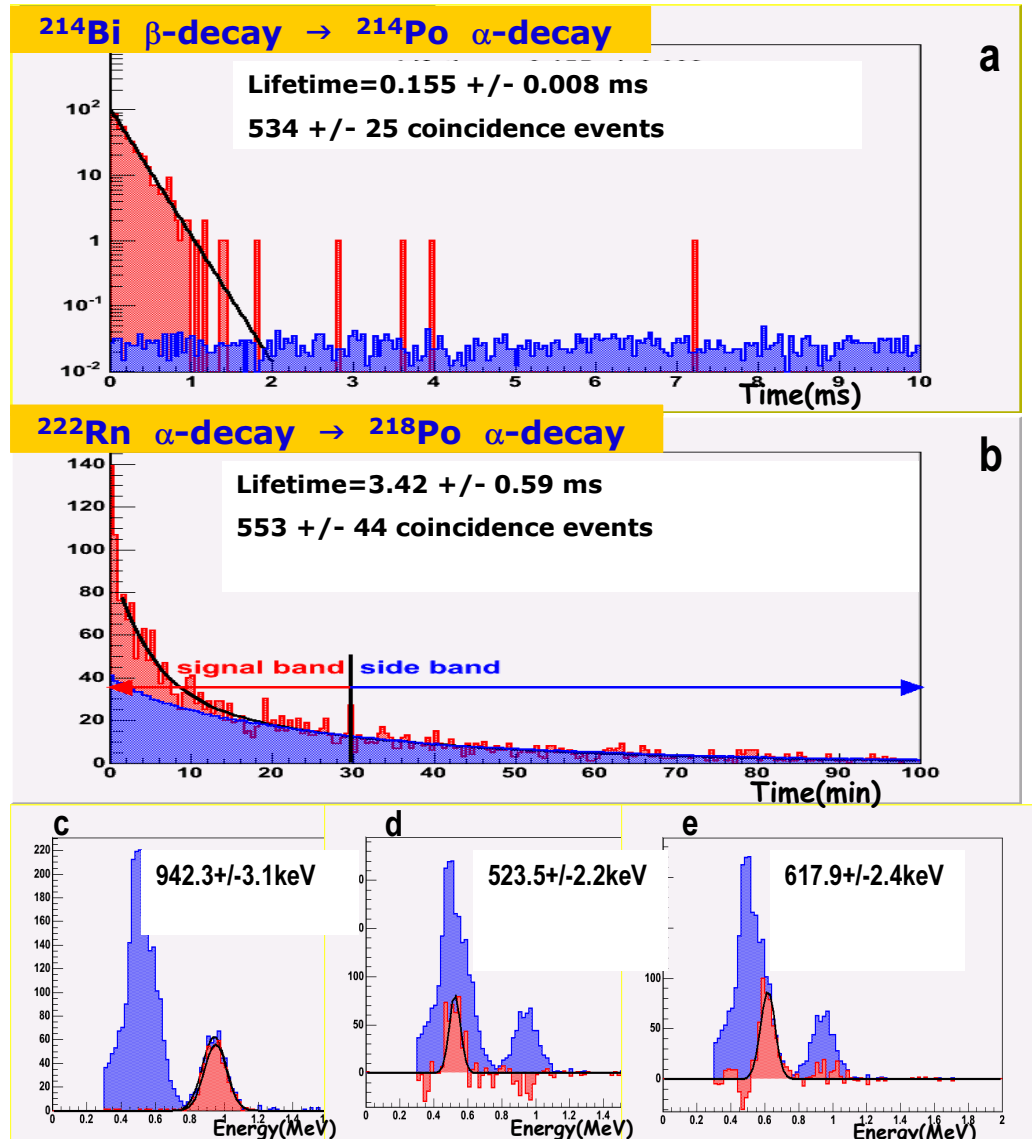
Figure 3.31: Coincidence events for ^{238}U chain
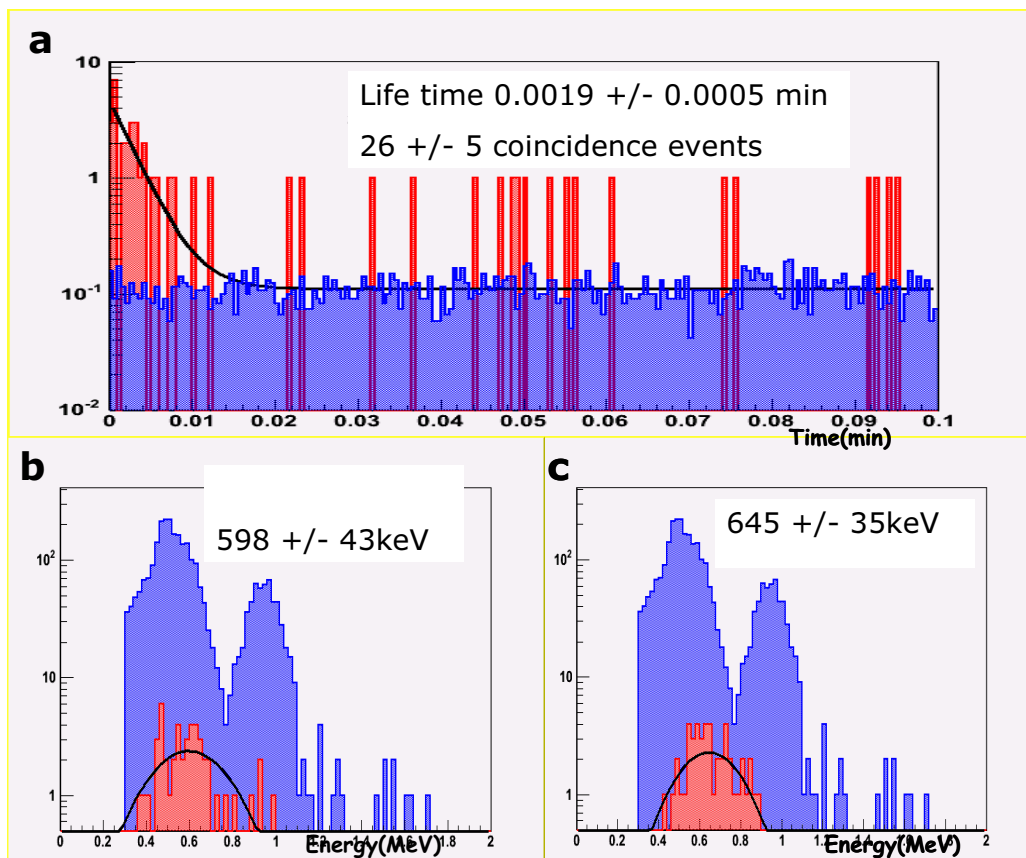
Figure 3.32: α-α Coincidence events between ^{220}Rn and ^{216}Po for ^{232}Th chain

Table 3.9: Decay Chain of ^{238}U

Isotope	Daughter	Lifetime	Decay	Q - value (MeV)
^{238}U	^{234}Th	4.47×10^9 year	Alpha	4.270
^{234}Th	^{234}Pa*	24.10 day	Beta	0.274
^{234}Pa*	^{234}Pa	1.18 min	Beta(IT)	2.117 (0.08)
^{234}Pa	^{234}U	6.70 hour	Beta	2.197
^{234}U	^{230}Th	2.46×10^5 year	Alpha	4.859
^{230}Th	^{226}Ra	7.54×10^4 year	Alpha	4.770
^{226}Ra	^{222}Rn	1600 year	Alpha	4.871
^{222}**Rn**	^{218}**Po**	3.824 **day**	**Alpha**	**5.590**
^{218}**Po**	^{214}**Pb**	3.10 **min**	**Alpha**	**6.115**
^{214}Pb	^{214}Bi	26.8 min	Beta	1.024
^{214}**Bi**	^{214}**Po**	19.9 **min**	**Beta**	**3.272**
^{214}**Po**	^{210}**Pb**	164.3 μ**s**	**Alpha**	**7.833**
^{210}Pb	^{210}Bi	22.4 year	Beta	0.064
^{210}Bi	^{210}Po	5.013 day	Beta	1.163
^{210}Po	^{206}Pb	138.4 day	Alpha	5.407

of ^{238}U chain we use measured α energy values as a function of real α energy with 2-dimensional polynomial fit as one can see in Fig. 3.33. Fig. 3.34 shows the energy spectrum of neutron band and best fit with MC simulation for equilibrium from ^{238}U (left) and ^{226}Ra (right). As a result we can conclude that the energy spectrum of neutron band is consistent with energy spectrum of α of ^{226}Ra equilibrium state. Best fit yield shows the $1.5 \pm 0.1 \times 10^{-6}$ ppt of ^{226}Ra contamination.

In the case of ^{232}Th chain, we consider the equilibrium from ^{232}Th. Then, overall estimated α events are 2823 ± 137. Because total events in the neutron bands are 2722 ± 52, the estimated neutron events are -101 ± 147 events which are converted as -1.25 ± 1.82 neutrons/ℓ/day. Therefore, neutron flux in the inside of main shield is consistent with zero. We can set the 90 % confidence level upper limit as 2.33 neutrons/ℓ/day.

We had installed the same NMD in the experimental hall with 5 cm lead blocks to measure the neutron flux in the experimental hall. Fig. 3.35
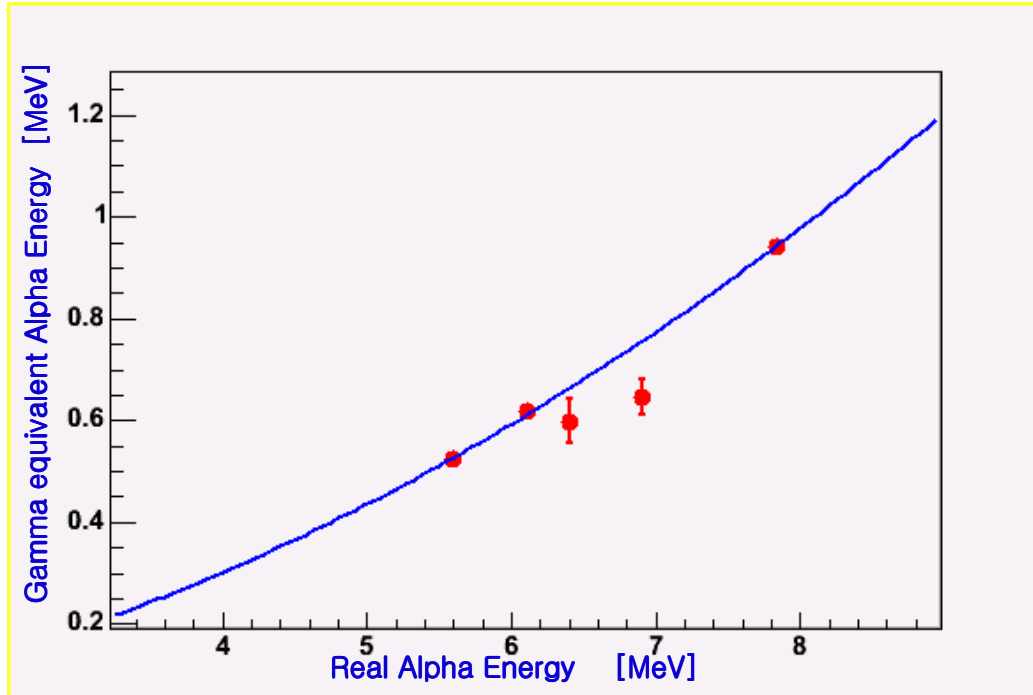
Figure 3.33: Measured α energy spectrum as a function of real energy
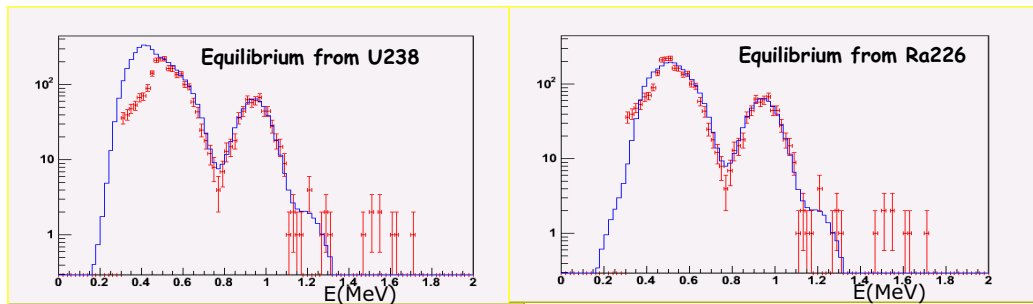
Figure 3.34: Energy spectrum of events in the neutron band from NMD of inside main shield (histogram with error bar) and best fit (solid histogram) with a MC simulation for equilibrium from ^{232}U (left) and ^{226}Ra (right)

Table 3.10: Decay Chain of ^{232}Th

Isotope	Daughter	Lifetime	Decay	Q - value (MeV)
^{232} Th	^{228} Ra	1.405×10^{10} year	Alpha	4.083
^{228} Ra	^{228} Ac	5.75 year	Beta	0.046
^{228} Ac	^{228} Th	6.15 year	Beta	2.127
^{228} Th	^{224} Ra	1.91 year	Alpha	5.520
^{224} **Ra**	^{220} **Rn**	3.66 **day**	**Alpha**	**5.789**
^{220} **Rn**	^{216} **Po**	55.5 **sec**	**Alpha**	**6.405**
^{216} **Po**	^{212} **Pb**	0.145 **sec**	**Alpha**	**6.906**
^{212} Pb	^{212} Bi	60.55 min	Beta (64.06%)	2.254
^{212} Po	^{208} Pb	299 ns	Alpha	6.207
^{212} Pb	^{208} Ti	60.55 min	Alpha (35.94%)	8.954
^{208} Ti	^{208} Pb	3.057 min	Beta	5.001

shows the energy spectrum of neutron band for NMD in the experimental hall. We have done similar delayed time coincidence study with NMD in the hall. Then we extracted neutron signals from α backgrounds. The measured neutron flux in the experimental hall is 8×10^{-7}/cm^2/s with neutron energy in the range 1.5 MeV $< E_n <$ 6 MeV which is about 40 times lower than that of CPL [100].

3.6   Muon Detection and active shielding

A high energy muon can generate neutrons by the interaction with surrounding materials such as rock and lead etc. Especially neutrons made in shielding materials are very harmful. Therefore we need to know the muon flux in our experimental hall and account the muon induced signals by coincidence study between muon detector and neutron detector.
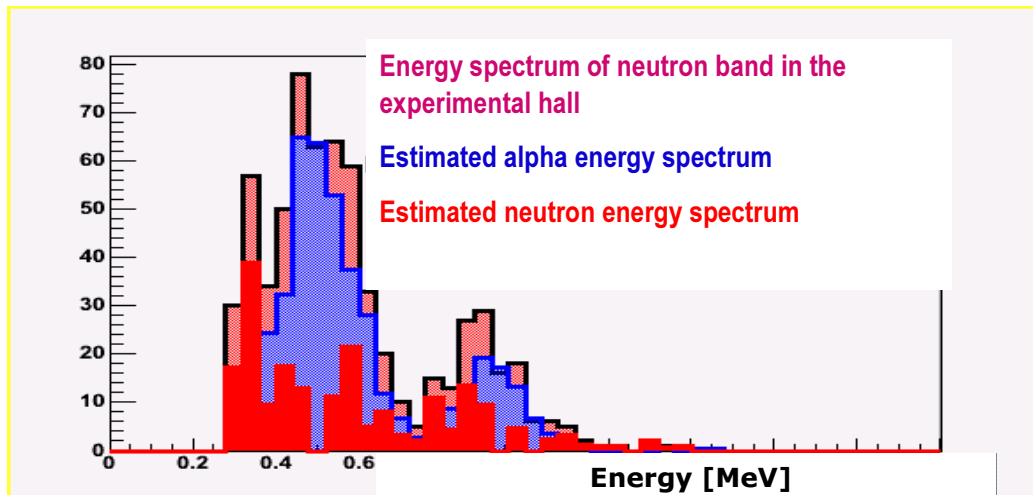
Figure 3.35: Energy spectrum of events in the neutron band from NMD of experimental hall. The estimated α and neutron energy spectrum are shown.

Figure 3.36: Picture of muon detector

95
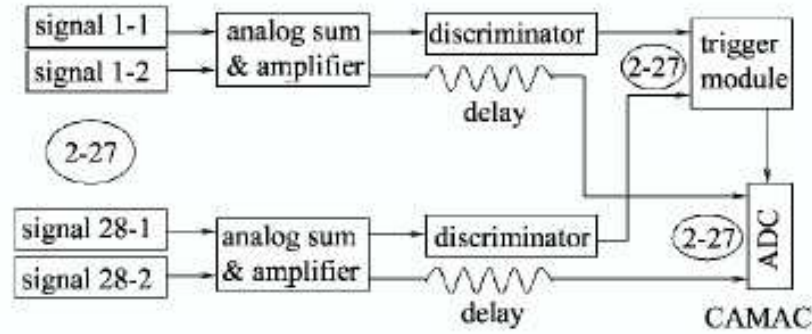
Figure 3.37: Scheme of MUD electronics

3.6.1 Muon Detector

For the continuous measurement of muon flux and for the study of muon induced signal, we make muon detector (MUD) by adding 5 % liquid scintillator in to the mineral oil of the neutron shield as one can see in Fig. 3.3. The composition of MUD is 95 % mineral oil and 5 % home-made liquid scitillator (Pseudo cummene+PPO+POPOP). The MUD have totally 8 quadrate detectors with 4π coverage (Fig. 3.36). The top and side modules are composed of one detector for each. But, the bottom is composed of three different modules. Overall volume is about 7800 ℓ.

There are glass windows on the surface of every module to read-out the scintillating signals. The read-out windows of top module is 6, each side module is 4, and each bottom module is 2. Two of 2-inch PMTs for total 28 windows are used to read-out of signals.

We use two PMTs for each window, the home-made analog sum modules are used to sum and amplify two different signals for one channel. To form a muon event trigger we made a camac trigger module which have 30 logic input and 8 logic output. The trigger module can calculate digital logic (AND, OR, NOR, NAND) among every input. We require 2 or more channels have hits in the one detector within 300 ns for event trigger. If one detector gives a trigger signal, the whole system has been triggered. The muon trigger output are taken together with the neutron detector and CsI detector to study of muon

induced signals. The schematic of MUD electronics is shown in Fig. 3.37.

3.6.2 Performance of MUD

We have checked the performance of muon detector with one of bottom module before underground installation. We have two signal read out windows at both sides. We attach the 3-inch PMT to each side window.

Attenuation length

The attenuation length of scintillation light is important parameter of big sized detector. We use relation between position of light source from PMT and intensity recorded by PMT to know the attenuation length. We use cosmic ray muon for interaction point with moving a 0.5 ℓ BC501A trigger detector to change the distance between the PMT and the interaction point. The intensity of PMT as a function of the distance between the interaction point and the PMT is shown in Fig. 3.38. This plot shows attenuation length spectrum.

We use two exponential function to fit the attenuation curve,

$$E = k \times \left[e^{p_0 + p_1 d} + e^{p_2 + p_3 d} \right], \tag{3.7}$$

where E is the light intensity in PMT, k is scale factor, d is the distance between the interaction point and the PMT, and p_0 to p_3 are fitting parameters which give two components of the attenuation length and the ratio between components. The fitted attenuation lengths are obtained as 36.2±4.9 cm and 178.6±34.1 cm for short component and long component respectively. The ratio between the short component and the long is about 2.4.

Detector Efficiency

To understand muon flux in our experimental environment, we need to understand the efficiency of the MUD. We use two trigger detectors to study
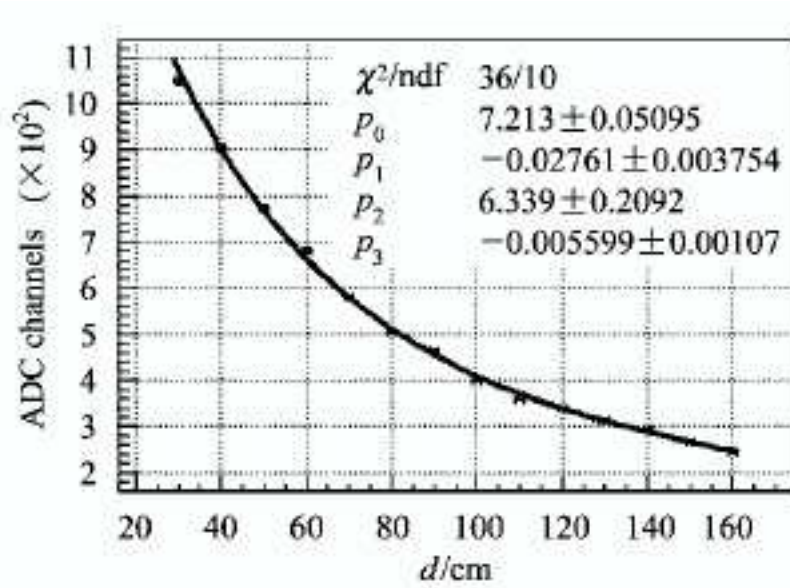
Figure 3.38:   Attenuation length test (dot point) with two exponential fit (solid curve)

the MUD efficiency, one is a 0.5 ℓ BC501A liquid scintillator and the other is a 20 cm $\times$ 20 cm plastic scintillator. The former one was put on the muon detector and the latter one was put under the muon detector. We use coincident signals between the BC501A detector and the plastic scintillator as a trigger.

We take data about 100000 events at the ground laboratory. In order to identify muon events, we give muon threshold cut to the each trigger detector. With this cut 26442 events are remained. The energy spectrum of the events in the muon detector is shown in Fig 3.39. We set the muon threshold in the muon detector to identify muon events properly. And then 25942 events are remained. Also, we consider the accidentally triggered events in the BC501A and the plastic scintillator originated from environments γ-ray. Standalone trigger rates of BC501A and plastic scintillator are measured with counter modules using same threshold of coincident measurement. The result shows 60 Hz of BC501A and 140Hz of plastic scintillator. Because we give 60 ns
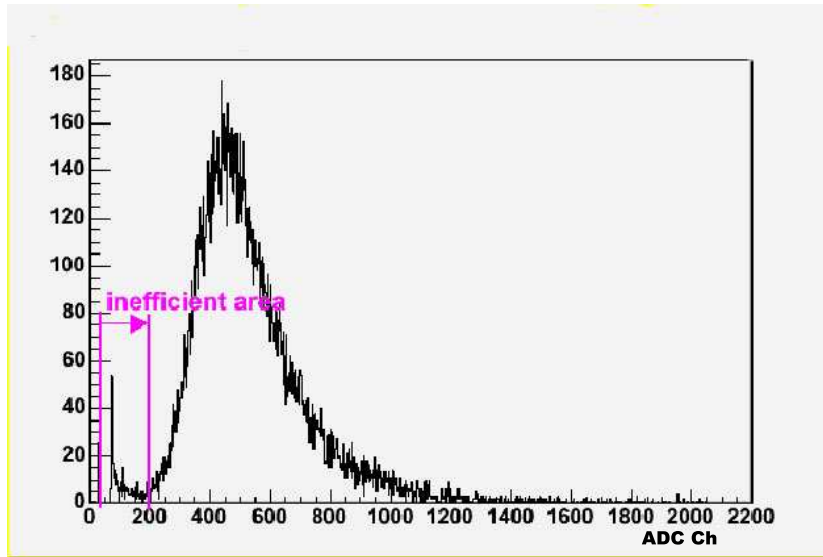
Figure 3.39: Muon detector light output spectrum with coincident condition between BC501A and plastic scintillator

time window for coincident condition, the accidental events rate is calculated as "2 x 60 ns x 140 Hz x 60 Hz $\sim$ 0.0015 Hz". Because the rate of coincident events is 1-2 Hz, the accidental trigger rate is negligible. Therefore, the muon detector efficiency is estimated to be 98.1 %.

3.6.3 Underground data

Muon flux

We have taken the MUD data from summer 2003 to now continuously. In this period, trigger rate of the MUD is very stable. Using these data we can calculate muon flux in Y2L. We account muons in the top module in coincidence with one of side or bottom module to tag muon events.

The detector efficiency, especially tagging efficiency, is important parameter to calculate muon flux. So we install plastic scintillator which is located at the top of the MUD. Using coincident signal between plastic scintillator and bottom detector, we can calculate top detector efficiency with similar
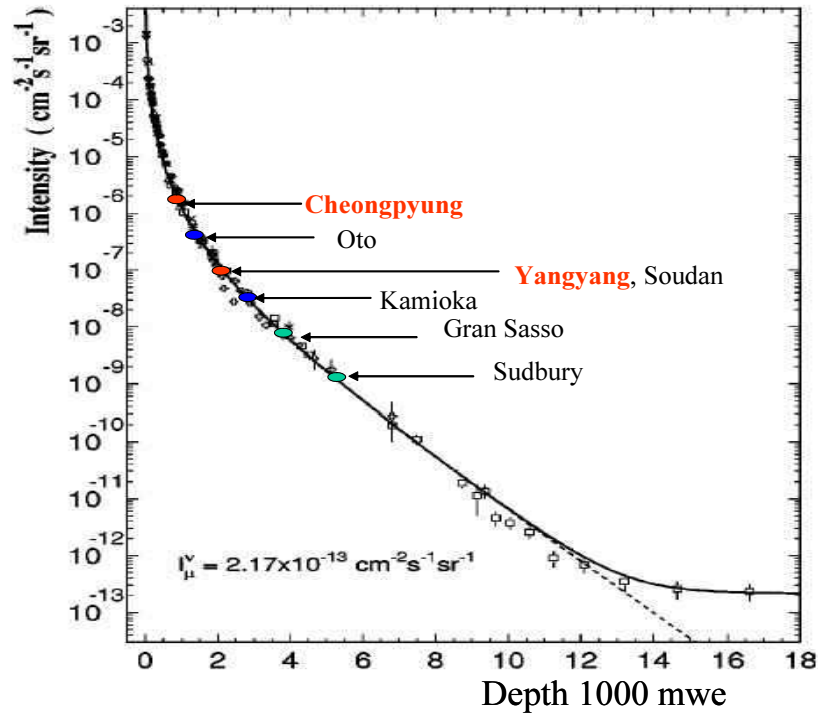
Figure 3.40:   Muon flux as a function of depth. Figure was obtained from Ref [120].

way in the ground laboratory. The muon trigger efficiency of single module is obtained as 97.0 % which is compatible with result from ground laboratory. The muon tagging efficiency, which is required coincident trigger between two detector (top and bottom), is obtained as 94.0 %. But, we give veto signal to CsI detector with muon trigger signal, the veto efficiency is much better than tagging efficiency. It is obtained as 99.9 %.

With 94.0 % tagging efficiency, we can calculate muon flux in the Y2L using tagged events as muons. The estimated muon flux in Y2L is 2.7×10^{-7} /cm^2/s. As one can see in Fig. 3.40, the muon flux of Y2L is compatible with Soudan mine (CDMS experiments).

Reconstruction of muon track

Muon direction is one of important parameter to understand muon induced signals in CsI(Tℓ) crystals. To identify the hit position in the detector we use χ^2 fit. As one can see in Eq. 3.7, the estimated light output in the window can be calculated with two exponential as a function of distance from hit position. For example, the top module has six signal read out windows. We give the light output for each window as $E[1]$ to $E[6]$. Suppose E_m for measured value and E_c for expected value, the procedure is as follow:

1) We can have 15 relative difference ratio $R_m[1]$ to $R_m[15]$ and the variation $ERR_m[1]$ to $ERR_m[15]$ with measured value $E_m[1]$ to $E_m[6]$ respectively.

$$R_m[k] = (E_m[i] - E_m[j])/(E_m[i] + E_m[j]),$$
$$ERR_m[k] = \sqrt{(E_m[i]^2 + E_m[j]^2)/(E_m[i] + E_m[j])^2}.$$
$$(i, j = 1 \sim 6 \, and \, i \neq j, k = 1 \sim 15)$$

2) For an arbitrarily point we have corresponding estimated values with simulated value $E_c[1]$ to $E_c[6]$.

3) We find out the minimized point of χ^2 value which is defined as follows:

$$\chi^2 = \sum_{i=1}^{15} \left(R_m[i] - R_c[i]\right)^2 / \left(ERR_m[i]^2 + ERR_c[i]^2\right). \qquad (3.8)$$

We use Minuit package [121] imposed in the ROOT [117] to use this method. For the other modules, the same method is applied.

With this process, we can reconstruct the position of muon hit in the each module. To verify this method and obtain the position resolution, we use plastic scintillator which is located at the center of top module. The dimension of the plastic scintillator is 85 cm x 20 cm. We can choose muon events passing the center position using coincidence with plastic scintillator. As one can see in Fig. 3.41, the reconstructed position is well matched with real position of plastic scintillator and the variation of x-axis is shown as 13 cm in the sigma value.
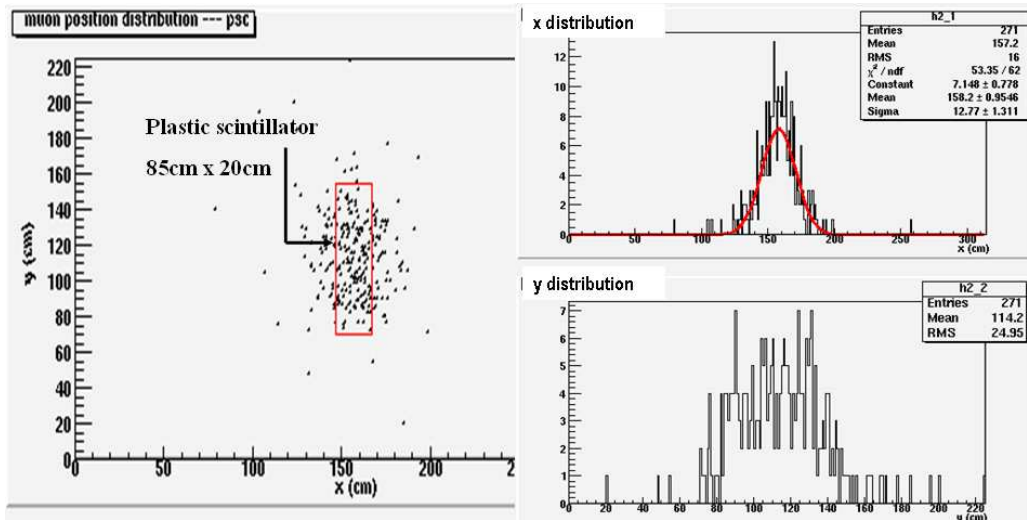
Figure 3.41: The reconstructed muon spectrum of coincident events with plastic scintillator. Projection to x-axis and y-axis are also displayed.
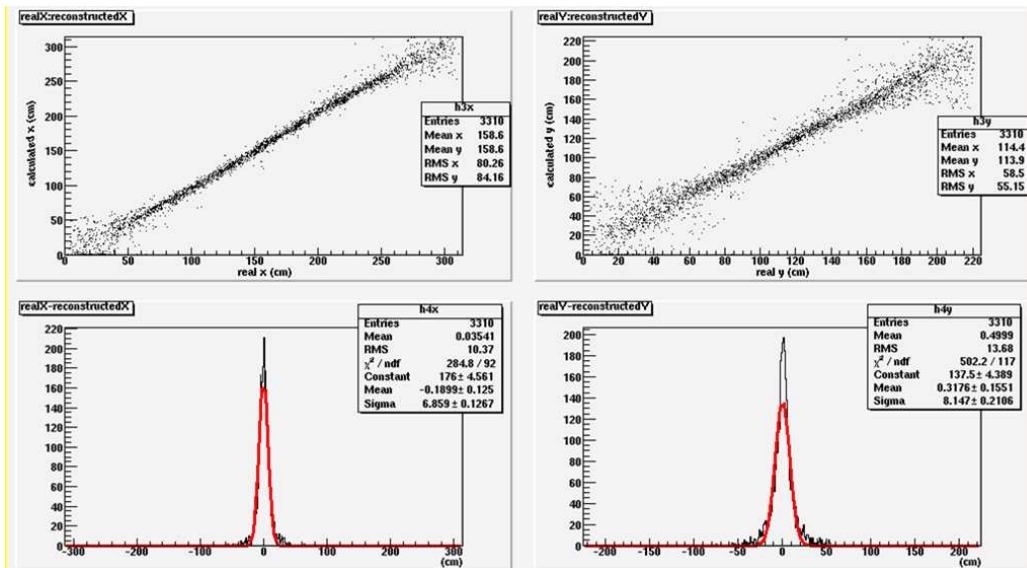
Figure 3.42: Upper plots show the two dimension spectrum of reconstructed muon hit position as a function of generated muon hit position in MC. Lower plots show the deviation between generated muon position and reconstructed muon position.

102

To understand the reconstruction of muon position better, we use GEANT4 [108] MC (monte carlo) simulation. Reconstructed muon hit position information as a function of generated muon hit position is shown in Fig 3.42. From this result, we can see about 7 cm position resolution in x-direction and 8 cm position resolution in y-direction. In the case of side detector, we have similar work to understand muon hit position. But, only 4 light read-out windows make poorer resolution. If we consider that the direction of muon is vertical, the side detector is not so critical to reconstruct muon tracks.

With reconstruction of muon hit position for muons passing through the detector, we reconstruct muon tracks. We obtain the information of muon hit position and angle of the muon track. We parameterize the muon track angle as θ for vertical direction (0-180 degree, upward is 0 degree) and ϕ for horizontal direction (0-360 degree). Using underground data we reconstructed muon positions and angles as one can see in Fig. 3.43. In Fig. 3.43 (a), the hit positions of muon background show more or less homogeneous distribution. But, the angle distributions from (b) show special structure. Since our laboratory is located in the underground of a mountain, the shape of mountain can affect muon flux. When we check the altitude record of mountain and position of our laboratory, the ϕ distribution is well matched with the mountain shape near of our laboratory.

3.6.4   Muon induced neutron

Because we installed the NMDs in the main shield, which are covered by MUD, we can analyze the muon-induced neutron signals by coincidence study between NMD and MUD. The time difference between two trigger time is calculated as follows:

$$\delta t = Min(Muon\ trigger\ time - Neutron\ trigger\ time).$$

We have 3 different SET of data as one can see in Table 3.11. The time difference from Set A was found under 10^{-6}s as one can see in Fig. 3.44 (a). The peak of coincident time shows about 100 ns offset, which is originated
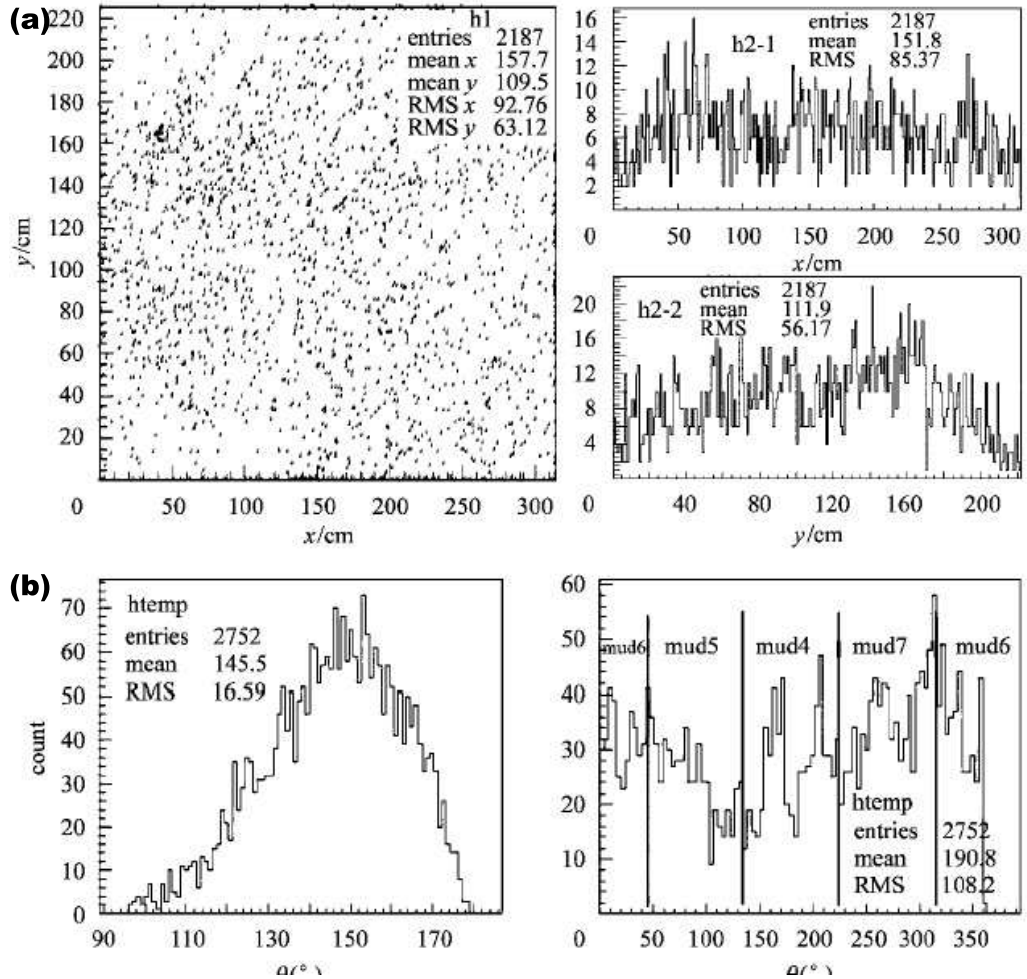
Figure 3.43: (a) Reconstructed muon hit position on the top detector, the left plot shows 2-dimensional distribution and the right shows the projected spectrum for x and y axis (b) Angle distribution of muon track are shown. Left and right plot shows θ and ϕ distribution respectively

from electronics. With rejection of the electronics offset, we have coincident timing spectrum (Fig. 3.44 (b), (c), and (d) for each data set). Fitting of the spectrum to the gaussian function shows that the resolution of δt is about 30 ns. We set 200 ns cut to select the coincident events.

Table 3.11: Data set for muon induced neutron study

Set-up	Data amounts	Muon Induced neutron
Set A	76.8 day·ℓ	2 events
Set B	203.0 day·ℓ	9 events
Set C	243.6 day·ℓ	11 events

As we described in Section 3.5.2, we can separate neutron signals from γs with PSD method.

The candidates of muon-induced neutron could be selected by the normalized PSD parameter and the coincidence of time. The PSD cut of -0.5 and the δt cut of 200 ns are applied for the energy range from 0.3 MeV to 2.5 MeV. We observed 2, 9, and 11 candidate events for Set A, B, and C respectively as shown in Fig. 3.45. In this study we find out the rate of muon induced neutron events is $(1.37 \pm 0.29) \times 10^{-2}$ counts/day/ℓ for the gamma equivalent energy from 0.3 MeV to 2.5 MeV.

The muon induced neutrons in CsI(Tℓ) crystals are more interesting issue. We are doing study of muon induced neutron in CsI(Tℓ) crystals with GEANT4 simulation. Using the muon induced neutron rate measured with neutron detector, we simulate muon induced neutron rate in CsI(Tℓ) crystal. The preliminary result is shown in Fig 3.46. This figure shows less than 0.003 CPD level of muon induced neutrons with 3 keV threshold which is negligible in our current background level.
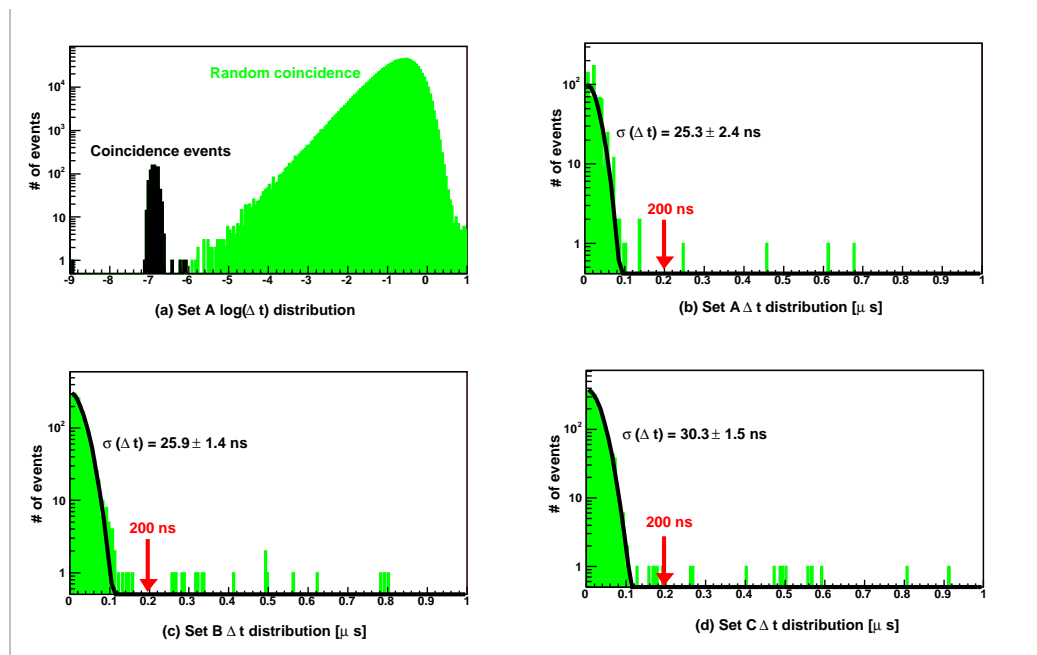
Figure 3.44: The time coincidence of signal between MUD and NMD. (a) shows the coincident time spectrum for Set A. (b) (c) (d) show the coincident time spectrum with rejection of offset for each data set.

(a) Set A PSD of coincidence events   (b) Set B PSD of coincidence events   (c) Set C PSD of coincidence events
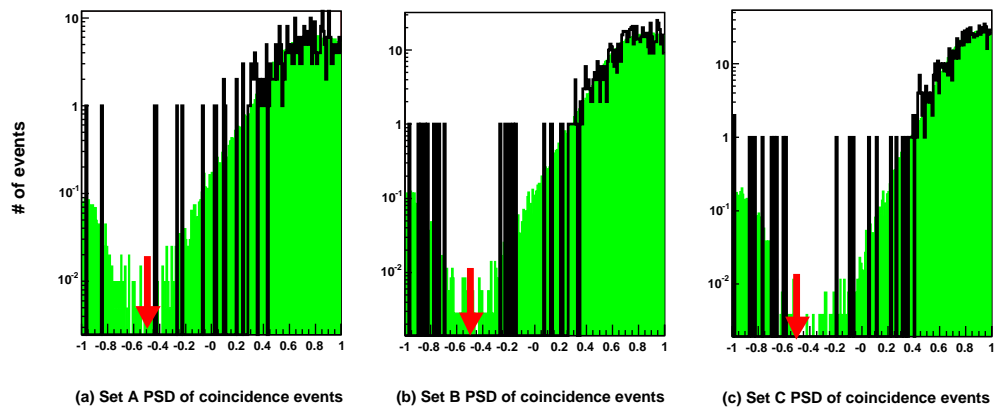
Figure 3.45: The normalized PSD distribution of coincident events for energy range from 300 keV to 2.5 MeV. In the neutron signal region, we found 2, 9, and 11 events for Set A, Set B, and Set C respectively. The distribution of PSD without coincident condition is shown with filled histogram. The scale was normalized with coincident events.
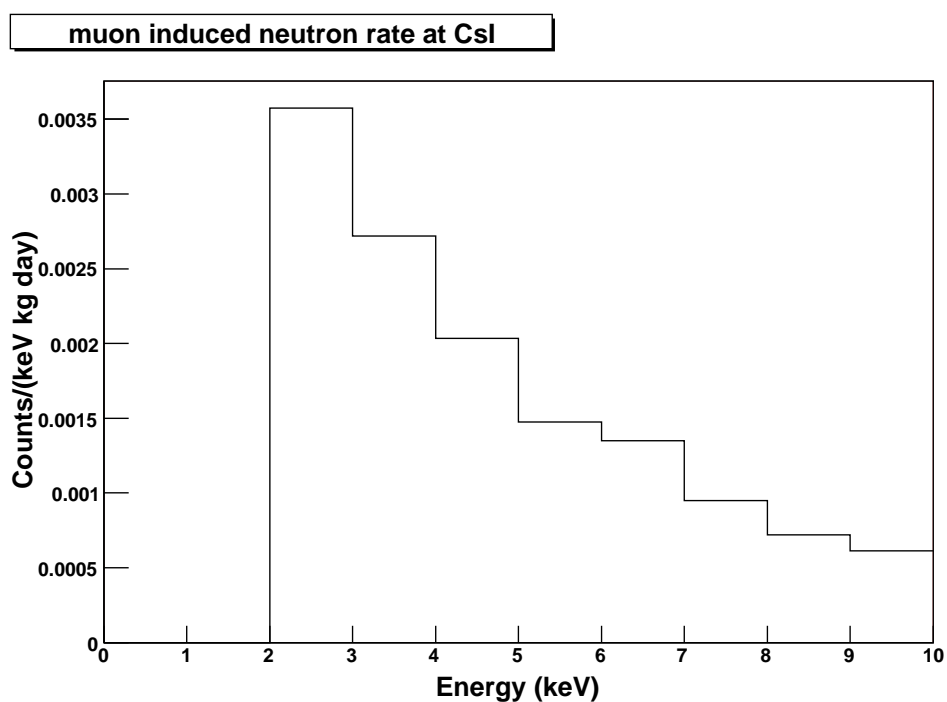
Figure 3.46:   Preliminary result of muon induced neutron rate in CsI(Tℓ) crystal with GEANT4 simulation is shown. The normalization of neutron rate is done using muon induced neutron measured with NMD and MUD coincidence.

3.7 Radon Monitoring

The air is a also important background source in the underground experiment. Typically, radon (^{222}Rn) and thoron (^{220}Rn), which are the decay products of ^{238}U and ^{232}Th, are major background components in the air. Because the thoron can decay to stable element of ^{208}Pb within a few tens of hours, the ^{222}Rn is much problematic as one can see in Table 3.9, 3.10. The ^{222}Rn generates a few MeV α and a few hundred keV γ. These γ rays are potentially significant background source in the case of low background experiments. Although we are flowing N$_2$ gas in the shielding to suppress the radon, we have been monitoring the radon contamination level of outside of shielding continuously.

3.7.1 Radon detector

Among the various well-known methods to measure the radon contamination in the air, we adopted the electrostatic method. Decay products of ^{222}Rn typically exist as positive ions (^{218}Po, ^{214}Pb, ^{214}Bi, and ^{214}Po) because of stripping effect [122]. We can detect α particles of subsequent decays of these ions by collecting them with applying electric fields. This method can be used for the continuous monitoring by the exchange of sample air and it is widely used to monitor the radon in the underground laboratories [123].

Fig. 3.47 shows the structure of the radon detector. We use 30 x 30 mm^2 Si photodiode by Sens Technology Inc. to measure α particles from subsequent decays. We apply negative high voltage (-500 V) to collect cascade ions and to operate photodiode (-70 V) with voltage divider. Fig. 3.48 shows the detector operation scheme. For the regular monitoring we make air flowing system with vacuum pump. We measure the radon amount every one hour automatically. Humidity, temperature, pressure, and high voltage are measured to check systematics.
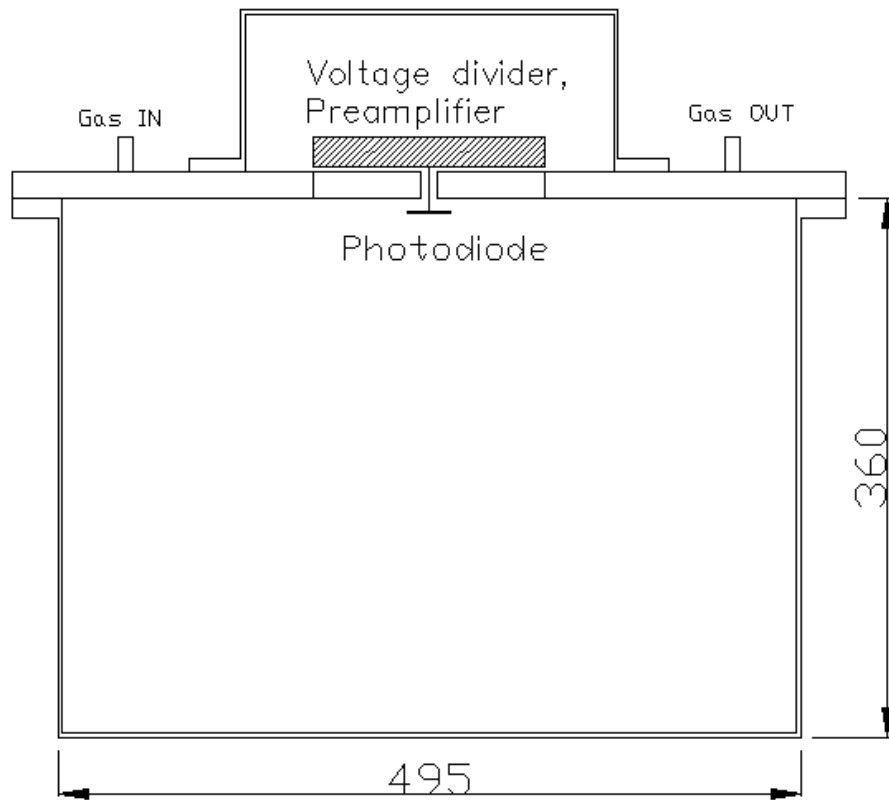
Figure 3.47: The schematic view of Radon detector which have 69.3 ℓ total volume.
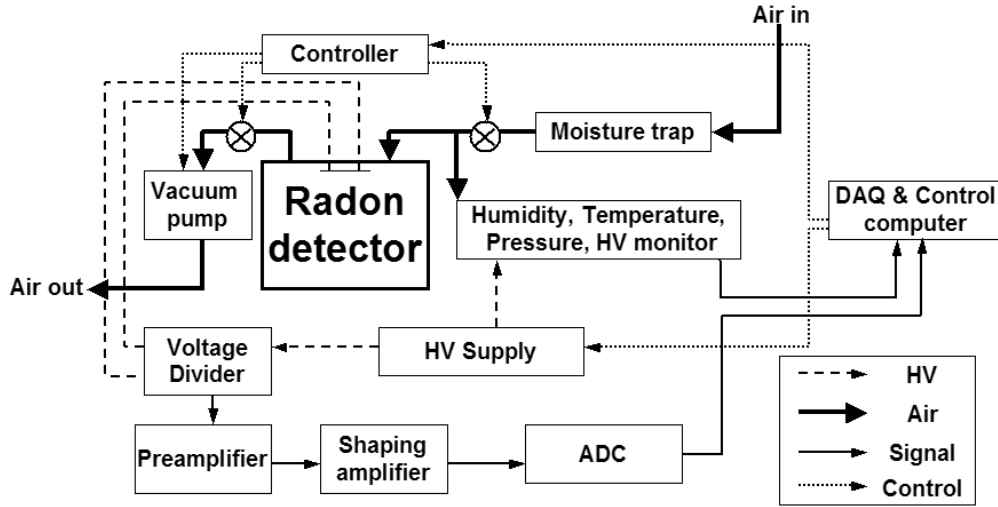
Figure 3.48: The scheme of operation of radon detector.

3.7.2   Calibration and measurement

We calibrate the radon detector with a standard radon source made at KRISS (Korea Research Institute of Standards and Science) by dissolving ^{226}Ra in 50 g of 5% HNO$_3$. The activity of this source is set to 130.3 ± 0.6 Bq correspondent as 50 pCi/ℓ in the 70 ℓ detector chamber. The schematic design of calibration is shown in Fig 3.49. At first we fill the chamber with radon-free air. Then we extract all the dissolved radon gas from the standard radon source to measure the rate of ^{214}Po decay events, which make 7.69 MeV α, with our radon detector. With about 1 Hz rate using the standard radon source, we obtain the calibration factor as 1.9 pCi/ℓ/Hz.

We installed the radon detector in the hall of detector room and continuously measure the radon contamination in the air of the detector room from October 17th 2004. Fig 3.50 shows the measured radon concentration in the air of the detector room from June 2005 for a period of 70 days. The average value of the radon in the air of Y2L in this period is 1.409 ± 0.001 pCi/ℓ. Our result of radon concentration in the tunnel air is slightly lower than those of other underground laboratories [124].
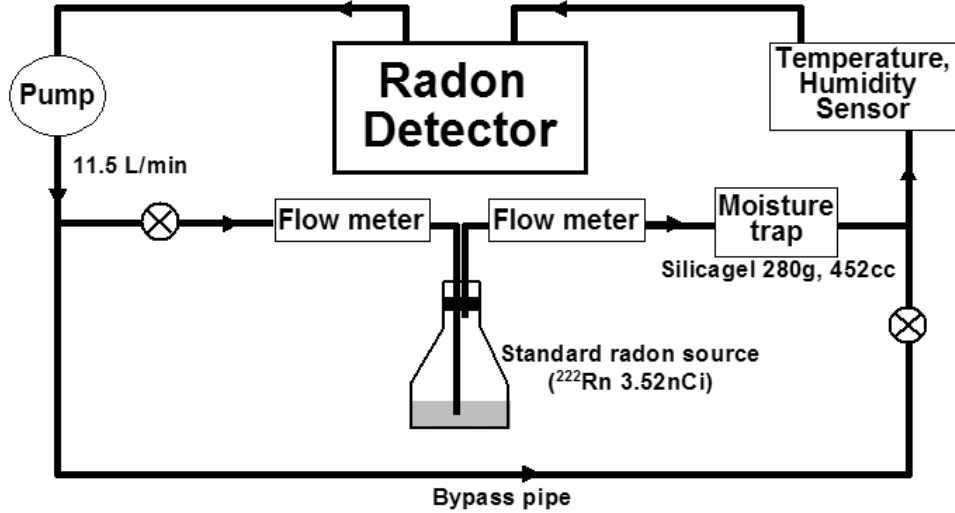
Figure 3.49:   Calibration setup of radon detector

3.8   Slow Monitoring

We need to monitor and understand the environment parameters like temperature and humidity of detectors and electronics as well as the high voltage (HV) of PMTs for reducing systematics. Because those information are very slowly changed, we make slow monitoring hardware and GUI (graphic user interface) software. This program can measure temperature and humidity of innermost side of main shield, detector room, outside, and electronics room and HV of PMTs.

For the measurements of temperature and humidity, we use home-made ADC box as shown in Fig. 3.51. The ADC box can convert DC voltage signal from temperature and humidity sensors to ADC values. We use bar-type thermal couples and home-made register-voltage converting boards for temperature measurements and capacity type humidity sensors for humidity measurements. The ADC values are read out for every 3 sec by a Linux-Operating PC through the USB interface.

We use CAEN 1527 (see Fig. 3.52) HV supply which is connected by the
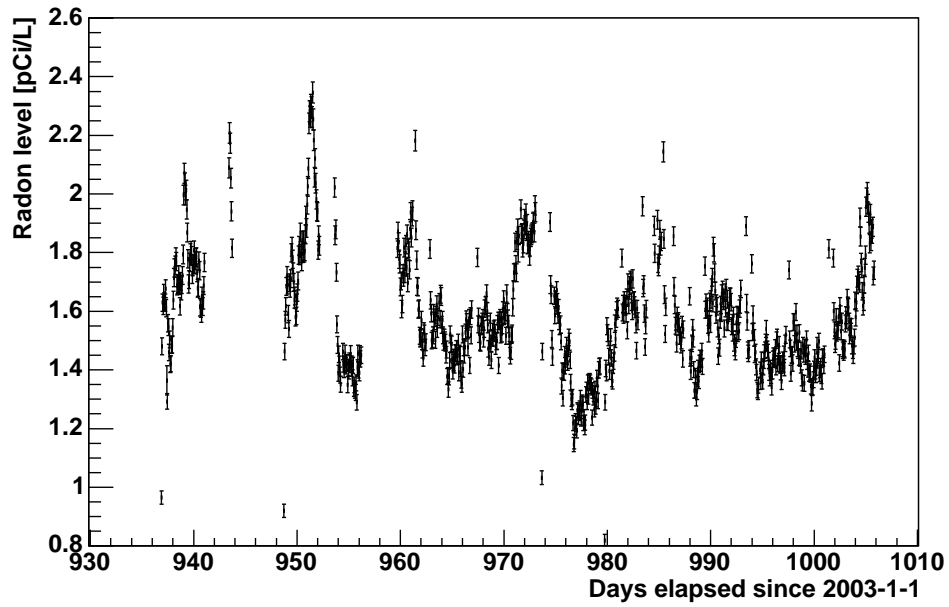
Figure 3.50: Radon concentration measured in the detector hall of Y2L from June 2005 to October 2005 with radon detector. The average value shows 1.409 ± 0.001 pCi/ℓ.

Figure 3.51: The ADC box for monitoring of temperatures and humidities.

Figure 3.52: The CAEN 1527 HV supply.

10 base T lan port. With TCP-IP programming we can monitor voltages, currents, and status of modules for every 3 sec.

Because we controlled the temperature and humidity in the detector room with air-control system, variation of temperature and humidity in the detector room are within 1 °C and 10 % respectively. Fig 3.53 shows temperature variation in each position from April 2004 to October 2005. Data taking for WIMP search was started in July 2004. In the case of electronics hut, we controlled the temperature with normal air-controller. Temperature variation of electronics hut is about 2 °C. Fig 3.54 shows humidity variation as a function of time. Relative humidity of main shield is controlled as about 0 % because we flow N_2 gas continuously. The fluctuation of humidity in this position is originated from opening the main shield. Relative humidity of detector room is controlled as about 55 % with 5 % deviation and electronics hut is about 30 %.

Fig 3.55 shows the value of HV applied to PMTs attached to CsI(Tℓ) crystals as a function of time. The voltage and current is seems to be very stable.
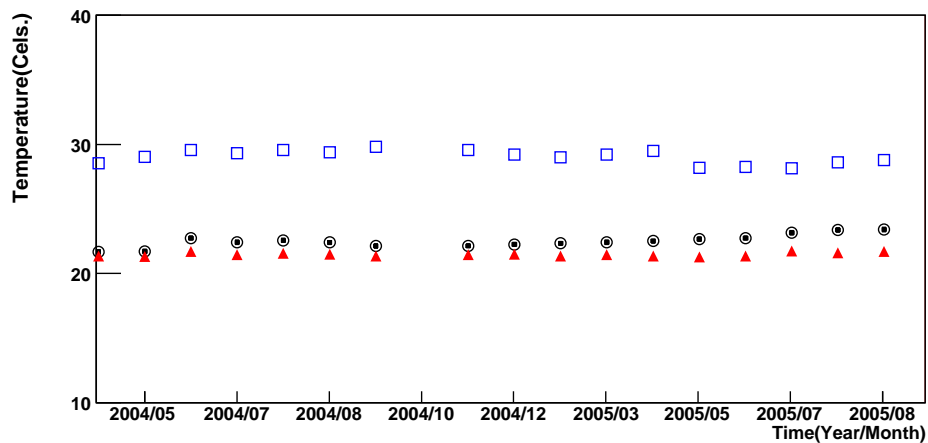
Figure 3.53: Continuous monitored temperature spectra from April 2004 to October 2005 for innermost side of main shield (open circles), the detector room (filled triangles), and the electronics hut (open squares).
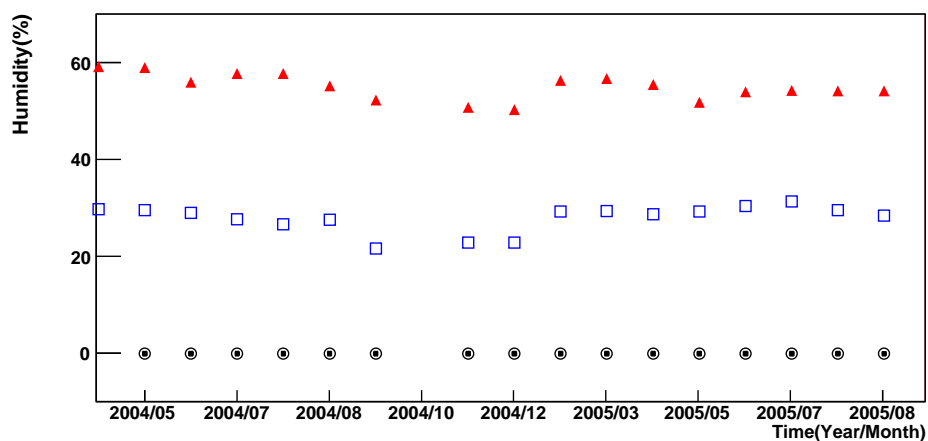
Figure 3.54: Continuous monitored humidity spectra from April 2004 to October 2005 for innermost side of main shield (open circles), the detector room (filled triangles), and the electronics hut (open squares).

115
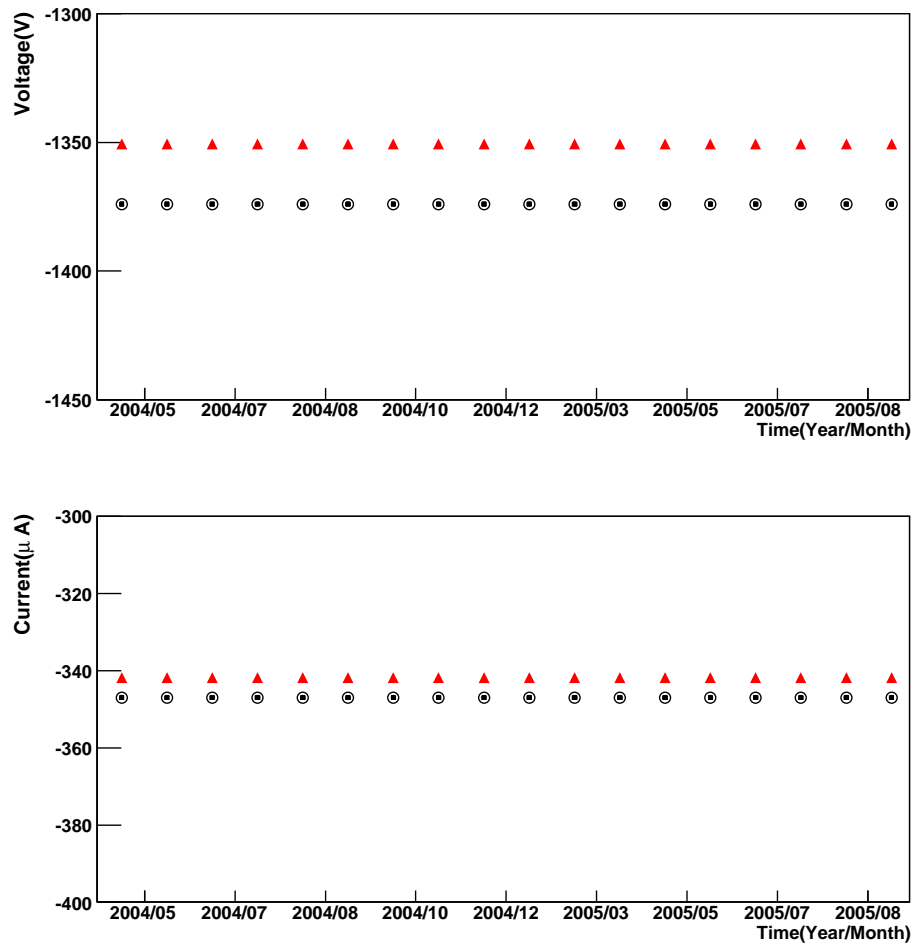
Figure 3.55:   Continuous monitored high voltage of PMTs attached to CsI(Tℓ) crystal for voltage (upside) and current (downside) from April 2004 to October 2005. Open circles show PMT1 and filled triangles show PMT2.

116
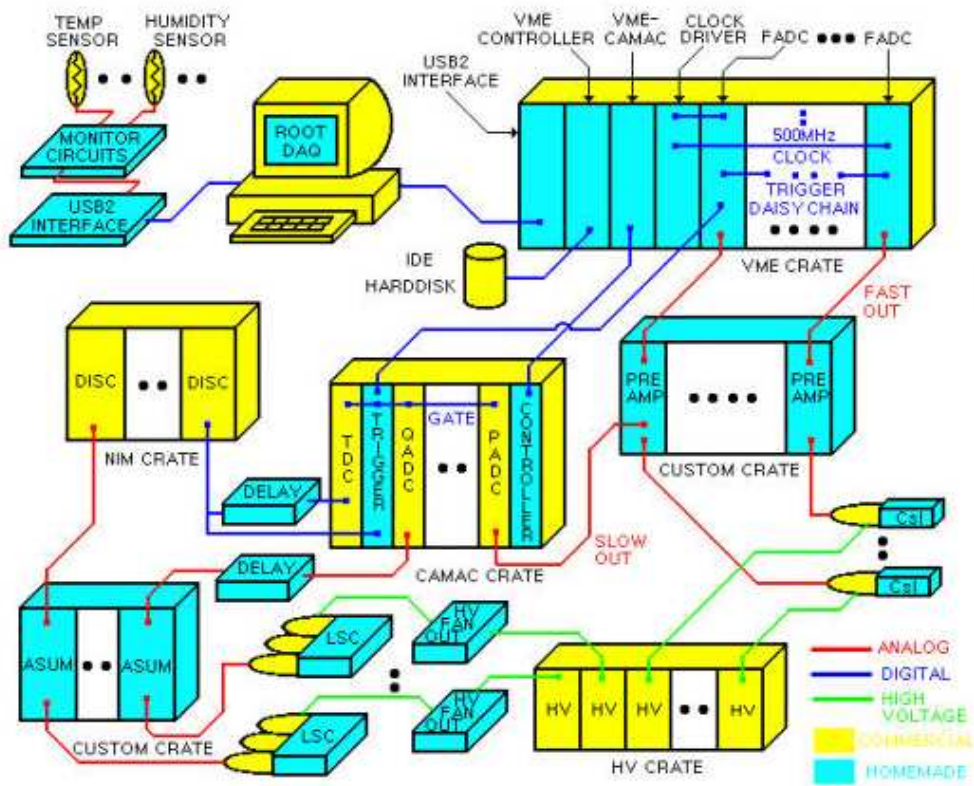
Figure 3.56: The scheme of KIMS electronics & DAQ

3.9 Electronics and DAQ

3.9.1 KIMS electronics

The KIMS electronics are composed of preamplifiers, 500 MHz waveform digitizers, and circuits for environmental monitoring as one can see in Fig. 3.56.

Signals from the PMTs attached to CsI(Tℓ) crystals and NMD are amplified to the proper amplitude by preamplifiers. The amplified signals are digitized with 500 M samplings/second flash ADC (FADC) modules. In the FADC, we make trigger logic on a FPGA. The information of real time trigger process goes to the master trigger unit, which give a final decision

to store the data into buffer memory. The stored data is read out by PC through USB2 interfacing VME-controller. The main chain of data readout for CsI(Tℓ) crystals are separated with neutron and muon detector chain using different VME crate and different PC. The additional circuits for environment monitoring such as temperature, humidity, high voltage and radon monitoring are also placed in the separated system. The signals from environment monitoring are digitized by the relatively slow ADCs. The data are stored by PC through USB2 interface.

3.9.2   Preamplifier

The KIMS preamplifier designed to amplify the single photoelectron (SPE) signals of a PMT without any loss of pulse information. The bandwidth of PMT signal is about 100 MHz which requires more than 200 MHz sampling rate. We use 200 MHz bandwidth OP-Amp to amplify the signal. The KIMS preamplifier has two functions, one is just amplification of the signal without any loss of signal pulse shape called as voltage sensitive amplifier, the other is converting of total charge to voltage signal called as charge sensitive amplifier. Fig. 3.57 shows the feature of the KIMS preamplifier.

The voltage signal from the PMT is amplified by $\times 10$ and $\times 100$ amplification factor. Two different dynamic range can help us to measure wide energy range. Especially in CsI(Tℓ) crystal, $\times 100$ signal is used to analyze WIMP signal and $\times 10$ signal is used to understand internal background of crystal. One additional output whose amplitude is proportional to the input pulse area is for the input of a peak sensing ADC for old setup. Now it is not used anymore.

3.9.3   500 MHz waveform digitizer

In order to measure the precise pulse shape we made 500 MHz waveform digitizers with 150 MHz analog bandwidth. To measure the clear waveform, 500 MHz flash ADC, TDA8718 from Phillips semiconductor, is selected. This
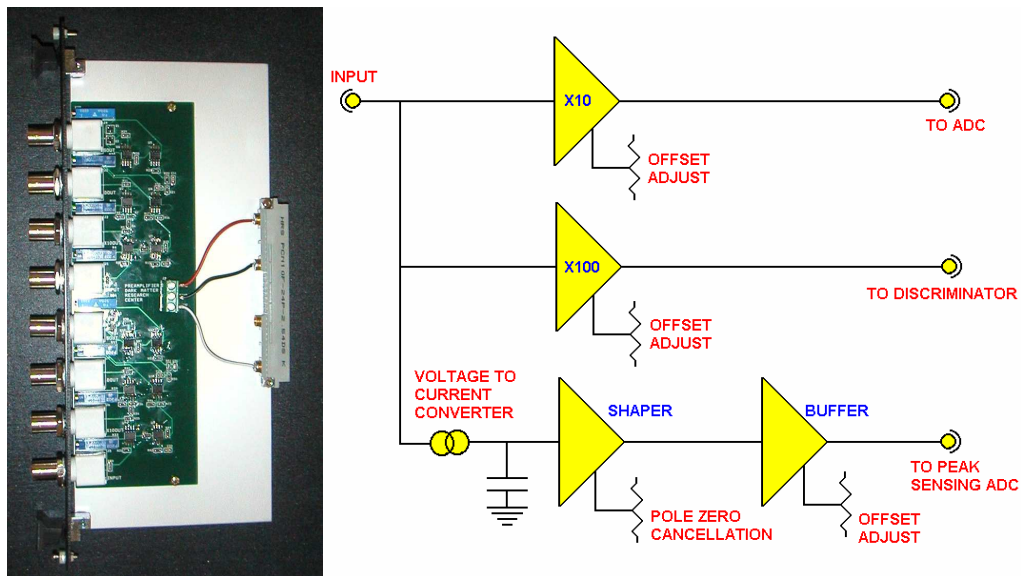
Figure 3.57: The picture of KIMS preamplifier (left) and block diagram (right)

ADC has 8 bit resolution with input dynamic range of 1.3 V. The 500 MHz digitizer module is composed of ADC, clock circuits, buffer memories, and programmable logics. Fig 3.58 shows the picture of FADC.

The 500 MHz clock signal is supplied by an external clock generator which is also home made VME module. The clock generator is made of a voltage controlled oscillator (VCO) having oscillation frequency of 1 GHz. Because VCO output has small amplitude and poor shape, it is shaped by MC100EL32 which divides the VCO's clock frequency by factor two. The input clock to the digitizer board is used for the sampling clock of ADC chip and another clock divider to control circuits. The clock fanout and dividing are realized by MC100LVEL14 and MC100EL32, respectively. The divided clock whose frequency is 250 MHz, is fanned out by MC100LVE111 clock driver for the control logics and data multiplexers.

The input signal of digitizer comes from the output signal of preamplifier. The dynamic range of ADC is 1.3 V. Because 500 MHz output data is too high to be handled by the following circuits, we make slow down output
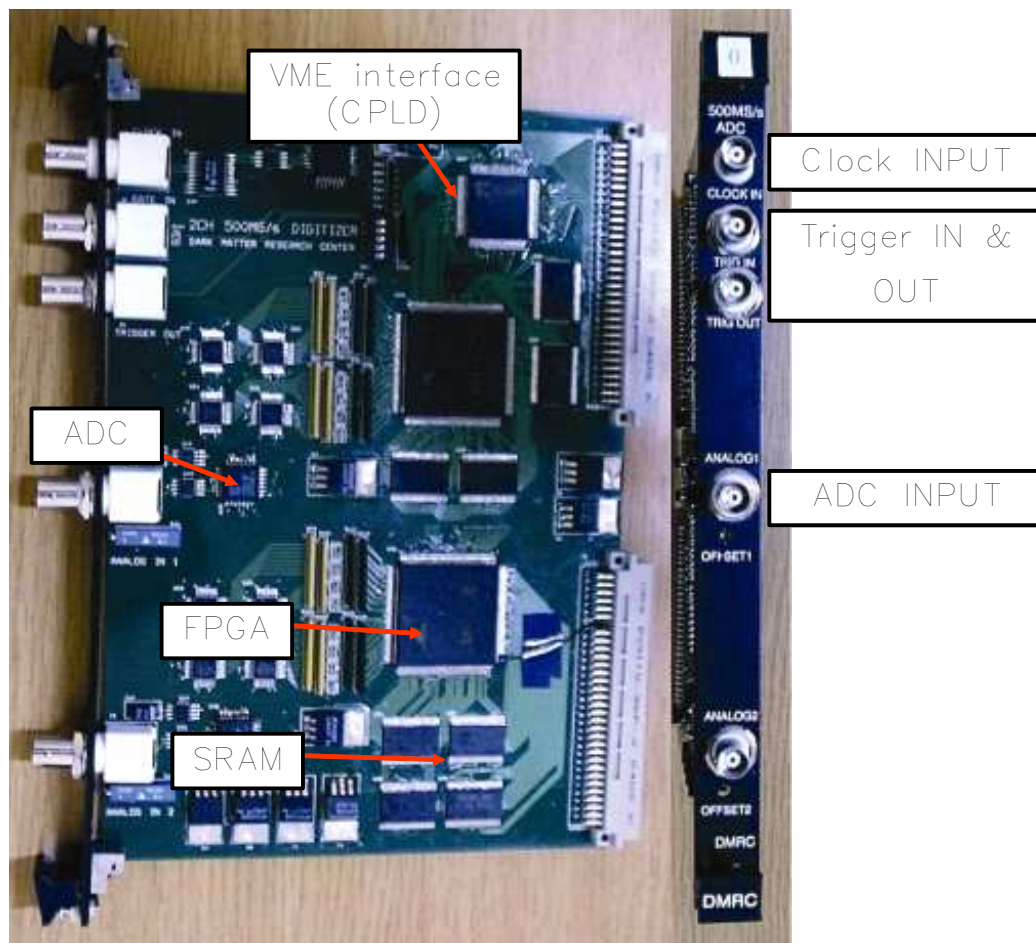
Figure 3.58: 500 MHz digitizer.
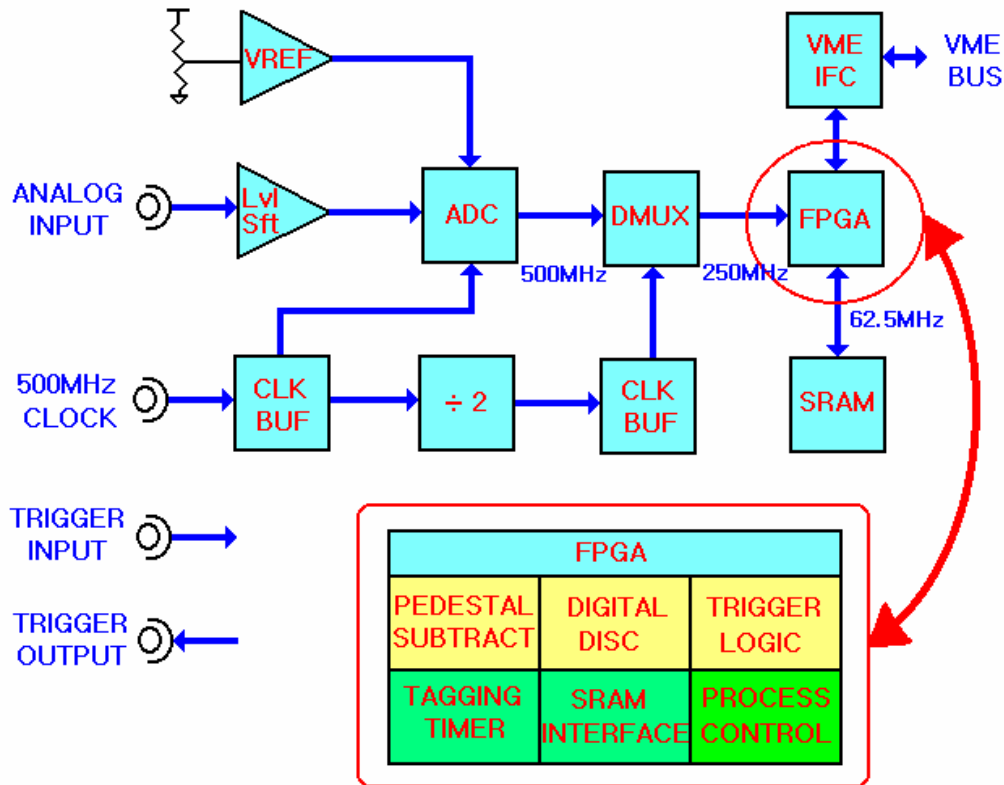
Figure 3.59: The block diagram of KIMS waveform digitizer.

rate to 250 MHz by multiplexing. 250 MHz rate data can be acceptable
by VirtexE FPGA (Field Programmable Gate Array) and all the following
processors. Although VirtexE FPGA can accept 250 MHz data input, it is
still impossible to perform the whole processes with 250 MHz. The data is
further multiplexed by four channels to 62.5 MHz. The triggered ADC data
are written to the external SRAMs at the rate of 62.5 MHz. There are 4 Mbit
of SRAM on the digitizer board, which can store ADC data of 1 ms. The
block diagram of whole process for data recording is shown in Fig. 3.59.

The trigger logic was written in the FPGA. In the FPGA logic, we also
measured the pedestal level with random trigger. The discriminator circuit
to generate logic signal is placed in the digitizer board. In addition, there is
a logic to select SPE, which has 10 ns width over the discriminator thresh-
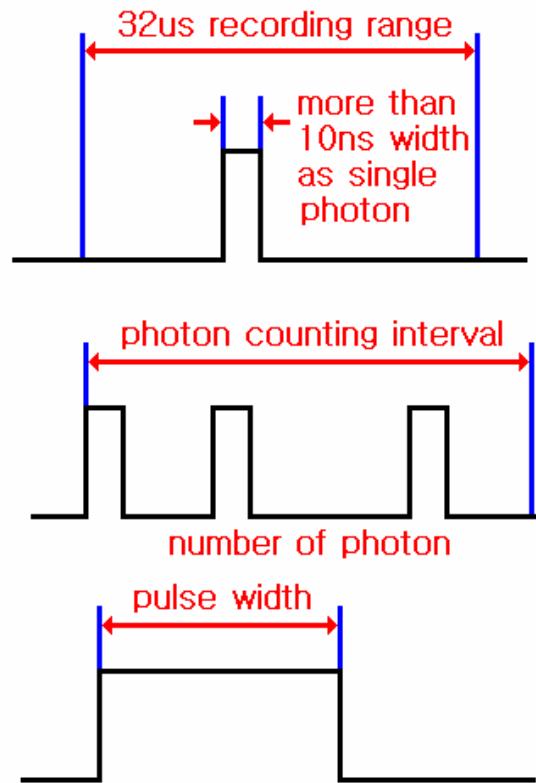
Figure 3.60: Trigger logic in the FADC chip

old.The number of SPEs in the photon counting interval can generate trigger signal. For high energy events where many single photon signals are merged into a big pulse condition on the pulse width is required. All parameters , number of SPEs, photon counting interval, discrimination threshold, and pulse width for high energy trigger, can be set by software. The trigger logic of 500 MHz digitizer is shown in Fig. 3.60.

The daisy chain of trigger signals is composed in the FADC board. The real trigger of board is generated by the signal from the trigger input. The trigger signal generated in the FADC board goes from trigger output to trigger input of neighbor. This daisy chain gives an easy way to take external trigger.

The waveform of triggered signal is stored in the SRAM buffer. As one

can see in Table 3.12, total buffer size of data storage is 1 Mbyte. We divide this one as two structure of up and down buffer. In the CsI(Tℓ) crystal detector, 16 events can be stored in each buffer. If 16 events were filled for one buffer, we transfer data to PC with VME interface during the other buffer store the triggered signals simultaneously. In principle, we reject DAQ dead time for data transfer if we can transfer all data of one buffer before the other buffer is filled.

VME interface is used for the readout and the control of the digitizers. The VME address and data translator is written at the Xilinx XC95144L CPLD (Complex Programmable Logic Device). The working VME mode is A24/D16, which has memory space of 16 Mbyte. Among 24 address bits, the most significant four bits are used to identify module number, and remaining bits are used for assigned functions. Table 3.12 shows brief summary of the VME memory map for the digitizer board.

Table 3.12: VME memory map of 500 MHz digitizer

ADDRESS	Contents	Size	Mode
0x300000 - 0x3FFFFF	CPLD Registers	1 MB	Read/Write
0x200000 - 0x2FFFFF	Control & Status Registers	1 MB	Read/Write
0x100000 - 0x1FFFFF	Tagging Time & Trigger Pattern	1 MB	Read
0x000000 - 0x0FFFFF	ADC data	1 MB	Read

The performance of 500 MHz digitizer is shown in Fig 3.61. This figure shows the pulse shape of low energy γ sample event in the CsI(Tℓ) crystal. In Fig 3.61 (b), we can see that SPEs are well reconstructed with digitizer.
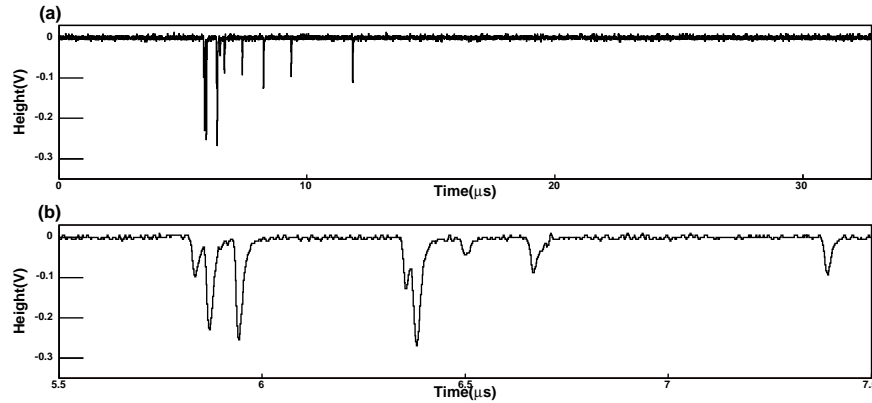
Figure 3.61: (a) shows typical low energy γ signal from CsI(Tℓ) crystal with 500 MHz home-made digitizer. Zoomed pulse shape of this events from 5.5 μs to 7.5 μs is shown at (b).

3.9.4 USB2-VME controller

The minimum band width for data transfer from 500 MHz digitizer can be easily estimated by the following equation:

$$BAND\ WIDTH = 8bit \times DATA\ POINT \times DAQ\ RATES \times Channel.$$

In CsI(Tℓ) crystal detectors, the recording window and DAQ rate are 32 μs which have 0x4000 (=16384) data point and less than 0.5 Hz respectively. With considering of two channels for each crystal, the minimum band width for one crystal is 0.02 MB/s. Because we will have 25 crystals in late, the requested band width is more than 1 MB/s. Two times larger rate is expected from the consideration of coincident events for each crystal and fluctuation of trigger rate.

We developed USB2-VME interface board to take data from CsI(Tℓ) crystal detectors. In principle, the maximum rate of USB2 interface is 40 MB/s. Usual USB2 devices such as USB2 hard disk driver and memory stick have 15 MB/s which is acceptable for our purpose. Fig 3.62 shows the picture of USB2 VME controller. Data occupied in the buffer of digitizer are transferred to the PC through USB2 VME controller. USB link convert the data
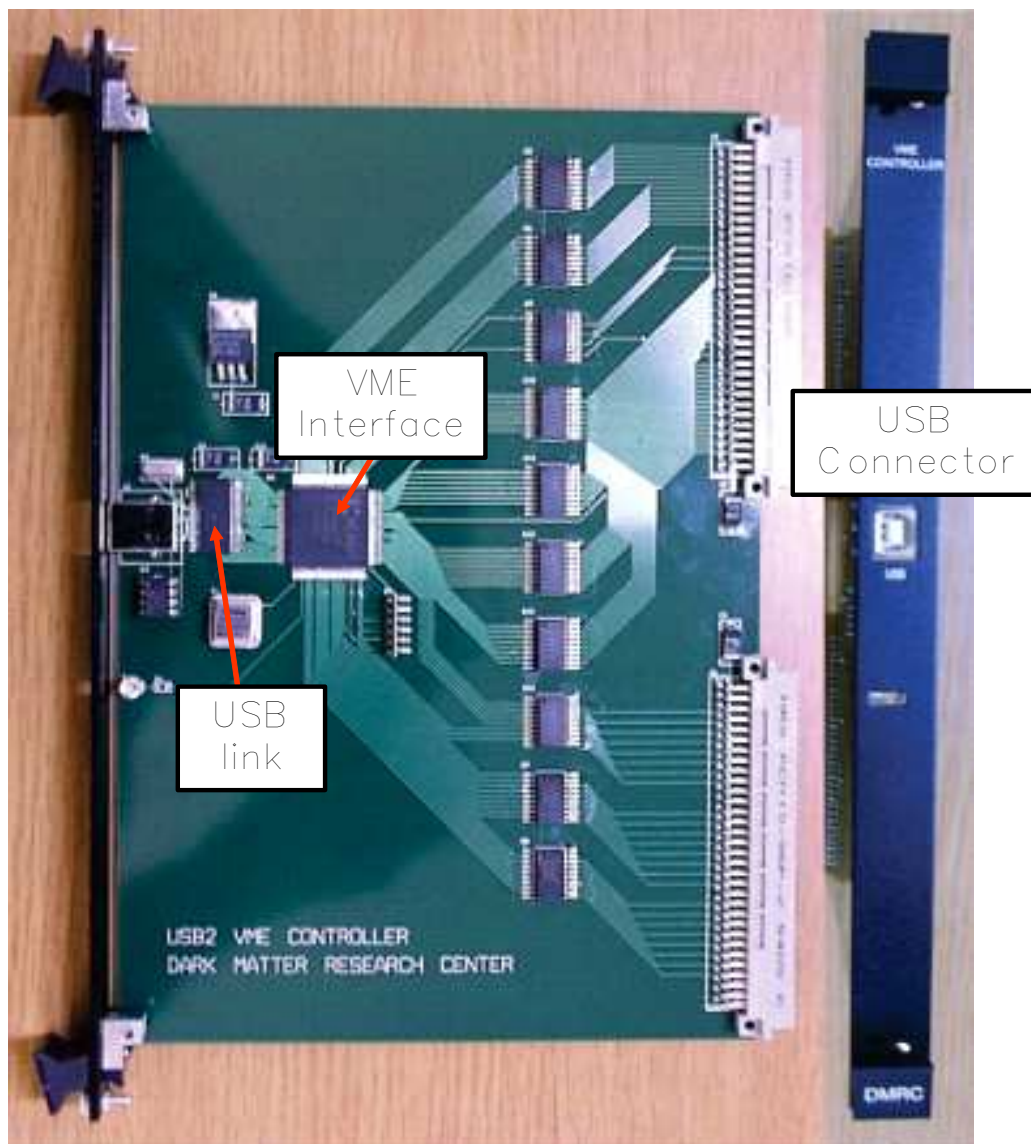
Figure 3.62: USB2-VME controller

of buffer of digitizer as USB character to transfer. USB connector in front of board is connected to the PC.

Table 3.13: Data transfer rata in KIMS USB2-VME controller

MODE	Rate	Mode	Rate
D32 write	15.4kB/s	D16 write	7.75kB/s
D32 read	4.88kB/s	D16 read	2.44kB/s
D32 blockread	**15.4MB/s**	D16 blockread	11.8MB/s

We tested the transferring rate of USB2 VME controller in the linux with linux kernel code. Although the rate of command signal (read and write) is too slow, the rate of data transfer (blockread) is fast enough to our purpose. When we check speed of real DAQ from the digitizer to the computer, about 4 MB/s is achieved. Linux driver and GUI DAQ program for control the digitizer and USB2 VME controller is developed with ROOT [117] package.

3.9.5 DAQ for CsI(Tℓ) crystals

We make DAQ system for CsI(Tℓ) crystal using home-made electronics as shown in Fig. 3.63. We use two 3-inch PMT to take photons from each CsI(Tℓ) crystal. The photoelectrons from PMTs are amplified with home-made preamplifiers with 100 times amplification factor. With 500 MHz home-made FADC modules, we record the signal to 32 μs window. Because our FADC modules have a FPGA logic to form the trigger signal, we make event trigger with FADC itself. We require trigger condition for CsI(Tℓ) crystal having more than two photoelectrons in each PMT within two μs. An additional trigger is generated if the width of the pulse is longer than 200 ns for high energy events where many single photon signals are merged into a big pulse. The trigger position of events is located at 6.8 μs in the total 32 μs window. Region up to 4 μs is used to calculate the pedestal level. An example of trigger for low energy gamma is shown in Fig. 3.64. After the event
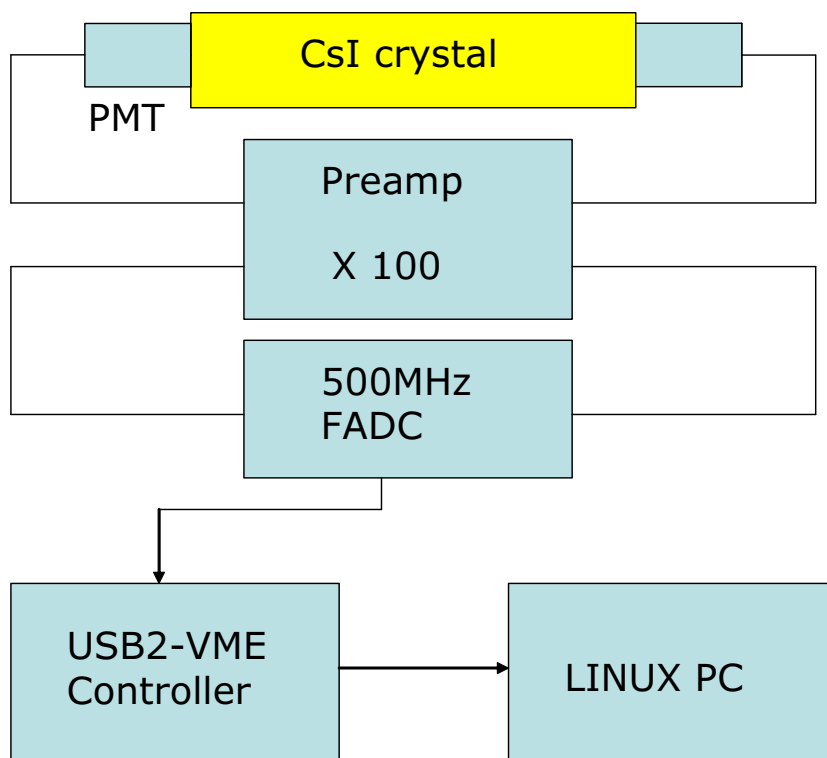
Figure 3.63: Scheme of DAQ for CsI(Tℓ) crystal

(a)

(b)
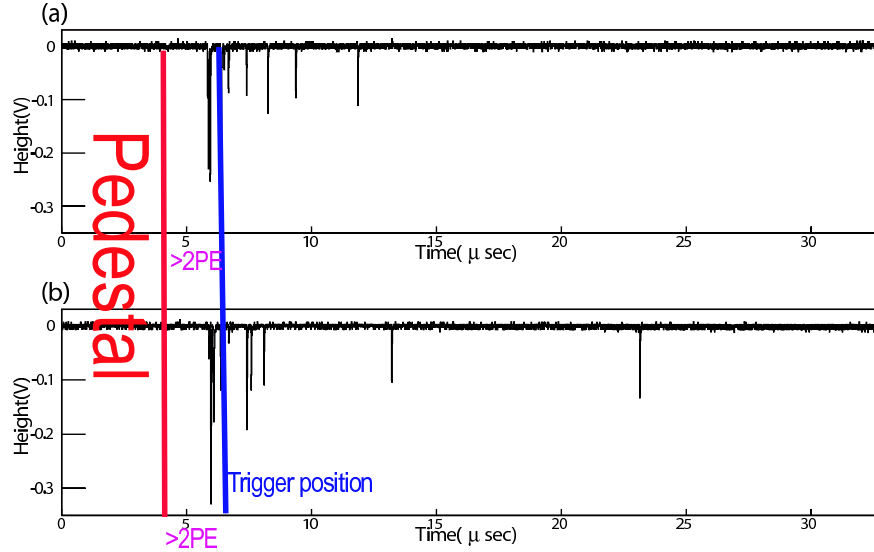
Figure 3.64: An example of events trigger in the CsI(Tℓ) crystal

trigger, we give 8 msec dead time to reject the tail events from pre-triggered events. Because typical DAQ rate of CsI(Tℓ) crystal is about 0.6 Hz, total dead time is only about 0.5 %. The triggered events are transferred to the LINUX PC system with home-made USB2 VME controller. Typical low energy signal is shown in Fig. 3.61. We can well reconstruct the SPE signal from the CsI(Tℓ) crystal with our DAQ system.

3.9.6 Trigger Efficiency

We calculate the trigger efficiency with GEANT4 simulation (see Appendix B). Because we account all of detector response in the simulation, we can accurately estimate the trigger efficiency with simulation.

To estimate the trigger efficiency of electron recoil, we generate γ-rays having 1-17 keV energy. We compare all generated events with events passing the trigger condition. The results of the MC simulation are shown in Fig. 3.65. In 2-3 keV energy bin, the trigger efficiency is 97 %. With our
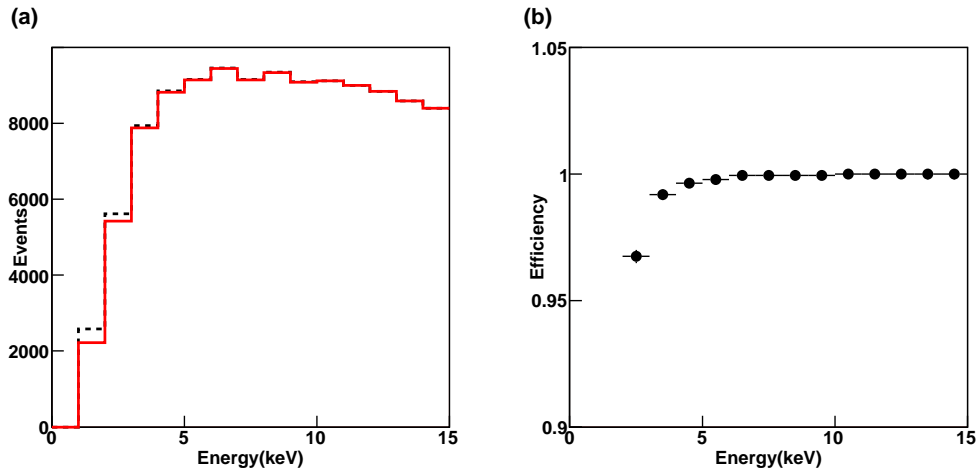
Figure 3.65: (a) Energy spectrum of γ events generated with Geant4 MC simulation are shown. Solid line shows all events and dashed line shows events passing trigger condition. (b) Trigger efficiency of electron recoil is shown.
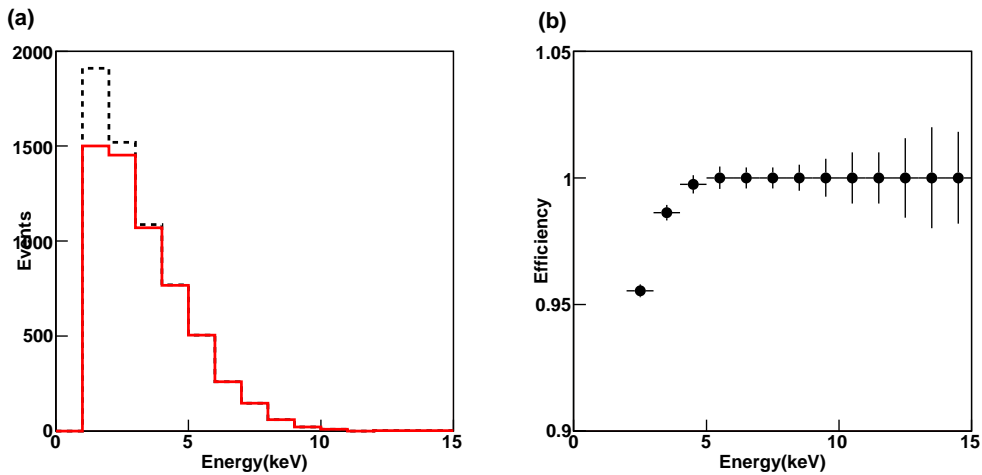
Figure 3.66: (a) Energy spectrum of WIMP (mass 100 GeV) events generated with Geant4 MC simulation are shown. Solid line shows all events and dashed line shows events passing trigger condition. (b) Trigger efficiency of nuclear recoil is shown.
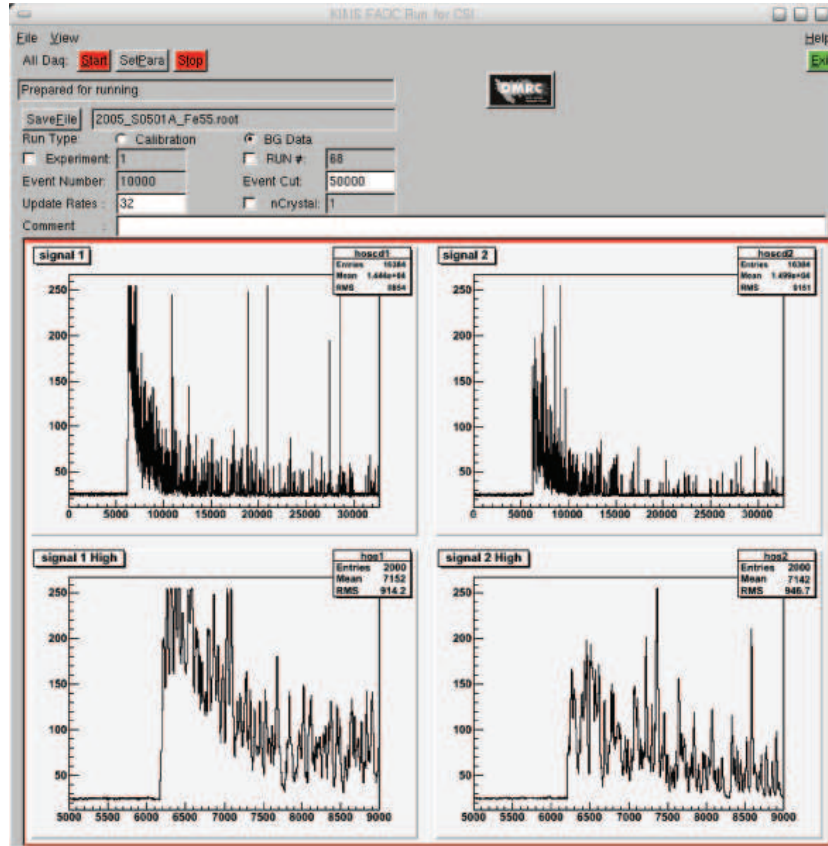
Figure 3.67: GUI Daq program for CsI(Tℓ) crystal detectors.

threshold (3 keV), we have more than 99 % trigger efficiency.

In the case of nuclear recoil, we generate 100 GeV WIMPs. The same procedures of gammas were performed to estimate the trigger efficiency. Fig. 3.66 shows the trigger efficiency of the nuclear recoil which is more than 99 % with energy threshold 3 keV.

We made GUI (Graphic User Interface) DAQ program using ROOT package as shown in Fig. 3.67. This program can set FPGA logic of FADC, trigger condition and hardware dead time, as well as recording parameters, file structure, file name, file size, and run number. Simultaneously we monitored DAQ status from the pulse shapes of events and accumulated energy spectrum for each crystal.

Chapter 4

Data & Analysis

4.1 Reconstruction of Events

The KIMS DAQ system records the pulse shape of 32 μs from the PMT at a rate of 500 MHz (16384 data points for each PMT). Because the pulse widths of SPEs passing the fast preamplifiers are about 40 ns, SPEs are well reconstructed in our DAQ (see Fig. 4.1).

Because the information for the scintillation light from the detector is included only in the SPE signal, we need to identify SPE to reduce the effect coming from the noise and to improve the energy resolution. A clustering algorithm is developed to identify SPEs. The main source of noise in KIMS DAQ is the baseline noise from a captured electromagnetic noise in the 20 m long cables and electronics circuit. The electromagnetic shielding and control of the temperature for cable and electronics make it very low and stabilized pedestal level. In Fig. 4.1 (a), time window before 4 μs shows the typical pedestal level of the FADC.

The other noise component is PMT dark current which is not separable from SPEs. Typical dark current rate measured with counter passing the discriminator is 1000 Hz $\sim$ 2000 Hz depending on the PMT. Contribution of
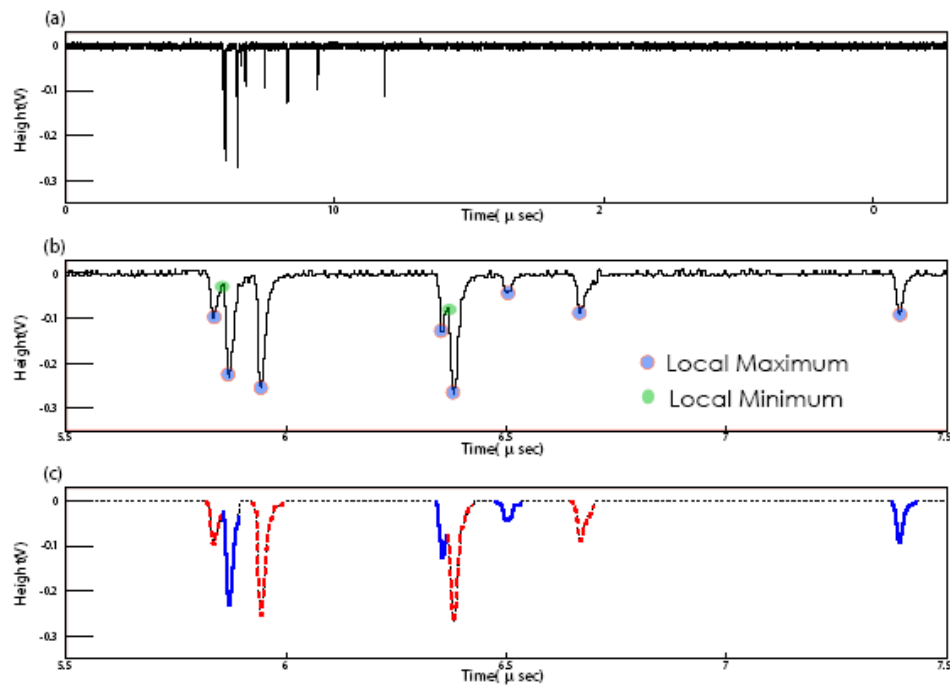
Figure 4.1: (a) shows typical low energy γ signal from CsI(Tℓ) crystal for one PMT obtained by Compton events from ^{137}Cs source. Zoomed pulse shape of this event from 5.5 μs to 7.5 μs is shown at (b) with identified local maximum point and local minimum points. The same pulse spectrum with clustering is shown in (c).

dark current in the 32 μs window is expected to be 0.03 to 0.06 SPE.

We developed the clustering algorithm to extract SPEs above pedestal. From the consecutive FADC bins above the pedestal, we find local maximum point to form isolated cluster. The separation of neighboring cluster in the case that two local maximum is found in a cluster is done by finding local minimum points between two SPEs as one can see in Fig. 4.1 (b).

For each isolated cluster, we calculate charge, height, and width. With low enough threshold, we obtain the height and width distribution of SPEs in low energy events as one can see in Fig. 4.2. To avoid the inclusion of pedestal fluctuation, we make SPE threshold for the height and the width at the valley as one can see in Fig. 4.2.

4.2 Calibration and Data

4.2.1 Energy Calibration

The energy deposition is evaluated from the sum of charges of all SPEs within the 32 μs window. Low energy calibration is done using a 59.5 keV γ peak from a ^{241}Am source.

We have performed measurements of γ-rays with various radioactive sources in the underground laboratory. The energy spectrum of 59.5 keV γ from the ^{241}Am sources is given in Fig. 4.3. In an attempt to understand the shape of the spectrum, a fit was done using gaussian function with 1-dimensional polynomial background function. In Fig. 4.3 the fit result (solid line) is overlaid. The energy resolution of S0406 crystal at 59.5 keV is about 7.3 %.

Numerous calibration sources such as ^{241}Am, ^{137}Cs, ^{54}Mn, ^{60}Co, and ^{208}Tl are used to understand the response of CsI(Tℓ) crystal detector. Fig. 4.4 shows the energy resolution curve of S0406 crystal. Energy dependence of
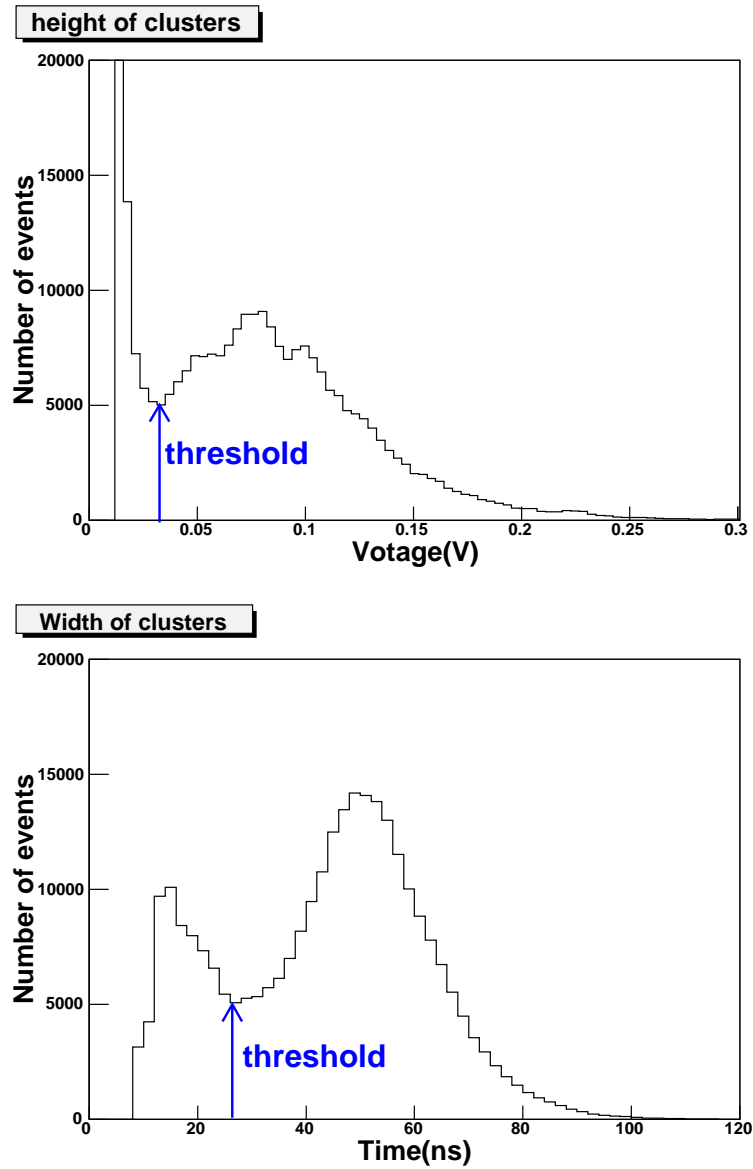
Figure 4.2: Single cluster height and width distribution obatined from 5.9 keV γs with a ^{55}Fe source. We identify the SPE threshold of the pulse height and width in the figure.
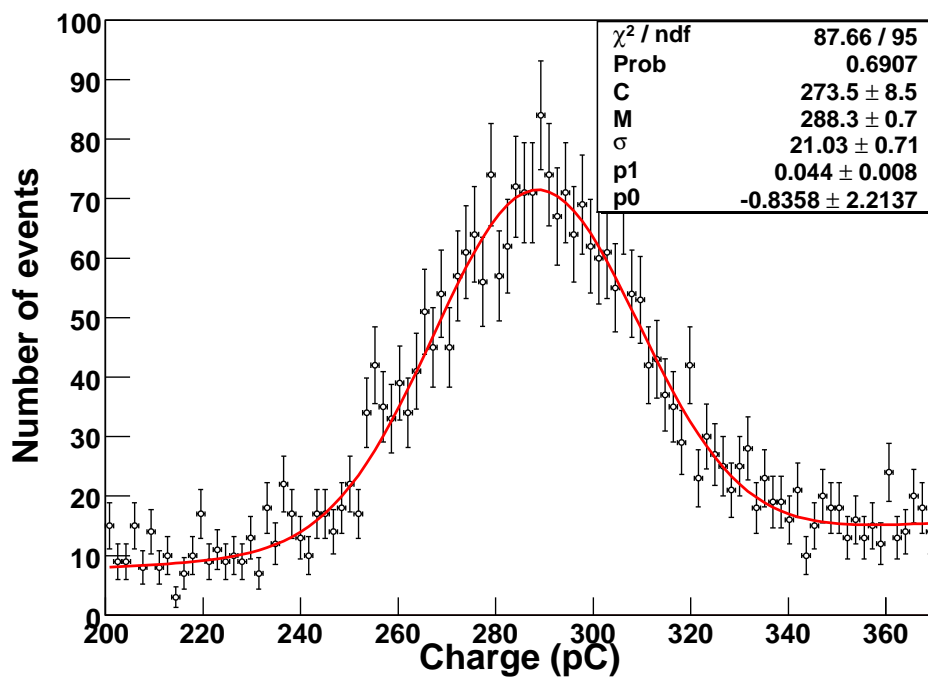
Figure 4.3: Total charge spectrum of S0406 crystal for 59.5 keV γs from a ^{241}Am source overlaided with gaussian fit function.
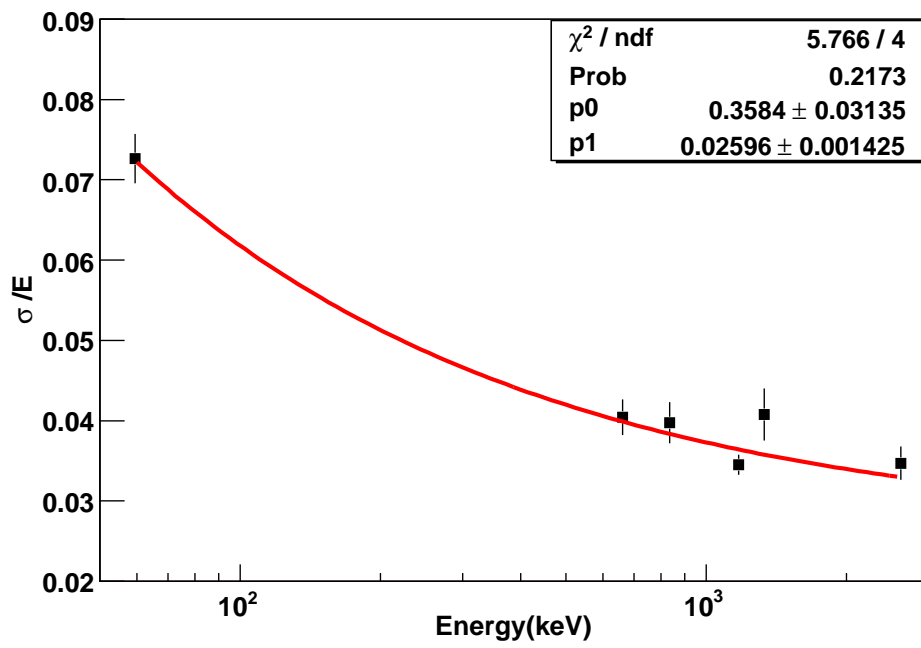
Figure 4.4: Energy resolution curve of S0406 crystal obtained with standard radioactive sources

the energy resolution is parameterized by the following equation

$$\frac{\sigma}{E} = \frac{p0}{\sqrt{E}} + p1.$$

The best fit result is overlaid in Fig. 4.4.

Fig. 4.5 shows the charge distribution of single cluster of 5.9 keV X-rays from a ^{55}Fe source without height threshold. The distribution is fitted by two superimposed Poisson functions (one for the SPE and the other for the SPE-overlapped signal) with exponential noise component.

$$f = A\frac{\mu^r e^{-\mu}}{\Gamma(r+1)} + B\frac{\mu'^r e^{-\mu'}}{\Gamma(r+1)} + Ce^{-x/\lambda},$$
$$r = xg, \ \mu = mg, \ \mu' = m'g,$$

where $m(m')$ is the mean of the Poisson distribution, and g is the gain factor of the PMT. The fitted curve is overlaid in the figure as a solid line. The ratio of the contribution of the two Poisson distributions is 9.3 %. Therefore, we conclude that $\sim$90 % of SPEs make single clusters and $\sim$10 % makes overlapped clusters. The ratio of the mean values of the two Poisson distributions, m'/m, is 2.11 $\pm$ 0.03 which is consistent with the expectation considering overlap of up to 3-SPEs.

In this fit, the most probable value (MPV) of the SPE is obtained as 0.86 pC. From the total charge of 59.5 keV from the ^{241}Am source, the photoelectron yield of S0406 crystal is obtained as 5.5/keV. Table 4.1 shows light yields of crystals obtained with the same process for different temperature conditions.

The photoelectron yields were calibrated at the beginning and at the end of each Run to monitor variations of light yields. The results show stability of the light output within 1 % for all crystals. The time-dependent gain variations are corrected by the MPV which is obtained from the SPE charge spectrum of low energy (4-8 keV) WIMP search data and its Poisson fit. Every one-week-long WIMP search data are accumulated for this purpose. Fig 4.6 shows that the gain is stable within 5 % for each PMT in the whole period. We consider gain variation as a systematic uncertainty to generate MC simulation which will be discussed later.
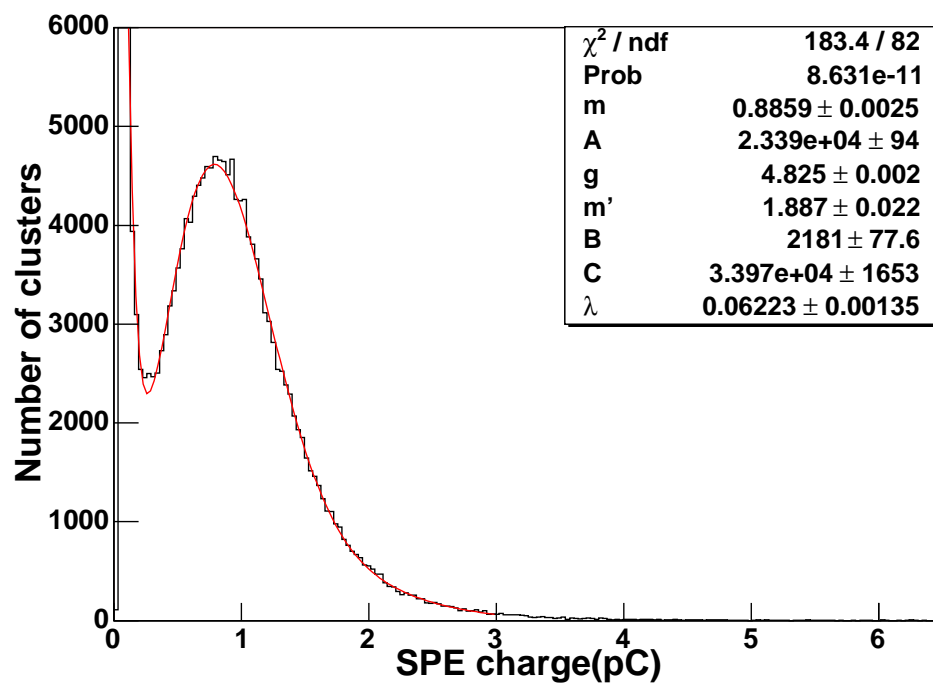
Figure 4.5: Single cluster charge spectrum. The distribution is fitted to two Poisson functions.
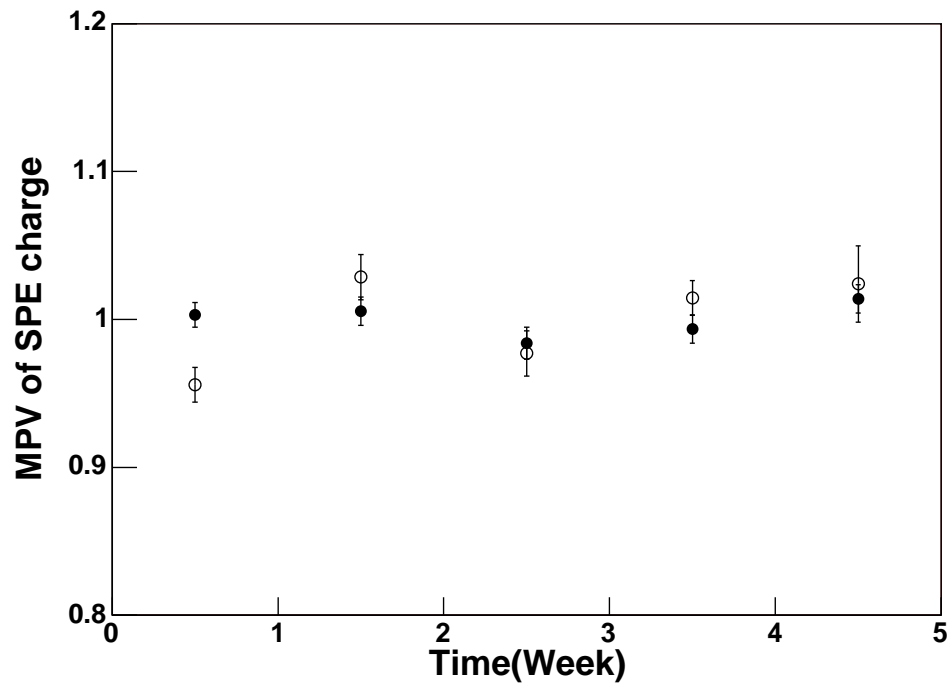
Figure 4.6: The most probable value (MPV) of the SPE charge, which is obtained from the same fit as Fig. 4.5 for the every one-week-long WIMP search data, for PMT1 (open circles) and PMT2 (filled circles) is shown. The values are normalized by the MPV obtained from the ^{55}Fe data.

Table 4.1: Light Yields of CsI(Tℓ) crystals

Crystal	Light Yield (PE/keV)	
	0 °C	Room temperature
S0406		5.5 ± 0.3
S0501A	4.6 ± 0.3	4.5 ± 0.4
S0501B	4.5 ± 0.4	4.2 ± 0.3
B0510A	5.9 ± 0.5	5.9 ± 0.4
B0510B	5.6 ± 0.4	5.3 ± 0.3
B0511		4.9 ± 0.3

4.2.2   Mean Time Calibration

The different timing characteristics between nuclear recoil and electron recoil in the CsI(Tℓ) crystals make it possible to statistically separate the nuclear recoil events from the γ background using the mean time distribution [94, 101, 102]. In order to have a good reference distribution of the mean time for them, we took calibration data of electron recoil from the γ source and nuclear recoil from the neutron source.

The γ calibration data were obtained with WIMP search crystals by a ^{137}Cs source in the copper chamber of Y2L. Identical setups and conditions as for the WIMP search data were used. We irradiated crystals during several weeks (somewhat different for crystal by crystal). We took low energy electron recoil events by Compton scattering of high-energy γ. The data amounts for each crystal are summarized in Table 4.2.

Neutron calibration data were obtained by exposing small-size test crystals to a neutron source. The two kinds of test crystal are used for the neutron calibration, one for Shanghai crystals and the other for Beijing crystals. The test crystal for Shanghai crystals was Tl006 which had $3 \times 3 \times 3$ cm^3 dimension. The Beijing crystals were used by B0506S crystal which had $3 \times 3 \times 5$ cm^3 dimension. We irradiated these test crystals to neutrons from 300 mCi Am-Be source, prepared at Seoul National University [125]. In order
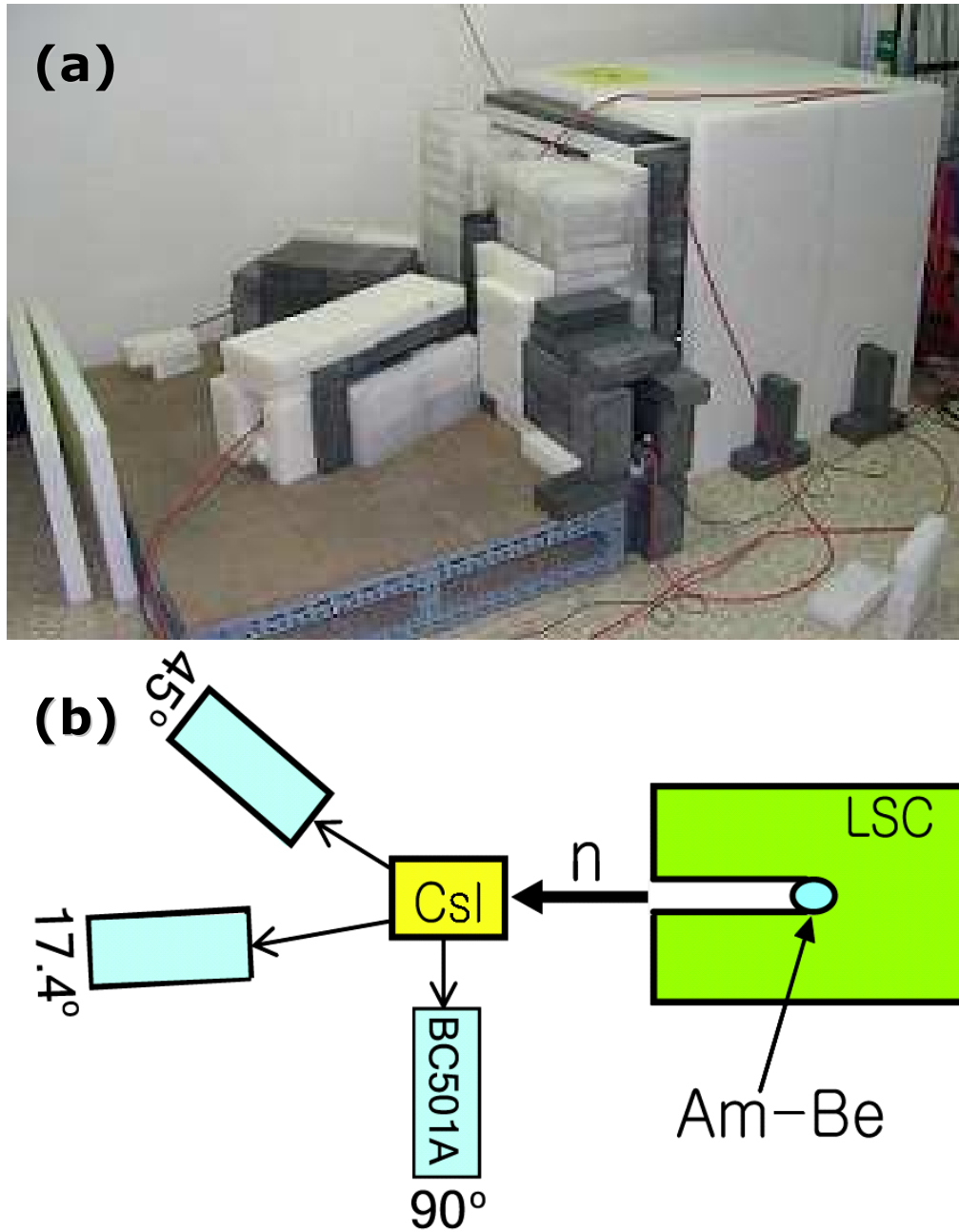
Figure 4.7: Neutron calibration setup. (a) shows the real picture and (b) shows the scheme of it.

Table 4.2: Summary of data

Data	Crystals	Period	Data amounts
WIMP Search	S0501A	June 2005 $\sim$ Mar. 2006	1147 kg·day
WIMP search	S0501B	June 2005 $\sim$ Mar. 2006	1030 kg·day
WIMP Search	B0510A	Dec. 2005 $\sim$ Mar. 2006	616 kg·day
WIMP search	B0510B	Dec. 2005 $\sim$ Mar. 2006	616 kg·day
Gamma	S0501A	4 weeks	1100 kg·day
Gamma	S0501B	4 weeks	1650 kg·day
Gamma	B0510A	2 weeks	910 kg·day
Gamma	B0510B	2 weeks	840 kg·day
Neutron	Tl006	1$\sim$2 month	500 kg·day
Neutron	B0506S	1$\sim$2 month	550 kg·day
PMT of S0501A	PMT Only	1 month	350 kg·day
PMT of S0501B	PMT Only	1 month	350 kg·day
PMT of B0510A	PMT Only	1 month	350 kg·day
PMT of B0510B	PMT Only	1 month	350 kg·day

to identify neutrons scattered from CsI, we used neutron detectors, made of BC501A contained in a cylindrical stainless steel vessel. Each neutron detector is shielded by 5 cm lead and 10 cm paraffin, and set up at various angles with respect to the incident neutron direction, this can be seen in Fig. 4.7. The Am-Be source is surrounded by liquid scintillator (LSC) composed of 95 % mineral oil and 5 % of pseudocumene with a collimation hole to the direction of the CsI(Tℓ) crystal. The LSC acts as a tagging detector of 4.4 MeV γ's which are simultaneously generated with neutrons from the Am-Be source as well as a neutron shield for the low surface neutron flux outside the source. We use 3 modules of 500 MHz FADC for the DAQ of the neutron calibration. Each module is used to take signals from CsI(Tℓ) crystal, BC501A liquid scintillators, and TOF signal from TAC module with LSC signal.

In order to identify neutron-induced events, we required a tag of a neutron

event in the BC501A liquid scintillators. As we discussed in Section 3.5.2, BC501A liquid scintillator can separate neutrons from γ's using PSD (see Fig. 3.27). In the neutron calibration, we use simply defined PSD parameter which is the peak height divided by the total charge. As one can see in Fig. 4.8 (a), the neutrons can be clearly separated from γ's. Furthermore, we required coincidence condition between the neutron detector and the CsI(Tℓ) crystal. To avoid contribution of background, we make 2 σ selection band from the coincident time peak as one can see in Fig 4.8 (b). Here the Δt is defined as '$t0\ of\ CsI - t0\ of\ BC501A$'. About 1 μs decay time of CsI(Tℓ) crystal can make this spectrum. With a good neutron separation capability and timing coincidence, we took neutron data, whose amount depended on energy (see Fig A.4) , equivalent to approximately 500 kg·days (Tl006, assuming 6 CPD) and 550 kg·day (B0506S, assuming 4 CPD) WIMP search data at 3-11 keV.

The gamma and neutron calibration data for each crystal are compared with one another in Fig. 4.9, 4.10, 4.11, and 4.12. These figures show that the MT of NR is faster than MT of electron recoil for each crystal and each energy bin.

We also took electron recoil data using a ^{137}Cs source for the test crystal used for the neutron calibration. This data is compared with the electron recoil calibration data obtained for WIMP search crystals to confirm that the neutron calibration data using the test crystal can be used for the WIMP search crystals. As one can see in Fig. 4.9, 4.10, 4.11, and 4.12, MT spectra of electron recoil for the test crystals are well matched with those of the WIMP search crystals.

4.2.3   PMT noise and PMT only data

PMT noise results from thermionic electrons that are spontaneously emitted by the phtocathode [105]. But, since this kind noise does not have correlation between single photoelectron signals, these events are not triggered in our
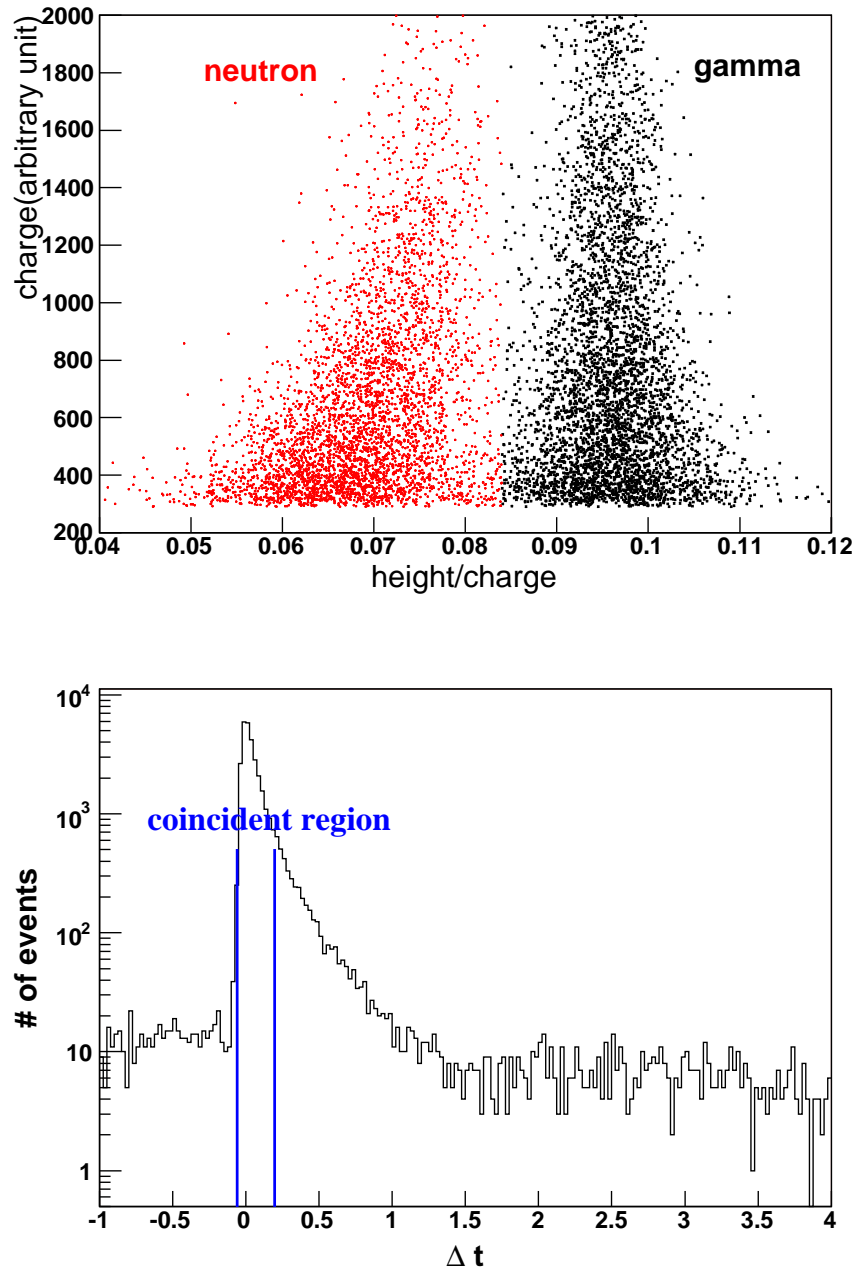
Figure 4.8: (a) neutron identification plot for neutron detector. (b) time coincidence (μs unit) plot between neutron detector and CsI(Tℓ) crystal.

144
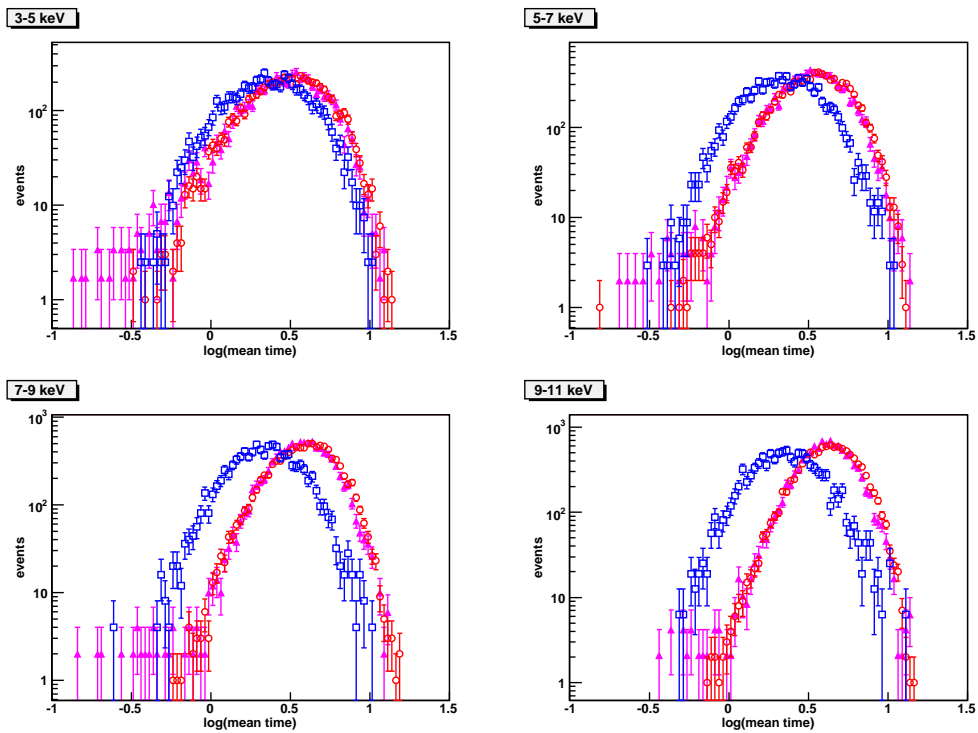
Figure 4.9: MT spectrum of Compton electron for the test crystal (filled triangles), S0501A crystal (open circles), and nuclear recoil for the test crystal (open squares).
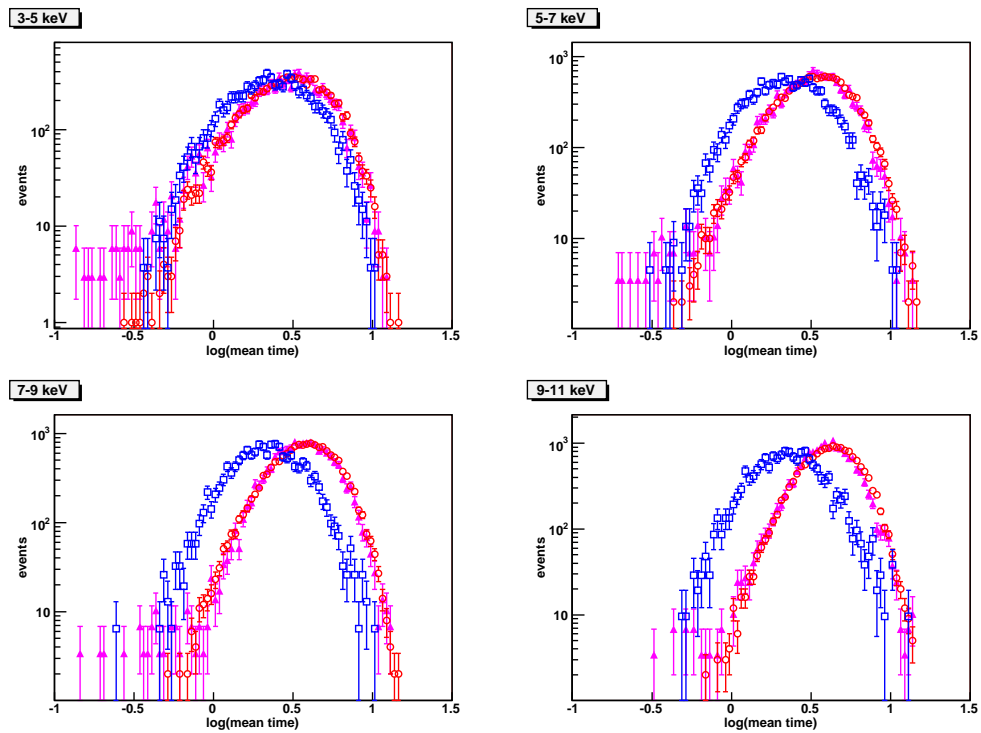
Figure 4.10:   MT spectrum of Compton electron for the test crystal (filled triangles), S0501B crystal (open circles), and nuclear recoil for the test crystal (open squares).
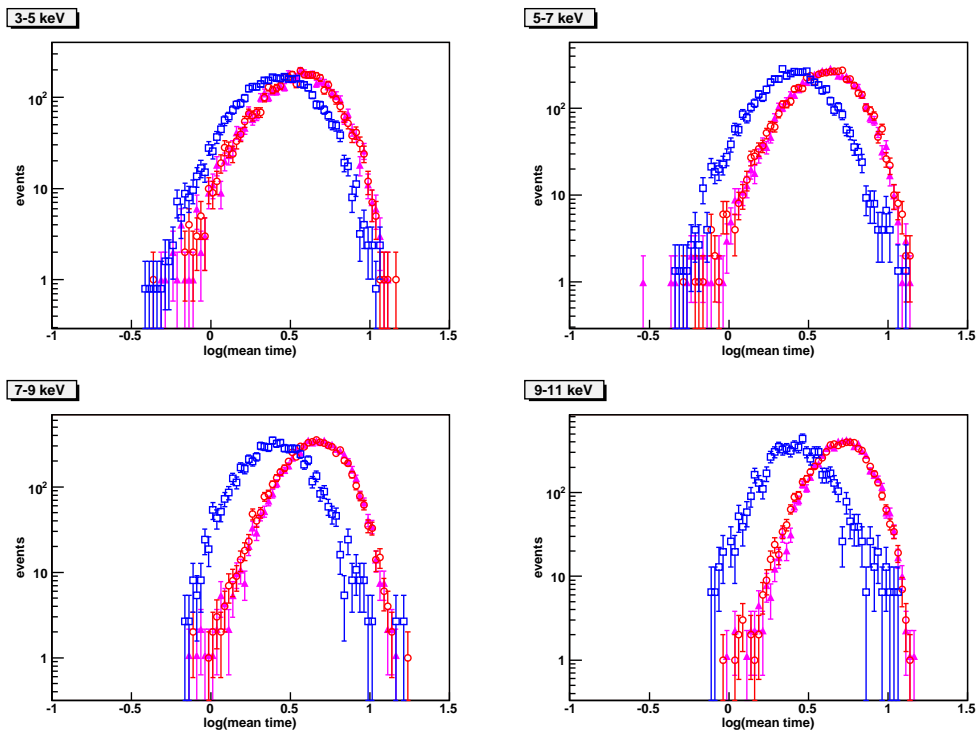
Figure 4.11: MT spectrum of Compton electron for the test crystal (filled triangles), B0510A crystal (open circles), and nuclear recoil for the test crystal (open squares).
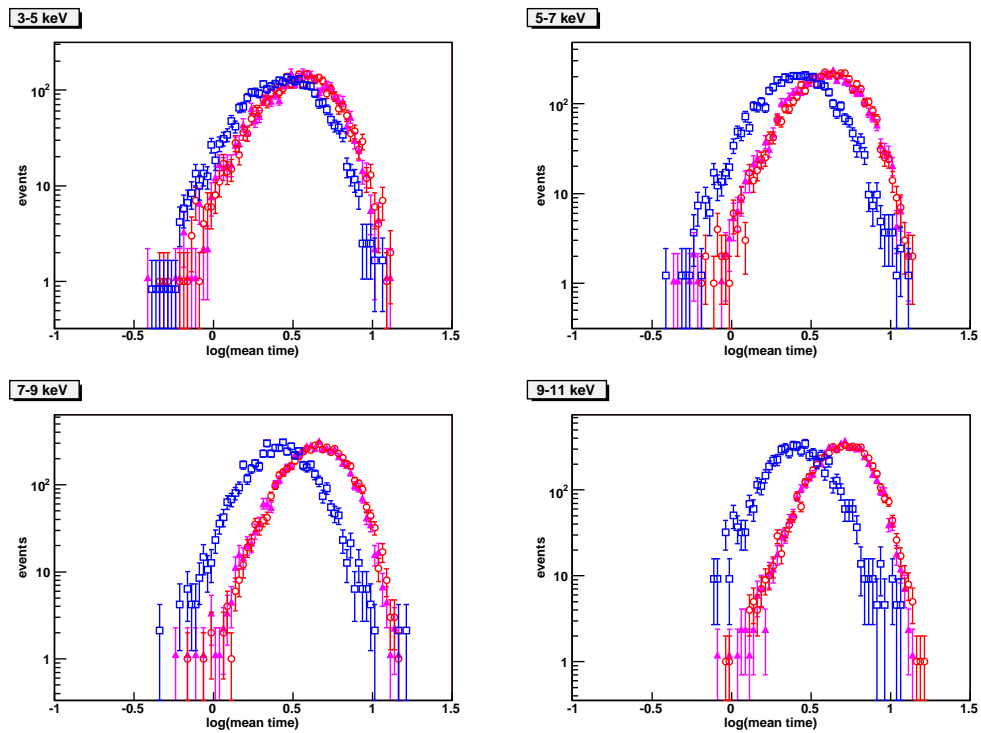
Figure 4.12:   MT spectrum of Compton electron for the test crystal (filled triangles), B0510B crystal (open circles), and nuclear recoil for the test crystal (open squares).

trigger condition (each two single photoelectrons in two μs) with the usual dark current rate of a few kHz. Randomly generated SPEs (random SPE generated in the CsI(Tℓ) crystal and thermionic electrons emitted in the photocathode) can be accounted for monitoring pedestal region which is first 4 μs in the full acquisition window because trigger position of CsI(Tℓ) crystal is fixed at 6.8 μs. Typical rate for one side is 3 kHz. In the 32 μs window the effect from random events are 0.1 SPEs for each PMT which is negligible to be accounted as events with more than 3 keV (15 SPEs).

Another source of dark pulses from PMT are Cherenkov radiation originated by natural radioactivity and cosmic radiation [126]. The most important components of natural sources are usually ^{40}K and ^{232}Th contained in the glass envelope. Because of the low light yield from the Cherenkov process, the corresponding dark pulses correspond to a few photoelectrons. Also, that kind of photoelectrons have time correlation they can generate trigger by themselves. Such noise may contribute to low energy region.

Afterpulses from a spark in the dynode structure or ionized gas in the traces are another type of noise [127]. These kinds noise have characteristics that the first pulse is relatively bigger than the normal SPEs but following signals are relatively smaller than the normal SPEs. Because of the following clusters, these events can be triggered. Fig. 4.13 shows typical pulse shape of normal electron recoil events which are obtained from the ^{137}Cs calibration and PMT noise events which are obtained from the PMT only data taking. As shown in this plot, PMT noises have much bigger first clusters. We compare the SPE charge spectrum between PMT noise events and normal electron recoil events in Fig 4.14. As seen in this plot, PMT noise events have much bigger clusters than normal events. These dark pulses contribute up to 10 keV. Similar noise was reported by another group [128].

The PMT noise can significantly limit the sensitivity of low background and low threshold experiments [97, 129]. To understand the PMT noise which have time correlation between clusters (afterpulses from a spark and Cherenkov radiation), we take the PMT noise events with the same system
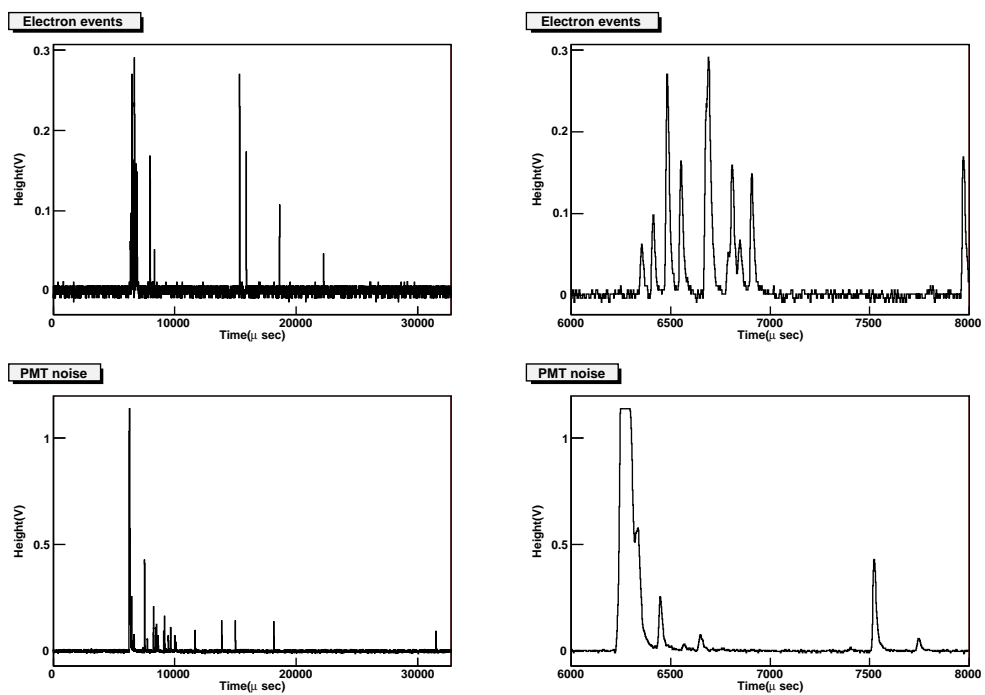
Figure 4.13: Pulse shape of typical low energy electron events (upper plot) and PMT noise events (lower plot).
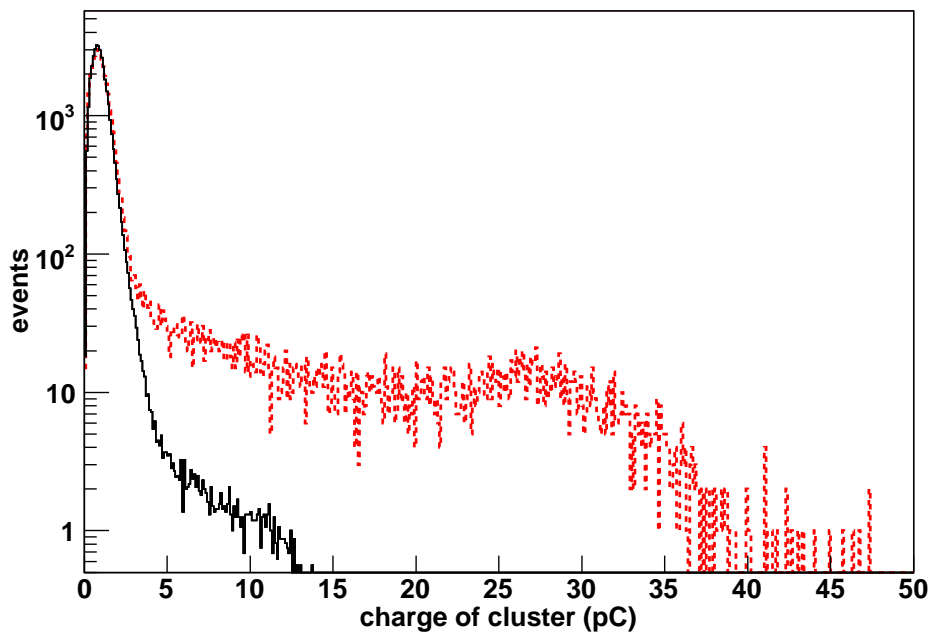
Figure 4.14: Charge distribution of single clusters (candidate of SPEs) with PMT noise events (dashed line) and low energy γ calibration data (solid line) for less than 6 keV events.
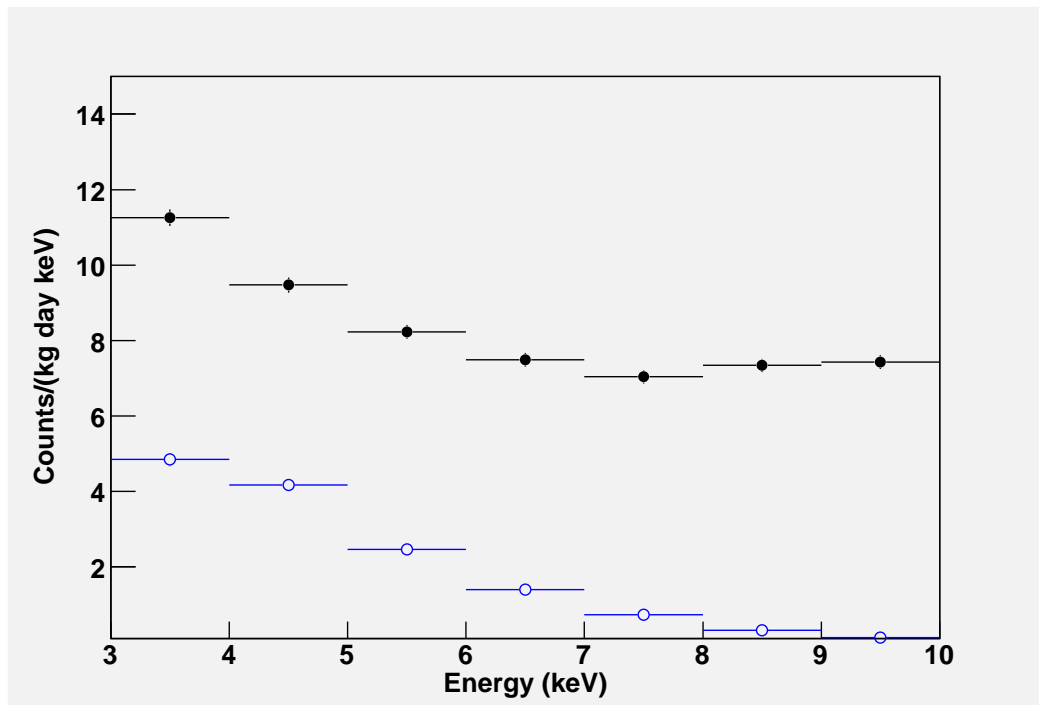
Figure 4.15: Energy spectrum of PMT noise (blue open circle) and WIMP search data (black filled circle) for S0406 crystal only with coincidence cut between two PMTs. The PMT noise data was normalized by assumption with crystal attached setup.
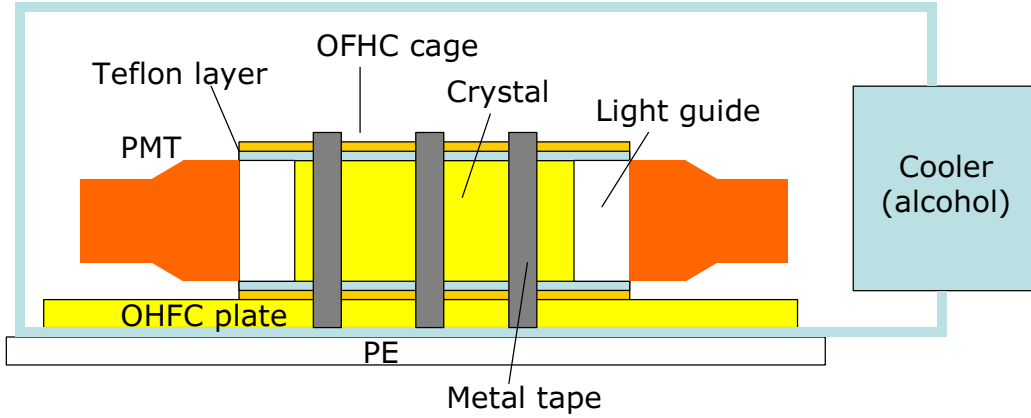
Figure 4.16: Scheme of cooling system.

and trigger condition without the CsI(Tℓ) crystal in the copper chamber. To simulate PMT attached setup, we make a box using clean acryl with the same dimension as the full size crystal ($8 \times 8 \times 30$ cm^3). The same PMTs, used in the WIMP search, were mounted in the acryl box face-to-face with optical greese. We took the PMT noise data equivalent to 350 kg· days WIMP search data for each data set (see Table 4.2). Energy spectrum of PMT noise events are shown in Fig. 4.15 with energy spectrum of WIMP search data. Background increasing at the lower than 10 keV energy range is well explained by PMT noise events.

4.2.4 WIMP search data

First WIMP search data with a low background crystal was done from July 2004 to September 2004 with S0406 crystal. During the two month period we took 237 kg·days WIMP search data and its result was published [97]. Detailed analysis of this data is explained in Appendix A.

In the process of data taking and analysis of first physics run, we understood the characteristics of background of the WIMP search data. Because the main contribution of low-energy background was the PMT noise events, we decided taking data in the lower temperature condition. We use an al-

cohol cooler, as shown in Fig. 4.16. Refrigerated alcohol was flown in the OFHC cooper pipe to cool the OFHC plate. Because we use OFHC cage to mount PMTs on the crystals, CsI(Tℓ) crystals could be cooled down. To improve thermal conductivity we used metal tape between OFHC plate and cage. All systems were thermally isolated with the copper shield using PE plate. The scheme of cooling system is shown in Fig. 4.16. We monitored temperature at the top of OFHC cage and OFHC plate. We also try to control the temperature of alcohol to keep OFHC cage as 0 °C.

From June 2005 to December 2005 we used three of Shanghai crystals to take data under the 0 °C condition. One is a little bit smaller (8 x 8 x 23 cm^3) and the others are full sized. In the December 2005 we had two more full size crystals made in the Beijing Hamamatsu Co. We installed two more CsI(Tℓ) crystals at that time. Because S0406 crystal have different size and also we didn't have enough DAQ modules, we removed S0406 crystal also. Because data amount from S0406 in the 0 ° C condition was relatively smaller than the other crystals, we only used other 4 full size data in this thesis. Until March 2006 we took about 3406 kg·days WIMP search data at the 0 °C condition. The data is summarized in Table 4.2.

During the data accumulation period, we monitor the temperature and the humidity variation with environment monitoring system (see Section 3.8) as shown in Fig 4.17. Temperature variation in the CsI(Tℓ) crystal is within 0.1 °C. Relative humidity is well controlled at about 0 %.

4.3   Event selection

The typical noise rejection cut developed for the first WIMP search data (see Appendix A) was applied to each data set. We found that PMT noise rejection cut (the biggest cluster cut and mean charge cut) distort the MT shape. We thus tried to make a new method of events selection to reject PMT noise events.
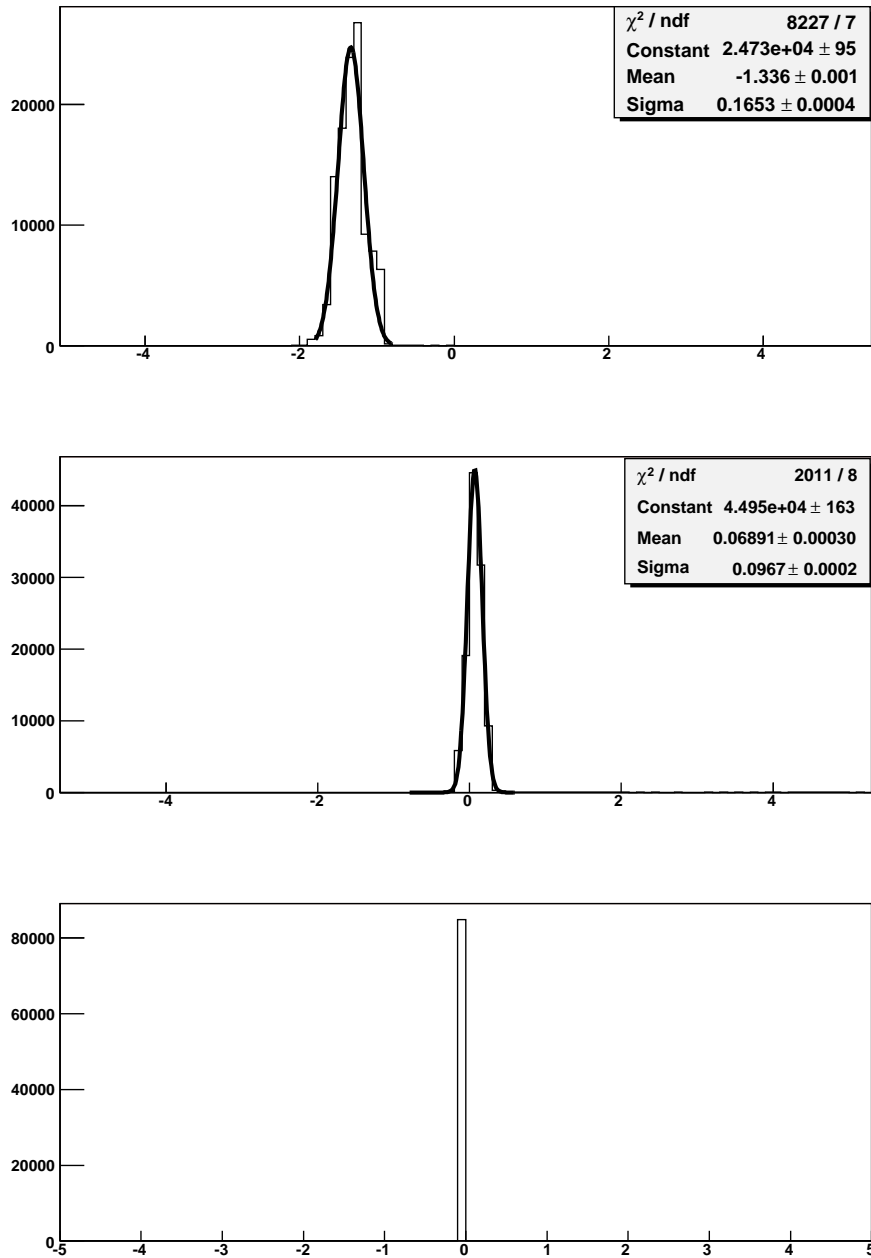
Figure 4.17: During data accumulation period (From June 2005 to March 2006), temperature on the OFHC plate (up) and on the OFHC cage (middle) and humidity of copper shield are shown.
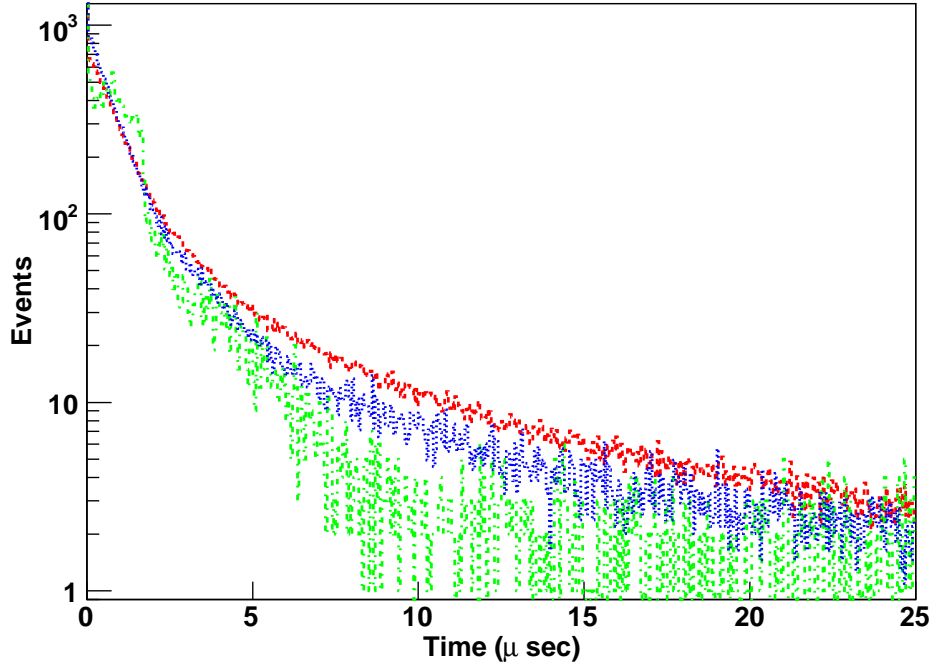
Figure 4.18: Time spectrum from γ calibration data (dashed line), neutron calibration data (dotted line), and PMT noise data (dotted-dashed line).

4.3.1 Decay time fit and fit quality cut

We studied the characteristics of pulse shape with decay curve fitting. The clustering algorithm for identification of SPE is applied to each event (see Section 4.1). Time distribution of identified clusters is fitted to the two exponential decay time component with probability density (PDF) function defined in Eq. 4.1 [94] (see also Fig. 4.18). The maximum likelihood method with unbinned data is used for this fit:

$$PDF(t) = \frac{1}{\tau_f}e^{-(t-t_0)/\tau_f} + \frac{R}{\tau_s}e^{-(t-t_0)/\tau_s}. \qquad (4.1)$$

As seen in Fig. 4.18, the decay time of PMT noise events are quite different from real γ or neutron events. Especially, PMT noise events do not have long decay components. Therefore we also try to fit the SPE decay spectrum with
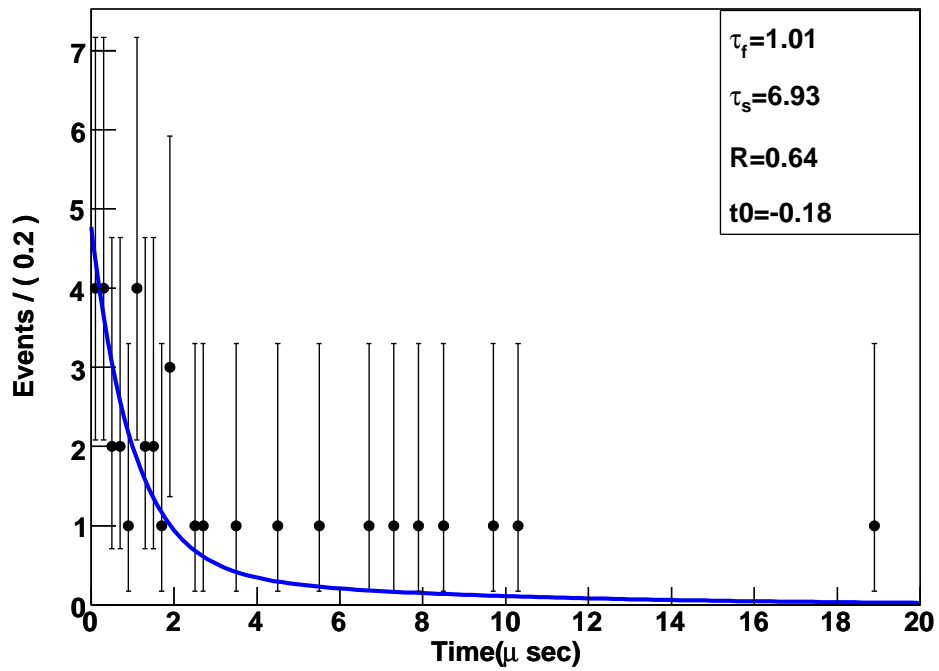
Figure 4.19: Fit example with two exponential decay time components.

one exponential PDF function. Fig 4.19 shows an example of decay time fit with unbinned likelihood method using two exponential PDF function. Event by event fit for each data set has been performed. Fig 4.20 (a) shows $log(\tau_f)$ distribution of each data set. We give an event selection condition with $log(\tau_f) > -1.5$ to reject PMT noise events. Fig 4.20 (b) shows log likelihood value difference between two exponential fit and one exponential fit. As one can see in this plot, PMT noises have different characteristics in this parameter. Therefore, we can reduce PMT background by the selection of good events using the condition from -0.5 to 0.5.

After decay time fit, we can fix the PDF function event by event. Using this function, we calculate MT as follow:

$$MT_{fit} = \int t \cdot PDF(t)dt / \int PDF(t)dt.$$

We compared this mean time with MT (we call it as MT_{calc}) calculated from SPE analysis. Fig 4.20 (c) shows $Log(MT_{calc}/MT_{fit})$ distribution for each data set. As one can see in this plot, PMT background have different components. So we have good events selection band from -0.5 to 0.3 for this parameter.

4.3.2   Asymmetry cut

Because the PMT background events originated from PMT itself, the light output can be concentrated on one PMT. We defined the asymmetry value as follow:

$$Asymmetry = (Q1 - Q2)/QT,$$

where $Q1$, $Q2$, and QT are charge signals from PMT1, PMT2, and their sum, respectively. Fig. 4.21 shows asymmetry distribution of S0501A crystal. We developed asymmetry cut with gamma calibration data. We make cut condition including 85 % of calibration data for each energy bin.
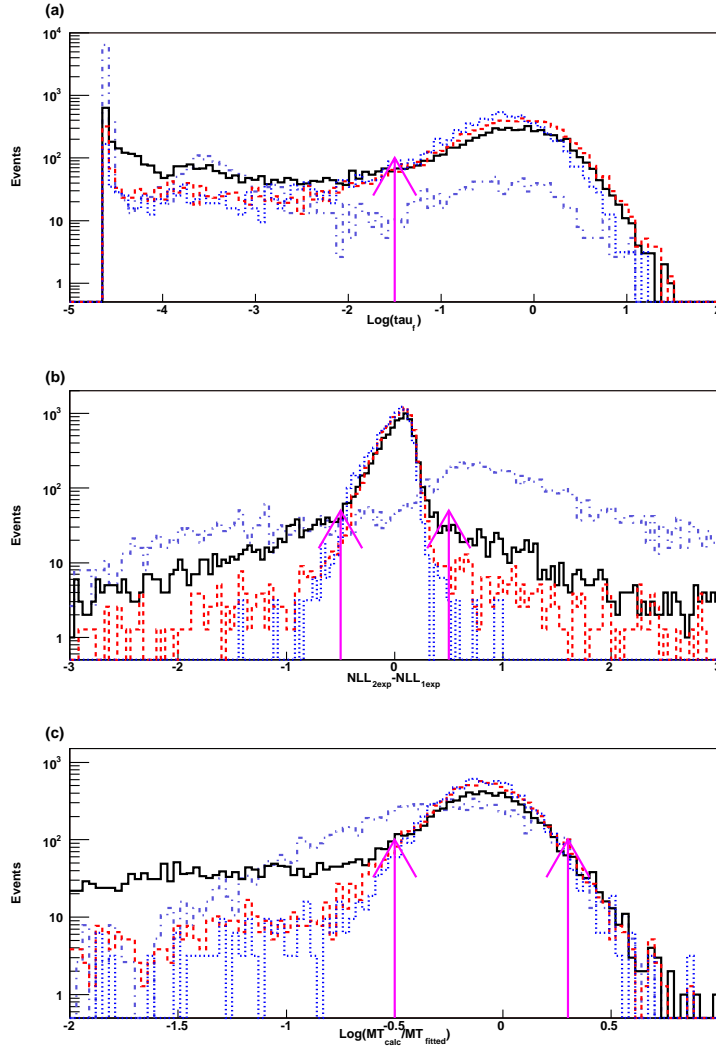
Figure 4.20: $log(\tau_f)$ distribution (a), log likelihood value difference for two exponential fit and one exponential fit (b), and ratio (c) between MT calculated from fit function (MT_{fit}) and MT calculated from SPE analysis (MT_{calc}) for background data (solid line), gamma calibration (dashed line), neutron calibration (dotted line), and PMT background (dotted-dashed line) for 5-6 keV events of S0501A crystal. We indicate cut position with vertical arrow.
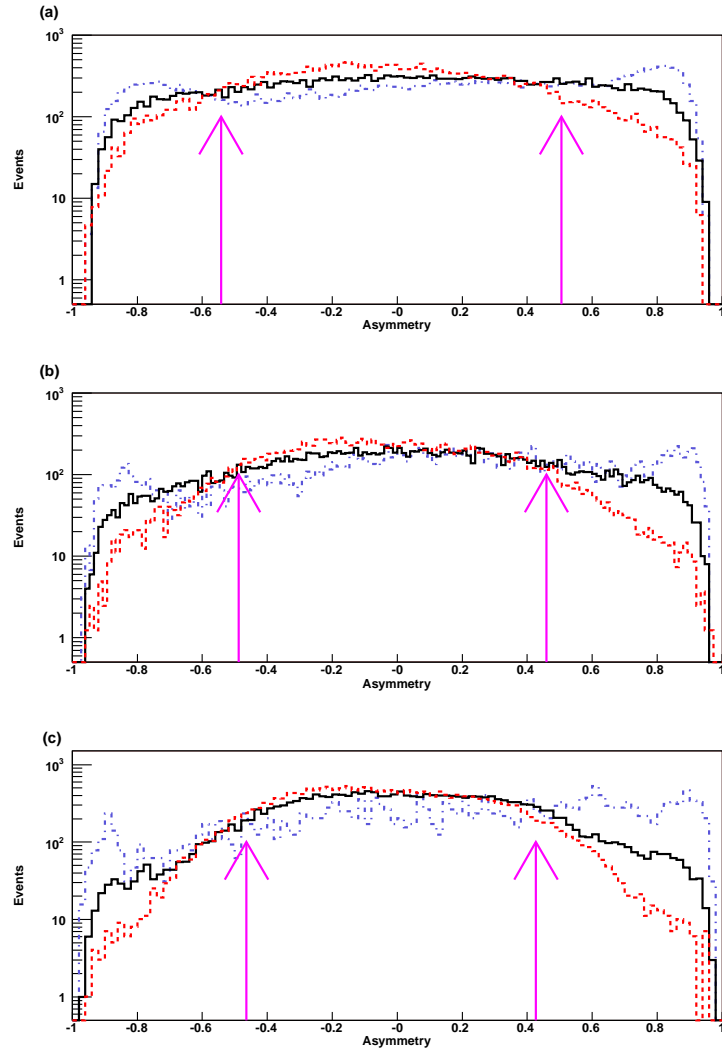
Figure 4.21:   Asymmetry distributions for background data (solid line), gamma calibration (dashed line), and PMT background (dotted-dashed line) for 3-5 keV (a), 5-7 keV (b), and 7-10 keV (c) of S0501A crystal. We indicate cut position with vertical arrow.
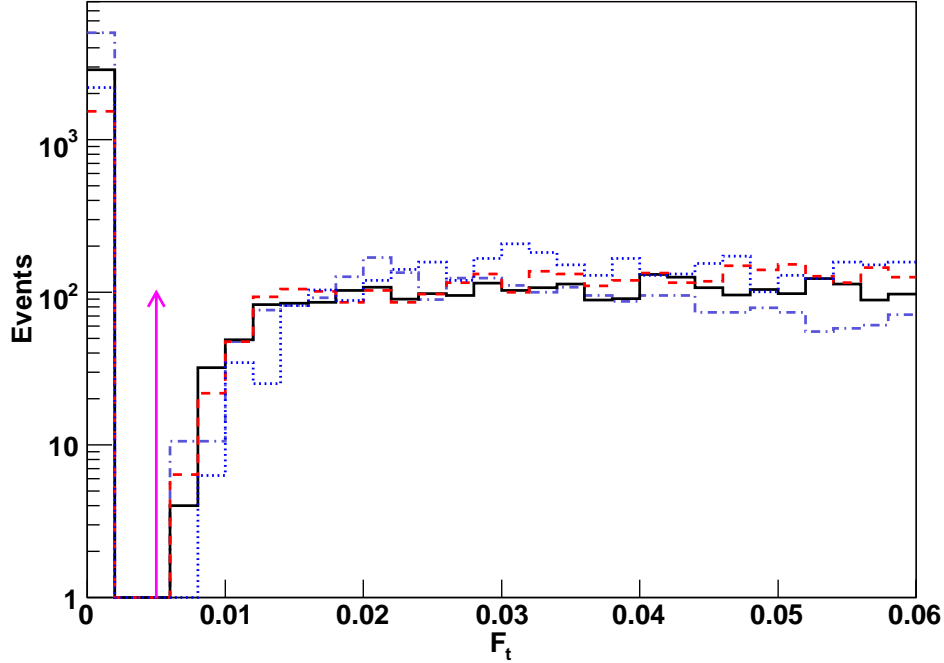
Figure 4.22:   Tail fraction value for background data (solid line), gamma calibration (dashed line), neutron calibration (dotted line), and PMT background (dotted-dashed line) for 5-6 keV events of S0501A crystal. We indicate cut position with vertical arrow.

4.3.3   Very short events rejection

Decay time composition of scintillating events is different with PMT noise events (see Fig. 4.18). We define the tail fraction value using followed function

$$F_t = (Q_t - Q_{10})/Q_t,$$

where Q_t is charge sum of the whole window (32 μsec) and Q_{10} is charge sum within 10 μsec from first SPE. Fig 4.22 shows tail fraction of each data set. We give selection condition of $F_t > 0.005$.
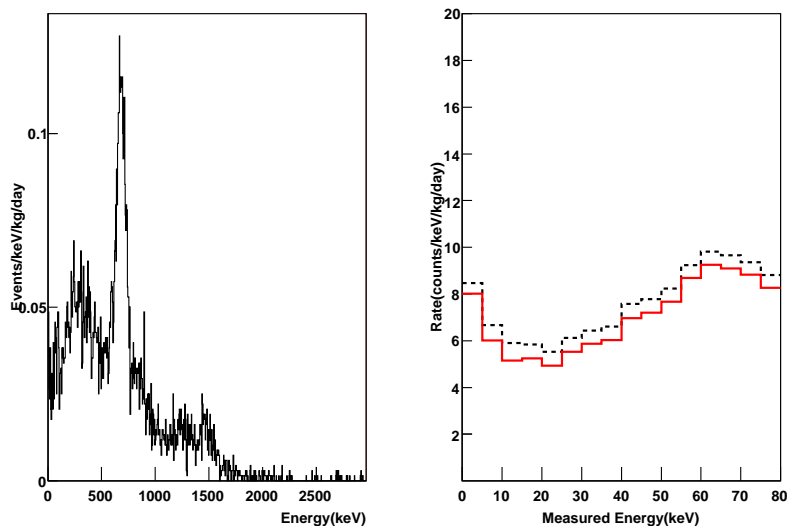
Figure 4.23: Energy sum of all crystal for coincident events (left), and background spectrum for S0501A crystal (right dashed line) were shown. We have energy spectrum of the crystal with coincident events rejection (right solid line).

4.3.4 Coincident events rejection

Because the cross section of WIMP-nucleus scattering is quite small, events with hits in more than one crystal may be rejected without any loss of efficiency. But, multiple scattering events are useful for background understanding. Main source of multiple scattering comes from the Compton scattering of γ, and thereby we can use these events as electron recoil calibration data (which is much pure calibration data than gamma source calibration because of tagging the other signal).

Since the time window for each event is 32 μsec and the trigger rate for a crystal is less than 0.6 Hz, the accidental coincidence probability is expected to be less than 0.05 % even for the case of 25 crystals data taking. This is negligible.

Fig. 4.23 shows energy sum of all crystal for coincident events. Clear peak from ^{137}Cs (661.6 keV) shows that Compton scattering events of γ mainly contribute to coincident events. The right plot of this figure shows background rejection with coincident condition. We achieved background reduction of about 0.7 CPD with this method.

4.3.5 Effect of Cut

We apply all cuts for each calibration data to estimate an efficiency. Table 4.3 shows the passing events in the different cut stage with gamma calibration data using S0501A crystal. In the same manner we have information for neutron and PMT calibration data in Table 4.4 and 4.5.

Table 4.3: Effect of cuts on scintillation events with gamma calibration data of S0501A crystal.

Energy	No cut	Base	Quality	Short	Asymmetry
3-4 (keV)	6951	6941	3083	2538	2279 (32.8 %)
4-5 (keV)	7021	7018	4260	3687	3308 (47.1 %)
5-6 (keV)	7147	7147	5133	4623	4061 (56.8 %)
6-7 (keV)	7014	6925	5530	5110	4478 (63.8 %)
7-8 (keV)	6925	6832	5835	5503	4771 (68.9 %)
8-9 (keV)	6832	6940	6039	5815	5003 (73.2 %)
9-10 (keV)	6940	6760	6336	6170	5353 (77.1 %)
10-11 (keV)	6760	6675	6349	6250	5404 (79.9 %)

As shown in these tables, more than 99.0 % of PMT noise events were rejected by currently developed cut with about 50 % efficiency for gamma and neutron calibration data.

Fig. 4.24 shows the log(MT) distribution in the different cut stage. We check the stability of MT as applying each cut. As seen in these plots, the shape of MT distribution does not change. Also we draw energy spectrum of WIMP search data before and after cuts for each crystal (Fig. 4.25).
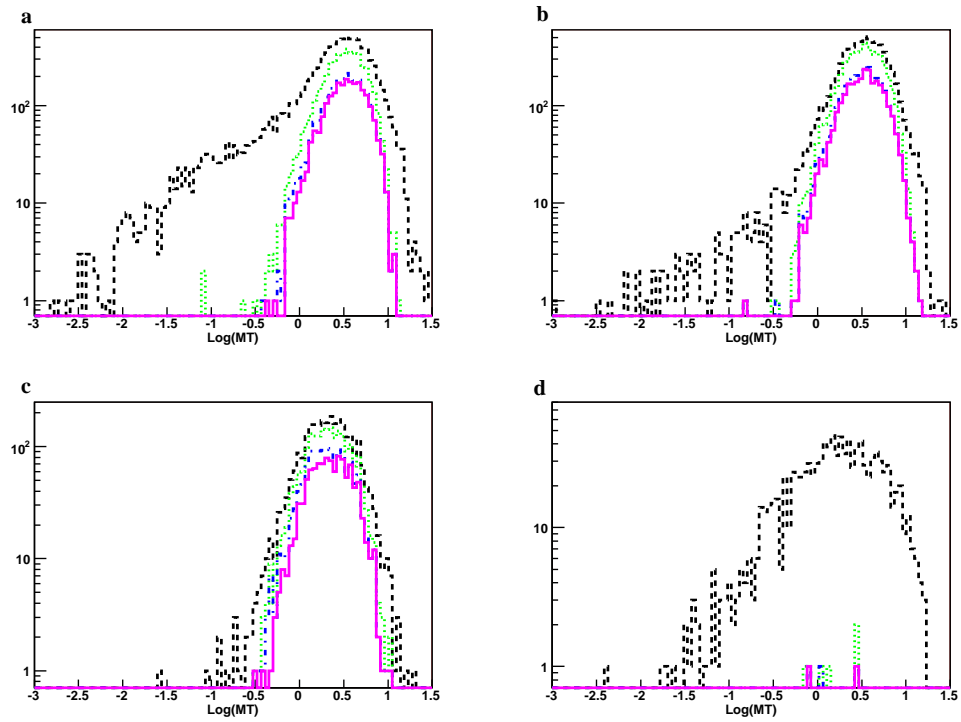
Figure 4.24:   Log(MT) distribution of WIMP search data (a), gamma cal-
ibration data (b), neutron calibration data (c), and PMT noise data (d)
for 5-6 keV events of S0501A crystal are shown with different cut stage -
only reference cut (dashed line), include fit quality cut (dotted line), include
asymmetry cut (dashed line), and include tail fraction cut (solid line).
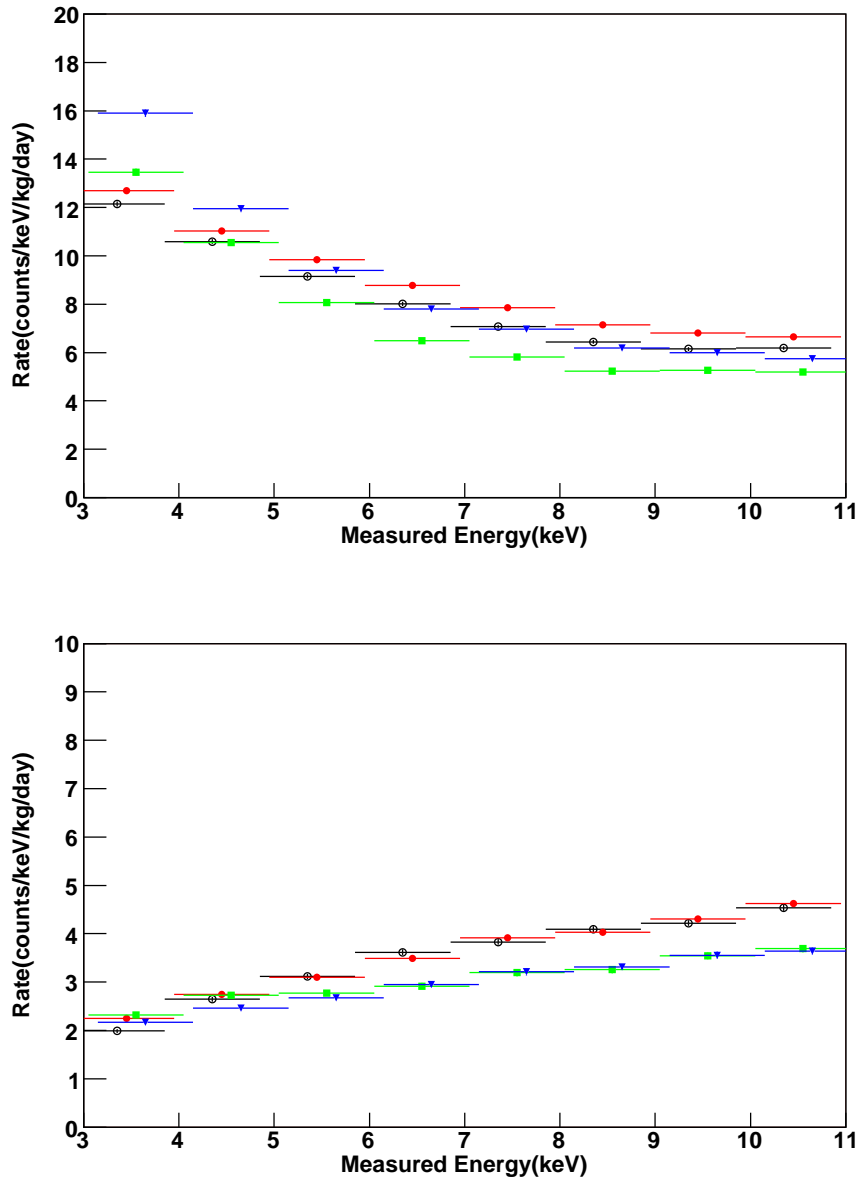
Figure 4.25: Energy spectra of WIMP search data before (upper plot) and after cuts (down plot) for S0501A (open circles), S0501B (filled circles), B0510A (filled squares), and B0510B (filled triangles).

Table 4.4: Effect of cuts on scintillation events with neutron calibration data.

Energy	No cut	Base	Quality	Short	Asymmetry
3-4 (keV)	2719	2716	1420	1077	941 (34.7 %)
4-5 (keV)	2902	2895	1888	1467	1279 (44.1 %)
5-6 (keV)	2914	2905	2174	1745	1502 (51.5 %)
6-7 (keV)	2489	2488	1948	1575	1371 (55.1 %)
7-8 (keV)	2167	2163	1780	1486	1311 (60.5 %)
8-9 (keV)	1782	1780	1471	1235	1086 (60.9 %)
9-10 (keV)	1397	1397	1187	1011	891 (63.8 %)
10-11 (keV)	1187	1185	1028	904	803 (67.6 %)

Table 4.5: Effect of cuts on PMT only data.

Energy	No cut	Base	Quality	Short	Asymmetry
3-4 (keV)	14717	11369	49	36	19 (0.13 %)
4-5 (keV)	8680	6528	40	29	15 (0.17 %)
5-6 (keV)	4698	3473	26	18	8 (0.17 %)
6-7 (keV)	2380	1662	20	13	7 (0.29 %)
7-8 (keV)	1174	780	10	9	3 (0.26 %)
8-9 (keV)	618	405	9	6	0 (0 %)
9-10 (keV)	264	159	5	5	1 (0.38 %)
10-11 (keV)	140	90	2	2	1 (0.71 %)

4.3.6 Efficiency

We calculated an efficiency of event selection condition with similar way explained in Appendix A. Because we use multi crystals, the coincident events can be used to calculate efficiency. Random coincident event rate is very small (less than 0.0001 Hz which give about a few events per day). We thus conclude that most of coincident events came from real scintillation events. Furthermore, we already know main production of coincident events are electron recoil events originated from beta-gamma events or Compton scattering events from ^{134}Cs decay and Compton scattering events from ^{137}Cs
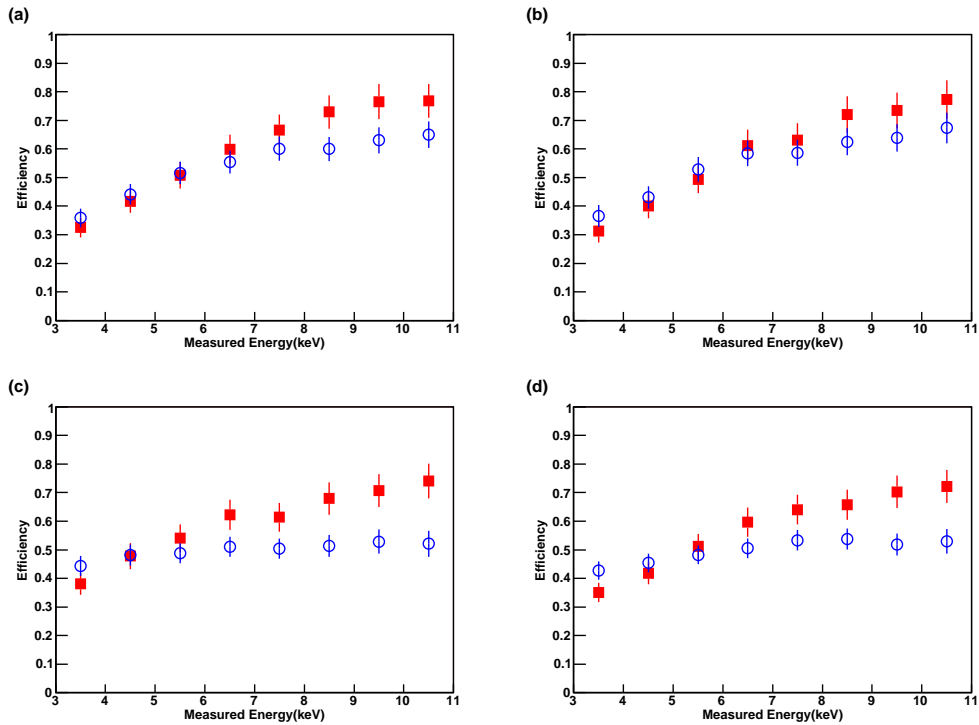
Figure 4.26: Efficiencies calculated with coincident events (filled circles) and neutron calibration data (open squares) for S0501A (a), S0501B (b), B0510A (c), B0510B (d).

decay. Therefore we can consider coincident events as gamma calibration data. Because the coincident events were simultaneously taken with WIMP search data, most systematic uncertainty in the efficiency calculation was solved. For example, there are gain changes in the PMT, temperature and humidity changes, and position dependences of signal. We use coincidence events to calculate efficiency for electron recoil of crystal.

We use different crystals (but same quality) to take neutron calibration data, especially sizes are quite different. So, the asymmetry effects are also different. Since the reason is to have different asymmetry spectrum between nuclear recoil and electron recoil, we use efficiency of coincidence events as efficiency of nuclear recoil for asymmetry cut.
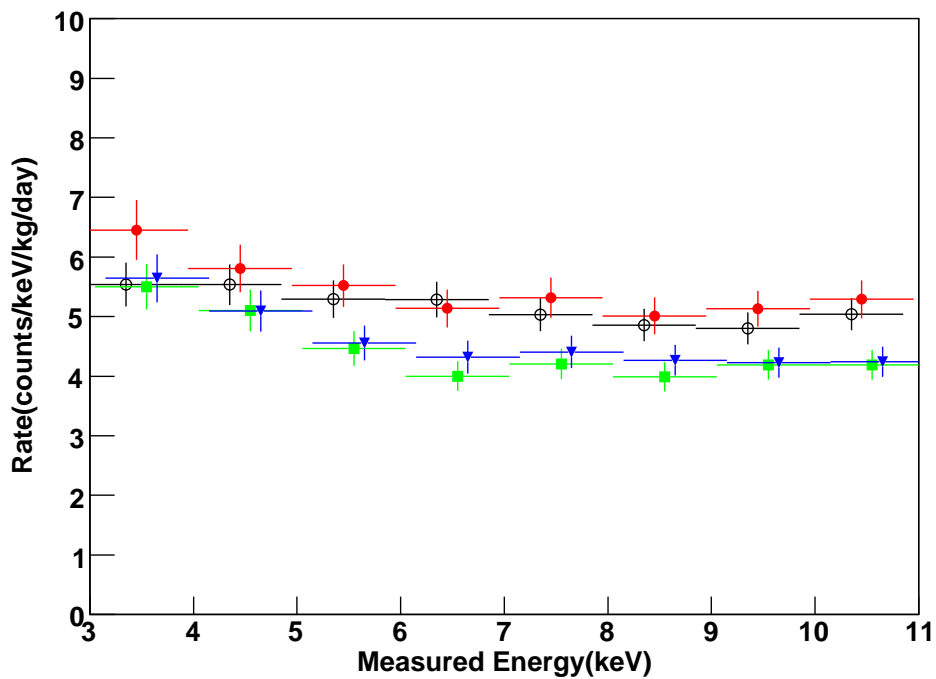
Figure 4.27: Energy spectra of WIMP search data with efficiency correction after cuts using Fig. 4.25 and Fig. 4.26 result. In this plot, we account errors of efficiency from statistical uncertainty. The points are shifted with respect to each other x-axis to avoid overlapping.

Fig. 4.26 shows the efficiency of nuclear recoil events and coincidence events for each crystal as a function of energy. We used efficiency of nuclear recoil events from neutron calibration as that of WIMPs. The efficiency difference between nuclear recoil and electron recoil is accounted for as systematic uncertainty. Table 4.6 shows summarized efficiency for S0501A crystal. With this result, we can draw background spectrum of WIMP search data from Fig. 4.25. The result obtained with efficiency correction is shown in Fig. 4.27.

Table 4.6: Efficiency of S0501A crystal.

Energy	Efficiency	Error	Statistical	Systematic
3-4 keV	35.8 %	4.7 %	3.2 %	3.3 %
4-5 keV	44.1 %	4.3 %	3.6 %	2.4 %
5-6 keV	51.6 %	4.0 %	3.9 %	0.8 %
6-7 keV	55.4 %	6.0 %	4.0 %	4.5 %
7-8 keV	60.0 %	7.8 %	4.2 %	6.6 %
8-9 keV	60.0 %	13.6 %	4.3 %	12.9 %
9-10 keV	63.1 %	14.2 %	4.6 %	13.4 %
10-11 keV	65.0 %	12.7 %	5.0 %	11.8 %

4.4   Annual Modulation study with our data

DAMA claims positive result with annual modulation signature of WIMPs [63, 64]. The annual modulation of the signal rate is induced by the Earth's revolution around the Sun. As a consequence, the Earth is crossed by a larger WIMP flux in June[I] and by a smaller one in December[II] (see Fig. 4.28).

Although our data is statistically much lower than that of DAMA data,

---

[I]When its rotational velocity is added to that of the solar system with respect to the galaxy.

[II]when the two velocities are subtracted.
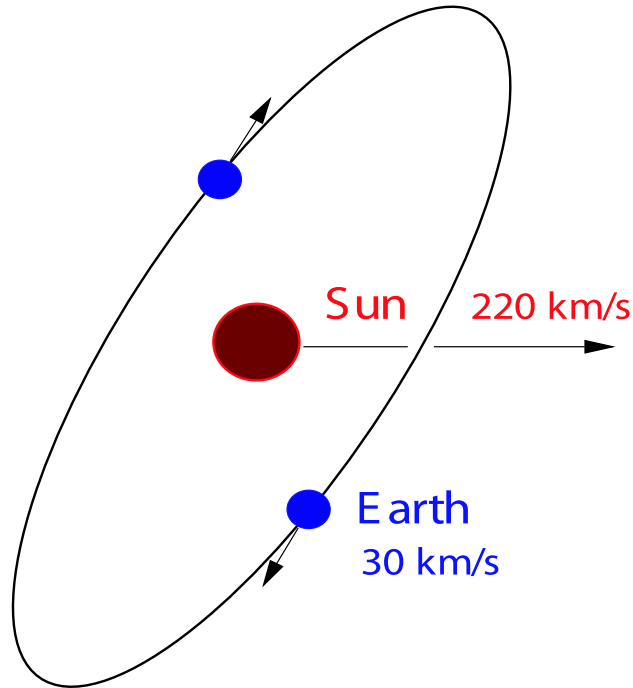
Figure 4.28: Schematic view of the Earth's motion around the Sun.

we have done quick analysis of annual modulation signature with our data. Because B0510A and B0510B crystals use to take data only at winter of 2006, we use two of Shanghai crystal (S0501A and S0501B) data for annual modulation study. Total data taking period with these two crystals are about 7 month and total data amounts are 2177 kg·day. Fig. 4.29 shows residual events rate in the particular energy bin (3-5 keV, 5-7 keV, 7-9 keV) as a function of the time. In this plot, we do not have evidence of modulation signature from WIMP scattering. But, we have tendency of background reduction by elapsing of time for all energy bin. We consider this result came from that decay of ^{134}Cs . Half life of ^{134}Cs is 2.065 year and ^{134}Cs contribute 1-2 CPD background at low energy. Therefore, 0.2-0.5 CPD background reduction during half year is possible.

Also our data is statistically not enough to search annual modulation signature claim by DAMA (modulation amplitude in NaI(Tℓ) is 0.0200 ± 0.0032 CPD). To search this level, we need ∼100 kg of crystal. If we have
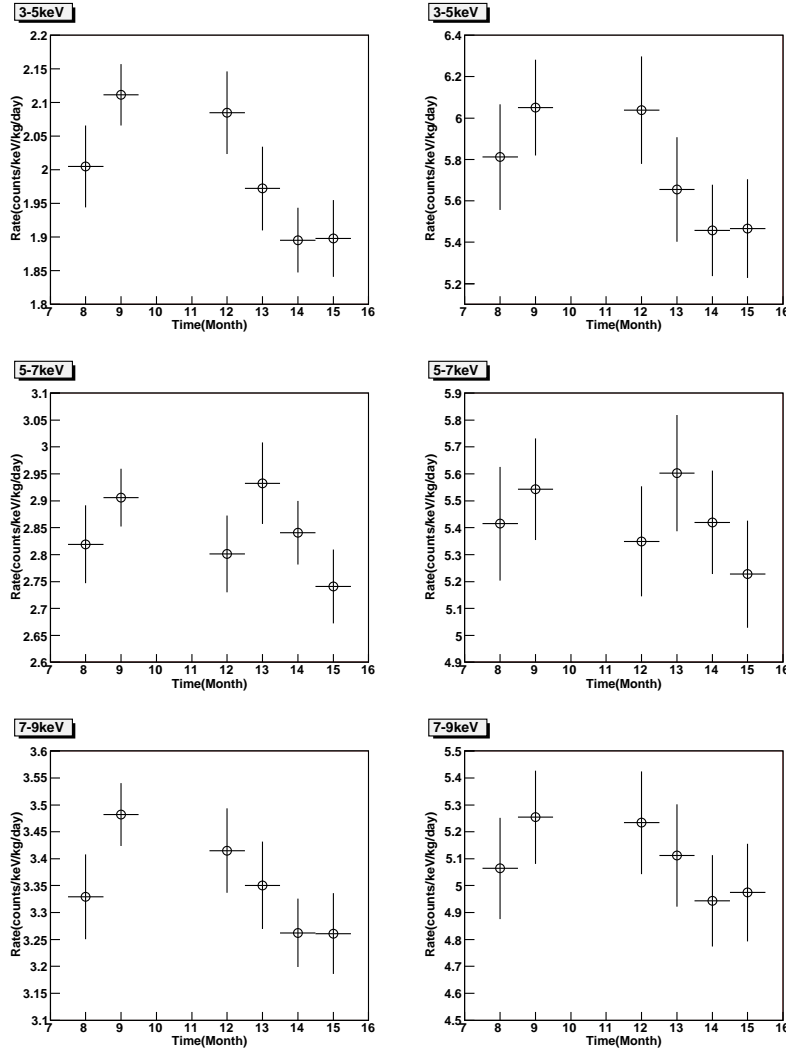
Figure 4.29: Events rate in the particular energy bin as a function of the time elapsed since June 2005. The left plots show events rate after applying events cut and right plots show events rate with efficiency correction. We include only statistical errors in this analysis.
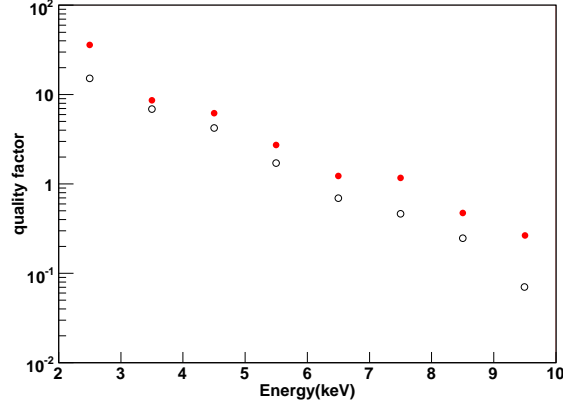
Figure 4.30: Quality factor of S0501A crystal using MT_{fit} (filled circles) and MT_{calc} (open circles).

100 kg of CsI(Tℓ) crystals with 4 CPD background level, the statistical error in one month data become 0.037 CPD level.

4.5 Extraction of nuclear recoil events

Although we used calculated MT (MT_{calc}) value to separate NR from gamma background in the first analysis [97], we used MT value from decay time fit (MT_{fit}) in this thesis. The main advantage of using MT_{fit} is better PSD power than using MT_{calc} (see Fig. 4.30).

Because we used different crystals for the neutron calibration, we need to confirm whether the two different crystals show the same MT characteristics. The gamma calibration data of the test crystal is compared with that of the full size crystal (see the Fig. 4.9, 4.10, 4.11, and 4.12). The MT distribution of Compton electrons in the test crystals are well matched with that of the full size crystals. Agreement between the test crystal and the full size crystal for the Compton electron allows us to use the neutron calibration data from the test crystal as a reference for nuclear recoil signal for the full size crystal.
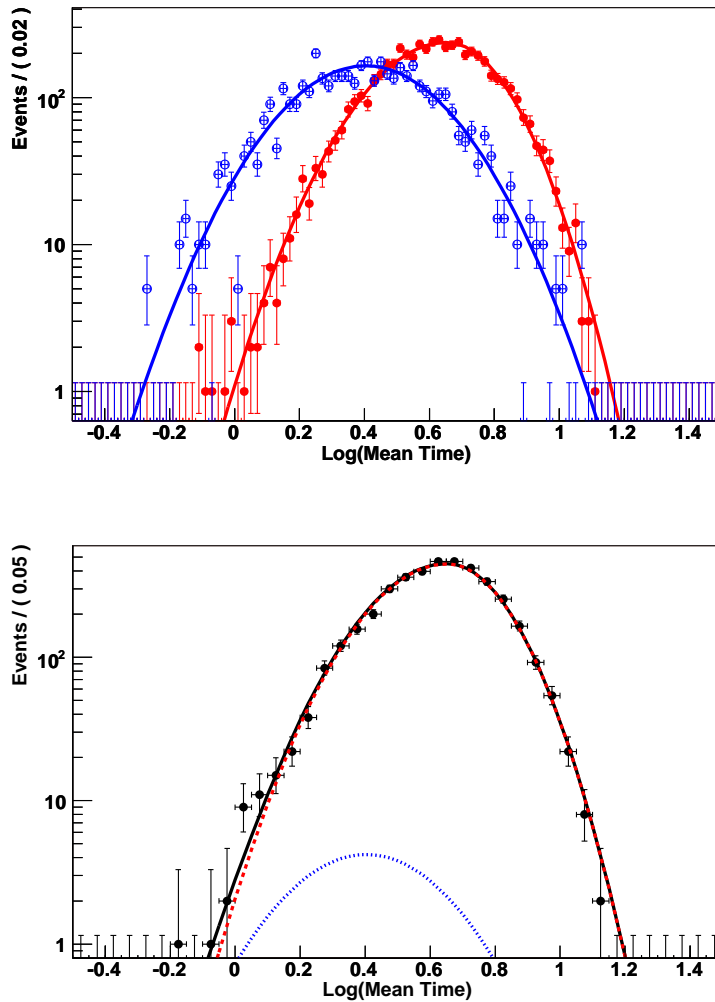
Figure 4.31: Typical $\log(MT_{fit})$ distributions (shown here for S0501A crystal) at energies 9-10 keV for gamma calibration (filled circles) and neutron calibration (open circles) are shown at up plot. The down plot shows an example of extraction of NR events for 9-10 keV events of 0501A crystal with electron recoil and nuclear recoil components. Where dashed line shows electron recoil components, dotted line shows nuclear recoil components, and solid line shows best fit curve.

A slight MT difference is adjusted by the assumption of a constant $R_\tau = \tau_n/\tau_e$ [128], where τ_n is the MT of the nuclear recoil and τ_e is the MT of the electron recoil.

For each 1 keV bin data, the $\log(MT_{fit})$ distribution for gammas and neutrons (see Fig. 4.32) were fitted with asymmetric gaussian function which is defined as following equation,

$$PDF(x) = \begin{array}{ll} \frac{1}{1/2(\sigma_L + \sigma_R)} e^{-\frac{1}{2}\left(\frac{x-m}{\sigma_L}\right)^2}, & x < m \\[3mm] \frac{1}{1/2(\sigma_L + \sigma_R)} e^{-\frac{1}{2}\left(\frac{x-m}{\sigma_R}\right)^2}, & x \geq m, \end{array}$$

where σ_L, σ_R, and m are standard deviation of left side, standard deviation of right side, and mean value respectively. For the maximum likelihood fit with unbinned data, we calculate likelihood value as follow:

$$L_i = \prod_{k=1}^{n} PDF_i(x_k), \tag{4.2}$$

where n is total events number in the ith energy bin. Minimization of $-log(L)$ value was applied with the ROOFIT package [131] included in the ROOT package [117] to decide parameters (σ_L, σ_R, and m). The top plot in Fig. 4.31 shows the fit sample for 9-10 keV gamma and neutron calibration data of S0501A crystal with maximum likelihood method using unbinned data. In this process, we can have parameters (σ_L, σ_R, and m) of electron recoil and nuclear recoil reference (PDF function). Then, we define the likelihood of data with an assumption that all of WIMP search data are composed with nuclear recoil signals and electron recoil backgrounds.

$$\mathcal{L}_i = \frac{1}{n!} \times exp(-N_{NR,i} - N_{ER,i}) \times \prod_{k=1}^{n} \left[N_{NR,i} PDF_{NR,i}(x_k) + N_{ER,i} PDF_{ER,i}(x_k) \right],$$

$$\tag{4.3}$$

where index i denote ith energy bin, $PDF_{NR,i}$, $PDF_{ER,i}$, $N_{NR,i}$, and $N_{ER,i}$ are PDF function of nuclear recoil, PDF function of electron recoil, yield of nuclear recoil, and yield of electron recoil for ith energy bin respectively.
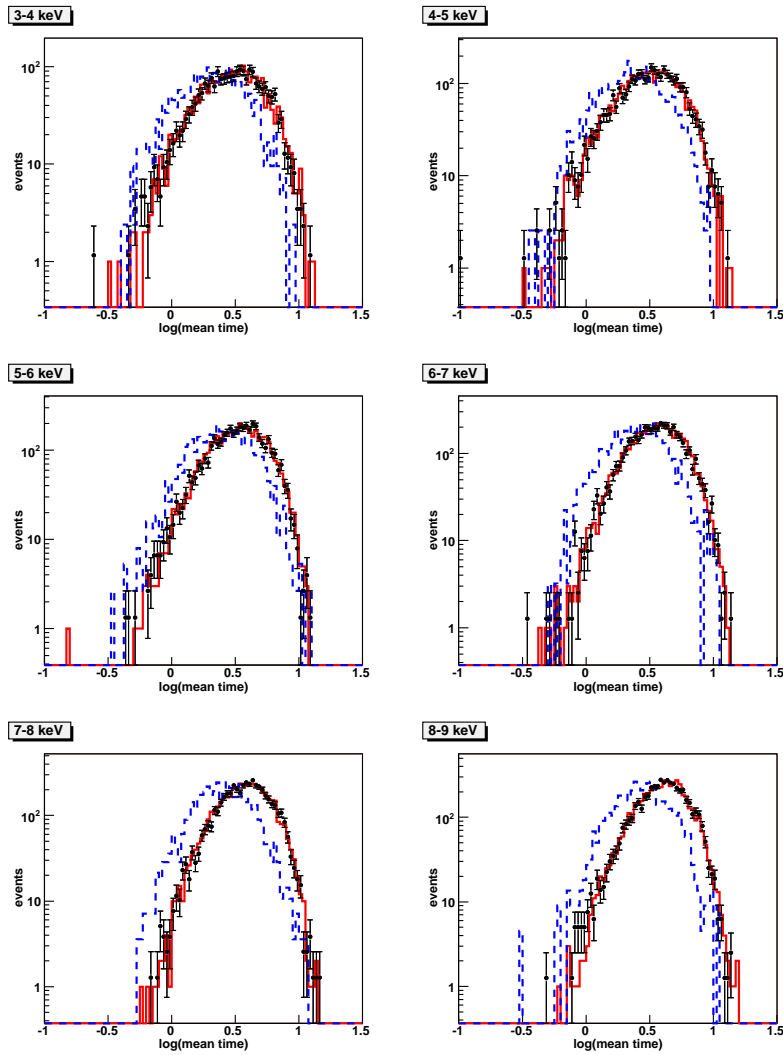
Figure 4.32: MT spectrum of WIMP search data (filled circles) for S0501A crystal is compared with gamma calibration data (solid line) and neutron calibration data (dashed line).

The maximum likelihood fit to extract $N_{NR,i}$ is applied. This is equivalent to minimize

$$F = -log(\mathcal{L}) = N_{NR} + N_{ER} - \sum_{k=1}^{n} log\left(N_{NR,i} PDF_{NR,i}(x_k) + N_{ER,i} PDF_{ER,i}(x_k)\right).$$
(4.4)

The minimizing with minuit package is applied to extract $N_{NR,i}$. Fig. 4.33, 4.34, 4.35, and 4.36 show the $-log(\mathcal{L})$ value as a function of N_{NR} for each energy bin with adjustment the minimum value as zero. Once F is minimized to F_0 with $N_{NR} = N_{NR}^0$, we can estimate δN_{NR} (the error of parameter N_{NR}) by the formula,

$$F_{min}^i(N_{NR}^0 + \delta N_{NR,i}) - F_0 = \frac{1}{2},$$
(4.5)

where $F_{min}^i(n)$ is the minimum of $F(N)$ when N_i is fixed at n.

The WIMP search data is well matched with electron recoil data as one can see in Fig. 4.32, the extracted $N_{NR,i}$ is consistent with zero. We summarized the result from NR extraction in Table 4.7 for S0501A crystal.

Table 4.7: WIMP search data and extracted NR with its error for S0501A crystal with 1147 kg·day exposure.

Energy	Data	NR	Statistical Error	Normalized rate (CPD)
3-4 keV	1885	26.6	64.2	0.065 ± 0.156
4-5 keV	2509	-62.0	85.6	-0.122 ± 0.170
5-6 keV	2969	-8.3	83.2	-0.014 ± 0.141
6-7 keV	3450	79.3	73.8	0.124 ± 0.117
7-8 keV	3647	-55.4	59.8	-0.080 ± 0.087
8-9 keV	3901	64.5	63.6	0.094 ± 0.095
9-10 keV	3999	45.3	32.6	0.063 ± 0.047
10-11 keV	4322	30.3	40.5	0.041 ± 0.055

The extracted NRs are corrected with efficiency calculated in the previous section. Also we normalize this result with CPD unit using total exposure (see Table 4.2). In Table 4.7, we also give normalized rate with efficiency
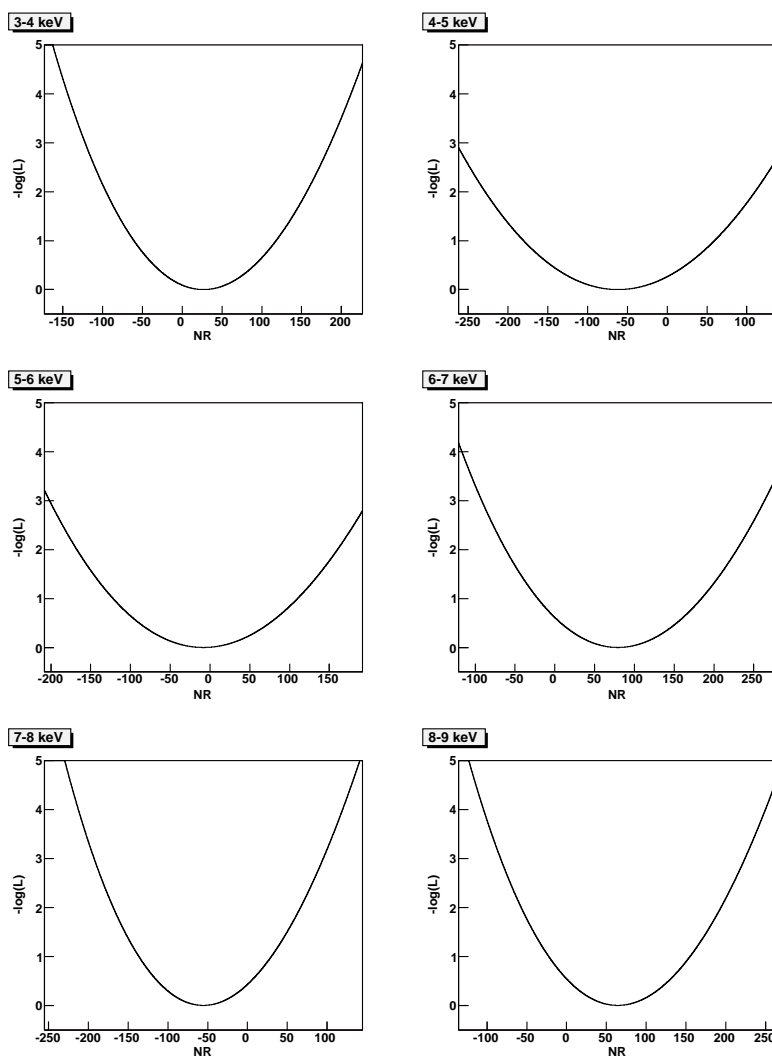
Figure 4.33: $-Log(\mathcal{L})$ values as a function of N_{NR} for S0501A crystal. The central value, which was adjusted as 0, was chosen by best fit points.
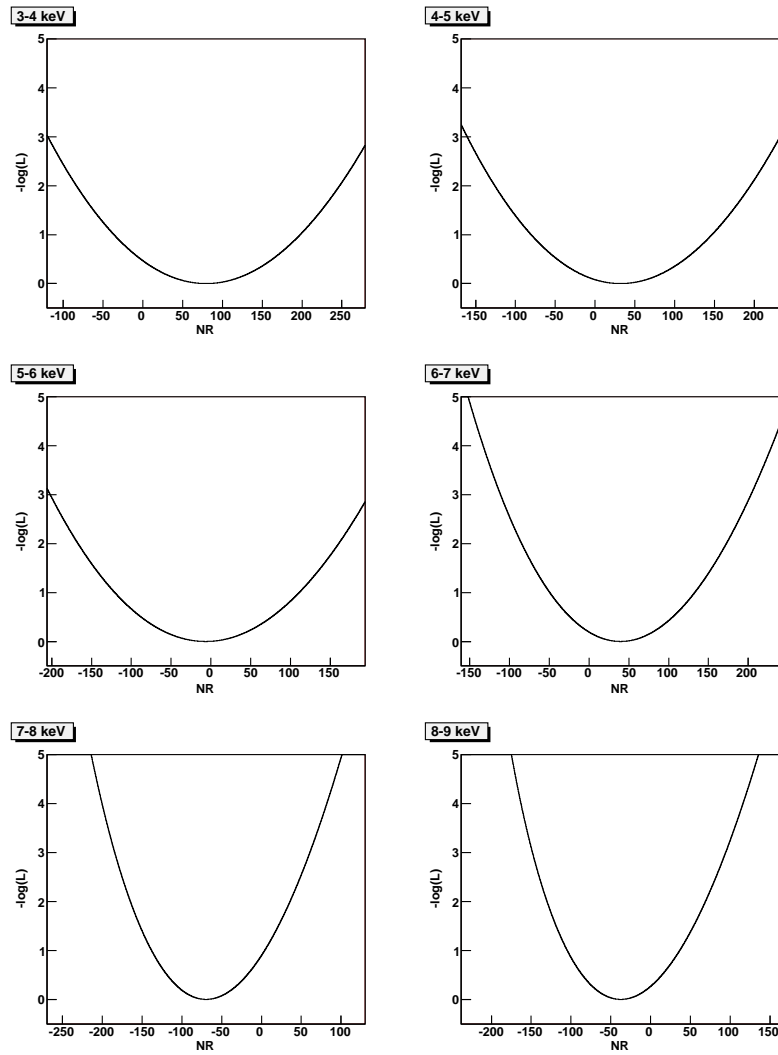
Figure 4.34: $-Log(\mathcal{L})$ values as a function of N_{NR} for S0501B crystal. The central value, which was adjusted as 0, was chosen by best fit points.
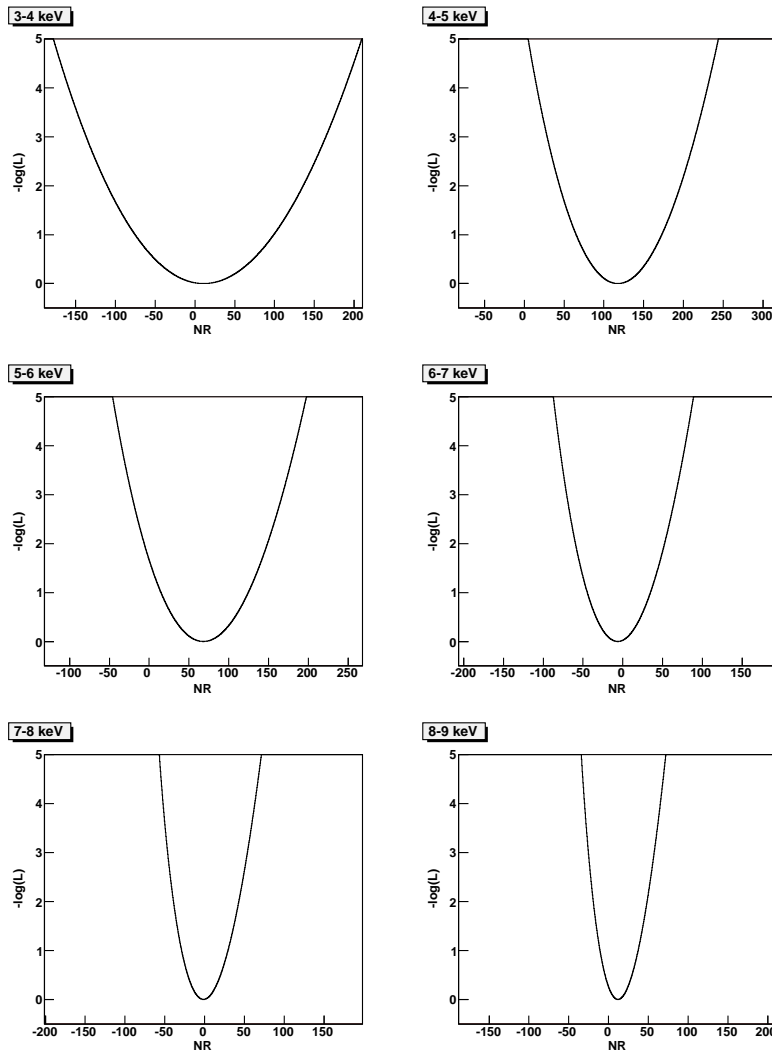
Figure 4.35: $-Log(\mathcal{L})$ values as a function of N_{NR} for B0510A crystal. The central value, which was adjusted as 0, was chosen by best fit points.
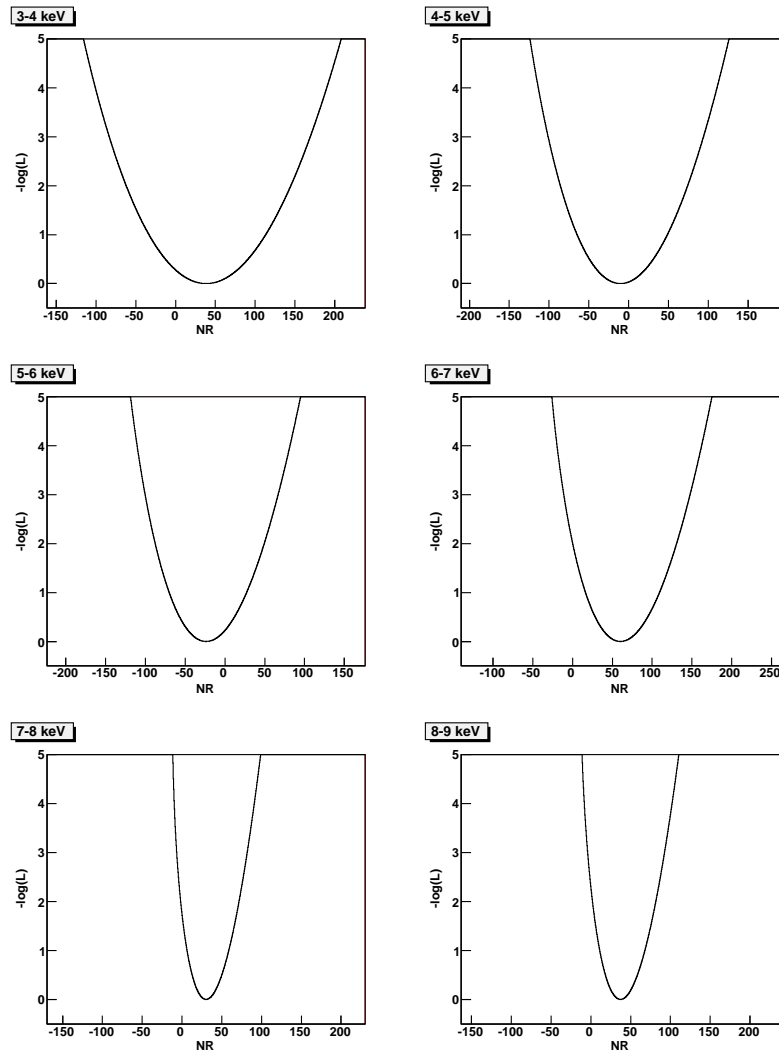
Figure 4.36: $-Log(\mathcal{L})$ values as a function of N_{NR} for B0510B crystal. The central value, which was adjusted as 0, was chosen by best fit points.
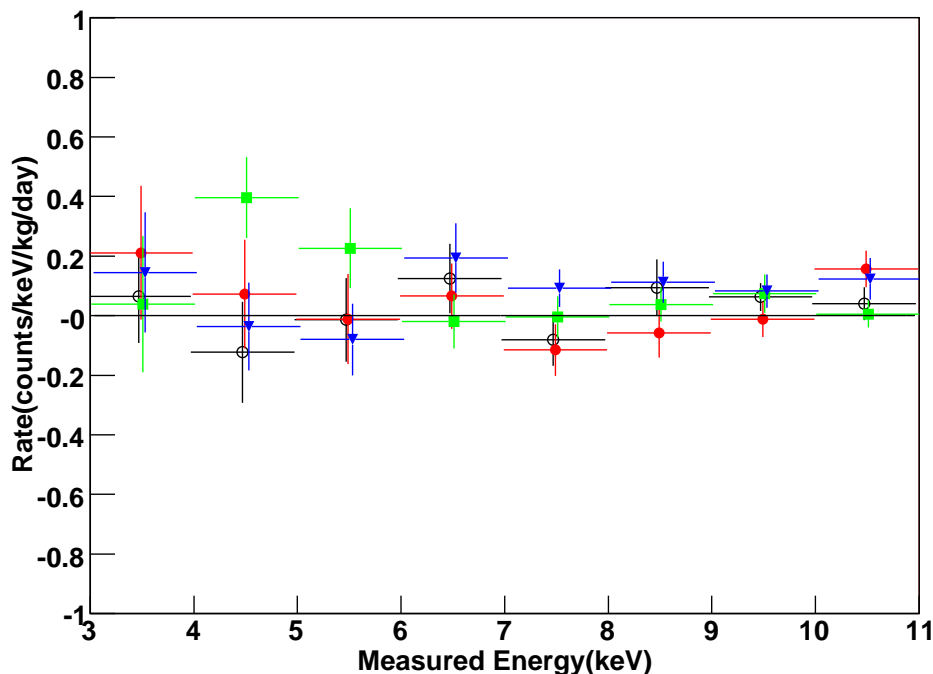
Figure 4.37: Estimated nuclear recoil rates for S0501A (open circles), S0501B (filled circles), B0510A (filled squares), and B0510B crystal (filled triangles). The points are shifted with respect to each other x-axis to avoid overlapping. We include only statistical error.

correction for S0501A crystal. We performed same process for the other crystal. Fig. 4.37 shows the extracted NR rate for each crystal with efficiency correction. In this figure, we consider only statistical error.

To prove zero consistence of NR events, we calculate χ^2 value as follow,

$$\chi^2 = \sum_{i=3}^{10} \frac{(NR_i - 0)^2}{(\delta_{NR_i})^2}.$$

The χ^2/ndf value for each crystal are obtained as 0.77, 1.30, 1.65, and 1.73 for S0501A, S0501B, B0510A, and B0510B crystal respectively. Therefore, our result is consistent with zero.

4.5.1   Systematic error

Because we use fixed parameters for electron and nuclear recoil model from
the best fit with finite calibration samples, we need to consider the fit sys-
tematics using variation of fit parameter. Before we vary the parameter with
1σ deviation, we check the correlation between parameters. In the 3-4 keV
bin γ calibration data of S0501A crystal, we find out the error matrix for
each parameters (mean (m), left side standard deviation (σ_L), and right side
standard deviation (σ_R)) as follow:

$$\begin{pmatrix} 1.84 \times 10^{-4} & 9.97 \times 10^{-5} & -9.82 \times 10^{-5} \\ 9.97 \times 10^{-5} & 8.15 \times 10^{-5} & -4.91 \times 10^{-5} \\ -9.82 \times 10^{-5} & -4.19 \times 10^{-5} & 6.93 \times 10^{-5} \end{pmatrix}.$$

In this matrix, we can find the correlation coefficient ($\rho_{m-\sigma}$) between m and
σ_L (σ_R) as follow:

$$\rho_{m-\sigma_L} = 0.82, \quad \rho_{m-\sigma_R} = -0.87.$$

As one can see in this result, the strong correlation between m and σ_L (σ_R)
is found. This correlation can be seen in the correlation contour between
parameters (see Fig. 4.38).

   We vary the mean value by 1σ. In this process, we consider the correlation
of σ_L and σ_R to the mean value. To have best value of σ_L and σ_R, we
performed fit with asymmetric gaussian function at a fixed mean value. Filled
circles in Fig. 4.38 shows the σ_L and σ_R plot when we vary the mean value
in the 1σ deviation.

   Fig. 4.39 and Fig. 4.40 shows the variation of result as a function of m
for gamma and neutron calibration data. The maximum change of NR_i is
accounted as systematic error from each calibration data sample.

   Because we use different crystal to take neutron calibration data, we need
to consider variation of neutron calibration data. With a good agreement of
electron recoil between two different crystals, we use the neutron calibration
from the test crystal as a reference for nuclear recoil signal for the full size
crystal. But, a slight MT difference was adjusted by assuming that the
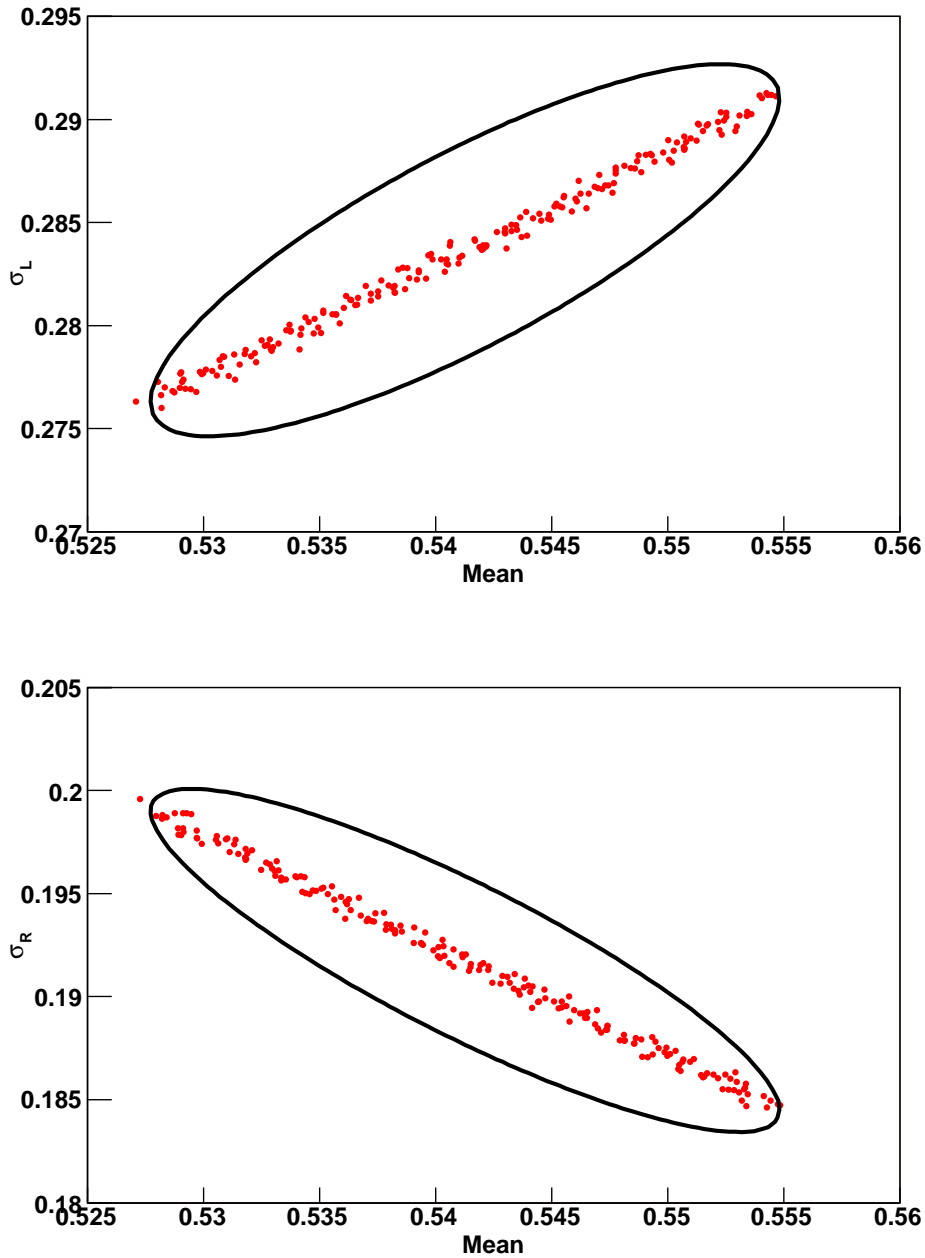
Figure 4.38: Correlation contour between m, σ_L (up plot) and σ_R (down plot) is shown. The ellipse shown corresponds to the contour for $-Log(\mathcal{L}_{max}) + \frac{1}{2}$. We vary the m with 1σ variation using best fit point of σ_L and σ_R (filled circles).
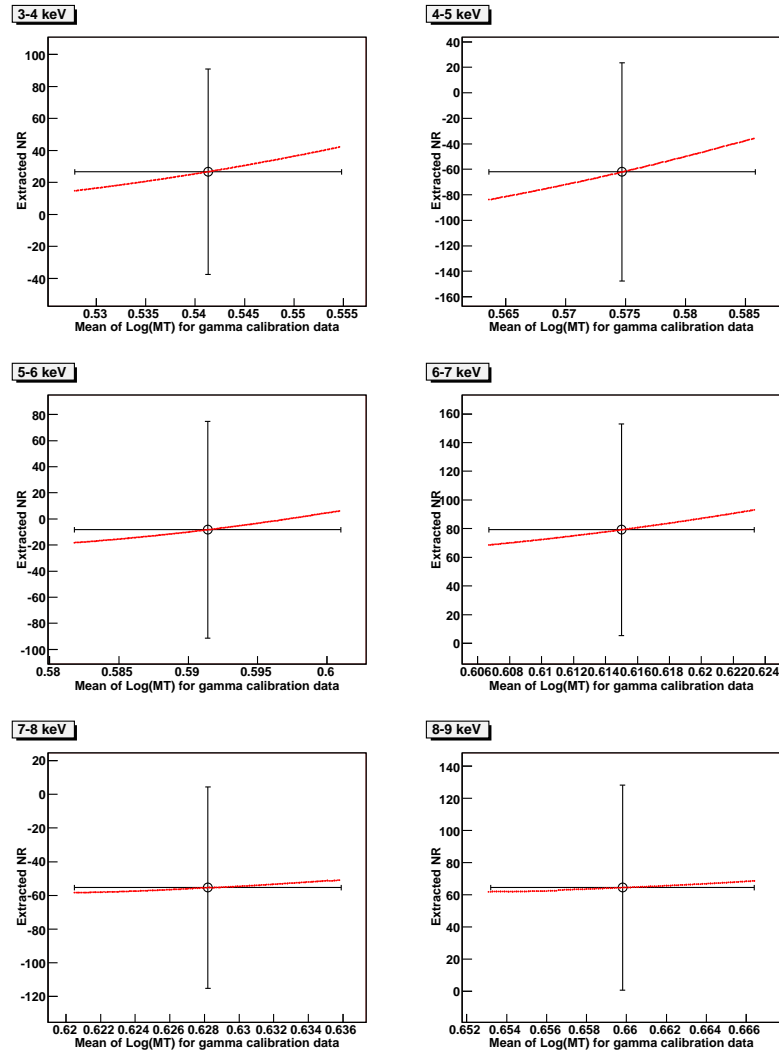
Figure 4.39: The center point shows the log(MT) value of gamma from best fit as a function of extracted NR with error bar. The another line shows the variation of result using variation of Log(MT) value of gamma calibration data. This plot obtained from S0501A crystal data.
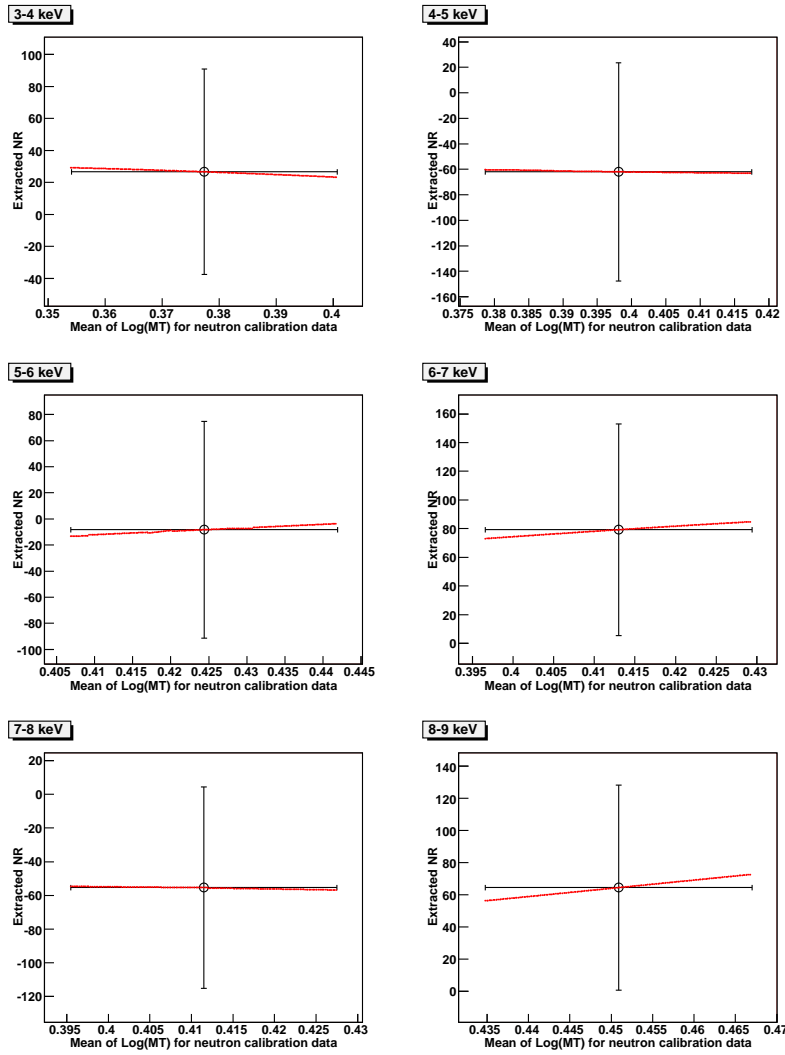
Figure 4.40: The center point shows the log(MT) value of neutron calibration data from best fit as a function of extracted NR with error bar. The another line shows the variation of result using variation of Log(MT) value of neutron calibration data. This plot obtained from S0501A crystal data.

ratio between the mean time of neutron and that of gamma, $R_\tau = \tau_n/\tau_e$, is constant. To make a proof of this assumption, we calculate R_τ value for two of small size crystal which are used to take neutron calibration data. In Table 4.8, the result of R_τ is shown for each crystal and temperature condition. The deviation is standard deviation for four of data points. We use central value of R_τ using correspondent data set. And we consider the variation of nuclear recoil data with one standard deviation of R_τ value. The maximum change of NR_i is taken as systematic error of this difference.

Table 4.8: R_τ value for sample crystals in the different temperature condition.

Energy	Tl006		B0504S		Deviation
	0°	Room temp.	0°	Room temp.	
3-4 keV	0.88	0.92	0.90	0.93	0.022
4-5 keV	0.84	0.90	0.88	0.87	0.026
5-6 keV	0.85	0.85	0.83	0.83	0.012
6-7 keV	0.82	0.82	0.82	0.81	0.005
7-8 keV	0.81	0.83	0.77	0.78	0.021
8-9 keV	0.78	0.80	0.77	0.77	0.006
9-10 keV	0.75	0.77	0.74	0.73	0.010
10-11 keV	0.75	0.76	0.72	0.73	0.015

In Table 4.9, we summarize fit systematic for S0501A crystal. Total value of fit systematics comes from quadratic sum of three components. In the 3-4 keV energy bin, total fit systematic error is 25.4 % of statistical error.

We performed same process for the other crystals to extract NR. The extracted NR are normalized in CPD unit using efficiency and total data amounts. Table 4.10 shows the result of NR extraction. We denote statistical error and systematical error separately. Typically systematic errors are about 20 % of statistical errors.

DAMA claim the observation of signal 0.0200 ± 0.0032 CPD in the 2-6 keV energy range [64]. Considering 9 % quenching factor of I, the recoil energy range is from 22.2 keV to 66.7 keV. Total events rate in this energy

Table 4.9: Extracted NR, statistical error, and fit systematics for S0501A crystal with 1147 kg·day exposure. In the fit systematic, we account systematics from finite γ calibration data sample, finite neutron calibration data sample, and different crystal uses to take neutron calibration data.

Energy	NR	Statistical	Fit Systematic			
			total	γ	neutron	different crystal
3-4 keV	26.6	64.2	16.3	15.7	2.6	3.9
4-5 keV	-62.0	85.6	33.0	26.5	1.6	19.5
5-6 keV	-8.7	83.2	15.9	14.6	4.7	4.2
6-7 keV	79.3	73.8	15.5	14.0	5.7	3.7
7-8 keV	-55.4	59.8	11.5	4.5	0.9	10.6
8-9 keV	64.5	63.6	9.0	3.6	8.2	0.4
9-10 keV	45.3	32.6	4.9	4.5	0.6	1.7
10-11 keV	30.3	40.5	8.3	6.5	4.4	2.9

range is 0.0768 ± 0.0124 counts/kg/day. Typically 6.5 % events from WIMP nucleus interaction contribute to annual modulation signal. Therefore, 1.18 ± 0.19 counts/kg/day events can be measured in the detector for 22.2 keV to 66.7 keV recoil energy range if DAMA is correct. The 3σ region of DAMA signature is calculated as 0.60 - 1.75 counts/kg/day. To compare DAMA result with ours, we consider 3-7 keV measured energy range which consistent with 20.2 - 72.5 keV recoil energy range. Total events rate is calculated as 0.28 ± 0.16 counts/kg/day. Therefore, the 90 % CL upper limit from our data, which is 0.54 counts/kg/day, fully reject 3σ region from DAMA signal.

4.6   Result

Table 4.10: Extracted NR for crystals are shown. We denote two kind error. The first and second errors are the statistical and systematical errors respectively.

Energy	Crystal			
	S0501A	S0501B	B0510A	B0510B
3-4 keV	0.07±0.16±0.04	0.21±0.22±0.06	0.039±0.23±0.05	0.15±0.20±0.05
4-5 keV	-0.12±0.17±0.07	0.07±0.18±0.05	0.40±0.14±0.11	-0.04±0.14±0.03
5-6 keV	-0.01±0.14±0.03	-0.01±0.15±0.04	0.23±0.13±0.02	-0.08±0.12±0.03
6-7 keV	0.12±0.12±0.02	0.07±0.11±0.01	-0.02±0.09±0.01	0.19±0.12±0.01
7-8 keV	-0.08±0.09±0.02	-0.12±0.09±0.04	-0.00±0.07±0.01	0.09±0.06±0.01
8-9 keV	0.09±0.95±0.01	-0.06±0.08±0.03	0.04±0.06±0.01	0.11±0.07±0.01
9-10 keV	0.06±0.05±0.01	-0.01±0.06±0.01	0.07±0.06±0.01	0.08±0.06±0.01
10-11 keV	0.04±0.05±0.01	0.16±0.06±0.02	0.01±0.05±0.02	0.12±0.07±0.01

4.6.1 WIMP nucleus cross section

Assuming a Maxwellian dark matter velocity distribution with a spherical halo model discussed in Chapter 2, the total WIMP rate is obtained as

$$
\begin{aligned}
R(E_0, E_\infty) &= \frac{k_0}{k_1} \int_0^\infty dE_R \left\{ c_1 \frac{R_0}{E_0 r} e^{-c_2 E_R/E_0 r} - \frac{R_0}{E_0 r} e^{-v_{esc}^2/v_0^2} \right\}, \\
R_0 &= 5.47 \left(\frac{GeV/c^2}{m_\chi} \right) \left(\frac{GeV/c^2}{m_t} \right) \left(\frac{\sigma_0}{pb} \right) \left(\frac{\rho_\chi}{GeV/c^2/cm^3} \right) \left(\frac{v_0}{km/s} \right), \\
E_0 &= \frac{1}{2} m_\chi v_0^2, \qquad r = \frac{4 m_\chi m_t}{(m_\chi + m_t)^2}, \quad (4.6)
\end{aligned}
$$

where R_0 is the event rate per kg·day for $v_E = 0$ and $v_{esc} = \infty$, $v_{esc} = 650$ km/sec is the local Galactic escape velocity of WIMP, m_t is the mass of a target nucleus, $\rho_\chi = 0.3$ GeV/cm^3 is local dark matter density, $v_0 = 220$ km/sec is a Maxwell velocity parameter, and c_1, c_2 are constants as discussed in Chapter 2. And the cross section of WIMP with the target nucleus can be rewritten as

$$
\sigma = \sigma_0 F^2(E_R), \quad (4.7)
$$

where σ_0 is WIMP nucleus cross section at zero recoil energy and $F(E_R)$ is the nuclear form factor. In order to estimate the expected event rates for each energy bin, we use MC simulation. The MC simulation based on GEANT4 [108] takes into account the recoil energy spectrum, form factor (spin dependent, independent), the QF, and the light transportation to the PMTs. Then the simulated events are analyzed in the same way as the data except for the applying any analysis cuts. The energy is tuned to provide good agreement with the calibration data using 59.5 keV γ-rays from the ^{241}Am source. Fig. B.5 shows good agreement between Monte Carlo and calibration data for the energy distribution. The Monte Carlo generated electron equivalent energy (E_{ee}) distributions for several WIMP masses are shown in Fig. B.6, B.7, B.8, and B.9 (see more detail in Appendix B).

From the rate of nuclear recoil in each energy bin, we can estimate total WIMP rate in comparison with the simulated E_{ee} distribution for each WIMP mass by the following relation. We defined χ^2 value to estimate WIMP signal rate for each m_χ,

$$
\begin{aligned}
\chi^2 &= \sum \frac{(NR_{E_k} - p0 \cdot N_{E_k, m_\chi})^2}{\delta NR_{E_k}^2}, \\
R(E_0, E_\infty)_{m_\chi} &= p0 \cdot N_{total, m_\chi},
\end{aligned}
\tag{4.8}
$$

where NR_{E_k} and N_{E_k, m_χ} are the measured nuclear recoil rate and the simulated WIMP events for each energy bin E_k respectively and, N_{total} is the total number of WIMP events generated by simulation.

Fig. 4.41 shows an example of this fit for S0501A crystal in the case of spin independent interaction. From this fit, we can find $R(E_0, E_\infty)_{m_\chi}$ value in Eq. 4.8.

Table 4.11 shows the extracted $R(E_0, E_\infty)$ value for each WIMP mass using ^{133}Cs isotope with S0501A crystal data. Because its results are consistent with zero for each WIMP mass, we can set the 90 % CL upper limit of $R(E_0, E_\infty)$ using Ref. [133] method. With Eq. (4.6) and Eq. (4.8), we can convert the total rate of WIMP ($R(E_0, E_\infty)$) to the WIMP-nucleus cross section ($\sigma_{\chi Cs, I}$) for each WIMP mass. In Table 4.11, we calculate 90 % CL
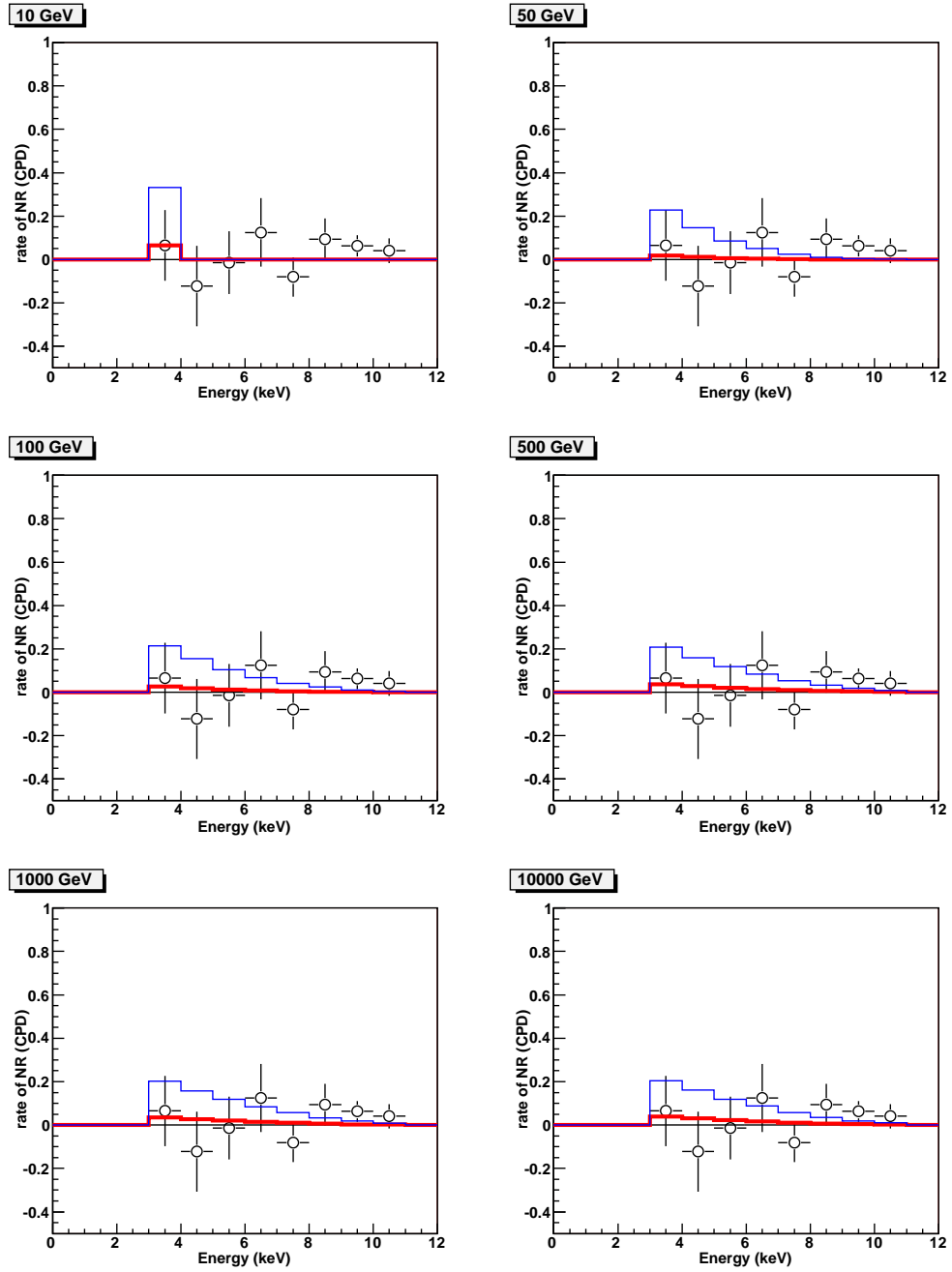
Figure 4.41: Extracted NRs (filled circles) are fitted with simulated WIMP signal shapes (thick solid line) for each WIMP mass. We indicate 90 % CL upper limit (thin solid line). This example use S0501A crystal result for spin independent interaction.

Table 4.11: The extracted $R(E_0, E_\infty)_{m_\chi}$ values with S0501A crystal in the case of spin independent interaction. We use ^{133}Cs isotope for this calculation. The 90 % CL upper limits were calculated with Feldman and Cousin method [133].

WIMP mass	$R(E_0, E_\infty)$ (/kg/day)	90 % CL	$\sigma_{\chi Cs}$ (90%CL)	$\sigma_{\chi n}$ (90%CL)
10 GeV	4414 ±11117	22646	1.8 pb	2.1×10^{-2} pb
50 GeV	8 ±37.3	69	0.0065 pb	5.1×10^{-6} pb
100 GeV	32 ±95	188	0.018 pb	5.8×10^{-6} pb
500 GeV	512 ±1066	2262	0.22 pb	2.2×10^{-5} pb
1000 GeV	1205 ±2538	5368	0.52 pb	4.3×10^{-5} pb

upper limit on WIMP-nucleus (especially Cs) cross section.

4.6.2 Systematic uncertainty in the MC generation

When we generate MC simulation of WIMP signal shape, we need to consider the quenching factor for nuclear recoil signal as discussed in Section 3.4.3. The quenching factor for CsI(Tℓ) crystal from previous experiment was shown in Fig. 4.42 (a). We use best fit curve from all data point as quenching factor of the CsI(Tℓ) crystal. We consider the error of parameters of fit. The dotted-dashed line in Fig. 4.42 shows lower bound of quenching factor and dashed line shows uppper bound.

To account systematics from quenching factor, we include deviation of quenching factor in the simulation process. Fig. 4.42 (b) shows the simulated energy spectrum using different quenching factor. The upper bound in the WIMP-nucleus cross section comes from lower quenching factor. We calculate $R(E_0, E_\infty)$ using each simulated spectrum. We obtain $R_{center} = 8.33 \pm 37.3$ and $R_{up} = 6.97 \pm 47.4$ using only Cs which give 90 % CL upper limit on WIMP-nucleon cross section as 5.12×10^{-6}pb and 6.25×10^{-6}pb respectively.
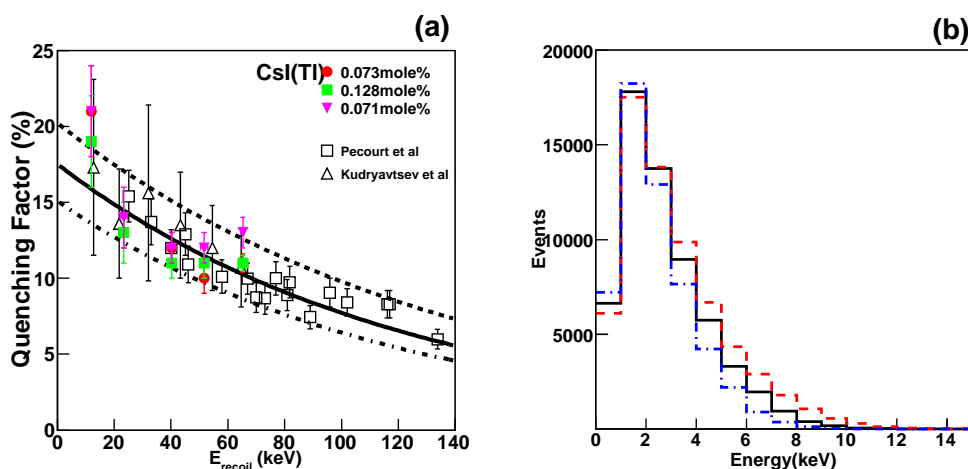
Figure 4.42: (a) Quenching factor of CsI(Tℓ) crystals from our beam test and other experiments was shown. (b) Simulated energy spectrum from WIMP-nucleus interaction in CsI(Tℓ) crystal with 50 GeV WIMP mass. The solid line show the case using best fit curve from quenching factor measurement. Using 1σ variation of best fit curve, we can consider upper bound (dashed line) and lower bound (dashed-dotted line).

We have 12.2 % limit increasing with quenching factor variation. We assign this value as systematic uncertainty from quenching factor.

As one can see in Fig. 4.6, maximum 5 % gain variation is happened for each PMT in the whole data taking period. Although we adjusted gain variation already, we consider about 2.5 % gain variation as systematics which is averaged variation of PMT gain. We generate MC simulation of WIMP-nucleus interaction with 2.5 % gain change as one can see in Fig. 4.43. We calculate 90 % CL upper limit on WIMP-nucleon cross section with different simulation spectrum. As a result, we have 1.5 % limit increasing with gain variation.

Another considering systematic uncertainty to generate MC simulation is energy resolution. The only possible parameter to change energy resolution
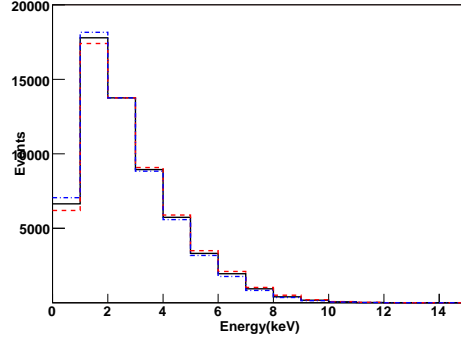
Figure 4.43: Simulated energy spectra from WIMP-nucleus interaction in the CsI(Tℓ) crystal with 50 GeV WIMP mass with different gain factors. The solid line shows the case using calculated gain factor from 59.54 keV peak. The dashed line and dashed-dotted line indicate using 2.5 % changes (up and down) of gain factor.

Table 4.12: Energy resolution at 59.54 keV for each crystal (%)

Crystal	S0501A	S0501B	B0510A	B0510B
Data	9.2±0.2	9.0±0.2	8.1±0.1	8.2±0.1
MC	8.3±0.1	8.6±0.1	7.6±0.1	7.7±0.1

in the MC is light yields of crystal. We use measured results (Table 4.1) of light yield to generate MC. Energy resolution of 59.54 keV peak from the MC and the data are shown in Table 4.12. As one can see in this table, the MC have a little bit better resolution than the real data. In the case of S0501A, the deviation of resolution at 59.54 keV is 0.9 %. We consider this deviation as systematic uncertainty. We generate MC simulation with tuning energy resolution with 59.54 keV data. Fig. 4.44 shows energy spectrum of WIMP-nucleus interaction with tuning of energy resolution with 59.54 keV data and light yield. The deviation of 90 % CL upper limit from this difference is 1.1 %.
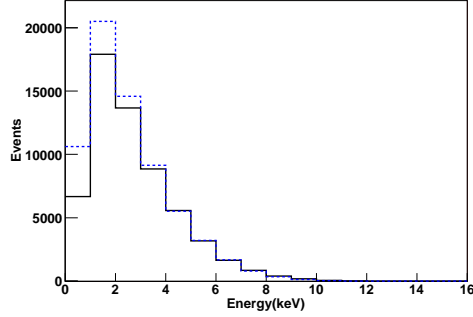
Figure 4.44: Simulated energy spectra from WIMP-nucleus interaction in the CsI(Tℓ) crystal with 50 GeV WIMP mass with different resolutions. The solid and dashed line are using the resolution of 59.54 keV peak from calibration data and using the light yield of crystal respectively.

The total systematic error from MC simulation is obtained from quadratic sum of each systematic error.

$$\sigma_{sys-MC} = 12.3 \ \%$$

Table 4.13: Summary of systematic errors. We consider the contribution to 90 % CL upper limit of each component.

Contents	Systematic Errors
Efficiency	0.3 %
Fit Systematic	5.1 %
Quenching Factor	12.2 %
Energy resolution	1.1 %
Energy calibration	1.5 %
Total	13.3 %

Systematic errors contribute to upper limit are summarized in Table 4.13. We calculate each contribution in the 90 % CL upper limit at 50 GeV WIMP mass. Main contribution of systematic error came from the quenching factor.

4.6.3   WIMP nucleon cross section

The WIMP-nucleon cross section can be obtained from WIMP-nucleus cross section by the following equation:

$$\sigma_{W-n} = \sigma_{W-A} \frac{\mu_n^2}{\mu_A^2} \frac{C_n}{C_A}, \tag{4.9}$$

where $\mu_{n,A}$ are the reduced masses of WIMP-nucleon and WIMP-target nucleus of mass number A and $C_A/C_n = A^2$ for spin independent interaction. In Table 4.11, there are calculated result for Cs in the S0501A crystal. The limit on the WIMP-nucleon cross section for each nucleus (Cs,I) can be combined by this expression

$$\frac{1}{\sigma} = \frac{1}{\sigma_{Cs}} + \frac{1}{\sigma_I}. \tag{4.10}$$

The limits from different crystals have been combined using the equation below, taking into account that the data were statistically independent and no positive signal was detected in any of the crystals,

$$\frac{1}{\sigma^2} = \sum_{i=0}^{i=n} \frac{1}{\sigma_i^2}, \tag{4.11}$$

where n is total number of crystals and σ_i is cross section of i-th crystal.

A 90 % CL upper limit on the WIMP-nucleon cross section from CsI for spin independent interaction is shown in Fig. 4.45. The result including systematic error have 13.3 % higher value of 90 % CL upper limit than the result considering only statistical error at 50 GeV WIMP mass. Our result is compared with the limits obtained from NAIAD experiments [73] which used NaI(Tℓ) crystals and same PSD method, CRESST [67] (long dashed line), EDELWEISS [66] (double dotted-dashed line), and CDMS [65] which gave the current best limit. Although the amount of data used to get our limit is less than that of NAIAD, we achieved a more stringent limit than that of NAIAD due to the better pulse shape discrimination and lower recoil energy threshold. Most of DAMA 3-sigma region on the WIMP-nucleon cross section for spin independent interaction is excluded by our result. This is

the first exclusion of DAMA result with crystal detector. Also our limit can start search of MSSM parameter space expected by Ref. [68].

We also set limits on spin dependent cross section because ^{133}Cs and ^{127}I have spin expectation values (Table 4.14). To understand WIMP signature in CsI(Tℓ) crystal with spin dependent interaction we need to know spin dependent form factor of ^{133}Cs and ^{127}I isotopes. The spin dependent form factor can be written as follow [55, 134]:

$$F^2(q) = \frac{S(q)}{S(0)},$$

where

$$S(q) = a_0^2 S_{00}(q) + a_1^2 S_{11}(q) + a_0 a_1 S_{01}(q),$$

$$a_0 = a_p + a_n, \quad a_1 = a_p - a_n.$$

The a_p and a_n are effective WIMP-proton and WIMP-neutron coupling. In the model independent calculation [55], we consider pure proton ($a_n = 0$) or pure neutron ($a_p = 0$) case. Therefore spin dependent form factor can be written as follow:

$$F^2(q)_{proton} = \frac{S_{00}(q) + S_{11}(q) + S_{01}(q)}{S_{00}(0) + S_{11}(0) + S_{01}(0)},$$

$$F^2(q)_{neutron} = \frac{S_{00}(q) + S_{11}(q) - S_{01}(q)}{S_{00}(0) + S_{11}(0) - S_{01}(0)}.$$

Various shell model calculations were done for various elements for spin dependent form factor and spin expectation values [135, 136, 137, 138, 139]. In the case of I, calculation from Ressel [135] using Bonn A potential was usually used because the calculated magnetic momentum with this interaction is well matched with experiment result. The calculation for ^{133}Cs was given by Toivanen [140]. He used similar shell model. The calculated magnetic momentum is 2.192 and is in better agreement with experimental data, 2.582, than other pervious calculations [136]. The understanding of spin dependent form factor for ^{133}Cs and ^{127}I isotopes give us to know signature in the CsI(Tℓ) crystal. Therefore we can generate signature of WIMP nucleus

scattering in CsI(Tℓ) crystal by using MC simulation (Fig. B.6, B.7, B.8, and B.9).

We perform the same analysis process with spin independent calculation for spin dependent WIMP-nucleon cross section. A little different thing comes from Eq. 4.9. With model independent calculation in Ref. [55] and Section 2.2, we have the following relation:

$$\frac{C_A}{C_{n,p}} = 4/3 < S_{n,p} >^2 (J+1)/J,$$

for proton and neutron. Where $< S_{n,p} >$ is spin expectation value of neutron and proton in the nuclei (^{133}Cs (IBFM [141]), ^{127}I (Bonn A [135])) as one can see in Table 4.14. Therefore we have limit on WIMP-proton (and neutron) cross section for spin dependent interaction as one can see in Fig. 4.46.

Table 4.14: Value of $< S_p >$ and $< S_n >$ for Cs and I

Isotope	J	$< S_p >$	$< S_n >$
Cs	7/2	-0.370	0.003
I	5/2	0.309	0.075

We can express our spin dependent result (Fig. 4.46) in the $a_p - a_n$ plane to explore more general models. From Eq. 2.10, Eq. 2.11, Eq. 2.13, and Eq. 2.14, we have following relation:

$$\left(\frac{a_p}{\sqrt{\sigma_p}} \pm \frac{a_n}{\sqrt{\sigma_n}} \right)^2 \leq \frac{\pi}{24 G_F^2 \mu_p^2}. \tag{4.12}$$

A sign of inequality of this equation is originated from auxiliary assumption that total WIMP-nucleus cross section is dominated by one type of nucleon (proton or neutron), to calculate limit on WIMP-proton (σ_p) and WIMP-neutron (σ_n) cross section (see the more detail in Ref. [55, 76]). Already we calculated σ_p and σ_n as a function of WIMP mass, we can draw allowed region in the a_p - a_n plane for fixed WIMP mass. As one can see in Fig. 4.47 our limit contributes to constrain the region higher than 50 GeV.

Although CDMS result give much lower limit on the WIMP-nucleon spin independent interaction and the WIMP-neutron spin dependent interaction, KIMS gives the best limit on the WIMP-proton spin dependent interaction in the region that WIMP mass is higher than 30 GeV. Furthermore, our result excluded DAMA 3σ region for all of interaction in the higher than 20 GeV WIMP mass. The possibility of mixed case of SD and SI interaction [64, 142] is excluded by our result for higher than 20 GeV WIMP mass. Furthermore if we consider HEP constraint ($M_\chi > 39$ GeV) [143], our result fully exclude DAMA 3σ region.
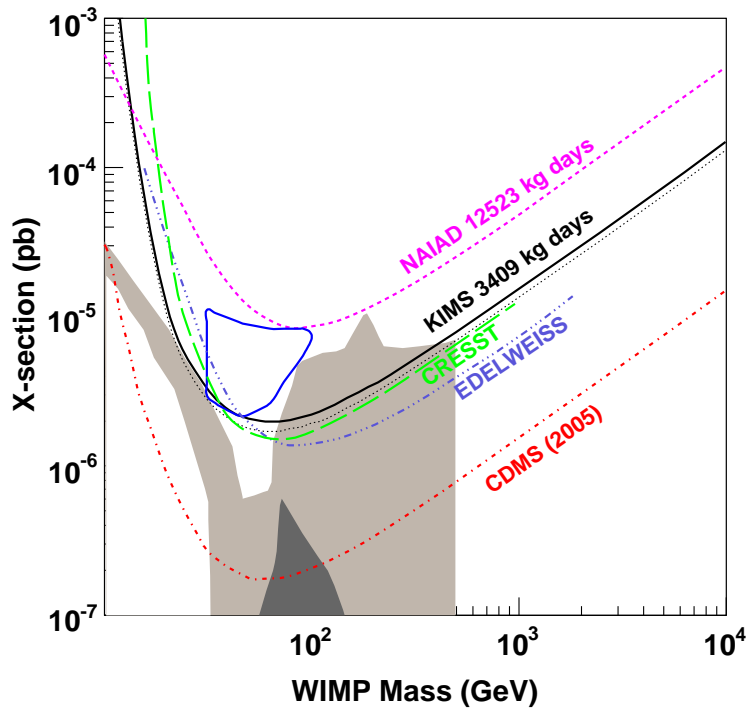
Figure 4.45: The KIMS limit on a WIMP-nucleon cross section for a spin independent interaction with 3409 kg·days exposure with considering of systematic uncertainty (solid line) and only considering statistical error (dotted line), DAMA positive [63] annual modulation signal (closed contour), NAIAD limit [73] with 12523 kg·days exposure (dashed line), CRESST [67] (long dashed line), EDELWEISS [66] (double dotted-dashed line), and CDMS limit [65] (dotted-dashed line) are presented. Supersymmetric models allow the largest shaded region [68], and the smaller shaded region [69]

199
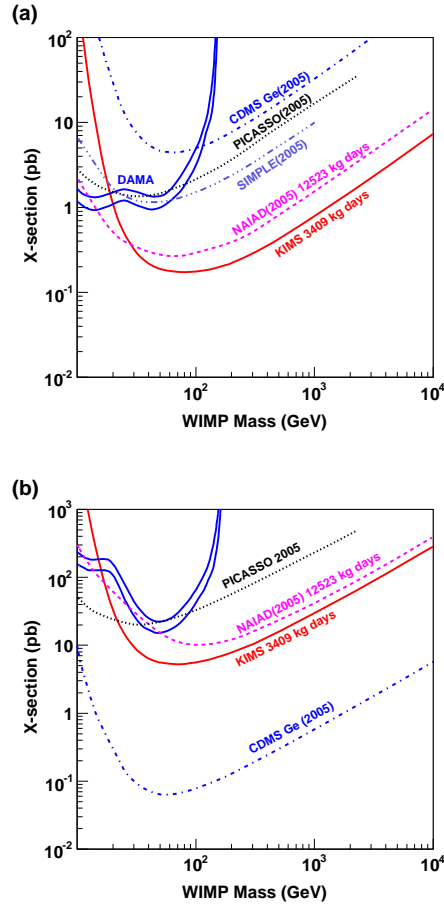
Figure 4.46: The KIMS limit on a WIMP-nucleon cross section for a spin dependent interaction (solid line) of pure proton (a) and pure neutron (b) case with 3409 kg·days exposure considering systematic uncertainty, DAMA positive [76] annual modulation signal (closed contour), NAIAD limit [73] with 12523 kg·days exposure (dashed line), CDMS Ge limit [72] (dotted-dashed line), PICASSO [74] (dotted line), SIMPLE [75] (dashed-double-dotted line), and DAMA 3 σ region [71] (closed curve) are presented.
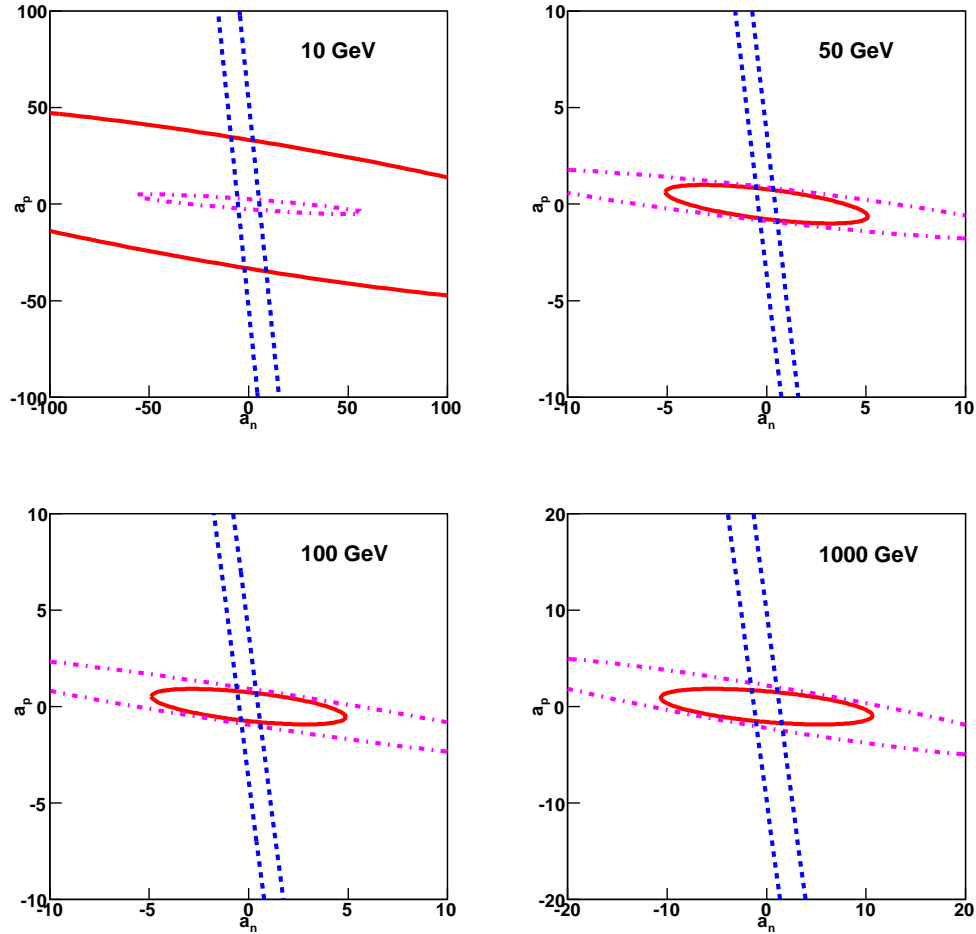
Figure 4.47: Allowed region in the a_p - a_n plane (90% CL) by KIMS experiment (solid line) for each WIMP mass (10 GeV, 50 GeV, 100 GeV, and 1000 GeV). Also we present CDMS (dashed line) and NAIAD (dotted dashed line) result (We calculated allowed region from WIMP-proton and WIMP-neutron cross section limit for other experiments).

Chapter 5

Conclusions

The KIMS collaboration had constructed Y2L to search WIMP dark matter. Shielding structure is well established. The KIMS collaboration have developed low background CsI(Tℓ) crystals for the WIMP search. As a result we could grow thirteen full size low background crystals which have 4 or 6 CPD background level.

With four crystals we had taken WIMP search data with 3409 kg·day exposure at the 0°C condition. Under the assumption of an isothermal dark matter (WIMP) distribution with a density 0.3 GeV/c^2/cm^3 and a characteristic velocity $v_0 = 220 km/s$, and mean Earth velocity $v_E = 232 km/s$, the 90 % CL WIMP exclusion limit on WIMP-nucleon interaction is obtained as shown in Fig. 5.1, 5.2. Our limit excludes most of the DAMA 3σ signal region in the spin independent interaction. Also, we exclude DAMA 3 σ region on WIMP-proton and WIMP-neutron spin dependent interaction for higher than 20 GeV WIMP mass. With HEP constraint, we fully exclude DAMA 3σ region in the all of interaction. Especially in the WIMP-proton interaction, we have the best result for the WIMP mass higher than 30 GeV. We also present out constraint on the a_p - a_n plane higher than 30 GeV (Fig. 5.3). Also, our result start searching of parameter space of MSSM model.

We are now upgrading for massive run with thirteen full size low back-

ground crystals. In this setup we can explore the annual modulation signal as well. We also will work to reduce internal background of CsI(Tℓ) crystals by the testing the condition of recrystallization and purification of water. The current experimental setup is designed to accommodate about 250 kg of CsI(Tℓ) crystals without any modification. We expect that the background rate will be reduced to the level of approximately 2 CPD or less for the new powder produced with purer water. The projected limit for 1 year of data taken with 250 kg crystals of 2 CPD background is shown in Fig. 5.1, 5.2, and 5.3 in comparison with the current best limit set by CDMS. In this setup, we can start search of parameter space from CMSSM. The future results from KIMS experiment will give better understanding of confliction between DAMA and other experiments.
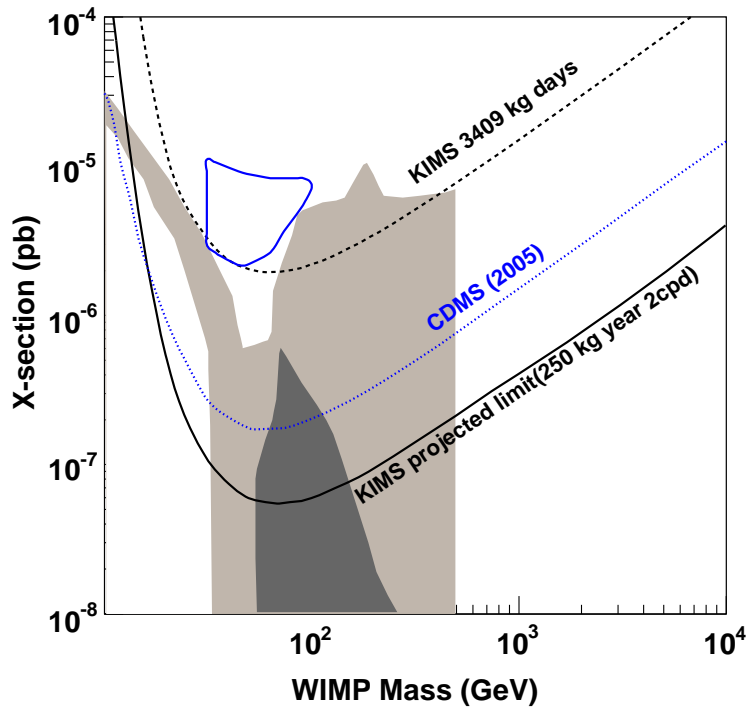
Figure 5.1: The KIMS projected limit on WIMP-nucleon cross section for spin independent interaction with 250 kg·year exposure of 2 CPD background level (solid line) is presented with current limit with 3409 kg·day exposure (dashed line). We also shows current best limit set by CDMS group (dotted line) and allowed region with MSSM (largest shaded region) and CMSSM (smaller shaded region).
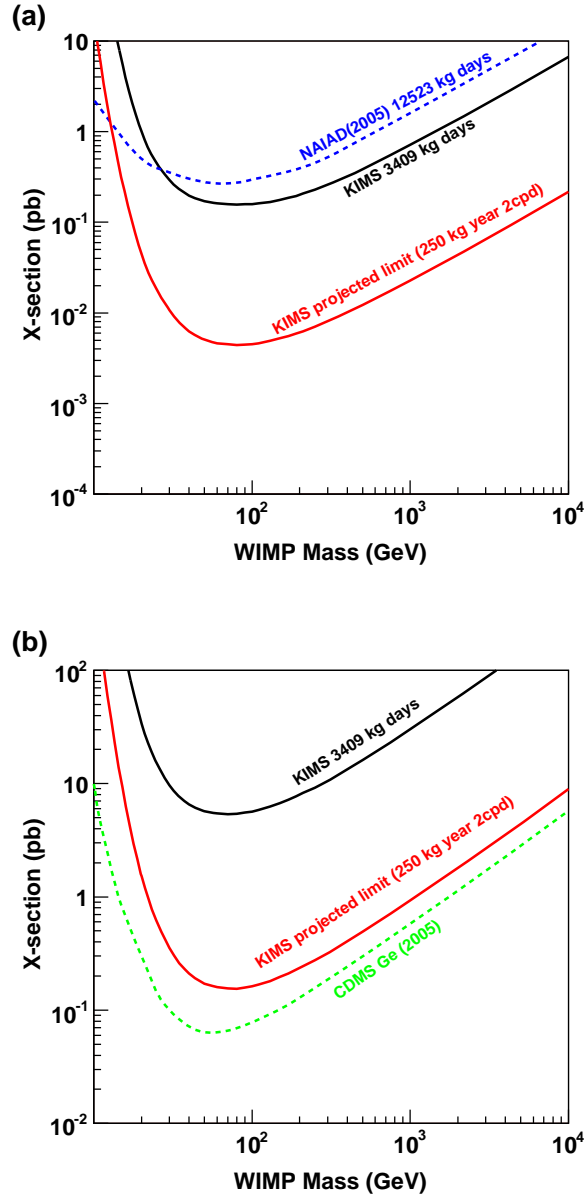
Figure 5.2: The KIMS projected limit on WIMP-nucleon cross section for spin dependent interaction with 250 kg·year exposure of 2 CPD background level (solid line) of pure proton interaction (a) and pure neutron interaction (b) are presented with current limit with 3409 kg·day exposure. We also present best limit set by other experiments.
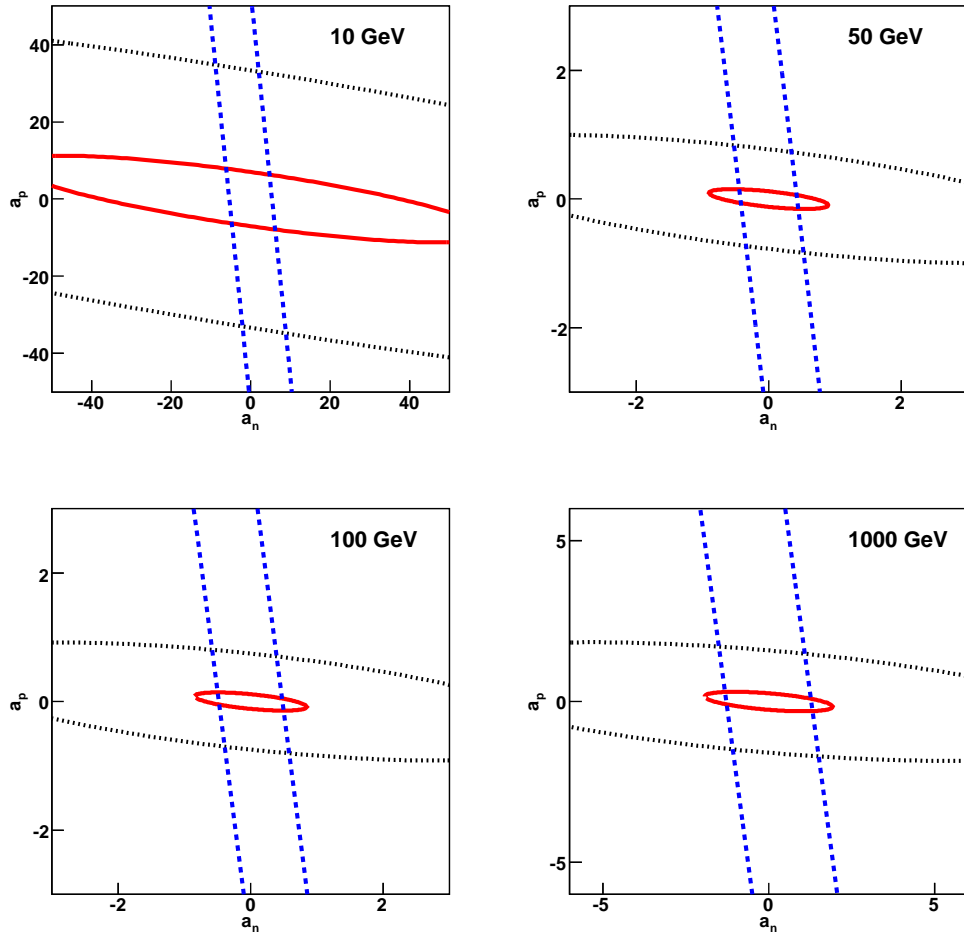
Figure 5.3: Allowed region in the a_p - a_n plane (90% CL) by KIMS projected limit with 250 kg·year exposure of 2 CPD background level (solid line) for each WIMP mass (10 GeV, 50 GeV, 100 GeV, and 1000 GeV) are presented with CDMS region (dashed line) and our current result (dotted line) using 3409 kg·day exposure.

Appendix A

First physics data and its analysis

A.1 Data

The underground data in the shield with S0406 crystal (8 x 8 x 23 cm^3) was taken from July 2004 to September 2004. During two month period we took 237 kg·day's WIMP search data. Fig. A.1 shows data accumulation as a function of real times. In this period we took calibration data of low energy gamma with ^{137}Cs and energy calibration data.

During data accumulation period, we monitored the temperature and humidity with environment monitoring system (see Section 3.8) as one can see in Fig A.2. Temperature variation in the main shield was within 0.1 °C. Relative humidity was well controlled as about 0 %. Also, the high voltages for the PMTs were very stable.

The gamma and neutron calibration data for the reference shape were also taken. The γ calibration data was obtained with WIMP search crystal (S0406 crystal) by a ^{137}Cs source in the copper chamber of Y2L. Identical setup and conditions as for the WIMP search data were used. We irradiated S0406
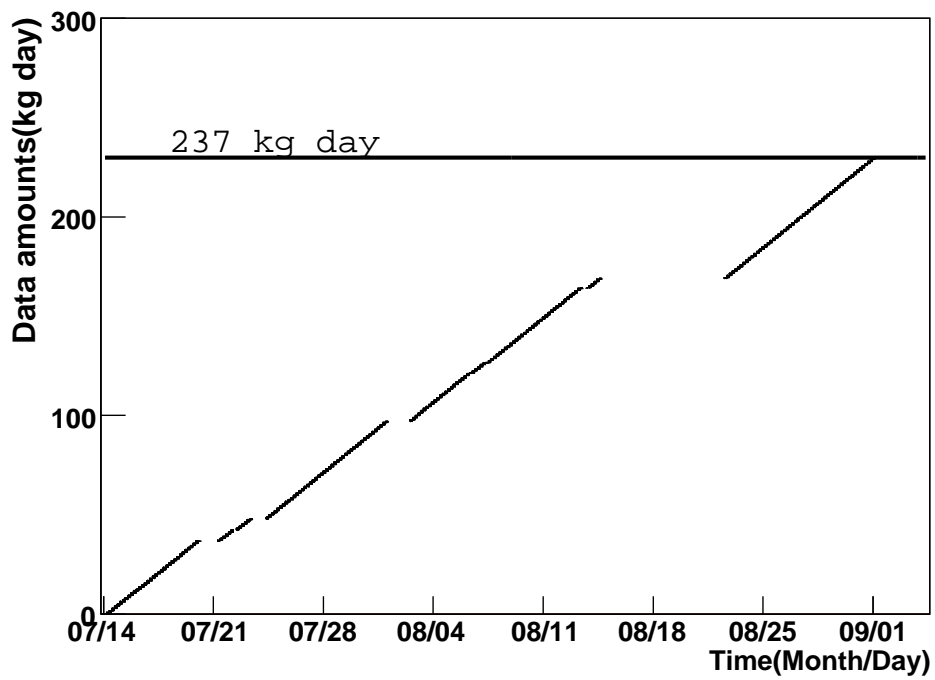
Figure A.1: Accumulated data amounts as a function of time. Total data amounts are 237 kg·days.
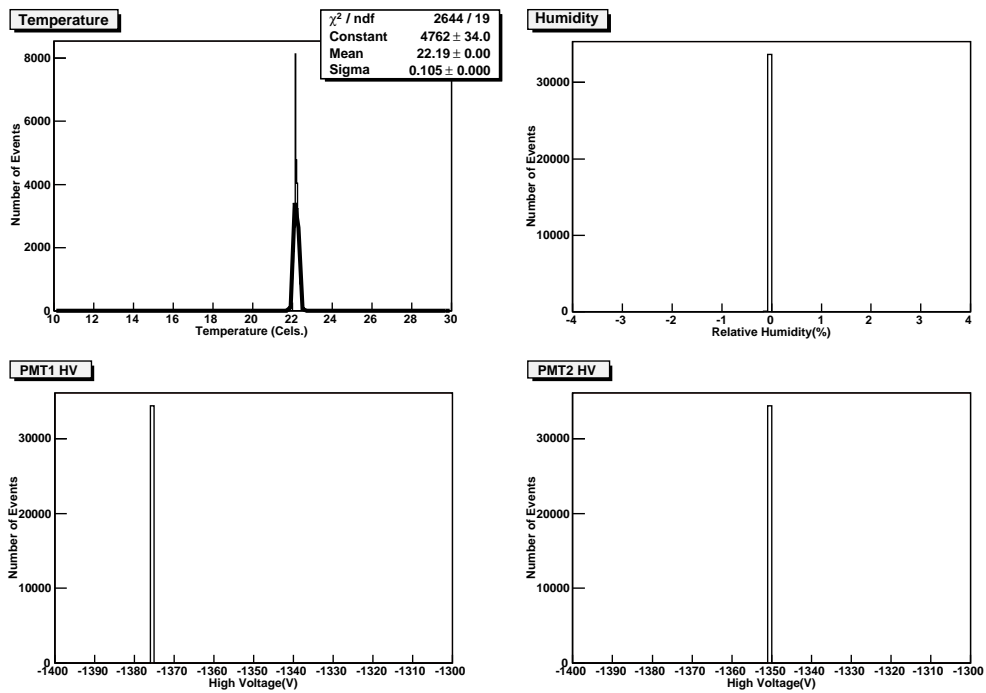
Figure A.2: During data accumulation period for S0406 crystal (From 14 July 2004 to 1 Sep. 2004), temperature and humidity variation of main shield and high voltage of PMTs are shown.
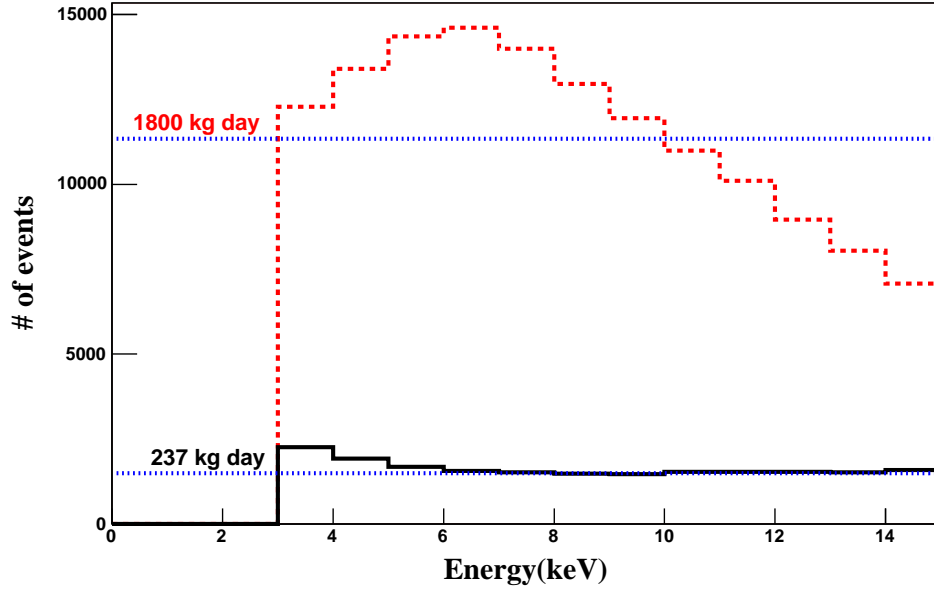
Figure A.3: Energy spectrum of WIMP search data (solid line) and low energy electron calibration data (dashed line). We indicate data amounts using dotted line with assumption of 6.3 cpd background level.

crystal during about one week. We took low energy electron recoil events by Compton scattering of high energy γs. As one can see in Fig. A.3, data amount of γ calibration is about 10 times larger than WIMP search data with about 5 times smaller data taking period.

Neutron calibration was performed with small size test crystal (Tl006). We irradiated test crystal to neutrons from a 300 mCi Am-Be source at the neutron calibration facility in the Seoul National University. About 1 month period we took neutron calibration data equivalent to 800 kg·day WIMP search data (see the Fig. A.4)
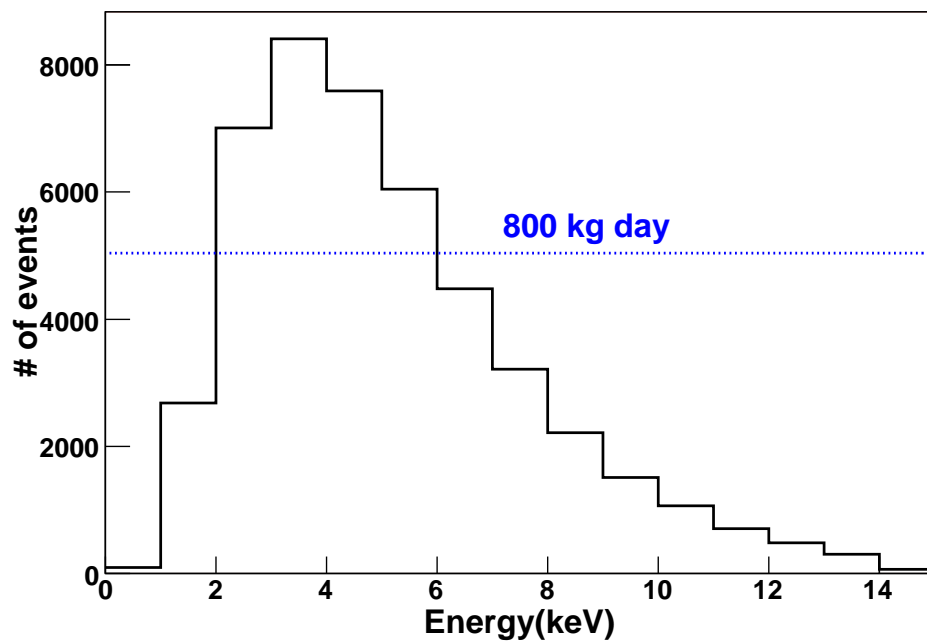
Figure A.4: Energy spectrum of neutron calibration data (solid line). We indicate data amounts using dotted line with assumption of 6.3 cpd background level.
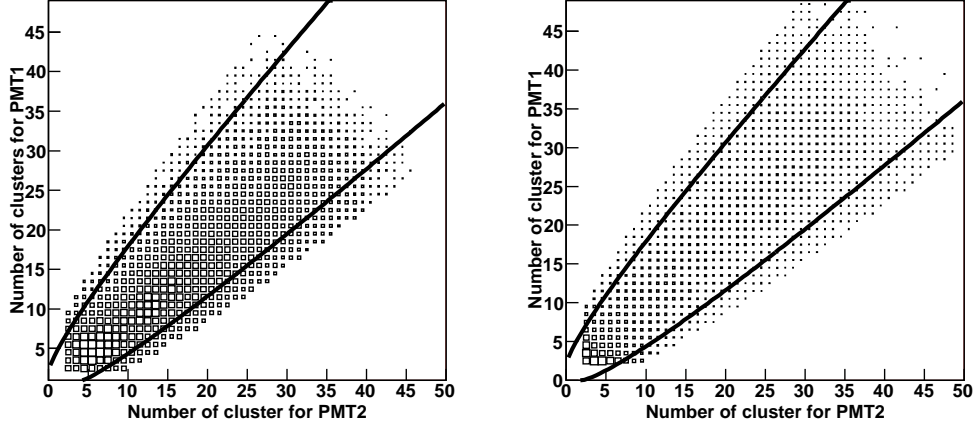
Figure A.5:   Left plot shows scattered plot of number of clusters for each PMTs using low energy γ calibration data. Solid line shows 3 σ selection band. Right plot shows same figure for WIMP search data.

A.2   Event selection

A.2.1   Rejection of asymmetry events

To eliminate side effect, we construct 3 σ selection band with low energy gamma calibration data as one can see in Fig A.5. Efficiency calculated with γ calibration data are about 95 % for events from 3 keV to 10 keV.

A.2.2   First SPE position (t0) cut

The energy deposition from high energy γ, α, and muon are too big. Therefore the tail photons from pretriggered high energy events can be triggered as low energy events. To reduce these events, we give 8 msec dead time after each trigger. But, a few events from tail of high energy events can be recorded. Because trigger condition of CsI(Tℓ) crystal require more than five

photoelectrons within 2 μsec with 6.8 μsec trigger position, we can request longer than 4.8 μsec of first SPE. But, about 5 % events have random SPE within 4.8 μsec because of random noise originated from PMT dark current or crystal as we discussed in Section 4.2.3. Therefore we use second SPE as a cut of tail events. We request time difference between second clusters of each PMT within 2 μsec for coincidence.

Because γ calibration data have too much tail events, we use ^{55}Fe calibration data to calculate efficiency of this cut. Fig. A.6 shows the spectrum of second SPE position and time difference between second SPE of each PMT. Efficiency calculated from ^{55}Fe data shows more than 99 %. Because WIMP search data have much lower trigger rate than calibration, efficiency of WIMP search data for tail cut is much larger than ^{55}Fe calibration data. Therefore we consider calculated efficiency from ^{55}Fe source as systematic error.

Due to 8 msec dead time for each trigger, we must consider the total dead time of WIMP search data. Fraction of dead time of data can be calculated as follow:

$$f_{dt} = TR \times DT,$$

where f_{dt}, TR, and DT are fraction of dead time of WIMP search data, trigger rate, and dead time of one event respectively. Because trigger rate of WIMP search data is approximately 0.6 Hz, the fraction of dead time of WIMP search data is about 0.5 %.

A.2.3   PMT noise rejection

To understand PMT noise we took PMT noise events which were taken from the same system and trigger condition without the CsI(Tℓ) crystal in the copper chamber. The distance between the two PMTs is maintained equal to that for the crystal-attached set-up. In the 25.4 days data, equivalent to 167 kg·days WIMP search data was obtained.

PMT sparks which have correlation between clusters usually induces an abnormally big cluster. Therefore, the charge of the biggest cluster and the
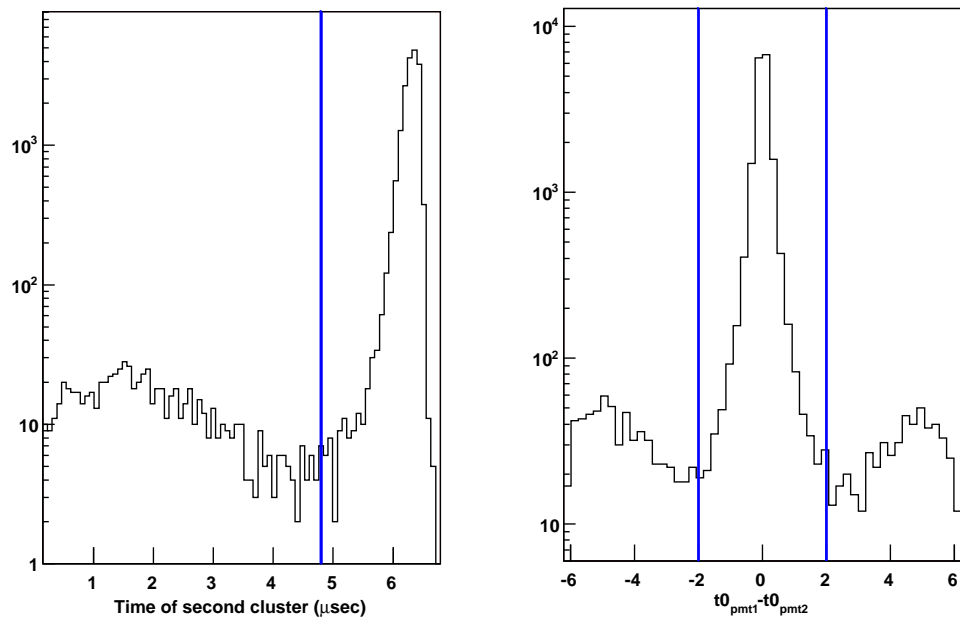
Figure A.6: Left: Position of second clusters with low energy gamma data from ^{55}Fe source and cut position (solid line). Right: Time difference between second clusters of each PMT and cut.

mean charge of clusters for each event can be used to reject these events. We construct a good event-band using the Compton scattering events from ^{137}Cs and they are compared with PMT noise events in Fig. A.7. In the all of PMT noise data (167 kg· days data) only two events passed all the cuts with the 3 keV energy threshold. We conclude that the PMT background after the cuts is negligible. The same cut is applied to the Compton scattering data and the efficiency was found to be approximately 60 % at the energy range from 3 keV to 11 keV as shown in the Table. A.1.

A.2.4 Efficiency

Table A.1: Calculated efficiency with cut list using γ calibration data for S0406 crystal

Energy	Cut list			total
	asymmetry cut	PMT noise cut	dead time	
3-4 keV	95.3 ± 0.82 %	63.7 ± 0.90 %		60.4 ± 0.88 %
4-5 keV	95.3 ± 0.83 %	63.8 ± 0.90 %		60.5 ± 0.84 %
5-6 keV	94.3 ± 0.80 %	62.5 ± 0.86 %		58.6 ± 0.79 %
6-7 keV	93.8 ± 0.78 %	61.4 ± 0.81 %	99.5 ± 0.1 %	57.3 ± 0.77 %
7-8 keV	93.9 ± 0.77 %	60.9 ± 0.82 %		56.8 ± 0.79 %
8-9 keV	93.5 ± 0.79 %	59.8 ± 0.84 %		55.6 ± 0.80 %
9-10 keV	93.1 ± 0.81 %	60.1 ± 0.88 %		55.7 ± 0.84 %

Because we did not take calibration data of nuclear recoil for S0406 crystal, γ calibration data with ^{137}Cs were used to calculate efficiency. The cut list and efficiency for each keV bin events of γ calibration data are shown in Table A.1. But we need to know the efficiency of WIMP (nuclear recoil events) which are obtained from the neutron calibration data with the test crystal. Because we use different crystal for neutron calibration data, the
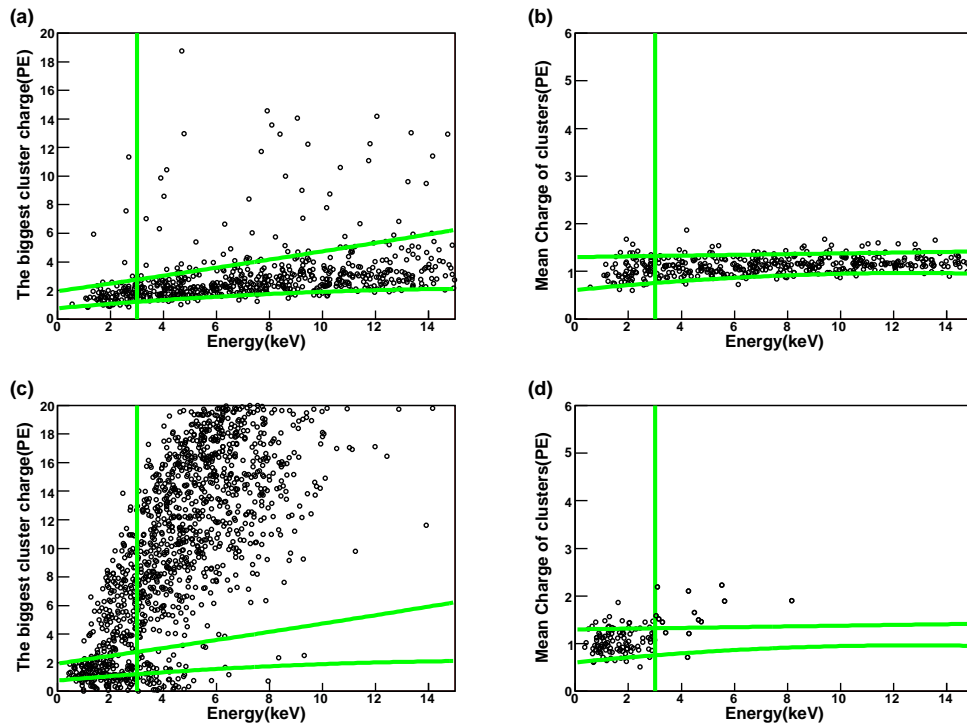
Figure A.7: (a) shows the charge of the biggest cluster normalized by the MPV of the SPE charge obtained from Fig. 4.5 fit, versus the measured energy for the calibration data with a ^{137}Cs γ source. Two solid lines indicate -1.65σ(lower solid line) and 1.28σ band (upper solid line). The vertical line is the 3keV analysis threshold. (b) is a similar spectrum for the mean charge of clusters for the events within the signal band of the biggest cluster cut. (c) and (d) are the corresponding plots for PMT noise events.

crystal difference was considered as systematic uncertainty. With γ calibration data for two crystals, one for S0406 crystal and the other for test crystal, we obtained efficiency values for each keV bin as one can see in Fig. A.8 with same cut listed in Table A.1. About 10 % efficiency difference for low energy events was obtained which is mainly due to different PMTs used. Also, the efficiency difference between nuclear recoil events and γ recoil events for test crystal (see Fig. A.8) was assigned as systematic uncertainty. With a similarity (only a few % difference for WIMP search energy region) of efficiency for the neutron and the γ calibration data in the test crystal, we can conclude that we can use γ calibration data as efficiency calculation of the WIMP search data. Summary of systematic uncertainty of efficiency calculation is shown in Table A.2. Total systematic error was calculated by following sum rule,

$$\sigma_{sys} = \sqrt{\sigma_1^2 + \sigma_2^2 + \sigma_3^2}.$$

Also, the error of efficiency calculation is calculated by following equation,

$$\sigma_{tot} = \sqrt{\sigma_{stat}^2 + \sigma_{sys}^2}.$$

In our system, the systematic error is dominated.

Table A.2: Systematic error of efficiency calculation of each keV events for S0406 crystal.

Energy	List			total
	t0 cut	different crystal	different recoil	
3-4 keV	0.9 %	6.8 %	2.9 %	7.4 %
4-5 keV	0.6 %	9.1 %	1.6 %	9.3 %
5-6 keV	0.6 %	10.5 %	0.4 %	10.5 %
6-7 keV	0.8 %	12.2 %	4.4 %	13.0 %
7-8 keV	0.7 %	9.0 %	3.9 %	9.8 %
8-9 keV	0.9 %	8.4 %	5.0 %	9.8 %
9-10 keV	1.1 %	7.1 %	2.7 %	7.7 %
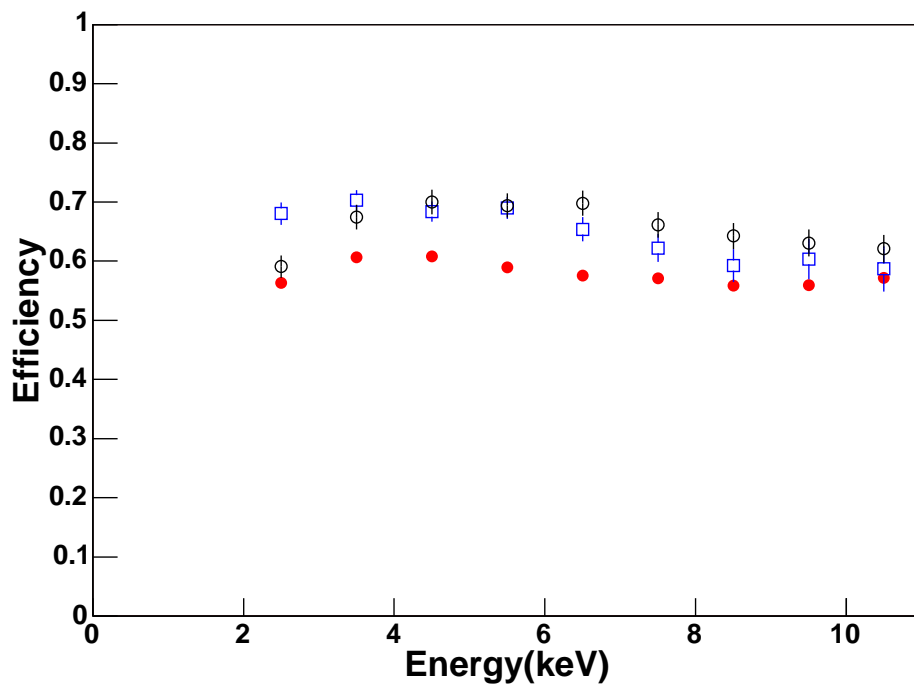
Figure A.8: Efficiency calculated with γ calibration data for S0406 crystal (filled circles), test crystal (open circles), and neutron calibration data for test crystal (open square) where only statistical errors are included.
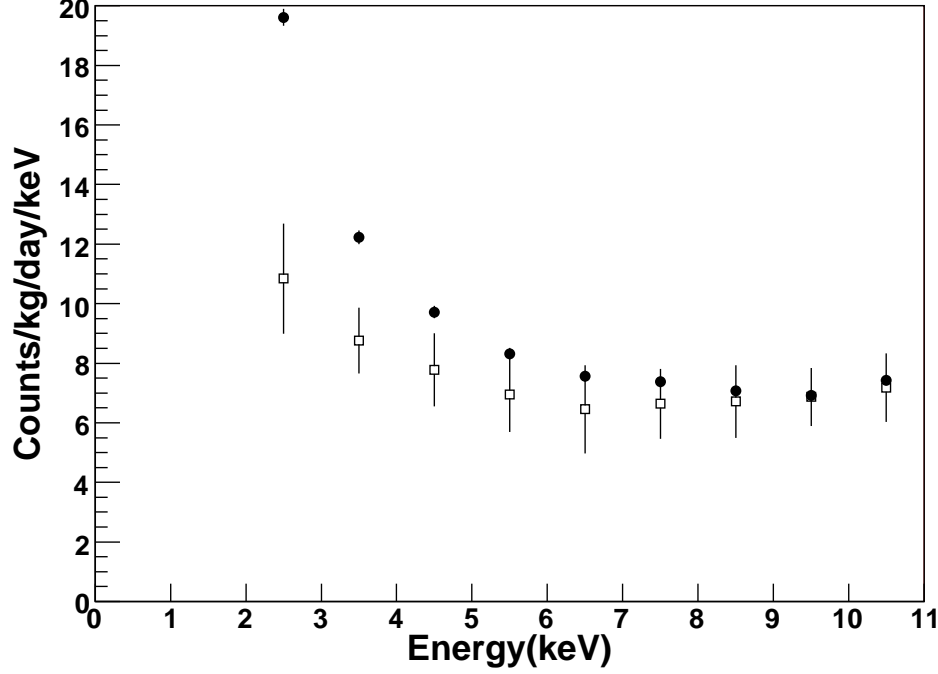
Figure A.9: Energy spectrum in WIMP signal region of WIMP search data before applying cuts (filled circles) and after applying all of cuts with efficiency correction (open squares) are shown.

A.3   Extraction of nuclear recoil events

The energy spectrum of WIMP search data is shown in Fig. A.9 before and after the cuts. Events below 11 keV are used for the WIMP search.

To estimate the WIMP signal fraction in the WIMP search data, we introduce a mean time (MT) value which is defined as,

$$< t >= \frac{\sum A_i t_i}{\sum A_i} - t_0, \qquad (A.1)$$

where A_i and t_i are the charge and the time of the ith cluster respectively, and t_0 is the time of the first cluster (assumed as time zero).

Because we use different crystals for the neutron calibration, we need to confirm whether the two different crystals show the same MT characteristics.

221
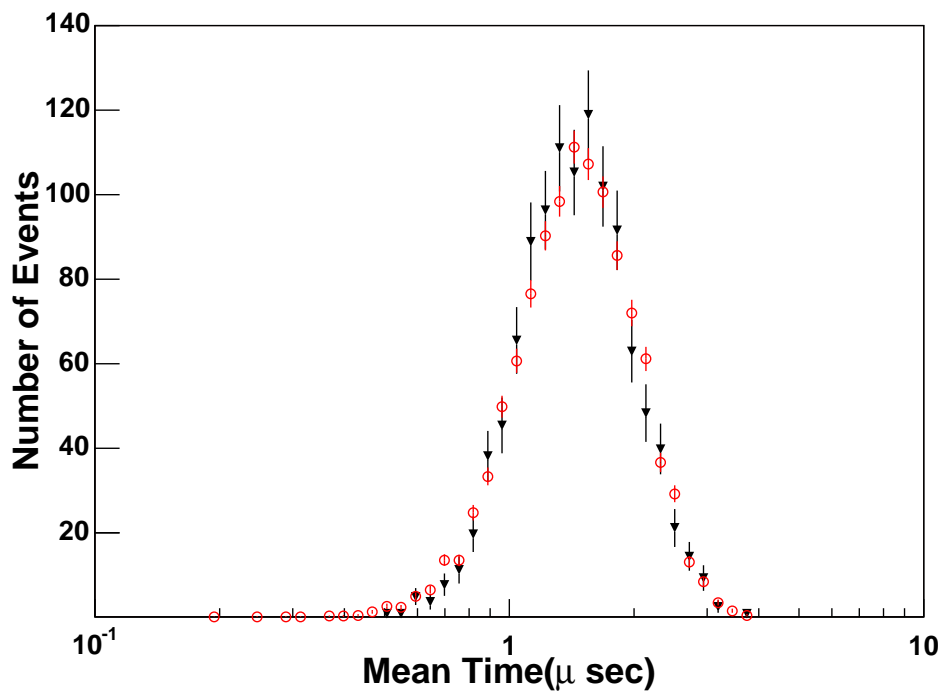
Figure A.10: Mean time distributions of Compton electrons for the test crystal (filled triangles) and S0406 crystal (open circles) in the 4-5 keV energy range.
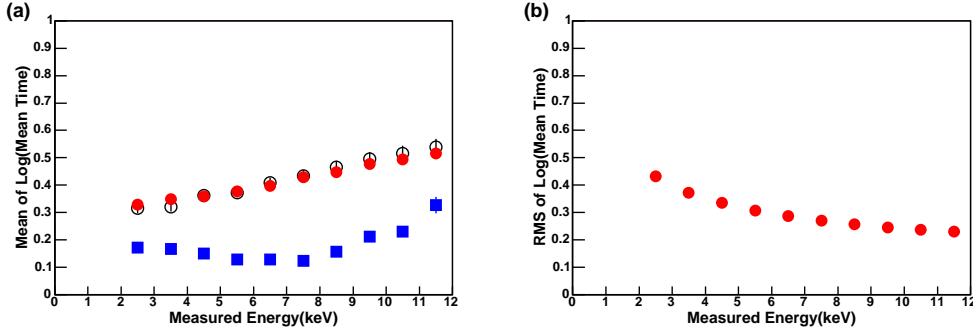
Figure A.11: (a) The mean value of log(MT) as a function of measured energy for Compton electrons with the test crystal (open circles), with the S0406 crystal (filled circles), and for the nuclear recoil with the test crystal (filled squares). (b) Root Mean Square (RMS) of log(MT) as a function of measured energy for Compton electrons with the S0406 crystal.

The ^{137}Cs calibration data of the test crystal is compared with that of the S0406 crystal. As one can see in Fig. A.10, the MT distribution of Compton electrons in the test crystal for 4-5 keV events is well matched with that of the S0406 crystal. The mean value of the log(MT) distribution as a function of energy is shown in Fig A.11. An excellent agreement between the test crystal and the S0406 crystal for the Compton electron allows us to use the neutron signal from the test crystal as a reference for nuclear recoil signal for the S0406 crystal. A slight MT difference is adjusted by the assumption of a constant $R_\tau = \tau_n/\tau_e$ [128]. Where τ_n is the MT of the nuclear recoil and τ_e is the MT of the electron recoil.

Since the MT distribution depends significantly on the measured energy in the low energy region, the log(MT) distribution in each keV energy bin is fitted to the reference distribution for the same energy bin. We have assumption that the WIMP search data have only two components, one is electron recoil (ER) (γ and β backgrounds) and the other is nuclear recoil (NR) (WIMP signal or neutron backgrounds). Therefore we can construct MT model of
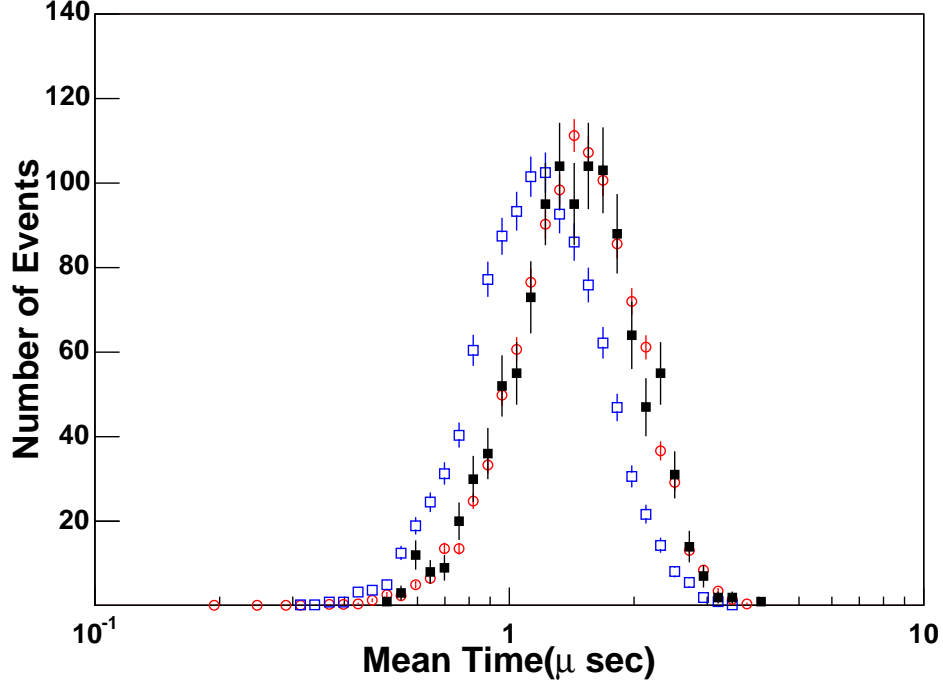
Figure A.12: In the 4-5 keV energy range, mean time distributions for nuclear recoil (open squares), Compton electrons (open circles), and the WIMP search data (filled squares) are shown.

WIMP search data for each keV events as follow.

$$N^i_{DATA}f^i_{DATA}(x) = N^i_{NR}f^i_{NR}(x) + N^i_{ER}f^i_{ER}(x) \tag{A.2}$$

where i is i-th energy bin, $f(x)$ is probability density function (PDF) of each data set, and x is log(MT) value.

Fig. A.12 shows the MT distribution of nuclear recoil and electron recoil for the 4∼5 keV energy bin with WIMP search data. To extract nuclear recoil events we calculate χ^2 value as follow:

$$\chi^2 = \sum_j (data^i[j] - N^i_{DATA}[j]f^i[j])^2/(\delta^2_{data^i[j]} + \delta^2_{N^i_{DATA}[j]f^i[j]}), \tag{A.3}$$

where $N^i_{DATA}[j]f^i[j]$ is model of data as we described in Eq. A.2 and j indicate j-th bin of log(MT) distributions for the i-th energy bin. The error of
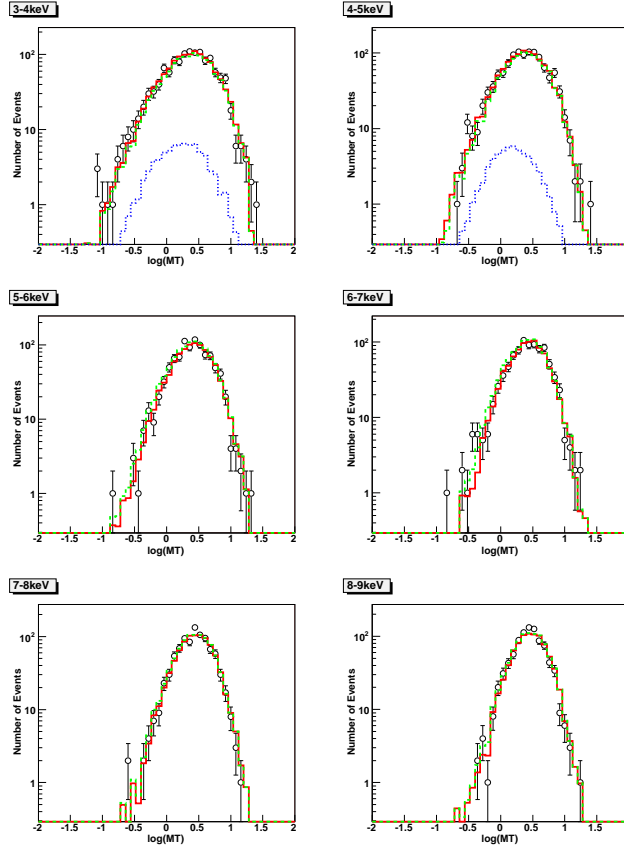
Figure A.13: The WIMP search data (black open circle) are fitted with NR (blue dotted line) and ER (green dashed line) components for each keV bin event. Total fit function was overlaid with solid line (red).

model was propagated from finite set of calibration data. In Eq. A.3 the minimizing algorithm with MINUIT [121] package including in the ROOT [117] are applied to estimate N_{NR}. Fig A.13 shows the result of fit of each keV bin event. Each component of NR and ER for WIMP search data is indicated with total fit function. To estimate the goodness of fit, we calculate χ^2/NDF value as a function of NR. Fig. A.14 shows χ^2 value of each keV bin event. The minimum value of χ^2/NDF is approximately 1 for each bin. We conclude that our fit method is well established.

This result is corrected with efficiency calculated in previous section.
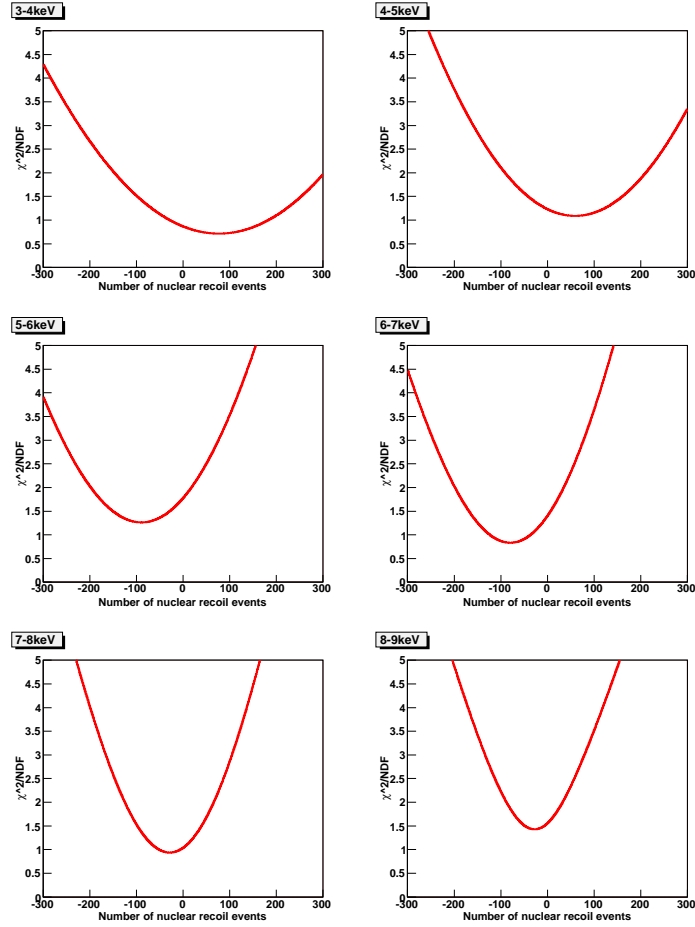
Figure A.14: χ^2 value of fit for each keV event as a function of NR events amount.

Summarized table of fit result is shown in Table A.3. The fitted nuclear recoil event rates after the efficiency correction for each energy bin is given in Fig. A.15 and Table A.3. The fitted nuclear recoil event rates are consistent with zero within one standard deviation error for all energy bins. A 90 % confidence level (CL) upper limit on nuclear recoil event rates are shown with a solid line. Since below 3 keV the PMT background contributes significantly and the pulse shape discrimination power is less effective, we do not use events below 3 keV. In order to evaluate nuclear recoil energy one needs

Table A.3: Fit result for each keV bin event for S0406 crystal. NR rate is corrected by calculated efficiency.

Energy	Fitted NR events	χ^2/NDF	Efficiency	NR rate (CPD)
3-4 keV	77.0 ± 105.1	0.72	60.4 ± 7.5 %	0.54 ± 0.73
4-5 keV	59.2 ± 61.9	1.09	60.5 ± 9.4 %	0.41 ± 0.43
5-6 keV	-89.2 ± 41.5	1.26	58.6 ± 10.5 %	-0.64 ± 0.32
6-7 keV	-79.6 ± 31.5	0.83	57.3 ± 13.1 %	-0.58 ± 0.27
7-8 keV	-28.6 ± 26.1	0.94	56.8 ± 9.9 %	-0.21 ± 0.20
8-9 keV	-27.6 ± 20.9	1.43	55.6 ± 9.9 %	-0.21 ± 0.16
9-10 keV	32.9 ± 29.3	1.70	55.7 ± 7.8 %	0.25 ± 0.22

to know the quenching factor (QF) defined by the γ equivalent measured energy divided by the nuclear recoil energy. We used the QF measured in our previous beam test [94]. Our threshold of 3 keV corresponds to 20 keV nuclear recoil energy.

A.4   Result

Similar procedure explained in Section 4.6 was used to set 90 % CL upper limit with first run data. We generate MC simulation for S0406 crystal. Fig. A.16 (a) shows good agreement between Monte Carlo and calibration data for the energy distribution. The Monte Carlo generated electron equivalent energy distributions (E_{ee}) for several WIMP masses are shown in Fig. A.16 (b).

From the rate of nuclear recoil in each energy bin, we can estimate the total WIMP rate in comparison with the simulated E_{ee} distribution for each WIMP mass by the following relation.

$$R(E_0, E_\infty) = R_{E_k} N_{total}/N_{E_k}, \tag{A.4}$$

227
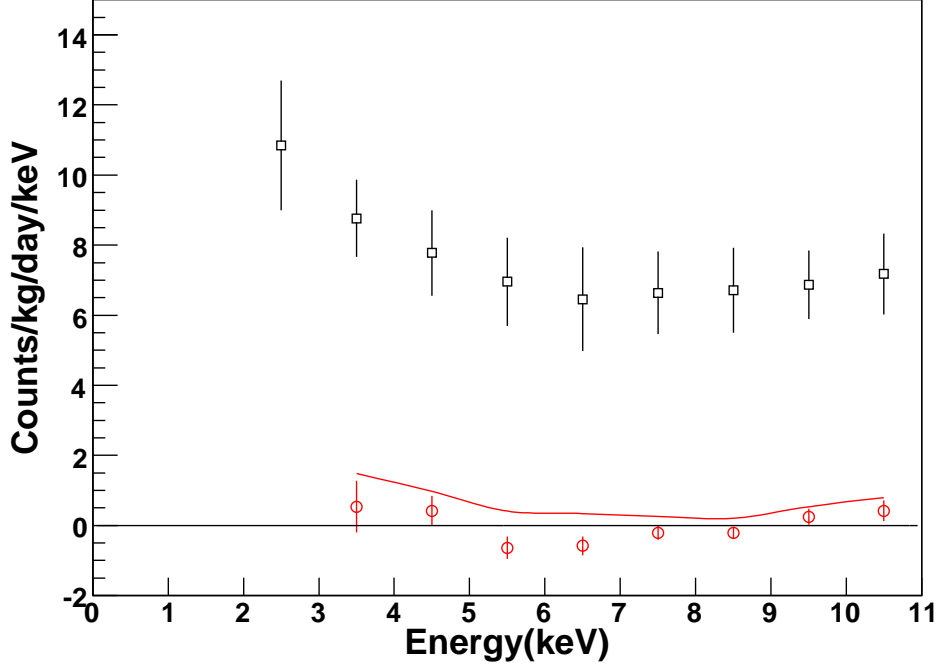
Figure A.15: Energy spectrum in WIMP search data after cuts (open square) and fitted nuclear recoil rate (open circles) with efficiency correction are shown. Where the errors include systematic uncertainty of efficiency. a 90 % upper limit on the nuclear recoil rate is shown with a solid line.

where R_{E_k} and N_{E_k} are the measured nuclear recoil rate and the simulated WIMP events for each energy bin E_k respectively and, N_{total} is the total number of WIMP events generated by simulation. With Eq. (4.6) and Eq. (A.4), we can convert the rate of nuclear recoil in each energy bin to the WIMP-nucleus cross section for each WIMP mass.

The limits on the cross-section for various energy bins and targets (Cs and I) have been combined following the procedure described in Ref [56] assuming the measurements for different energy bins are statistically independent. The combined result from energy bins for a WIMP-nucleus cross section is
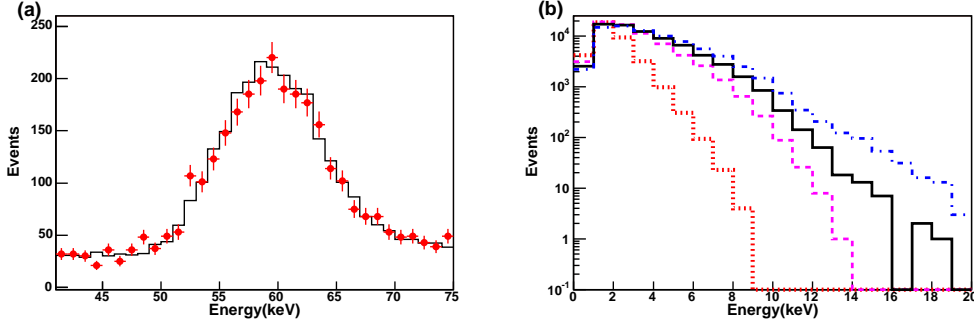
Figure A.16: (a) Distribution of E_{ee} for the MC simulation (solid line) and calibration data (filled circles) for a ^{241}Am source are compared. (b) Simulated E_{ee} spectra for several WIMP masses (20 MeV - dotted line, 50 MeV - dashed line, 100 MeV - solid line, 1000 MeV - dotted dashed line) are shown.

obtained from this expression,

$$
\begin{aligned}
\sigma_{W-A} &= \frac{\sum \sigma_{W-A}(E_k)/\delta\sigma^2_{W-A}(E_k)}{\sum 1/\delta\sigma^2_{W-A}(E_k)}, \\
\frac{1}{\delta\sigma^2_{W-A}} &= \sum \frac{1}{\delta\sigma^2_{W-A}(E_k)},
\end{aligned}
\tag{A.5}
$$

where σ_{W-A} is a combined WIMP-nucleus cross section, $\sigma_{W-A}(E_k)$ is a WIMP-nucleus cross section calculated in an energy bin E_k. As one can see in Fig. **??**, the rate of nuclear recoil events is consistent with zero. Therefore, we can set the 90 % CL upper limit on the WIMP-nucleus cross section with Eq. (A.5). In this process, we assign zero as the mean value for the event rate for the bins with negative means. The WIMP-nucleon cross section can be obtained from WIMP-nucleus cross section by following equation:

$$
\sigma_{W-n} = \sigma_{W-A}\frac{\mu_n^2}{\mu_A^2}\frac{C_n}{C_A},
\tag{A.6}
$$

where $\mu_{n,A}$ are the reduced masses of WIMP-nucleon and WIMP-target nucleus of mass number A and $C_A/C_n = A^2$ for spin independent interaction. The form factor for spin independent interaction is given by Ref. **??** in the

Eq. 4.7. The limit on the WIMP-nucleon cross section for each nucleus can be combined by this expression.

$$\frac{1}{\sigma} = \frac{1}{\sigma_{Cs}} + \frac{1}{\sigma_I}. \tag{A.7}$$

90 % CL upper limit on the WIMP-nucleon cross section from CsI for spin independent interaction is shown in Fig. A.17, together with the limits obtained from two NaI(Tℓ) crystal based WIMP search experiments with similar pulse shape analyzes, NAIAD (UKDMC) [128] and DAMA [62]. Although the amount of data used to get our limit is 10 times less than that of NAIAD, we achieved a more stringent limit than that of NAIAD due to the better pulse shape discrimination and lower recoil energy threshold.
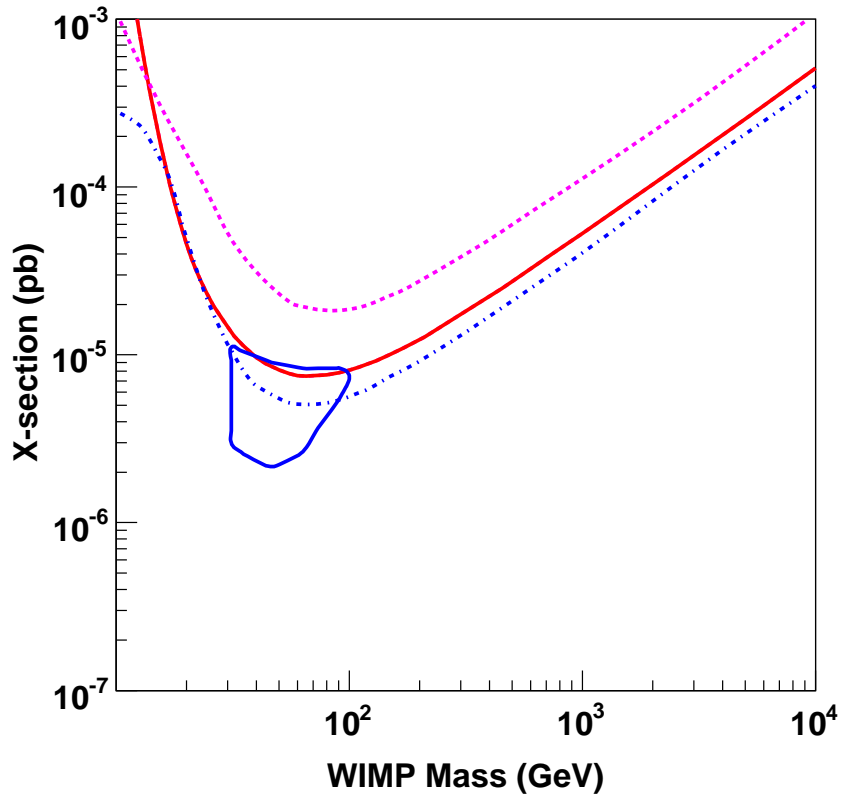
Figure A.17: The KIMS limit on a WIMP-nucleon cross section for a spin independent interaction with 237 kg·days exposure (solid line), DAMA positive [63] annual modulation signal (closed curve), NAIAD limit [128] with 3879 kg·days exposure (dashed line) and, DAMA limit [62] with 4123 kg·days (dashed-dotted line) are presented.

Appendix B

A Monte Carlo Generation for WIMP signal spectrum

B.1 Introduction

As we discussed in chapter 2, the differential recoil rate of WIMP in the material can be written as a function of WIMP mass and cross section (see the section 2.3.2). To understand measured energy spectrum in the CsI(Tℓ) detector, we need to know quenching factor and detector response (energy resolution, detection efficiency, and energy threshold). We use solid line of Fig. 3.9 as a quenching facotr of nuclear recoil. To understand detector response we have full simulation for detection processes which are energy deposition of events, photon generation, transportation of light to PMT, and amplification in PMT. We also apply our trigger condition for simulation data to account trigger efficiency.

B.2 Detector Response & Energy Resolution
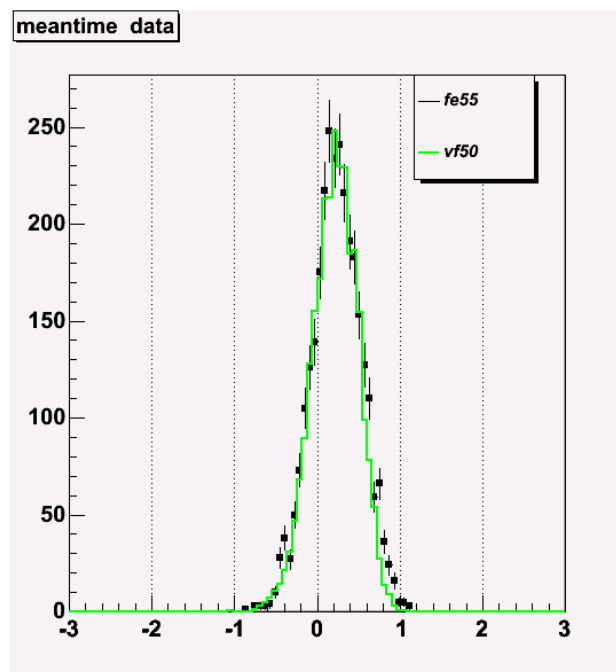
Figure B.1: MC tuning of decay time with 5.9 keV gamma.

The energy deposition in the detector is translated as electron-hole pairs. pairs and phonon. The excited electron could recombine with a photon which have band gap energy of crystal [105]. The time response of photons for electron recoil and nuclear recoil events were measured with neutron calibration and γ calibration respectively. We had accumulated decay time spectrum of low energy events for electron recoils and nuclear recoils as one can see in Fig. 3.5. The decay time for each recoil was fitted by Eq 4.1 fit function. We generate photons with PDF. Fig. B.2 shows the tuning of light yield with 5.9 keV gamma for calibration and simulation.

We need to consider photon propagation in the CsI(Tℓ) crystal. The photon reached to the face of PMT can make SPE. We consider penetration depth of light in the CsI(Tℓ) crystal and reflectance of light on the teplon. The photon generations in a photocathode were affected by a quantum efficiency of PMT. The photoelectrons were amplified in the dynode. With Ref [144] and Ref [145] we simulated amplification of photoelectrons.
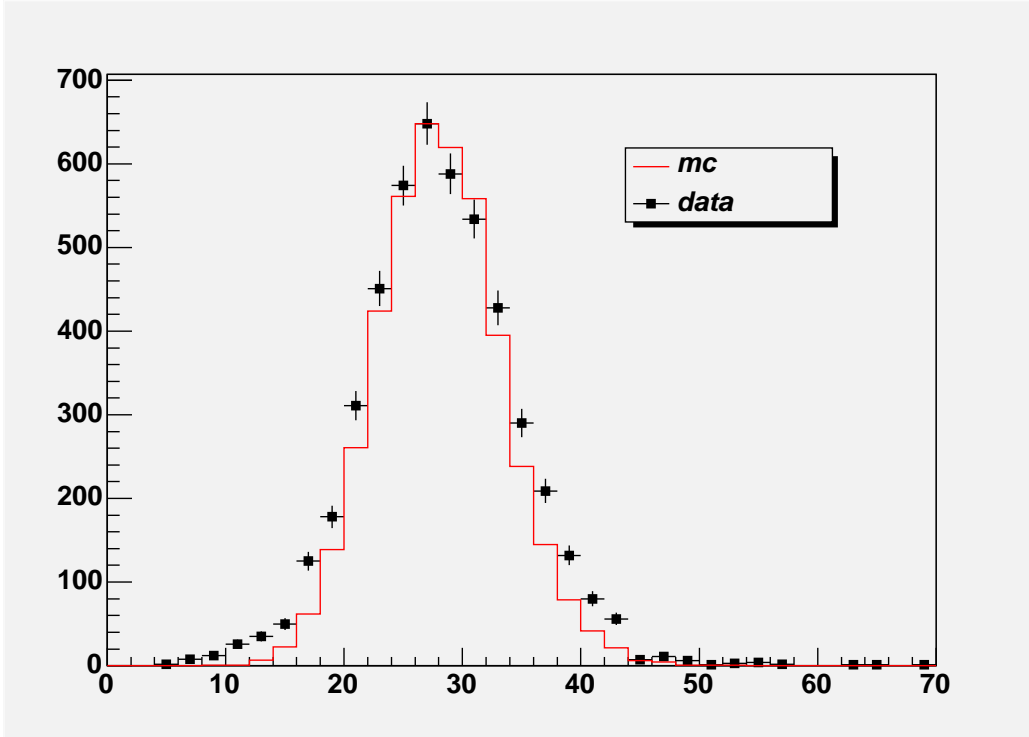
Figure B.2: MC tuning of light output with 5.9 keV gamma.

The shape of SPEs were obtained from calibration data of low energy X-ray with ^{55}Fe source. Fig B.3 shows the SPEs shape of calibration data. The shape was fitted with gaussian convoluted landau function (thick solid line). We account the distribution of parameters.

We need to consider the fluctuation of base line (pedestal) because it affect the energy resolution. The measured pedestal data (see the Fig. B.4) were used to determine pedestal level of MC data.

We also included random photoelectrons which were originated from PMT dark current or random photons of crystal. The measured rate of random photoelectrons as we discussed in Section 4.2.3 were included in the MC generation.

The generated shape of events were digitized in the every 2 ns with 32 μs windows which were compatible with real data. We also include trigger condition to determine the recording of data. To the consistency between
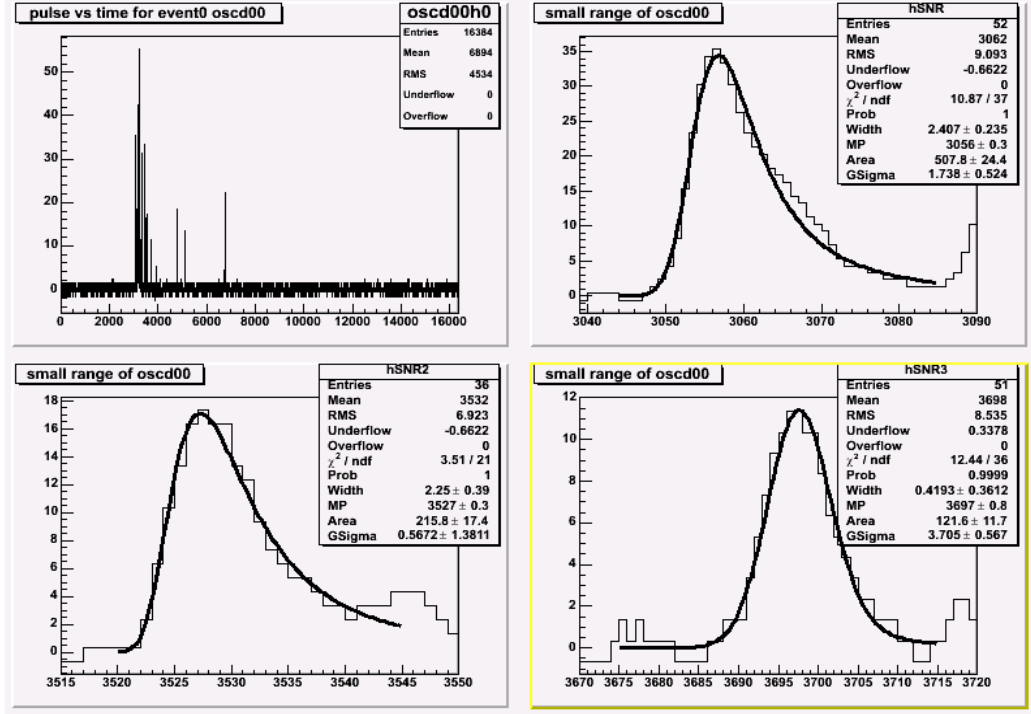
Figure B.3: Typical ^{55}Fe source signal in the 32 μ sec window (top left) are shown with zoomed SPE shape overlaid with its fit using gaussian convoluted landau function.

data and MC, the data structure of MC was same with data. We analyze the MC data using same analysis program with real data.

We tuned MC simulation data with ^{55}Fe and ^{241}Am source calibration data. The number of photoelectrons for 5.9 keV X-ray data for S0406 crystal is shown in Fig. B.2. As one can see in this figure, NC (number of cluster) tuning is well working. With the light yield of each crystal (table 4.1), we generated 59.5 keV γs for calibration of energy. Fig. B.5 shows the energy spectrum of 59.5 keV γ from data (filled circle) and MC (solid line). As one can see in this figure, the MC well explain the data.
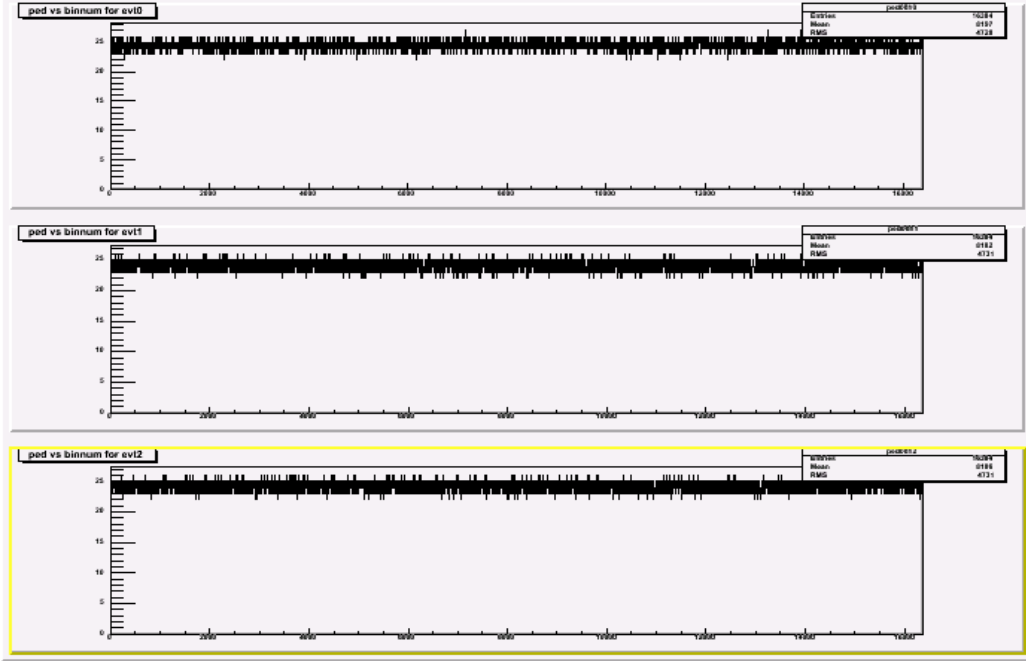
Figure B.4: Measured pedestal spectrum.

B.3 WIMP generation

As we discussed in Section 2.3.2, the differential recoil rate in Cs and I for WIMP signal can be calculated as a function of WIMP mass and cross section for each interaction type. For fixed WIMP mass and cross section, we can calculate recoil rate as a function of energy. For example Fig. 2.5 shows recoil rate as a function of energy in the CsI(Tℓ) crystal for WIMP proton cross section with $\sigma_{\chi p} = 7.2 \times 10^{-6}$ pb and a WIMP mass $M_\chi = 50$ GeV in the case of spin independent interaction. Therefore the deposited energy of WIMP interaction is considered as probability of Fig. 2.5 spectrum in this case. We had done this process for different case (WIMP mass and interaction type).

We need to consider an quenching factor for accouting measured energy discussed in Section 3.4.3. We use quenching factor obtained from neutron beam test (Fig. 3.9). The electron equivalent energy (E_{ee}) were used to
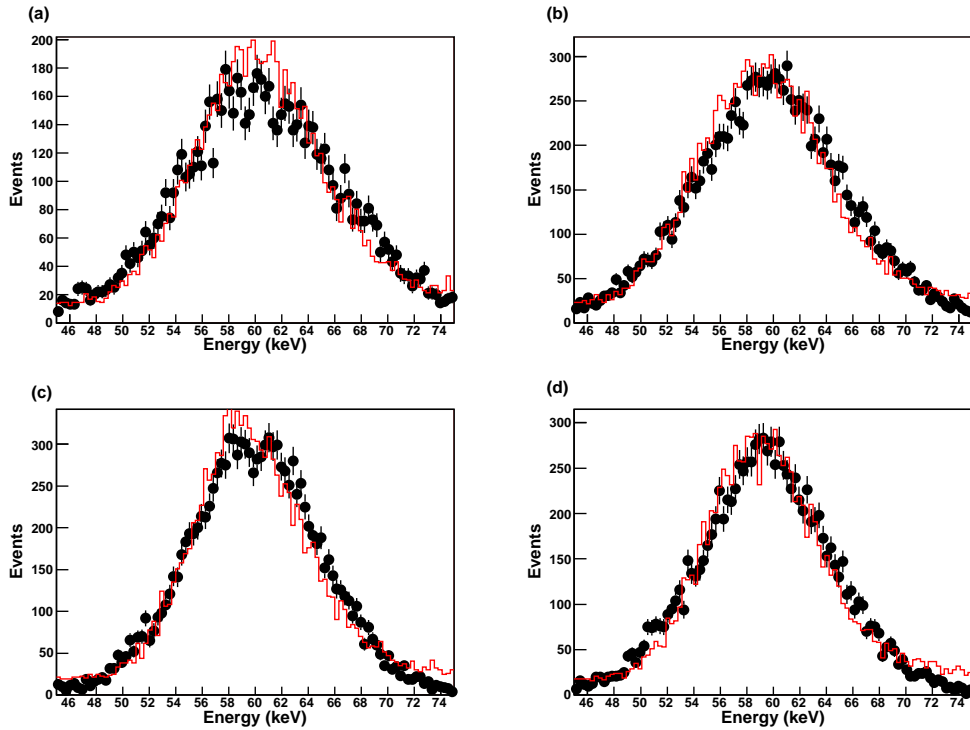
Figure B.5: 59.54 keV peak spectrum from ^{241}Am calibration data (filled circle) and simulation (solid line) for S0501A (a), S0501B (b), B0510A (c), and B0510B (d).

determine parameters of photon generation. The following process were fully simulated. Fig. B.6, B.7, B.8, and B.9 show WIMP signal shapes for different crystals, WIMP masses, and interaction types.
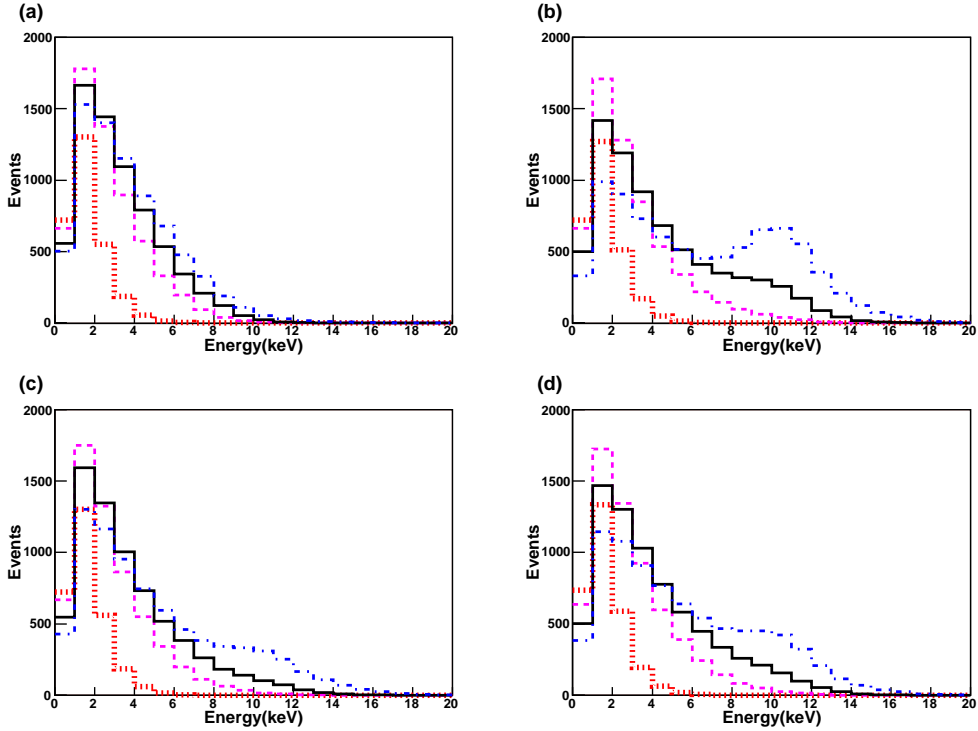
Figure B.6: Simulated E_{ee} spectrum in the S0501A crystal for several WIMP masses (20 GeV -dotted line, 50 GeV - dashed line, 100 GeV - solid line, 1000 GeV - dotted dashed line) and WIMP nucleon spin independent interaction (a), WIMP proton spin dependent interaction in the Cs (b), WIMP proton spin dependent interaction in the I (c), and WIMP neutron spin dependent interaction in the I (d).
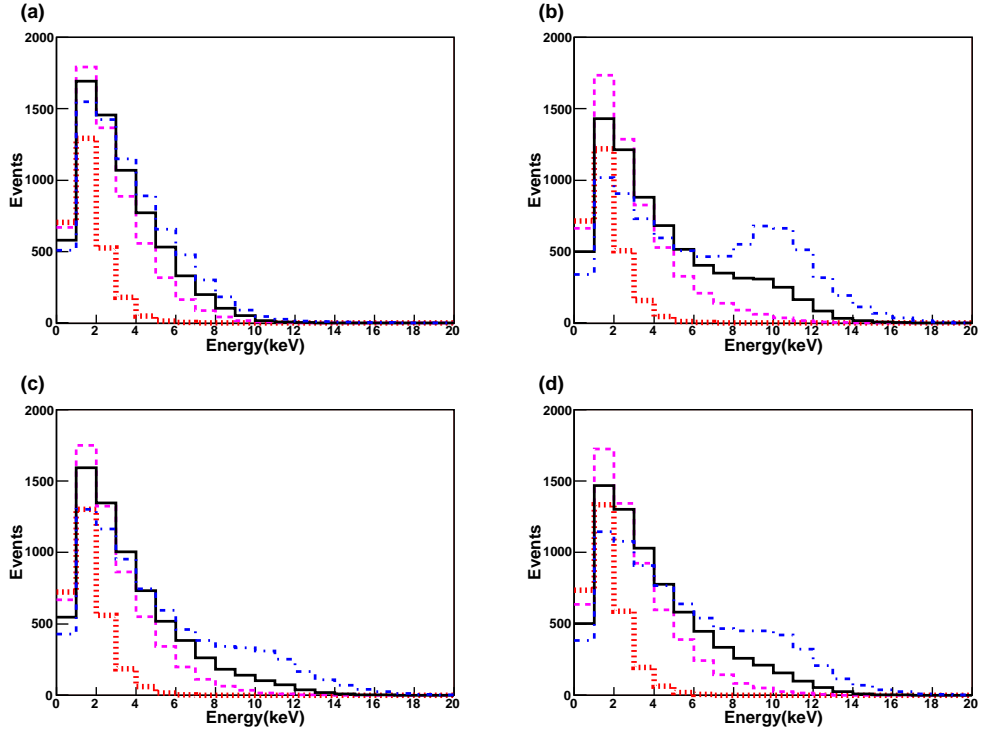
Figure B.7: Simulated E$_{ee}$ spectrum in the S0501B crystal for several WIMP masses (20 GeV -dotted line, 50 GeV - dashed line, 100 GeV - solid line, 1000 GeV - dotted dashed line) and WIMP nucleon spin independent interaction (a), WIMP proton spin dependent interaction in the Cs (b), WIMP proton spin dependent interaction in the I (c), and WIMP neutron spin dependent interaction in the I (d).
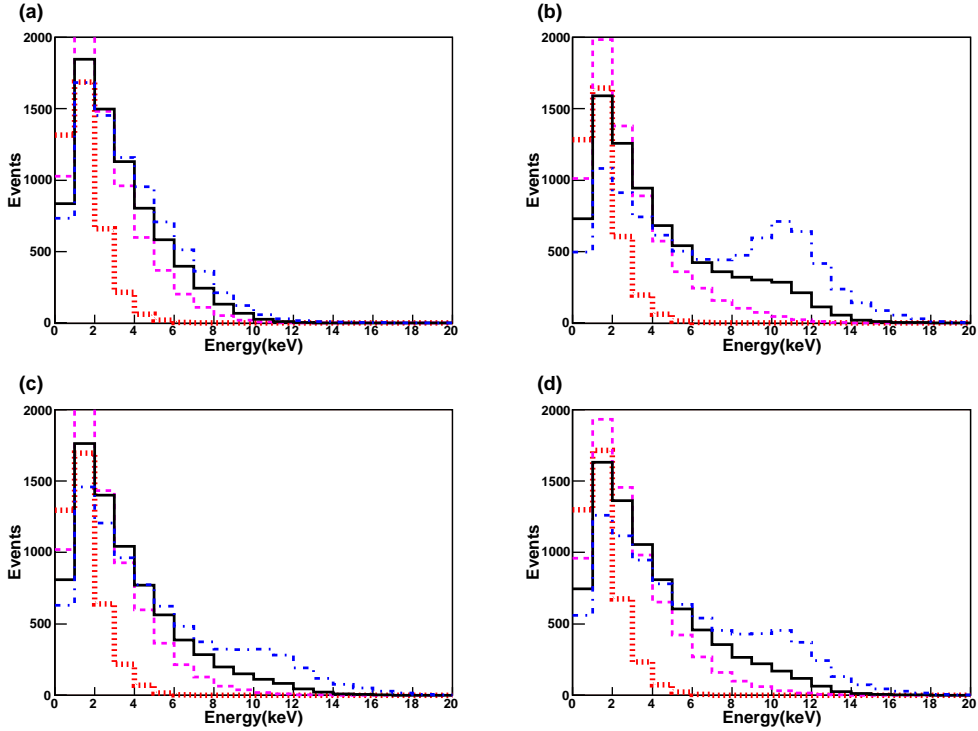
Figure B.8: Simulated E_{ee} spectrum in the B0510A crystal for several WIMP masses (20 GeV -dotted line, 50 GeV - dashed line, 100 GeV - solid line, 1000 GeV - dotted dashed line) and WIMP nucleon spin independent interaction (a), WIMP proton spin dependent interaction in the Cs (b), WIMP proton spin dependent interaction in the I (c), and WIMP neutron spin dependent interaction in the I (d).
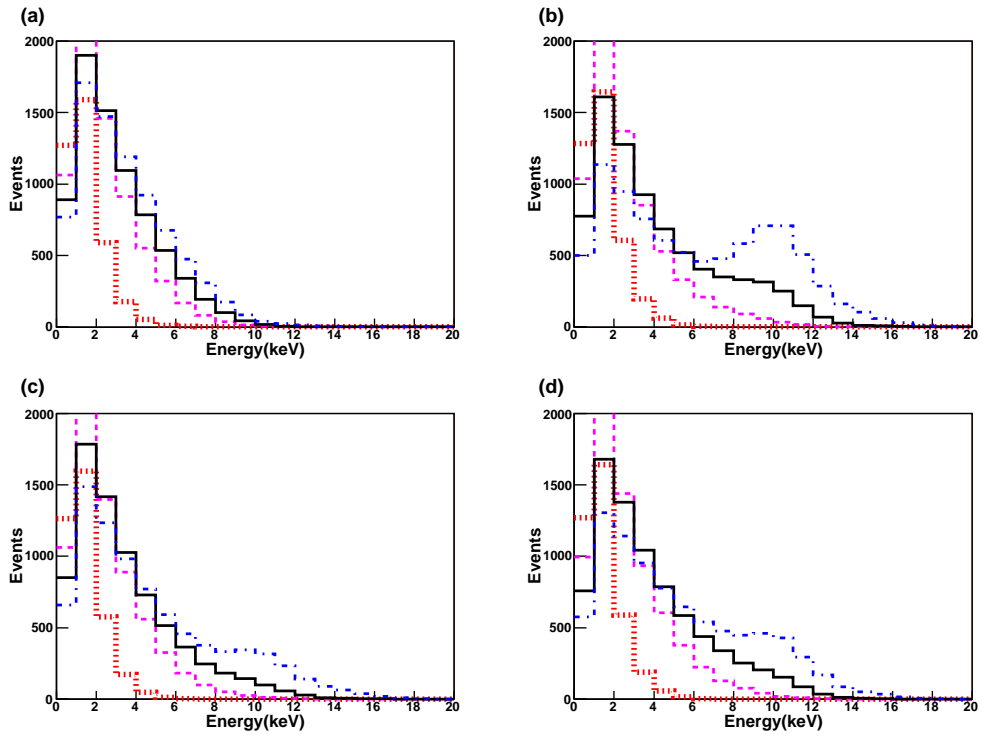
Figure B.9: Simulated E$_{ee}$ spectrum in the B0510B crystal for several WIMP masses (20 GeV -dotted line, 50 GeV - dashed line, 100 GeV - solid line, 1000 GeV - dotted dashed line) and WIMP nucleon spin independent interaction (a), WIMP proton spin dependent interaction in the Cs (b), WIMP proton spin dependent interaction in the I (c), and WIMP neutron...

Appendix C

How to set the projected limit on WIMP cross section of future experiments

To consider a power of future experiment we need to set projected limits of experiment. If we do not have understanding for detectors and systems, it is impossible to expect the projected limits.

We calculate the projected limits with an assumption of null signal from WIMPs. Furthermore we expect that the external background from neutron could be negligible. Also we assume that all of PMT noises are rejected by events selection cut. The efficiency of event selection cut is assumed as 0.6±0.1.

It is possible to have full simulate of the detector response as discussed in the Appendix B. But, it takes too much time and also the simulation of MT (mean time) characteristics is enough to calculate projected limit. We have the MT spectrum of calibration data. It was modeled with asymmetric gaussian functions as one can see in Fig. 4.31. From the reference shape of electron recoil we generate γ background with an assumed background level

and experiment time. Because we will accommodate 250 kg of CsI(Tℓ) crystals with 2 CPD background level, we consider 1 year data taking with this setup. We generate γ backgrounds from 3 keV to 10 keV for each 1 keV bin with the reference shape. Fig C.1 shows that the MT spectrum of this energy bin events with 1 year data taking of 250 kg crystals which have 2 CPD background level. We performed same fit to extract signal as we discussed in Section 4.5. The zero consistent result can allow us to set 90 %CL upper limit.
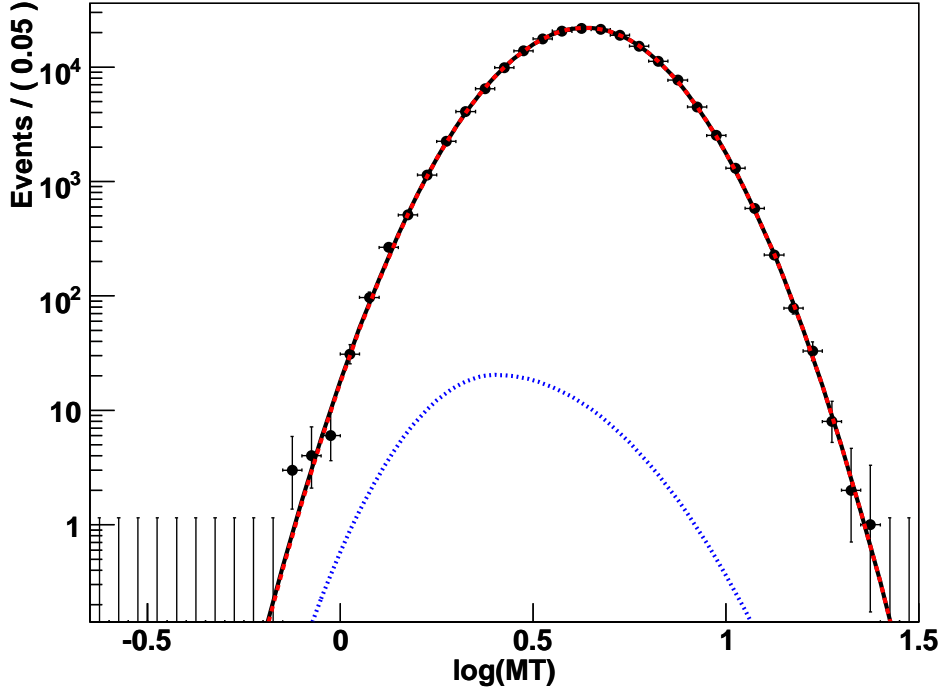
Figure C.1: MT spectrum of 9-10 keV bin events for that we have 250 kg with 2 CPD background level and take 1 year data is shown at the filled circle. We have assumption of null signal of WIMP. Also, we performed fit to extract nuclear recoil.

We consider future setup with the 1 ton CsI(Tℓ) crystals which have

0.1 CPD background level. Fig. C.2 C.3 show the projected limits of our
experiment for each interaction type.
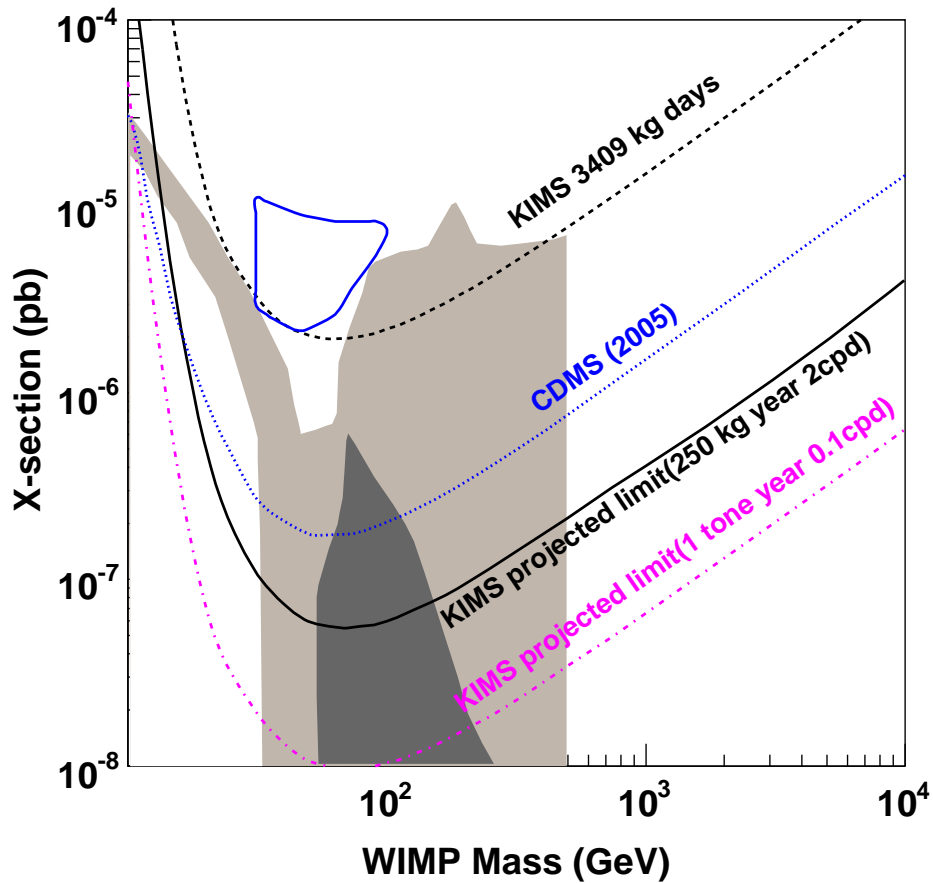
Figure C.2: Projected limit on WIMP nucleon cross section for spin inde-
pendent interaction with other leading experiments result.
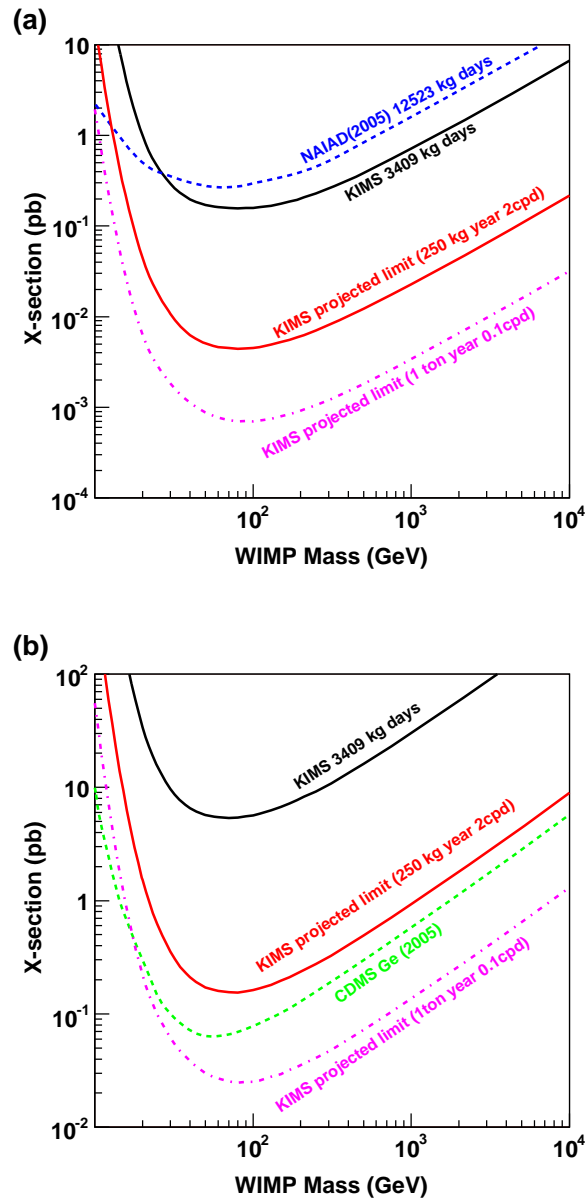
Figure C.3: Projected limit on WIMP nucleon cross section for spin dependent interaction of pure proton (up) and pure neutron (down) with other leading experiments result.

Bibliography

[1] F. Zwicky, Helv. Phys. Acta **6**, 110 (1933).

[2] G. Bertone, D. Hooper, and J. Silk, Phys. Rep. **405**, 279 (2005), arXiv:hep-ph/0404175/.

[3] G. G. Raffelt, Lectures at European School of High-Energy Physics, Menstrup, Denmark, June (1997), arXiv:hep-ph/9712538.

[4] S. R. Golwala, Ph.D thesis of UC Berkeley (2000)
G. Wang, Ph.D thesis of Case Western Reserve University (2005).

[5] D. N. Spergel *et al.*, Astrophys. J. Suppl. **148**, 175 (2003), arXiv:astro-ph/0302209.

[6] S. Perlmutter *et al.*, Nature **391**, 51 (1998)
A. Riess *et al.*, Astrophys. J. **116**, 1009 (1998)
A. G. Riess *et al.*, Astrophys. J. **607**, 665 (2004)
B. Barris *et al.*, Astrophys. J. **602**, 571 (2004)
S. Perlmutter *et al.*, Astrophys. J. **517**, 565 (1999)
P. Astier *et al.*, Astron. Astrophys. **447**, 31 (2006), arXiv:astro-ph/0510447.

[7] V. Sahni *et al.*, Lect. Notes Phys. **653**, 141 (2004), arXiv:astro-ph/0403324
L. Perivolaropoulos *et al.*, AIP Conf. Proc. **848**, 698 (2006), arXiv:astro-ph/0601014.

[8] V. Trimble, Annu. Rev. Astron. Astrophys. **25**, 425 (1987).

[9] K. G. Begeman, A. H. Broeils and R. H. Sanders, Mon. Not. Roy. Astron. Soc. **249**, 523 (1991).

[10] P. Salucci, and M. Persic, arXiv:astro-ph/9703027.

[11] P. Salucci and A. Borriello, Lect. Notes Phys. **616**, 66 (2003), arXiv:astro-ph/0203457.

[12] J. N. Bahcall *et al.*, Astrophys. J **265**, 730 (1983).

[13] R. R. Caldwell and J. P. Ostriker, Astrophys. J **251**, 61 (1981).

[14] M. S. Turner, Phys. Rev. D **33**, 889 (1986).

[15] R. P. Olling and M. R. Merrifield, arXiv:astro-ph/9907353.

[16] R. G. Carlberg *et al.*, Astrophys. J. **462**, 32 (1996).

[17] D. A. White and A. C. Fabian, Mon. Not. Roy. Astron. Soc. **273**, 72 (1993).

[18] S. W. Allen, R. W. Schmidt and A. C. Fabian, Mon. Not. Roy. Astron. Soc. **334**, L11 (2002).

[19] S. D. M. White *et al.*, Nature **366**, 429 (1993).

[20] D. Clowe *et al.*, Astrophys. J. **604**, 596 (2004), arXiv:astro-ph/0312273.

[21] C. L. Bennett *et al.*, Astrophys. J. **464**, L1-L4 (1996), arXiv:astro-ph/9601067.

[22] W. C. Jones *et al.*, Astrophys. J. **647**, 823 (2006), arXiv:astro-ph/0507494.

[23] C. L. Bennett *et al.*, Astrophys. J. Suppl. **148**, 1 (2003), arXiv:astro-ph/0302207.

[24] P. Coles, and G. F. R Ellis, Is the Universe Open or Closed? (Cambridge, UK, 1997).

[25] E. Kolb, and M. S. Turner, The Early Universe, (Addison-Wesley, 1990).

[26] D. Tytler *et al.*, Phys. Scr. **T85**, 12 (2000)
D. Tytler *et al.*, The Astronomical Journal **117**, 63 (1999).

[27] J. A. Peacock *et al.*, Nature **410**, 167 (2001)
J. A. Peacock *et al.*, arXiv:astro-ph/0204239.

[28] M. Tegmark and M. Zaldarriaga, Phys. Rev. D **66**, 103508 (2002).

[29] B. Sadoulet , Rev. of Mod. Phys. **71**, 97 (1999).

[30] C. Alcock *et al.*, Phys. Rev. Lett. **74**, 2969 (1995).

[31] C. Renault *et al.*, Astron. Astrophys. **324**, L69 (1997)
C. Alcock *et al.*, Astrophys. J. **471**, 774 (1996)
C. Alcock *et al.*, Astrophys. J. **486**, 697 (1997)
C. Alcock *et al.*, Astrophys. J. **491**, L11 (1997)
N. Palanque-Delabrouille *et al.*, arXiv:astro-ph/9710194.

[32] Y. Fukuda *et al.*, Phys. Rev. Lett. **81**, 1562 (1998)
Q. R. Ahmad *et al.*, Phys. Rev. Lett. **89**, 11301 (2002)
K. Hagiwara *et al.*, Phys. Rev. D **66**, 10001 (2002).

[33] C. Weinheimer, Proceedings of 10th International Workshop on Neutrino Telescopes, Venice, Italy, 2003, arXiv:hep-ex/0306057.

[34] M. Tegmark *et al.*, Phys. Rev. D **69**, 103501 (2004).

[35] J. R. Bond, G. Efstathiou and J. Silk, Phys. Rev. Lett. **45**, 1980 (1980)

[36] J. E. Kim, Phys. Rep. **150**, 1 (1987)
H. Y. Cheng, Phys. Rep. **158**, 1 (1988).

[37] J. Ellis and K. Olive, Phys. Lett. B **193**, 525 (1987)
     G. Raffelt and D. Seckel, Phys. Rev. Lett. **60**, 1793 (1988).

[38] L. Abbott and P. Sikivie, Phys. Lett. B **120**, 133 (1983)
     J. Preskill, M. Wise and F. Wilczek, Phys. Lett. B **120**, 127 (1983)
     M. Dine and W. Fischler, Phys. Lett. B **120**, 137 (1983).

[39] C. Hagmann and P. Sikivie, Nucl. Phys. B **363**, 247 (1991)
     S. Chang and C. Hagmann and P. Sikivie, Nucl. Phys. B (Proc. Suppl.)
     72, 81 (1999).

[40] K. Zioutas *et al.*, Phys. Rev. Lett. **94**, 121301 (2005).

[41] P. Sikivie, Nucl. Phys. B. (Proc. Suppl.) **87**, 41 (2000), arXiv:hep-ph/0002154
     J. E. Kim, arXiv:hep-ph/0612141.

[42] K. Grist and M. Kamionkowski, Phys. Rev. Lett. **64**, 615 (1990).

[43] G. Jungman, M. Kamionkowski and K. Griest, Phys. Rep. **267**, 195
     (1996).

[44] B. W. Lee and S. Weinberg Phys. Rev. Lett. **39**, 165 (1977).

[45] L. E. Ibanez Phys. Lett. B **137**, 160 (1984)
     T. Falk *et al.*Phys. Lett. B **339**, 248 (1994).

[46] J. L. Feng, A. Rajaraman and F. Takayama, Phys. Rev. Lett. **91**,
     011302 (2003), arXiv:hep-ph/0302215.

[47] E. W. Kolb *et al.*, arXiv:hep-ph/9810361.

[48] L. Roszkowski, Pramana **62**, 389 (2004), arXiv:hep-ph/0404052.

[49] U. Amaldi, W. de. Boer and H. Furstenau, Phys. Lett. B **260**, 447
     (1991).

[50] H. Goldberg, Phys. Rev. Lett. **50**, 1419 (1983)
     J. R. Ellis *et al.*, Nucl. Phys. B **238**, 453 (1984).

[51] K. Hagiwara *et al.*, Phys. Rev. D **66**, 10001 (2002).

[52] G. Jungman *et al.*, Phys. Rep. **267**, 195 (1996).

[53] J. Engel, Phys. Lett. B **264**, 114 (1991).

[54] J. Engel, Phys. Lett. B **264**, 25 (1991).

[55] D. R. Tovey *et al.*, Phys. Lett. B **488**, 17 (2000).

[56] J. D. Smith, Astropart. Phys. **6**, 87 (1996).

[57] R. J. Gaitskel, Annu. Rev. Nucl. Part. Sci. **54**, 315 (2004).

[58] A. Morales, Nucl. Phys. B (Proc. Suppl.) **114**, 39 (2003).

[59] L. Mosca, Nucl. Phys. B (Proc. Suppl.) **114**, 59 (2003).

[60] L. Baudis *et al.*, Phys. Rep. **307**, 301 (1998).

[61] I. G. Irastorza *et al.*, Proceedings of the 4th International Workshop on the Identification of Dark Matter, York (2002), arXiv:astro-ph/0211535/.

[62] R. Bernabei *et al.*, Phys. Lett. B **389**, 757 (1996).

[63] R. Bernabei *et al.*, Phys. Lett. B **480**, 23 (2000).

[64] R. Bernabei *et al.*, Riv. N. Cim. **26**, 1 (2003).

[65] D. S. Akerib *et al.*, Phys. Rev. Lett. **96**, 011302 (2006).

[66] V. Sanglard *et al.*, Phys. Rev. D **71**, 122002 (2005).

[67] G. Angloher *et al.*, Astropart. Phys. **23**, 325 (2005).

[68] A. Bottino *et al.*, Phys. Rev. D **69**, 037302 (2004).

[69] J. Ellis *et al.*, Phys. Rev. D **71**, 095007 (2005).

[70] R. J. Gaitskell and V. Mandic, http://dmtools.brown.edu.

[71] C. Savage, P. Gondolo, and K. Freese, Phys. Rev. D **70**, 123513 (2004).

[72] D. S. Akerib *et al.*, Phys. Rev. D **73**, 011102 (2006).

[73] G. J. Alner *et al.*, Phys. Lett. B **624**, 186 (2005).

[74] M. Barnabe-Heider *et al.*, Phys. Lett. B **624**, 186 (2005).

[75] T. A. Girard *et al.*, Phys. Lett. B **621**, 233 (2005).

[76] F. Giuliani , Phys. Rev. Lett. **93**, 161301 (2004).

[77] P. Gondolo *et al.*, Phys. Rev. D **71**, 123520 (2005).

[78] R. Foot, Mod. Phys. Lett. A **19**, 1841 (2004)
R. Foot, arXiv:astro-ph/0510705.

[79] R. Foot, Phys. Rev. D **69**, 036001 (2004)
R. Foot, arXiv:astro-ph/0403043.

[80] R. Bernabei *et al.*, Int. J. Mod. Phys. D **13**, 2127 (2004).

[81] J. Ahrens *et al.*, Phys. Rev. Lett. **92**, 071102 (2004).

[82] V. I. Lyashuk *et al.*, Physic of Atomic Nuclei **66**, 509 (2003).

[83] S. Yoshida *et al.*, Phys. Rev. D **69**, 103004 (2004).

[84] S. Desai *et al.*, Phys. Rev. D **70**, 083523 (2004).

[85] T. Kifune, 21st Rencontres de Moriond Workshop.

[86] F. Aharonian *et al.*, Astron. Astrophys. **425**, L13-L17 (2004).

[87] D. Horns, Phys. Lett. B **607**, 225 (2005).

[88] A. Cesarini *et al.*, Astropart. Phys. **21**, 267 (2004).

[89] S. W. Barwick *et al.*, Phys. Rev. Lett. **75**, 390 (1995)
S. W. Barwick *et al.*, Astrophys. J. **482**, L191 (1997)
S. Coutu *et al.*, in Proceedings of 27th ICRC, 2001.

[90] E. A. Baltz *et al.*, Phys. Rev. D **65**, 063511 (2002).

[91] E. Won *et al.*, Nuclear Physics B (Proc.Suppl.) **78**, 449 (1999)
H. J. Kim *et al.*, Nucl. Instrum. Meth. A **457**, 471 (2001).

[92] Y. D. Kim *et al.*, J. Kor. Phys. Soc. **40**, 520 (2002)
Y. D. Kim *et al.*, Nucl. Instrum. Meth. A **552**, 456 (2005).

[93] T. Y. Kim *et al.*, Nucl. Instrum. Meth. A **500**, 337 (2003)
Y. D. Kim *et al.*, Proceedings of the 4th International Workshop on the Identification of Dark Matter, World Scientific, 2002, p.345.

[94] H. Park *et al.*, Nucl. Instrum. Meth. A **491**, 460 (2002).

[95] H. S. Lee *et al.*, Proceedings of the 5th International Workshop on the Identification of Dark Matter, World Scientific, 2004, p.390
H. S. Lee *et al.*, Nucl. Instrum. Meth. Ain press.

[96] J. W. Kwak *et al.*, Proceedings of the 5th International Workshop on the Identification of Dark Matter, World Scientific, 2004, p.236.

[97] H. S. Lee *et al.*, Phys. Lett. B **633**, 201 (2006).

[98] J. J. Zhu *et al.*, High Energy Physics and Nuclear Physics **29**, 2005 (721).

[99] M. J. Lee *et al.*, submitted to Nucl. Instrum. Meth. A.

[100] H. J. Kim *et al.*, Astropart. Phys. **20**, 549 (2004).

[101] S. Pecourt *et al.*, Astropart. Phys. **11**, 457 (1999).

[102] V. A. Kudryavtsev *et al.*, Nucl. Instrum. Meth. A **456**, 72 (2001).

[103] R. J. Gaitskell *et al.*, Nucl. Phys. B (Proc. Suppl.) **51**, 279 (1996).

[104] G. Gerbier *et al.*, Astropart. Phys. **11**, 287 (1999).

[105] G. F. Knoll, Radiation Detection and Measurement, John Wiley and Sons (2000) New York.

[106] J. B. Birks, The theory and practice of scintillation counting, perganmon Press, Oxford, 1964.

[107] D. R. Tovey *et al.*, Phys. Lett. B **433**, 150 (1998)
N. J. C. Spooner *et al.*, Phys. Lett. B **321**, 156 (1994)
R. Hazama *et al.*, Nucl. Instrum. Meth. A **482**, 297 (2002)
C. Bacci *et al.*, Astropart. Phys. **2**, 117 (1994)
D. Akimov *et al.*, Phys. Lett. B **524**, 245 (2002)
E. Eimon *et al.*, Nucl. Instrum. Meth. A **507**, 643 (2003).

[108] S. Agostinelli *et al.*, Nucl. Instrum. Meth. A **506**, 250 (2003), see also http://geant4.web.cern.ch/geant4.

[109] E. M. Burbidge *et al.*, Rev. Mod. Phys. **29**, 547 (1957).

[110] Special Metals Division, Chemetall GmbH (http://specialmetals.chemetall.com).

[111] Zubrick, W. James, The organic Chemistry Laboratory Survival Manual, John Wiley and Sons (2001) New York.

[112] D. R. Lide, CRC handbook of chemistry and physics, 84th edition, CRC Press (2003), see also http://www.crcpress.com.

[113] Y. F. Zhu *et al.*, Nucl. Instrum. Meth. A **557**, 490 (2006).

[114] B. C. Barton *et al.*, Nucl. Instrum. Meth. A **443**, 227 (2000).

[115] R. Bernabei *et al.*, II Nuovo Cimento **112A**, 545 (1999).

[116] P. Theodorsson *et al.*, Nucl. Instrum. Meth. A **506**, 143 (2003).

[117] R. Brunn and F. Rademakers, ROOT - An Object Oriented Data Analysis Framework, Proceedings of AIHENP '96 Workshop, Lausanne, Sep. 1996; Nucl. Instrum. Meth. A **389**, 1997 (81), see also http://root.cern.ch.

[118] J. J. Zhu *et al.*, J. Kor. Phys. Soc. **47**, 202 (2005).

[119] S. Marrone *et al.*, Nucl. Instrum. Meth. A **490**, 299 (2002).

[120] E. V. Bugaev *et al.*, Phys. Rev. D **58**, 054001 (1998).

[121] F. James, MINUIT-function minimization and error analysis, CERN Program Library Long Writeup D506.

[122] E. Albrecht *et al.*, Assessment of Airborne radioactivity, Proceeding of IAEA symposium, Vienna (1967).

[123] Super-Kamiokande Collaboration, Nucl. Instrum. Meth. A **497**, 414 (2003)
Borexino Collaboration, Nucl. Instrum. Meth. A **460**, 272 (2001)
SNO Collaboration, Nucl. Instrum. Meth. A **421**, 601 (1999)
Elegant V Collaboration, Nucl. Instrum. Meth. A **459**, 177 (2001).

[124] F. Bella and W. Plastino, INFN-LNGS annual report 1999, 199 (1999)
D. A. Bauer, Topical workshop on low radioactivity techniques 2004, AIP Conf. Proc. 785, 65 (2005)
I. Blevis *et al.*, Nucl. Instrum. Meth. A **517**, 139 (2004).

[125] J. Lee *et al.*, paper in preparation.

[126] G. Gangopadhyay, D. Banerjee, and R. Bhattacharya, Nucl. Instrum. Meth. A **336**, 186 (1993).

[127] H. R. Krall, IEEE transactions on Nuclear Science NS-14 455 (1967)
G. A. Morton, H. M. Smith, and R. Wasserman, IEEE transactions on Nuclear Science NS-14 443 (1967).

[128] V. A. Kudryavtsev *et al.*, Astropart. Phys. **19**, 691 (2003).

[129] M. Robinson *et al.*, Nucl. Instrum. Meth. A **545**, 225 (2005).

[130] V. A. Kudryavtsev *et al.*, Astropart. Phys. **17**, 401 (2002).

[131] see the http://roofit.sourceforge.net/.

[132] L. Lyons, Statistics for nuclear and particle physicists, Cambridge University Press (1986) New York.

[133] G. J. Feldman and R. D. Cousins, Phys. Rev. D **57**, 3873 (1998), arXiv:physics/0001031.

[134] V. A. Bednyakov *et al.*, arXiv:hep-ph/0412067.

[135] M. T. Ressel and D. J. Dean, Phys. Rev. C **56**, 535 (1997).

[136] V. A. Bednyakov and F. Simkovic, Phys. Part. Nucl. **36**, 131 (2005), arXiv:hep-ph/0406218.

[137] E. Holmlund *et al.*, Phys. Lett. B **584**, 31 (2004)
M. Kortelainen *et al.*, Phys. Lett. B **632**, 226 (2006).

[138] J. Engel *et al.*, arXiv:hep-ph/9504322.

[139] M. T. Ressel *et al.*, Phys. Rev. D **48**, 5519 (1993).

[140] Private comunication with J. Toivanen.

[141] F. Iachello, L. M. Krauss, and G. Maino, Phys. Lett. B **254**, 220 (1991).

[142] A. Kurylov and M. Kamionkowski, Phys. Rev. D **69**, 063503 (2004).

[143] R. Barate *et al.*, Phys. Lett. B **499**, 67 (2001).

[144] T. Tabarelli de Fatis, Nucl. Instrum. Meth. A **385**, 366 (1997).

[145] J. Rademacker, Nucl. Instrum. Meth. A **484**, 432 (2002).